THE SHALLOW ATMOSPHERIC COAL FIRED FLUIDIZED-BED COMBUSTOR FURNACE

-by-

DONALD P. NAUDÉ

Submitted to the University of Cape Town in fulfilment of the requirements for the degree of Doctor of Philosophy.

September 1980

ABSTRACT

The fluidized bed combustor furnace is considered as being made up of two zones, the fluidized bed itself and an upper free-board zone for the disengagement of ejected particles and in which further combustion may take place simultaneously with the radiative transfer of heat to the surrounding walls. A general review of the literature pertaining to the combustion of coal in a fluidized bed of inert particles as well as the transfer of heat from the fluidized bed to immersed cooling surfaces is presented. In view of the fluidized bed furnace incorporating the freeboard region, a review of furnace design methods is also presented. The status of research and development in various parts of the world is considered with particular reference to the generation of steam by means of the combustion of coal in an atmospheric fluidized bed combustion unit.

A 1 000 mm diameter water cooled furnace was built to study the phenomenon on an industrial scale. The unit represents the furnace section of a small industrial boiler capable of generating 3 000 kg/h of steam. The test facility has been extensively instrumented to enable the measurement of the heat transferred throughout the furnace flue i.e. both within the fluidized bed and to the freeboard region extending above the bed. Further instrumentation was utilized to enable the evaluation of a heat balance, the analysis of entrained particulates, and the analysis of the resulting products of combustion. Provision was made to enable the introduction of secondary air so that the fluidized bed could be operated substoichiometrically thereby promoting a secondary combustion reaction in the freeboard region. A horizontal cooling pipe was introduced into the bed to enable a study of the heat transfer to an immersed cooling surface to be made. Two methods of introducing the fuel to the bed have been provided. The first enables the coal to be screw fed into the bottom of the bed whilst the second feeder distributes the coal onto the upper surface of the bed.

Two coals were burnt in relatively shallow fluidized beds of coarse particles (having a harmonic mean diameter of 0,847 mm). The operating parameters were selected to be similar to those which would most likely be utilized commercially. The ranges over which the main parameters were investigated can be summarized as :

Bed Temperature	:	780 to 1000°C
Superficial gas velocity	:	1,0 to 3,0 m/s
Static bed height	:	100 to 250 mm

Correlations were established for the expanded bed height, the heat transfer coefficient from the bed to the peripheral surface and from the bed to an immersed horizontal tube. Heat transfer and the extent of combustion in the freeboard zone were evaluated with the aid of an analytical model as well as from specific measurements. However no correlations could be obtained for either the overall combustion efficiency or the entrainment rate. Analysis of the entrained material did indicate that the size grading of the resulting ash was dependent upon the type of coal fired as well as the fuel feed system employed.

The heat transfer mechanism in the fluidized bed has been described by a packet theory modified by the introduction of a contact resistance. The use of the theory has indicated that the heat transfer at the peripheral surface is largely effected by the particle residence time at the surface and hence the dynamic bed height, whilst the heat transferred to an immersed surface within the bed is largely effected by the frequency of the bubble motion. This leads to the postulate that a general motion takes place in shallow beds too, with an upward motion in the central region and a downflow of particulates along the peripheral walls. A zone method of analysis was utilized to describe the heat transfer phenomenon in the freeboard region enabling the overall performance of the furnace to be described in terms of the fluidized bed operating parameters. A simpler one gas-zone two surface-zone model was formulated which led to the development of a characteristic equation describing the heat transfer in the freeboard zone of a fluidized bed reactor furnace.

The thesis makes a contribution to existing knowledge in the following areas:

(i) A detailed analysis of the heat transfer and combustion phenomena in the freeboard of and within a shallow fluidized bed of relatively coarse inert particulates on an industrial scale has been presented.

(ii) The heat transfer to both peripheral and immersed surfaces can be explained by a packet theory mechanism modified by means of a contact resistance which leads to a description of the general flow of particulates with an upward flow in the central region and a downward flow of the particulates along the peripheral walls. This is supported by experimental evidence.

(iii) The formulation of a simplified expression which characterizes the heat transfer performance of the freeboard region of the fluidized bed combustor.

(iv) The use of the characteristic equations of the above bed furnace region for predicting the amount of combustion which takes place in the freeboard from simple heat balance data.

ACKNOWLEDGEMENTS

The author wishes to express his sincere thanks and appreciation to Professor R.K. Dutkiewicz for his active interest and valued advice, and further for his confidence and promotion of fluidized combustion.

Further he would like to acknowledge the support of John Thompson Africa (Pty.) Ltd. who funded the entire project and in particular to Mr. N. Magasiner for his advice and valued comments. The assistance of the workshop staff of John Thompson Africa (Pty.) Ltd., particularly Mr. H. Marshall and Mr. L. de Swardt as well as the enthusiastic assistance of Mr. R. Holing is gratefully acknowledged.

The author's thanks are extended to Associate Professor R.M. Stegan for his advice and comments, and to the staff of the Mechanical Engineering workshop of the University of Cape Town, particularly Mr. L.R. Watkins who manufactured much of the complex instrumentation associated with the test rig.

A word of thanks is also extended to Mrs. M. Stewart who so willingly typed this entire thesis, and finally the patience and encouragement of the author's wife is gratefully acknowledged.

CONDENSED TABLE OF CONTENTS*)

*) NOTE: The complete table of contents, list of tables and list of figures are contained in Appendix J at the end of the thesis.

NOMENCLATURE

			Units
Lower Case Symbols			
a	-	fraction of ash in coal	-
	-	constant defined by equation (38)	-
	-	distance between bed pressure tappings	m
	-	thickness of the heat flux pad	mm
$a_{g,i}$	-	weighting factor for gases in the gas emissivity model	-
a_{gt}	-	weighting factor for gases at temperature 't' in the gas emissivity model	-
$a_{p,i}$	-	weighting factor for dust clouds in the gas emissivity model	-
b	-	constant defined by equation (31)	m
	-	constant defined by equation (38)	-
	-	length of the heat flux pad	mm
b_i	-	coefficients of the multiple regression equation	-
c	-	constant defined by equation (38)	-
c_c	-	fraction of carbon contained in the ash	
c_p	-	specific heat where c_{pg} refers to the gas and c_{ps} refers to the solids	kJ/kgC
d	-	particle diameter	m
d_B	-	bubble diameter at a height h above the distributor	m
d_{BM}	-	maximum bubble diameter as a result of coalescence	m
d_{BO}	-	initial bubble diameter at the distributor	m
d_p	-	mean particle diameter	m
d_x	-	particle diameter for mass fraction x	m
f_b	-	fraction of bubbles in the bed	-
f_d	-	fraction of particles in the bed of size smaller than d	-

Lower Case Symbols

			Units
g	-	gravitational constant	m/s^2
g_{ij}	-	element of the inverted bivariate correlation coefficient matrix	
$\overline{g_i g_j}$	-	direct exchange area between gas zone i and gas zone j	m^2
h	-	heat transfer coefficient where the subscripts b, p,c, g,c, c, r, t, w, and o refer to the bubble, particle convective, gas convective, convective, radiative, total, wall and outside components of the heat transfer coefficient.	W/m^2C
h	-	height at a point in the bed	m
h_c	-	unburnt carbon loss	-
k	-	first order particulate phase velocity constant	s^{-1}
	-	thermal conductivity where the subscripts f, and m refer to the gas and combined gas-particle phase respectively	W/mC
k^*	-	dimensionless velocity constant	-
k_g	-	mass transfer coefficient	m/s
$k_{g,i}$	-	gas absorption coefficient for the ith gas component	$m^{-1}atm^{-1}$
$k_{p,i}$	-	particle absorption coefficient for a cloud of particles represented by as a compound grey gas.	m^{-1}
l	-	distance between an inner and an outer thermocouple junction in the heat flux pad.	m
m	-	number of independent variables in the regression analysis	-
$m(d)$	-	mass of particles of size d	kg
m_a	-	mass of air per kg of fuel burnt	kg

Lower Case Symbols

			Units
m_{ao}	-	mass of air required for the stoichiometric combustion of 1 kg of fuel	kg
m_g	-	mass of gas per kg of fuel burnt	kg
m_{go}	-	mass of gas produced from the stoichiometric combustion of 1 kg of fuel	kg
n	-	molar flow of oxygen to a coal particle	mol/s
	-	feeder speed	rpm
	-	number of points used in the regression analysis	-
Δp_{mf}	-	pressure drop through a bed of particulate material at a velocity of u_{mf}.	Pa
p	-	partial pressure where the subscripts c and w refer to carbon dioxide and water vapour respectively	atm
$p_c(d)$	-	size distribution of the combustible particles within a fluidized bed	m^{-1}
$p_o(d)$	-	size distribution of the feed material.	m^{-1}
$p_1(d)$	-	size distribution of the bed overflow material	m^{-1}
r	-	particle radius, equation (I3)	m
r_{ij}	-	bivariate correlation coefficient between x_i and x_j.	-
s	-	fraction of total air supplied as secondary air.	-
$\overline{s_i g_j}$	-	direct exchange area between surface zone i and gas zone j	m^2
$\overline{s_i s_j}$	-	direct exchange area between surface zone i and surface zone j.	m^2
s_{Xi}	-	sample variance of X_i	-
s_{XiXj}	-	covariance between X_i and X_j.	-

Units

Lower Case Symbols

t	-	percentile of Student t-distribution	-
	-	temperature where subscript g refers to gas	^{o}C
u	-	velocity where the subscripts f, mf, and t refer to the superficial, minimum fluidizing and particle terminal velocities respectively	m/s
u_B	-	natural velocity of rise of a bubble.	m/s
u_{BS}	-	absolute velocity of rise of a bubble.	m/s
x	-	mass fraction of particles in a particular size interval	-

Upper Case Symbols

A	-	constant	-
	-	abrasion rate of constant	m^{-1}
	-	surface area	m^2
A_i	-	area of surface zone i	m^2
A^*	-	modified abrasion rate constant	m^{-1}
B	-	constant	-
B_i	-	standard normal correlation coefficient	-
B_i^1	-	interval estimate of the standard normal correlation coefficient	-
C	-	concentration of a particular component, where the subscripts b and o refer to the molar oxygen concentration of the bubble phase and of the inlet air respectively	mol/m^3
C_p	-	concentration of particulates in the flue gas, equation (66).	kg/m^3
	-	molar oxygen concentration of the particulate phase	mol/m^3

Upper Case Symbols

			Units
D'	-	reduced firing density, equation (90)	-
E	-	hemispherical black body emissive power	kW/m^2
F	-	percentile of F-distribution.	-
	-	mass flow rates where the subscripts 0, 1 and 2 refer to the feed material, overflow material and entrained material respectively.	kg/s
G	-	gas diffusion coefficient	m^2/s
$\overline{G_iG_j}$	-	total exchange area between gas zone i and gas zone j	m^2
GW,GB	-	total exchange areas defined by the two surface zone one gas zone model	m^2
H	-	incident radiant flux density	kW/m^2
	-	bed height where the subscripts st, dyn and mf refer to the static bed height, the expanded dynamic bed height and the height at minimum fluidization velocity respectively.	m
H_f	-	dynamic bed height evaluated from equation (31)	m
$H_{st,r}$	-	ratio of the static bed height to a bed height of 100 mm and referred to as the reduced static bed height	-
$I(d,d_{max})$	-	function defined by equation (125)	-
K	-	elutriation rate constant	s^{-1}
	-	absorption coefficient of a gas and particulate cloud generally used to form the product KL or the absorption strength of the cloud	m^{-1}
K^*	-	elutriation rate constant.	kg/m^2s
K^1	-	entrainment rate constant	kg/m^2s
K_{bp}	-	gas interchange coefficient between the bubble and the particulate phases.	s^{-1}

Upper Case Symbols

			Units
K_i	-	combined absorption coefficient for the ith component defined by equation (24).	m^{-1}
L	-	mean beam length	m
M	-	bed mass where the subscripts b, c and d refer to the total bed mass, the mass of carbon in the bed and the mass of particles of diameter d.	kg
	-	mass flow rate where the subscripts 1/2, f, fu, fo, a and g refer to the primary air flow rate to one of the primary air windboxes, the coal flow rate, underbed coal flow rate, above bed coal flow rate, total air and total gas flow rates respectively.	kg/s
N	-	fluidization index defined as $(u_f-u_{mf})/u_{mf}$	-
O	-	overflow rate	kg/s
Q'	-	reduced rate of heat transfer from the gases equation (89)	-
Q_B	-	effective volumetric interchange between bubble and bed	m^3/s
Q_F	-	rate of heat input to the freeboard zone	kW
Q_g	-	heat removed in the exhaust gases	kW
Q_G	-	heat absorbed by cooling surfaces in the freeboard zone	kW
Q_{lib}	-	heat liberated where the subscripts f and b refer to the freeboard and bed zones respectively	kW
$\bar{Q}_{lib}$	-	heat liberated per unit plan area of reactor vessel	kW/m^2
R	-	multiple correlation coefficient	-
	-	reflected radiant flux density	kW/m^2
	-	rate coefficients defined by equations (25) and (26), where the subscripts t, m and c refer to the overall, the mass transfer and the chemical reaction rates respectively	kg/m^2skPa

Units

Upper Case Symbols

R	-	thermal resistance where the subscripts p and w refer to the resistance due to a 'packet' of solids and to the wall contact resistance respectively	$m^2{}^oC/W$
S	-	splashing rate constant	s^{-1}
S_1	-	stirring factor	s^{-1}
S_p	-	specific surface area per unit mass of particle, equation (66)	m^2/kg
$\overline{S_iS_j}$	-	total exchange area between surface zone i and surface zone j	m^2
$\overline{S_iG_j}$	-	total exchange area between surface zone i and gas zone j	m^2
T	-	absolute temperature where the subscripts b, t, w refer to the bed, tube and peripheral wall respectively	^oK
	-	absolute temperature where the subscripts to and ti refer to the outer and inner thermocouple temperatures of the heat transfer probe.	^oK
T_F	-	pseudo flame temperature, equation (49).	^oK
T_o	-	surrounding temperature.	^oK
V_i	-	volume of the ith gas zone	m^3
V_B	-	bubble volume	m^3
W	-	leaving radiant flux density	kW/m^2
X	-	transfer factor denoting the number of times a bubble interchanges its volume as it moves through a bed of height H.	-
X_i	-	independent variable of multiple regression analysis	-
Y	-	dependent variable of multiple regression analysis	-
Z	-	mean removal rate constant defined by equation (I31).	s^{-1}

Dimensionless Numbers

Ar	–	Archimedes number $\left(\frac{\rho_s - \rho_f}{\mu^2} \cdot g \cdot \rho_f \cdot d^3\right)$
Nu_{max}	–	maximum Nusselt number $(h_{max} \cdot d_p / k_f)$
Nu_p	–	Nusselt number referred to the particle diameter $(h \cdot d_p / k_f)$
N_{to}	–	Nusselt number referred to the tube diameter $(h \cdot d_{to} / k_f)$
Re_{mf}	–	Reynolds number $(\rho_f \cdot u_{mf} \cdot d_p / \mu_f)$
Re_p	–	Reynolds number $(\rho_f \cdot u_f \cdot d_p / \mu_f)$
Re_t	–	Reynolds number $(\rho_f \cdot u_i \cdot d_p / \mu_f)$
Re_{to}	–	Reynolds number $(\rho_f \cdot u_f \cdot d_{to} / \mu_f)$
Pr	–	Prandtl number $(c_p \cdot \mu_f / k_f)$
Sh	–	Sherwood number $(k_f \cdot d / G)$.
Z	–	dimensionless number defined by equation (30)

Greek Symbols

			Units
$\bar{\alpha}$, α_{mf}	–	mean bed voidage and voidage at the minimum fluidization velocity	–
α_g	–	gas absorptivity	–
δ_w	–	extent of region adjacent to the wall used in the definition of the contact resistance	–
δ_{ij}	–	Kronecker delta defined on page 150	–
	–	gas emissivity	
η_c	–	combustion efficiency, equation (54)	
η_f	–	furnace efficiency, equation (84).	
θ_g θ_w θ_o θ_Δ	–	ratio of Tg, Tw, To and Δ to the pseudo flame temperature.	–
λ	–	excess air factor	–
μ_f	–	dynamic viscosity of the gas	kg/ms

Greek Symbols			Units
ν, ν_d, ν_s	-	frequency of bubble contact with an immersed tube, mean frequency of variation of the particle convective heat transfer coefficient between the bed and a cooling tube for a deep and a shallow fluidized bed, equation (48)	s^{-1}
ρ_f, ρ_s, ρ_c, ρ_e	-	density of the fluidizing gas, the solid particles, the coal and the effective density of a gas containing entrained particulates as in equation (7).	kg/m^3
σ	-	Stefan-Boltzmann constant ($56,7 \cdot 10^{-12} kW/m^2 \cdot K^4$)	
τ, τ_b	-	time, period for bubble to traverse the height of the fluidized bed	s
ϕ_s	-	particle shape factor	-
$\Gamma(d)$	-	rate expression for particle shrinkage	m/s
$\Gamma_a(d)$	-	rate expression for particle shrinkage due to abrasion	m/s
$\Gamma_c(d)$	-	rate expression for particle shrinkage due to combustion	m/s
Δ	-	difference between freeboard radiating temperature gas exhaust temperature	^oK
Θ	-	ratio of bed temperature to 273^oK	-
Φ	-	heat flux	kW/m^2
ψ	-	reactivity of a fuel as defined by equation (25)	-

Greek Symbols			Units
ν, ν_d, ν_s	-	frequency of bubble contact with an immersed tube, mean frequency of variation of the particle convective heat transfer coefficient between the bed and a cooling tube for a deep and a shallow fluidized bed, equation (48)	s^{-1}
ρ_f, ρ_s, ρ_c, ρ_e	-	density of the fluidizing gas, the solid particles, the coal and the effective density of a gas containing entrained particulates as in equation (7).	kg/m^3
σ	-	Stefan-Boltzmann constant ($56,7 \cdot 10^{-12} kW/m^2 \cdot K^4$)	
τ, τ_b	-	time, period for bubble to traverse the height of the fluidized bed	s
ϕ_s	-	particle shape factor	-
$\Gamma(d)$	-	rate expression for particle shrinkage	m/s
$\Gamma_a(d)$	-	rate expression for particle shrinkage due to abrasion	m/s
$\Gamma_c(d)$	-	rate expression for particle shrinkage due to combustion	m/s
Δ	-	difference between freeboard radiating temperature gas exhaust temperature	^oK
Θ	-	ratio of bed temperature to 273^oK	-
Φ	-	heat flux	kW/m^2
ψ	-	reactivity of a fuel as defined by equation (25)	-

ABBREVIATIONS

AIChE	-	American Institute of Chemical Engineers
ASME	-	American Society of Mechanical Engineers
BCURA	-	British Coal Utilization Research Association
CEGB	-	Central Electricity Generating Board
CRE	-	Coal Research Establishment
CSIRO	-	Commonwealth Scientific and Industrial Research Organization
DOE	-	Department of Energy
EPA	-	Environmental Protection Agency
EPRI	-	Electric Power Research Institute
ERDA	-	Energy Research and Development Authority
FRI	-	Fuel Research Institute of South Africa
NCB	-	National Coal Board
NEI	-	Northern Engineering Industries
NRDC	-	National Research Development Corporation

CHAPTER 1

INTRODUCTION

The twentieth century has been characterised by a desire, especially on the part of the Western world, for improved living standards. This has led to dramatic and exponential increases in energy consumption. South Africa as a developing nation, has not escaped this trend (1) and it is therefore imperative that the finite energy reserves of the country be utilized in the most economic and efficient manner. The primary source of energy in South Africa has been based and will continue to be based for the foreseeable future, on coal and this increased energy consumption can be equated to increased demands for coal.

Coal besides being utilized as a source of energy, forms an important raw material for the chemical industry as well as being consumed by the iron and steel-making industry. In the former, coal is upgraded to form other products, while only high grade metallurgical coal can be used in the ferro-alloy industry. Low calorific value coals having correspondingly high ash contents constitute the major portion of the coal reserves (2) with the ash being more inherently or homogeneously dispersed in the coal body than the ash found in coals in the northern hemisphere (3). South African coals are therefore difficult to wash to produce a low ash quality material. Proven, extractable coal reserves, on the basis of coals having an ash content of less than 35 per cent have been estimated as 25 000 million tons (2) of which only a small proportion is made up of metallurgical coal, anthracite and low ash steam coal. This coal should be conserved for use in specific industries while the poorer grades of coal can be burnt as a source of energy for steam raising in both the industrial and electricity supply industries. Further, the possible utilization of coals having ash contents in excess of 35 per cent would greatly increase the available coal reserves.

It is therefore evident, that the coal resources though large, are nevertheless finite and must be used as wisely as possible. This means that coal previously unmined because of its poor quality, and coal discarded from coal washing associated with the export-market, must be used for energy production. Further wastage has occurred due to the over supply of duff coal (i.e. coal of size less than 6,3mm)to the industrial market which cannot utilize this fuel efficiently on traditional forms of coal burning equipment. This wastage of duff coal "is therefore a problem area where solutions must be found; not only in putting good coal to use but also by decreasing the pollution of the atmosphere by the burning of the fines on a dump" (2). Poor quality coal can therefore be defined as that which is not easily utilized.

Earlier work by Naudé and Dutkiewicz (4) indicated the potential of fluidized bed combustion for burning these poor quality fuels. The combustion efficiencies were largely affected by the proportion of fines contained in the fuel and in many instances large carbon losses were measured.

1.1 THE FLUIDIZED BED COMBUSTOR FURNACE

In order to utilize the energy contained in these poor quality fuels, the chemical energy has to be converted to heat for raising the temperature of a working medium, or more commonly for the generation of steam. The fluidized bed combustor furnace utilized for steam raising therefore is made up of a fluidized bed zone and a radiant furnace chamber extending above the fluidized bed and forming the freeboard or disengagement space for those particles ejected into the region above the bed. The main components of the furnace are illustrated diagramatically in Figure 1.

The major proportion of the energy in the fuel is liberated in the bed zone, whilst the high heat transfer coefficients associated with fluidized beds ensure that a considerable amount of heat is transferred to cooling surfaces in contact

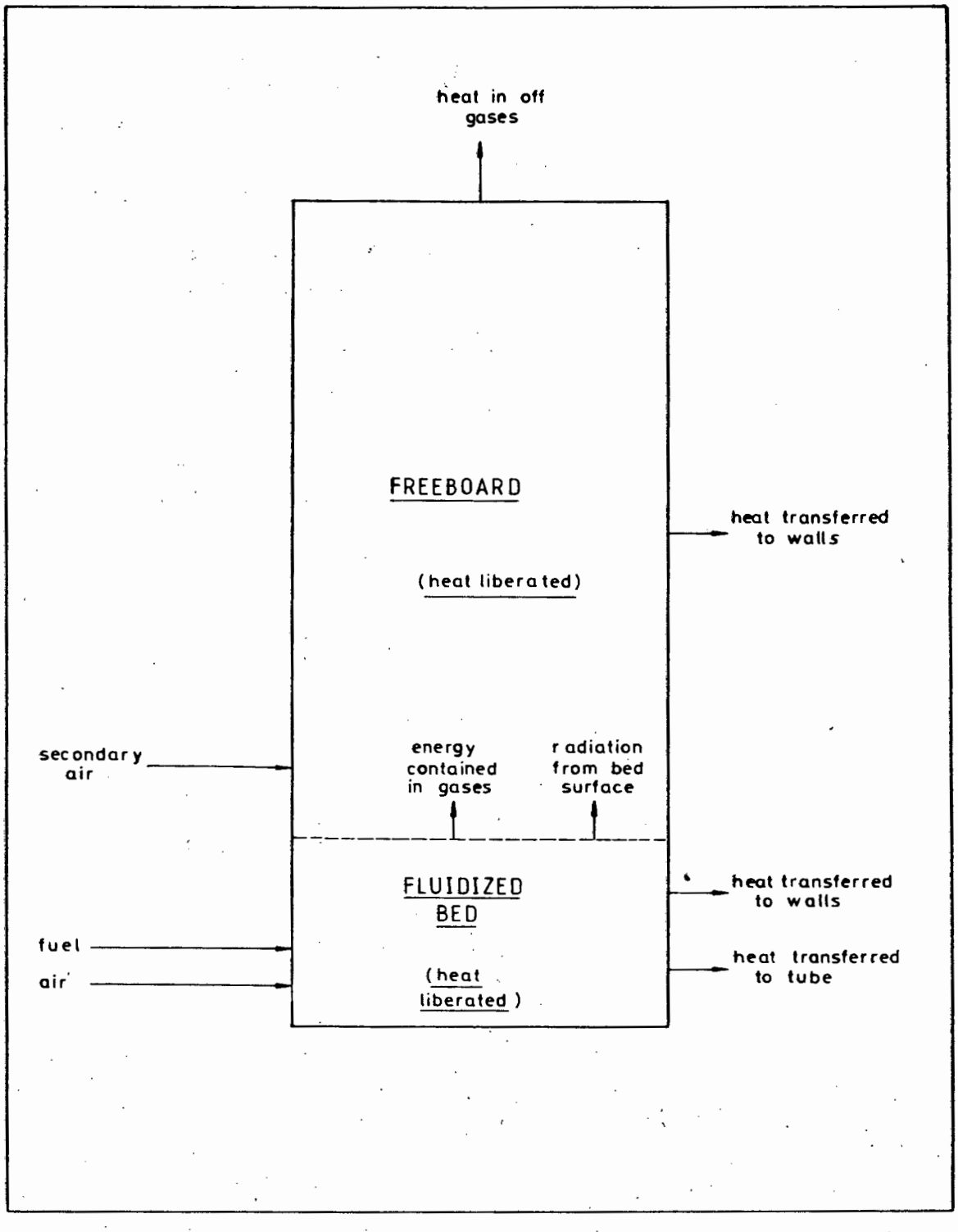

Figure 1 : Diagrammatic representation of a fluidized bed combustor furnace.

with the fluidized bed. The freeboard section above the bed forms a radiant heat-transfer chamber in which both homogeneous gas combustion and the further combustion of entrained fuel may take place.

A definite physical boundary between the two zones is not apparent due to the expansion of the fluidized bed as the operating conditions change and in particular as the gas velocity increases. It is therefore evident that the coal-fired fluidized bed combustor furnace accommodates both heat transfer and combustion processes in each of the two zones.

The work done by a number of investigators into each of these phenomena viz. fluidization, heat transfer above and within the fluidized bed, combustion and the entrainment of particulates is reviewed in the following sections. Although both liquid and gaseous fuels may be burnt in a fluidized bed, only the combustion of coal was considered in view of its relevance to South African industry.

1.2 FLUIDIZATION

Fluidization is not a new technique, but has been used extensively in the chemical industry, becoming "after 1940 one of the chemical engineers' and extractive metallurgists' most important tools" (5). Since then a vast quantity of information both theoretical and empirical has been accumulated on the subject.

The process of gas fluidization can be described by considering a bed of particles resting on a perforated or porous plate or similar device which would serve as an air distributor. At low flow rates, the air passes upwards through the bed between the particles which behave as a fixed bed. As the flow rate is increased, a point will be reached at which the pressure drop across the bed becomes equal to the weight per unit area of the bed and the bed is then at the point of becoming fluidized. The velocity measured in terms of the empty

vessel is designated as the superficial gas velocity and its value at which fluidization occurs is called the minimum fluidizing velocity. If the flow rate is increased above this value, "one of two things will occur; either the bed will continue to expand so that the average distance between the particles will become greater, or the excess fluid will pass through the bed in the form of bubbles giving rise essentially to a two phase system. These two types of fluidization are referred to as being respectively 'particulate' and 'aggregative' " (6, p.26). In general, aggregative fluidization is associated with most gas-solid systems and particulate fluidization is associated with most liquid-solid systems. Harrison et al (7) have suggested that the type of fluidization could be related to the maximum stable bubble size which can exist in the bed. They have also found that this can be related to the mean diameter of the particles. Kunii and Levenspiel (8, p.80) attribute the difference between particulate and aggregative fluidization to the difference in the densities between the particulates and the fluidizing medium.

The work described in this thesis makes exclusive use of aggregative fluidized beds and only this system is considered in the following discussion. As the gas flow is increased through the bed the fluidization becomes steadily more vigorous taking on the appearance of a violently boiling liquid. Further increases in the gas velocity may result in a transition from the bubbling regime to a slug flow regime which is also dependent on the geometrical configuration of the system. A limiting condition will eventually be reached at which the gas velocity becomes equal to the free fall velocity of the particles, in other words the particle terminal velocity. At this point the particles are carried out of the vessel in the fluidizing gas. The fluidizing vessel then behaves as a pneumatic conveying tube. The qualitative differences between the various fluidization regimes have been illustrated by Zenz and Othmer (9, p.231) and their diagram

is reproduced in Figure 2.

The fluidization process is therefore limited by the minimum fluidization velocity on the one hand, and the particle terminal velocity on the other. Further, fluidization across the cross section of the bed should be uniform to overcome problems which may arise as a result of channelling due to preferential gas flow through the bed or random slumping of various sections of the bed.

1.2.1 The Minimum Fluidizing Velocity

The determination of the minimum fluidizing velocity is of the utmost importance in the design of fluidized beds as it sets a lower limit for the fluid throughput and is a basic variable of those mathematical models based on the two phase theory of fluidization. The definition of the minimum fluidizing velocity may be simply stated as the velocity at which the bed of particles becomes fluidized. In practice the point of fluidization is not as clearly defined as the preceding definition may imply and the definition is best described by considering Figure 3. Point A represents the bed of particles when a gas is passed through the bed for the first time. As the velocity is increased, the pressure drop increases in accordance with a fixed-bed pressure-drop to velocity relationship. Because of the tendency of the particles to interlock with one another, partial bridging can occur and pressure drops in excess of the theoretical value will be obtained (6, ch.3). The curve passes through a maximum pressure drop exhibiting a small characteristic "hump" as shown in Figure 3. On increasing the velocity still further, the pressure drop across the bed remains constant until the velocity attains a value equal to the particle terminal velocity. At this point the fluidized bed reactor vessel behaves as a pneumatic conveying tube. On decreasing the velocity from point E to B, the pressure drop through the bed remains constant once again. Point B represents a deviation from the ideal de-fluidizing curve which is shown by the dashed lines. The deviation is a result of

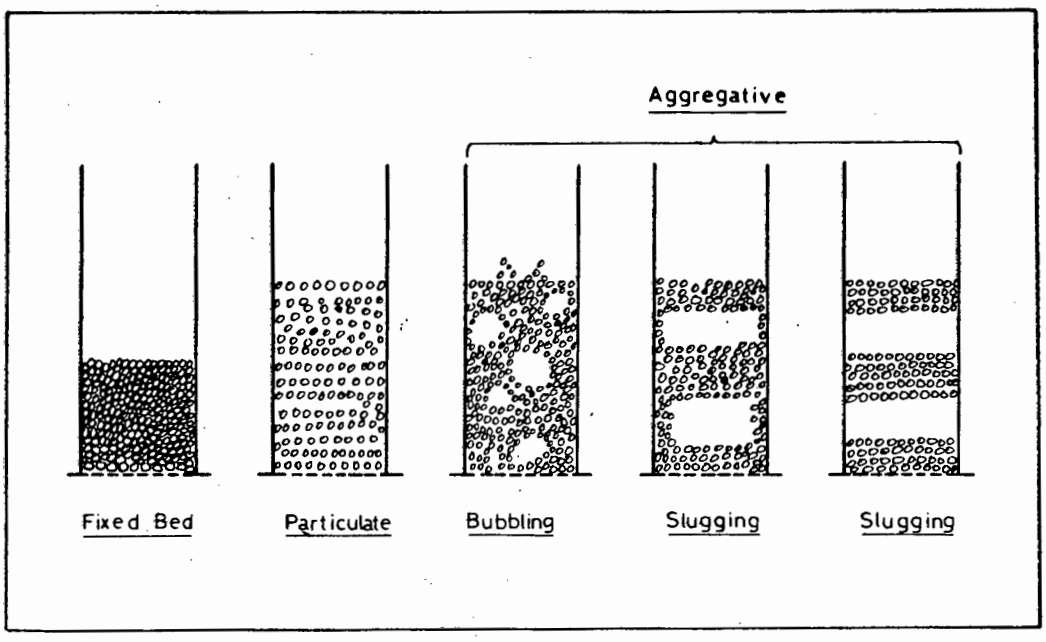

Figure 2 : Qualitative representation of the different regimes of fluidization.

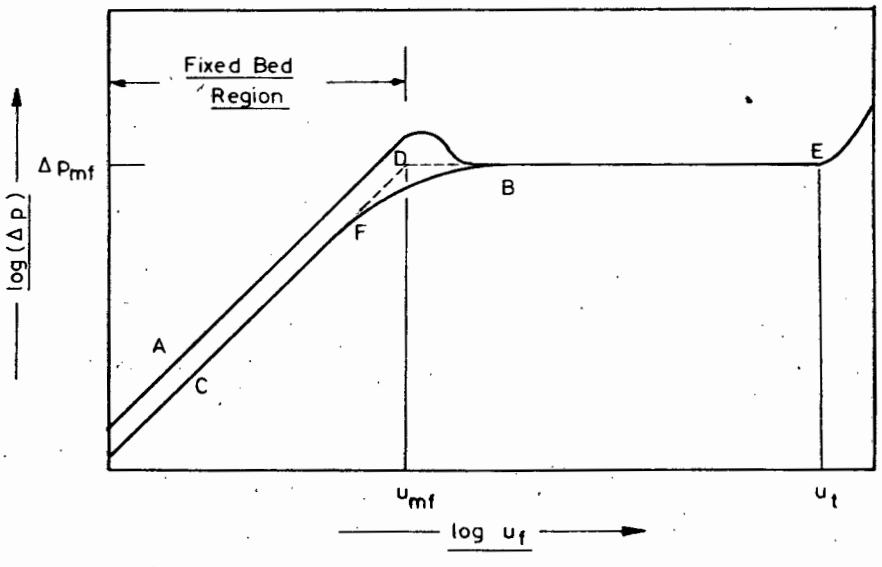

Figure 3 : Fluidization curve to illustrate some deviations from ideal behaviour.

non-uniformity in the bed structure resulting in fixed and fluidized regions coexisting within the bed. Although the bed may appear to be well fluidized, part of the bed may be supported by the distributor resulting in the pressure drop being less than expected. Further decreases in velocity result in a pressure drop characteristic displaced to the right of the original line. This is as a result of the particles becoming rearranged so that the resistance to flow is minimized and in general the voidage will have increased to the value existing at the point of minimum fluidization. Further increasing and decreasing of the gas velocity will be represented by the line CFBE. The minimum fluidizing velocity can be obtained in practice by determining the intersection of the constant pressure line and the straight section of the line CF obtained on slowly decreasing the velocity. The intersection of these two lines is indicated by the point D in figure 3.

In view of the variation of the minimum fluidization velocity with temperature (10) it is necessary to be able to calculate the minimum fluidizing velocity. Three different semi-empirical methods have been employed. The first involves the determination of the drag coefficient for a single particle which is found to be related to the drag force of the multi-particle system by the voidage fraction raised to some power (11), (12). The second approach adopted in a later paper (13) proposes that the incipient fluidization conditions be characterized by a generalized fluidization and sedimentation correlation. Finally, the most common method is based upon a fixed bed pressure drop correlation where the pressure drop is set equal to the effective solid weight of the bed. The voidage draction at minimum fluidization conditions is then used in this correlation. The bed pressure drop under these conditions is simply the constant pressure indicated in Figure 3 and can be obtained from equation (1).

$$\Delta p_{mf} = H_{mf} \cdot (1 - \alpha_{mf}) \cdot (\rho_s - \rho_f) \cdot g \qquad (1)$$

For small particles, where the flow can be assumed to be laminar, a Kozeny-Carman type relation is generally used to relate fixed bed pressure drops to velocity. As the particle Reynolds number increases from about 20 to 500, the flow would be in the transitional flow regime and Leva (14, ch.3) recommends that the pressure drop be proportional to velocity raised to a power, the value of the exponent depending on the Reynolds number and ranging from unity to two. Hence for larger particles a more general equation such as the Ergun pressure drop equation for fixed beds would yield the best results (6, p.35). Equation (2) represents this relationship at minimum fluidizing conditions from which the minimum fluidizing velocity can be calculated after the particle Reynolds number has been evaluated.

$$Ar = \frac{150 \cdot (1-\alpha_{mf})}{\phi_s^2 \cdot \alpha_{mf}^3} Re_{mf} + \frac{1,75}{\phi_s \cdot \alpha_{mf}^3} Re_{mf}^2 \qquad (2)$$

The first term on the right hand side of equation (2) is proportional to the losses as a result of viscous forces, whilst the second is proportional to the kinetic energy losses. It is of interest to note that the Archimedes number Ar, is dependent only on the temperature of the fluid and the particle diameter raised to the third power. Wen and Yu (12) have correlated the data of numerous workers into an equation in which the particle shape factor and the bed voidage at minimum fluidizing velocity have been eliminated as parameters. This correlation is represented by equation (3) and has a standard deviation of 34% from the data used in its derivation.

$$Ar = 1650 \cdot Re_{mf} + 24,5 \cdot Re_{mf}^2 \qquad (3)$$

Another simplified relationship of Todes (6, p.513) obtained by assuming the voidage to be 0,4 at the minimum fluidizing velocity is given by equation (4).

$$Re_{mf} = \frac{Ar}{1400 + 5,22\sqrt{Ar}} \qquad (4)$$

Pata and Hartmann (15) have compared the results obtained from a number of different sizes of lime and limestone particles with the predicted values for minimum fluidizing velocities with a number of different empirical relationships. The Ergun relationship given by equation (2) was found to yield the best predictions whilst the use of equation (4) yielded results only marginally inferior to those of equation (2) in most instances. In some cases, and particularly with the limestone particles, better results could be obtained from the use of equation (4). In view of the simplicity of this latter relationship, it was decided to utilize equation (4) for the evaluation of minimum fluidization velocities in this thesis.

1.2.2 Entrainment and Elutriation

Kunii and Levenspiel (8, ch.10) make a distinction between entrainment and elutriation. They state that "in general, entrainment refers to the removal of solids from the bed by the fluidizing gas...." and that "elutriation refers to the separation or removal of the fines". From this it is evident that the elutriation rate approaches the entrainment rate as the freeboard height becomes very large. Thus elutriation refers only to the removal of those particles less than the particle size d_t, whose terminal velocity is the same as the superficial gas velocity.

A number of workers have correlated elutriation rates in terms of an elutriation rate constant by an equation of the form

$$\frac{1}{A}\frac{dm(d)}{d\tau} = -K^{*}\frac{m(d)}{M} \qquad (5)$$

Two of these correlations by Wen and Hashinger (16), and Yagi Aochi (2, p.646) have established elutriation rate constants in terms of a number of parameters but including the parameter $(u_f - u_t)$, i.e. the difference between the superficial gas velocity and the particle terminal velocity. Merrick and Highley (17) have found such existing correlations of elutriation rate constants to be inadequate, particularly for the finer particles and the coarser particles. Most of the correlations

predict that particles of diameter greater than the particle of size d_t, are not elutriated whereas it has been found (17) that even with freeboards of about 4 metres this is incorrect. Merrick and Highley conclude that the existing empirical and semi-empirical correlations which have generally been obtained from small slugging beds are not applicable to their data. They derive a new form of correlation based upon dimensionless groups incorporating the particle terminal velocity, the minimum fluidizing gas gelocity, the gas mass flow rate, and the particle entrainment rate. Their relationship is given by equation (6).

$$\frac{K'}{\rho_f \cdot u_f} = A + 130 \cdot exp \{ - 10,4 \cdot (\frac{u_t}{u_f})^{0,5} \cdot (\frac{u_{mf}}{u_f - u_{mf}})^{0,25} \} \quad (6)$$

It is interesting to note that the use of the parameter (u_t/u_f) enables the prediction of particle entrainment rates even for those particles having terminal velocities in excess of the prevailing superficial gas velocity.

Geldart et al (18) have presented a similar equation and calculation procedure which also enables the prediction of the entrainment of particles greater than the particle of size d_t. They have further noted a significant increase in the carry-over rate of coarse particles when fine and coarse particles are mixed. They have incorporated this effect into their relationship for the entrainment rate constant by making use of an effective gas density $'\rho_e'$. Their relationship is given by equation (7).

$$\frac{K'}{\rho_e \cdot u_f} = B \cdot exp (- C \cdot \frac{u_t}{u_f}) \quad (7)$$

It should be noted that equations (6) and (7) are used for the derivation of the entrainment rate constant K^1 as opposed to the elutriation rate constant K. It should be evident that the elutriation rate constant K will be independent of the physical dimensions of the fluidized bed reactor vessel whereas the entrainment rate constant K^1 is dependent on the physical dimensions of the plant, the type of distributor and

so on. This dependence on the plant is accommodated by the constants A, B and C.

Gibbs (19), in his development of a combustion model, introduces a splashing rate constant to account for the entrainment of those particles of a size larger than would be elutriated. This second approach considers entrainment as being made up of two mechanisms, splashing and elutriation. This elutriation rate constant could be obtained from one of the well established correlations for elutriation (16), whilst the splashing rate constant would have to be obtained empirically. This latter constant would clearly be dependent on the plant dimensions and corrections to this value would have to be made when comparing the results from different fluidized bed reactors.

1.2.3 The Particle Terminal Velocity

Inherent in the determination of the elutriation and the entrainment rates is a knowledge of the particle terminal velocity. This is easily obtained from Stokes' law for low Reynolds numbers, the Schiller Naumann equation for intermediate values and Newton's law for high values (6,p.51). Pata and Hartmann (20) have investigated the use of various equations for predicting the terminal velocities of lime and limestone particles. From their results, the single relation proposed by Todes (20) and represented by equation (8) gave predictions of similar accuracy to those proposed by more complex formulations.

$$Re_t = Ar \,/\, (18{,}0 + \sqrt{Ar}) \qquad (8)$$

In view of its simplicity and its accuracy in velocity and particle size ranges close to those employed in the work described by this thesis, equation (8) has been employed for the determination of particle terminal velocities.

1.2.4 The Mean Particle Diameter

The bed material will be made up of particles having a range of diameters. It is therefore of value to define a mean particle diameter. A large number of different means or averages may be defined (9, ch.3), the significance of which is largely dependent on the use to which the material is to be applied. A number of workers have found that the volume to surface ratio of a particle best characterises the mean particle diameter for use in the fluidization relationships (21, p.68). For spherical particles, equation (9) should be applied.

$$d_p = \frac{1}{\Sigma\, x/d_x} \qquad (9)$$

The above equation can be used for non-spherical particles if the diameter of the sphere with the same specific surface as the particles is used. A shape factor or particle sphericity, is defined by equation (10) to allow the equations derived for spherical particles to be used for particles of different shapes.

$$\phi_s = \frac{\textit{surface area of equivalent volume sphere}}{\textit{surface area of the particle}} \qquad (10)$$

The diameter d_x of equation (9) is thus replaced by $\phi_s \cdot d_x$ for the equation to apply to a different shaped particle.

1.2.5 Large Particle Fluidization in Shallow Beds

Davidson and Harrison (22, p.19) have proposed the two phase theory of fluidization as a means of describing aggregative fluidization. The model is developed by considering a bed as a two phase system, consisting of a particulate phase in which the flow rate is equal to the flow rate at incipient fluidization, i.e. the voidage in this phase remains essentially the same as that at incipient fluidization; and a bubble phase carrying the flow in excess of that required to fluidize the bed. This two phase model was developed from work on relatively fine particles on small laboratory scale rigs.

Yerushalmi and Cankurt (23) define three fluidization regimes for fairly small particles (about 0,03 to 0,3 mm diameter) operating at high gas velocities. Initially a bubbling fluidized bed exists, "as the velocity across the bed is raised, the heterogeneous two phase character of the bed first peaks, then gradually changes giving way to a condition of increasing uniformity culminating in the turbulent state in which large or discrete bubbles or voids are absent. In the turbulent fluidized bed, there is an upper bed surface though it is considerably more diffuse than in a bubbling fluidized bed because of the greater freeboard activity attending operation at higher gas velocities" (23). On increasing the velocity still further, the fast fluidized bed develops in which all the particles are entrained and reintroduced after being separated from the gas stream in a cyclone. This third flow regime is similar to the circulating fluidized bed described by Reh (11). The original identification of a turbulent flow regime has been attributed to Lanneau (24) who also used very fine particles.

Fluidized beds of coarse particles, about 1 mm diameter particles, are generally employed in fluidized bed coal combustors. Further, these combustors have large cross sectional areas, and particularly in the case of atmospheric combustors the bed depths are limited to reduce the fan power requirements. This results in very low bed height to reactor-vessel diameter ratios and the well developed slug flow illustrated in Figure 2 may not be possible.

Canada et al (25) have also defined a bubbly flow and a turbulent flow regime for gas fluidized beds. However, in the transition from bubbly to the high velocity turbulent flow a further two regimes are identified; apparent slug flow, and a subset of the apparent slug flow called plug flow.

Bubbly flow was characterized by small diameter individual bubbles passing through the bed, whilst in apparent slug flow

the bubbles coalesce into large diameter voids which produce large bed oscillations and cyclic heaving of the bed surface. The term apparent slug flow regime was used as the beds were shallow thus preventing the classical train of large diameter bubbles required for established slug flow. Plug flow was used to define those situations in which a one dimensional plane wave was observed near the distributor. This wave would break down before reaching the bed surface to form a number of slugs. Turbulent flow, which occurred at high velocities was characterised by smaller voids and more extensive lateral mixing than the apparent slug flow. The turbulent flow regime was further accompanied by a reduction in the amplitude of the periodic pressure fluctuation.

It would appear that the amplitude and frequency of the bed pressure could be utilized to define different fluidization flow-regimes for coarse particles in shallow fluidized beds. Tamarin (26) has correlated the frequency of periodic bed fluctuations in terms of a modified Froude number. Verloop and Heertjies (27) have shown that by considering the damping mechanism of a fluidized bed of solids, pressure fluctuations can only occur in systems with a high ratio of solids to fluid density. They (27) further indicate that purely periodic pressure fluctuations occur in shallow fluidized beds, as long as the height of the bed is smaller than the wavelength. A limitation of these studies is the low ratios of u_f/u_{mf} employed. The maximum value being of the order of 2,0. They establish the natural frequency of the bed by the relationship given by equation (11).

$$\nu = \frac{1}{2\cdot\pi}\sqrt{\frac{g\cdot(2-\alpha)}{H_{dyn}\cdot\alpha}} \qquad (11)$$

from which the period of rise of a bubble can be obtained from equation (12) using the static bed height

$$\tau_b = 2\pi\sqrt{\frac{(1-\alpha_{mf})\cdot H_{st}}{(1-\alpha)\cdot(2-\alpha)\cdot g}} \qquad (12)$$

Catipovic et al (28) have presented a qualitative map of the regimes encountered when large particles are fluidized. They define two main regimes, the bubbly flow regime and the turbulent flow regime. The bubbly flow regime is then subdivided into slow, fast and rapidly growing bubbles. A map (28) of the flow regimes is represented by Figure 4. From their analysis it is apparent that for much of the work into fluidized bed coal combustors using coarse particles of size greater than 0,5 mm, the fluidization conditions would best be represented by the rapidly growing bubble regime. This regime is characterised by large pressure drop fluctuations and is similar to the apparent slug flow regime of Canada et al (25).

1.3 HEAT TRANSFER

In considering a fluidized bed combustion chamber which would typically be applied to the generation of steam, two distinct regions or zones can be distinguished. The fluidized bed zone in which high rates of heat transfer are apparent, and the above-bed zone or freeboard in which the bulk of the heat transfer takes place due to radiation. These two zones have been diagramatically represented in Figure 1.

1.3.1 Fluidized Bed Heat Transfer

A considerable amount of interest has been generated in the heat transfer properties of fluidized beds over the last twenty years leading to a wealth of information both theoretical and empirical. However, care has to be taken in employing many of the correlations and theoretical models in view of many being dependent on narrow operating ranges for which they were derived. Further fluidized-bed processes have traditionally involved the use of deep beds of fine solids.

In considering the heat transfer in fluidized beds a distinction is generally drawn between the heat transfer between a

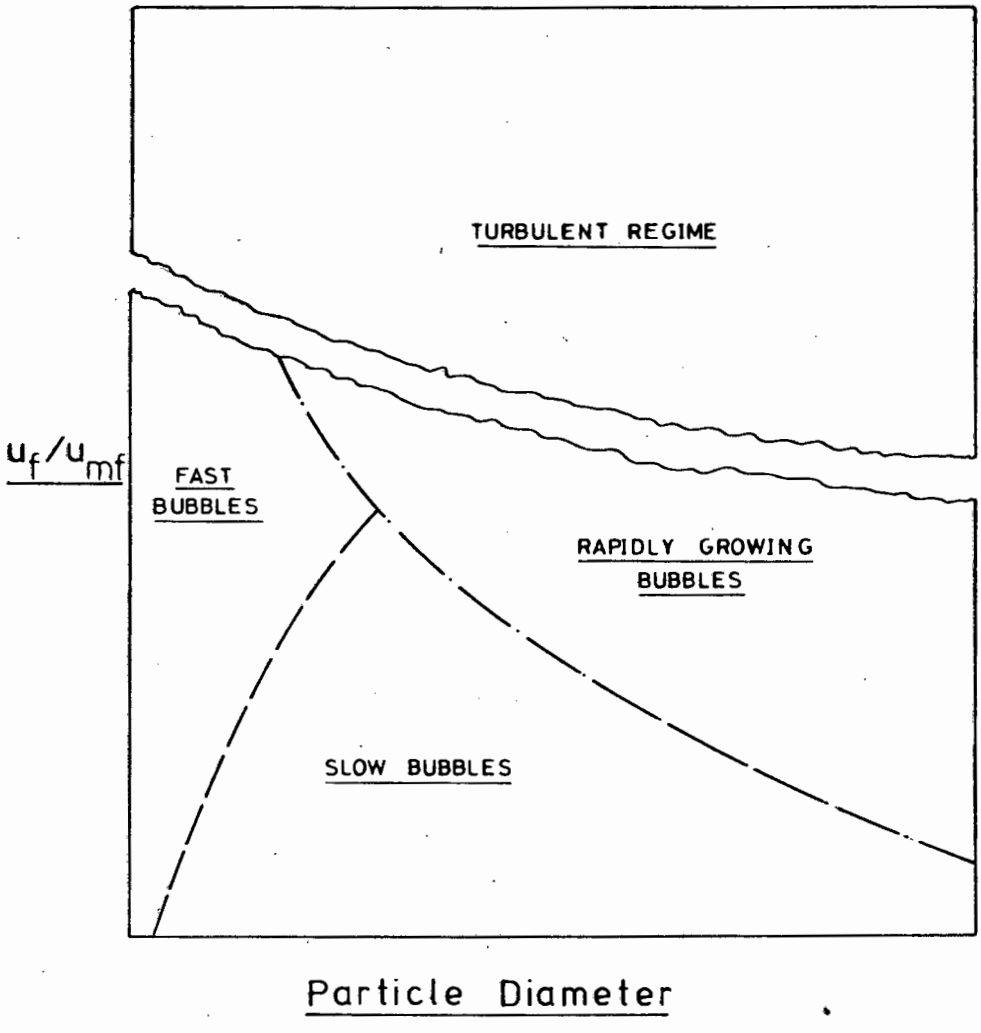

Figure 4 : Map of large particle fluidization regimes (28).

surface and a fluidized bed, and between the solid particles and fluidizing agent. Only the former will be considered in detail. In plotting the heat transfer coefficient as a function of velocity (6, ch.10), this coefficient is observed to rise rapidly after the minimum fluidizing velocity U_{mf} is reached, attain a maximum at some velocity a little greater than U_{mf}, and then to diminish steadily with increasing velocity. The form of the relationship is represented by Figure 5.

In view of the vigorous mixing of the particles, heat transfer within the bed is very rapid leading to the bed being considered as practically isothermal. The particles act as local sources or sinks of heat. In the combustion of coal particles within a fluidized bed, the burning coal particles are effectively cooled by transferring heat to the inert bed material or to the fluidizing medium and then to the inert particulates. The bed particles then transfer heat to the immersed cooling surfaces. When radiant heat exchange is small, the particles transfer heat to the surface by conduction through a gas film. The particles usually remain in the bulk of the bed for a sufficient length of time such that they attain the temperature of the bulk of the bed. Fresh particles are periodically swept into contact with the immersed surface. The temperature difference at which the transfer takes place decays steadily thus reducing the heat transferred until these particles in contact are replaced by new particles at the temperature of the bulk of the bed thus restoring the maximum temperature between particles and cooling surface. Thus highest heat transfer rates are to be expected when there is a rapid replacement of particles at the surface.

a) Mechanisms of fluidized bed heat transfer

The basic mechanisms of heat transfer between a fluidized bed and a contacting surface are firstly due to the convective transfer as a result of both particulates and gas, and secondly due to the conduction of gas through the thermal boundary layer

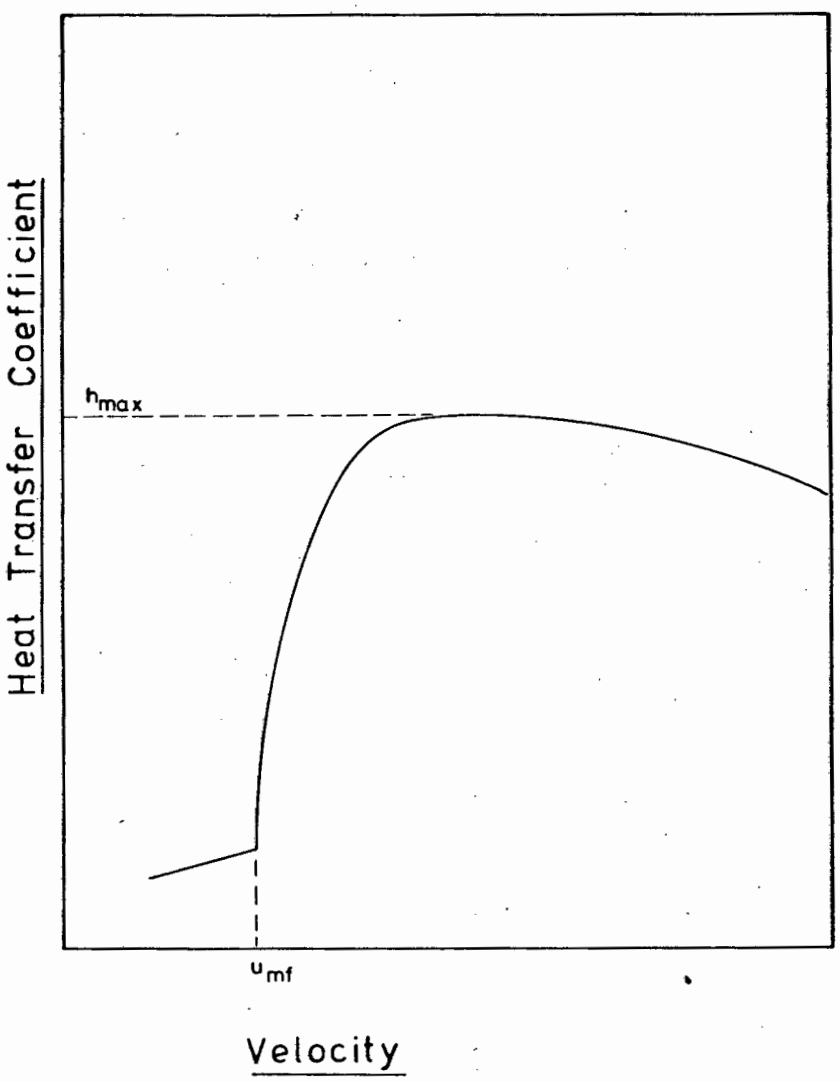

Figure 5 : Typical dependence of heat transfer coefficient on fluid velocity.

at the surface (21, ch.4). Two basic models can be discerned. The first approach considers the bed as a simple system comprising a continuous phase made up of the gas and a discrete phase comprising the solid (29). The heat conduction equations are solved for a single spherical particle during its residence time at the surface. Gabor (30) has reported on extensions of this model to consider two and four particle thick layers.

The second approach is based on the "packet" theory of Mickley and Fairbanks (31) who considered a packet of constant voidage fraction to be swept into contact with the heat exchange surface for a period of time. During this interval, heat is exchanged until the packet is replaced. In developing the packet heat transfer model, a number of components to the total heat transfer coefficient can be defined as being due to gas bubbles, the packets of solids and gas. The total heat transfer coefficient is (6, pg.478)

$$h_t = h_b \cdot f_b + (1 - f_b) \cdot (h_{p,c} + h_{g,c}) + h_r \qquad (13)$$

where f_b is the fraction of the heat transfer surface occupied by gas bubbles. In practice, the convective component is very much larger than that contributed by the bubble, and as such the bubble component can be neglected. Therefore the heat transfer coefficient to a gas fluidized bed can be thought of as being made up of three components

(i) the particle convective component,
(ii) the gas convective component, and
(iii) the radiative component.

The first of these is dependent on the particle exchange rate and has been fairly well researched in low temperature small scale apparatus. On the other hand, the gas convective component is difficult to measure, and Botterill and Denloye (32) have continued the earlier work (33) into its evaluation. The convective component is only of significance in high pressure beds using large particles, whilst the

radiative component is only of significance under fairly high temperature conditions in excess of 800°C.

Mickley and Fairbanks (31) have established that the rate of heat transfer between the surface and the packet is dependent on the bed properties and a stirring factor which accounts for bed motion and geometry. Their relationship is presented in equation (14)

$$h_{p,c} = \sqrt{k_m \cdot \rho_m \cdot c_{ps}} \cdot \sqrt{S_l} \qquad (14)$$

which can further be written in terms of a packet residence time as given by equation (15)

$$h_{p,c} = \frac{2}{\pi} \sqrt{k_m \cdot \rho_m \, c_{ps}} \; / \; \tau^{\frac{1}{2}} \qquad (15)$$

Baskakov (34) extended this model by introducing a contact resistance which can be considered to be independent of time and to be in series with the packet resistance. Thus

$$R_p = 1 \; / \; h_t \qquad (16)$$

$$R_w = \delta_w \; / \; k_m \qquad (17)$$

From equation (17) it is seen that an average gas film thickness has to be evaluated. This film thickness is generally assumed to be proportional to the particle diameter. Various workers have accorded different values for this film thickness ranging from $0{,}1 \cdot d_p$ to about $0{,}5 \cdot d_p$ (35), (36). It is evident that the evaluation of a contact resistance is based upon empirical considerations which enable a good data-fit to be obtained. Kubie and Broughton (37) have attempted to overcome this limitation by describing the voidage variations near the surface from simple geometric considerations. The modified packet theory developed is in good agreement with data where conduction is the predominant mode of heat transfer. Yoshida et al (38) consider the heat transfer mechanism to take place as a combination of the unsteady state absorption of heat by fresh packet elements (31) and as the result of steady state conduction through the emulsion layer which

is not often swept away (39). It is clear that the two mechanisms (38) may occur as a combination or in certain instances one may predominate. This is particularly true, where solid flow patterns may result in isolated heat transfer surfaces immersed in a bed being subject to more violent bubble action whilst the heat transfer at the peripheral walls may be as a result of a steady downflow of solids. In this latter instance the steady state conduction of heat will predominate for large residence times.

It is evident that in view of the wide range of parameters associated with fluidized bed heat transfer a unifying theory or mechanism is not apparent. It is therefore prudent to utilize the simplest mechanism which adequately describes the phenomenon in the range considered. Although some of the models, such as those employing a contact resistance can be considered as a curve fitting technique for the available data, they nevertheless provide a valuable tool for design and for empirical studies.

b) The Radiative Component

Equation (13) suggests that the effect of radiation may be considered as being purely additive, a view shared by many investigators (21, p.237), (40). However, although Zabrodsky (41) has indicated that this may not be the case, the simple addition of the radiative component often suffices. Indeed, the relative magnitude of the radiative component has been disputed. Some workers (42), (43) have found the contribution to be very small below 1000°C, whilst relatively high contributions by radiation of about 5% at 500°C rising to values of some 50 to 60% of the total heat transferred at 1400°C have been reported (44). Yoshida et al (45) have considered radiation to take place when the surface is in contact with the bubble, whilst when in contact with the emulsion phase, heat is transferred by conduction through the gas layer. Whilst this may be true for fine particles, the effect of large particles will be to expose a larger area of particle surface at a greater distance from the cooling

d) Heat Transfer to Immersed Surfaces

In view of the disturbance caused by the immersion of tubes in a fluidized bed being less affected by the scale of the equipment, more general applicability of existing correlations can be expected when utilizing deep fluidized beds. However, for the shallow bed, immersed tubes can easily be affected by conditions existing close to the distributor which could be very different from the bulk of the bed. As the work performed in this thesis is concerned with horizontal tubes as the immersed surface, only this form of immersed surface is considered.

Vreedenberg (49) was able to correlate his data for coarse particles for an immersed horizontal tube to within ± 29% by a relationship which can be written in the following form.

$$Nu_{to} = 420 \cdot Re_{to}^{0,3} \cdot Pr^{0,3} \cdot Ar^{-0,3} \qquad (19)$$

Al Ali and Broughton (50) obtained the Nusselt number as a function of the Archimedes number only, when considering the heat transferred from a low temperature shallow fluidized bed to an immersed tube. More recently (51) an attempt has been made to obtain a universal correlation for horizontal tube bundles which was not dependent on the apparatus for use in the scale-up of fluidized bed coal combustors. However even this work (51) tended to utilize deep beds, having static heights of the order of 600 mm. Andeen et al (52) have found their information correlated best in a form given by equation (19) but including the factor $(1 - \bar{\alpha})$ to take into account the bed expansion.

It is evident, therefore, that though some form of correlation may be possible for deeper beds, the same cannot be said for immersed horizontal tubes in shallow fluidized beds. Whilst there is no clear-cut definition of a shallow bed, those beds of height less than 300 mm and where the bed height to bed width is less than 0,5 are generally regarded as being shallow. Al Ali and Broughton (50) refer to thermal gradients which can readily be established in shallow beds as

well as entry effects, both of which could easily affect the measured heat transfer coefficient.

1.3.2 Above-Bed Heat Transfer

The shallow fluidized bed combustion chamber contains a freeboard zone above the bed. This zone provides a region in which particulate matter ejected from the surface of the bed can disengage from the transporting gas stream and return to the bed. The combustion process is also completed in this region whilst this zone above the bed enables the further transfer of heat and a cooling of the product gas stream. At the interface between the bed and the freeboard zone, a lean phase cloud is formed which affects both radiation and reaction processes (53).

The above-bed zone can therefore be regarded as a radiant furnace chamber with one of its boundaries being a high temperature radiating source viz. the upper surface of the bed. The gases leaving the bed are normally at the bed temperature and can clearly be considered as part of the heat input to the furnace i.e. the above-bed zone. A number of methods are available for assessing the performance of such a radiant type furnace ranging from the very basic well stirred furnace models to more complex approaches having large computational storage requirements.

Lihou (54) has presented a very good review of the available furnace design methods. The long furnace model assumes that the adiabatic flame temperature occurs at the burner and that the flue gas flows in plug flow through the furnace exchanging heat to the periphery without any gas backmixing. In the zone method of analysis (55) the furnace is divided into a number of gas and surface zones. The direct exchange factors for a clear gas, and the total exchange factors for a grey gas, for each of the zone pairs have to be evaluated before the method can be utilized (56, ch.14). The smaller the zones, the closer the system approaches reality; however the complexity increases rapidly. In the event that details

of the heat flux through the furnace walls are not required, the zone method of analysis can be simplified to the single gas zone model (57). This model is also known as the stirred furnace model and assumes three zones; a sink and refractory forming two surface zones enclosing the combustion products which form a gas zone. Assuming that the gas leaves the system at some temperature being less than the mean gas temperature by an amount Δ, Hottel and Sarofim (56, p.461) derive the following dimensionless equation.

$$Q' \cdot D' + \theta_w^4 = (1 + \theta_\Delta - Q')^4 \qquad (20)$$

which can be considered as a 'characteristic' type equation of a well-stirred furnace.

Lihou (55) also discusses flux methods which enable the modelling of continuous changes in gas temperature and optical properties which cannot be described by discrete homogenous zones. The Monte Carlo method (55) allows gas zones to be defined which match the shape of the furnace and its flow patterns. The Monte Carlo method is particularly useful when unusually shaped zones are encountered. For simple shapes, the extra computational effort required in the Monte Carlo method is not usually justifiable.

Radiation from gases is a complex phenomenon and is described in most standard texts on heat transfer (58). If the reflectivity of the gas is negligible and the gas is grey, the emissivity and absorptivity can be obtained from equation (21).

$$\varepsilon_g = \alpha_g = 1 - exp(- KL) \qquad (21)$$

Hottel (58) has derived gas emissivity charts for the evaluation of combustion products. In order to retain the accuracy of the gas emissivity over a wide range of mean beam lengths, the gas can be represented as the weighted sum of grey gases. For engineering calculations, no more than four terms would normally be required. This representation of the gas as a sum of grey gases in reality represents an exponential type of curve fitting technique. Thus for a particular gas

temperature the gas emissivity will be given by

$$\varepsilon_g = \sum_i a_{g,i}(1 - exp \{ - k_i \cdot pL \}) \qquad (22)$$

It is further found that the weighting factors a_{g_i} can carry the full burden of expressing the effect of temperature on ε_g (56, p.251).

In the coal fired fluidized bed combustor, particulates will be entrained in the gas stream and these will have an effect on the radiative properties of the gas. However, allowance for the effect of particulates is not readily effected and a number of approximations have to be made. Johnson et al (59) allowed for the emissivity of soot in oil flames by representing the soot as a weighted sum of grey gases in the same way as a real gas was represented, cf equation (22). This is not strictly correct, as the soot absorption coefficient is found to be a linear function of temperature (60). However, for use of the zone method of analysis, it is expedient to obtain the absorption coefficients in a form independent of temperature. Johnson et al (59) impose the further restriction that the weighting factors for the soot equations are similar to those for the gas emissivity equations a_{g_i}. Thus it is possible to obtain an emissivity equation for the combined gas soot mixture as

$$\varepsilon_m = \sum_i a_{g,i}(1 - exp \{ - K_i \cdot L \}) \qquad (23)$$

where

$$K_i = k_{s,i} + k_{g,i} \cdot (p_w + p_c) \qquad (24)$$

Although the above equations have been expressly determined for soot particles having diameters less than 0,05 microns, Field et al (61, ch.3) and Becker et al (62) have utilized a similar approach when describing the radiation from clouds of particles arising from pulverized coal fired furnaces. With the larger particles, the effect of scattering of the radiation on the absorption should also be considered (61, p.93).

1.4 THE COMBUSTION PHENOMENON

"When coal is heated to a sufficiently high temperature it begins to decompose producing tars and gases termed volatile matter or just volatiles. The volatiles consist of a mixture of combustible gases, carbon dioxide and water vapour. Apart from the carbon dioxide and hydrogen the combustible gases are mainly hydrocarbons, although there are small quantities of phenolic and other compounds" (61, pg.155). The combustion of coal thus comprises two reactions, a homogeneous gas phase combustion reaction, and the heterogeneous reaction that takes place at the surface of the char that remains after the evolution of the volatiles.

The rate at which the volatiles are evolved, or the rate at which the coal particle decomposes depends on the time/temperature history of its heating. Two classes of decomposition reactions are distinguished (61, ch.4), rapid decomposition involving a particle heating rate of the order of 10^4 ^{o}C/s or more with a decomposition period of less than one second, and slow decomposition in which the particle is heated at a rate of 10^{o}C/min. Rapid decomposition rates can only be attained with very small coal particles, less than 100 micron, as a finite time is required for a large particle to be uniformly heated, as well as to allow for the diffusion of the volatile matter away from the surface of the remaining char particle.

Pitt (63) has studied the rate of evolution of volatile matter from coal particles by mixing coal with preheated sand in a preheated reaction vessel. The sand and coal particles were then fluidized with nitrogen and the rate of decomposition measured. The minimum time scale of decomposition was limited to 10 seconds whilst temperatures of 300^{o} to 650^{o}C were used. The results indicated that a major portion of the volatile matter was evolved within the first 10 seconds even at the lower temperatures. Skinner (64, pg.104) states that the volatiles are evolved within the first two to three seconds after the coal enters the fluidized bed. The volatiles would be emitted in close proximity to the coal feed point,

and should the oxygen supply be limited in the region of this point, poor combustion efficiency may result. Bishop et al (65) have reported the existence of areas of unburnt hydrocarbons close to the coal feed point situated to the side of an 1800 mm by 450 mm bed. Complete combustion of the volatiles in the bed section was achieved by increasing the static bed height to 300 mm (750 mm expanded). They (65) report further that at low bed temperatures, and with an excess air level limited to 5%, the hydrocarbon concentrations were found to be relatively high, at between 800 to 1000 ppm. At higher bed temperatures, the hydrocarbon concentration was reduced to near zero with an increase in the excess air to 17%.

Little work has been done in assessing the combustion of the volatiles in a coal fired fluidized bed combustion chamber. Although the time taken for the combustion of the volatiles would appear to be of the order of two seconds in comparison to a residence time of between 60 to 350 seconds for coal particles between 0,2 and 2 mm in a fluidized bed (66), work in this field may be of value particularly in assessing combustion mechanisms and combustor efficiencies. Basu et al (67) point out that on evolution of the volatile matter, swelling of the remaining char particle may take place which would alter the surface structure. This may explain differences in the combustion of different coals in fluidized beds, and in particular differences in the combustion of the volatile component of the different coal types.

After the liberation of the volatiles, the second step in the combustion process can be considered, i.e. the combustion of the remaining char. An evaluation of the mechanism and the burning rates of individual particles is of importance in the prediction of the oxygen throughput, the bed carbon loading and the combustion efficiency of the fluidized bed combustor. Field et al (61, ch.6) consider the overall reaction process to involve a number of steps in sequence, viz the transport of oxygen to the particle surface, reaction at the surface

and the transfer of the products away from the surface. Basu et al (67) consider two different mechanisms for the combustion of the carbon particle with oxygen. In the first, designated as Model 1, oxygen comes in contact with the carbon surface to form carbon monoxide and carbon dioxide. The escape of the carbon monoxide into the surroundings is dependent on the prevailing bed velocity and temperature conditions. If the temperature is above the ignition temperature of carbon monoxide (about 650°C) then this gas burns in a reaction zone surrounding the carbon particle (67). The reactions pertinent to Model 1 are illustrated in Figure 6.

The second mechanism, Model 2, has also been proposed by a number of authors who have shown (61, ch.6) that if the reactions of carbon dioxide with carbon and of carbon monoxide with oxygen were fast enough then the mechanism of combustion would be completely different from the direct oxidation of carbon. This model has been called the two film theory and is diagramatically represented by Figure 7. According to this model, carbon dioxide reacts with the carbon surface to produce carbon monoxide, which in turn diffuses outwards to meet oxygen diffusing inwards. Two moles of carbon monoxide burn in a thin film surrounding the particle with a single mole of oxygen to form two moles of carbon dioxide. Half of the carbon dioxide diffuses back towards the char particle whilst the remainder diffuses into the free stream. The reactions taking place in Model 2 are illustrated by the partial pressure profiles of Figure 8.

Basu et al (67) have attempted to determine the actual combustion mechanism under the temperature and velocity conditions prevailing in fluidized beds. They propose that a changeover from Model 1 to Model 2 takes place, though further experiments would be required to mark this changeover in terms of temperature and particle size.

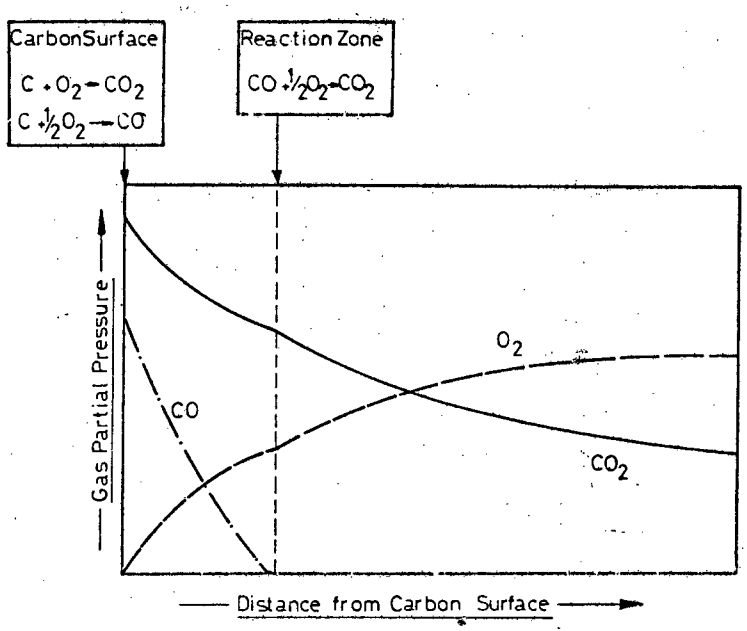

Figure 6 : Partial pressure profiles in the gas surrounding a particle burning according to Model 1.

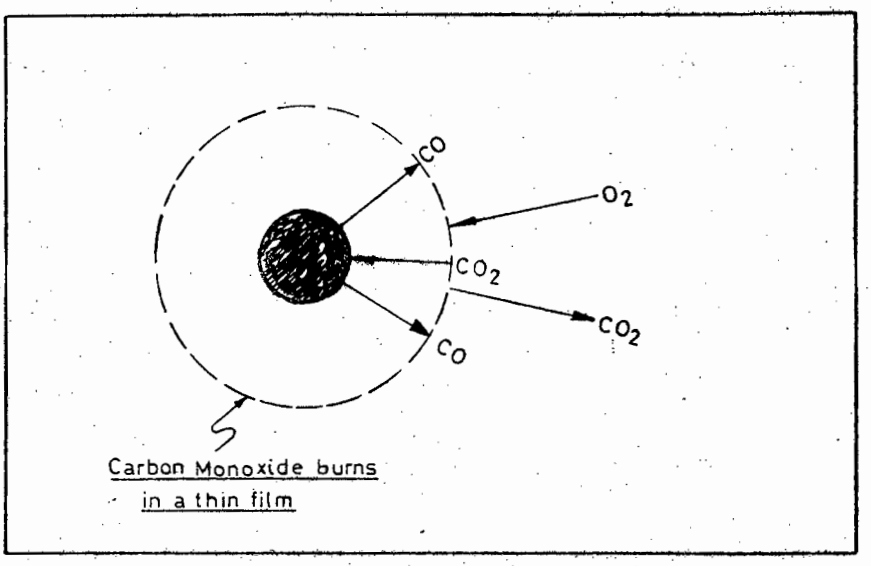

Figure 7 : Diagrammatic representation of the combustion mechanism of Model 2, Field et al (61, p. 205).

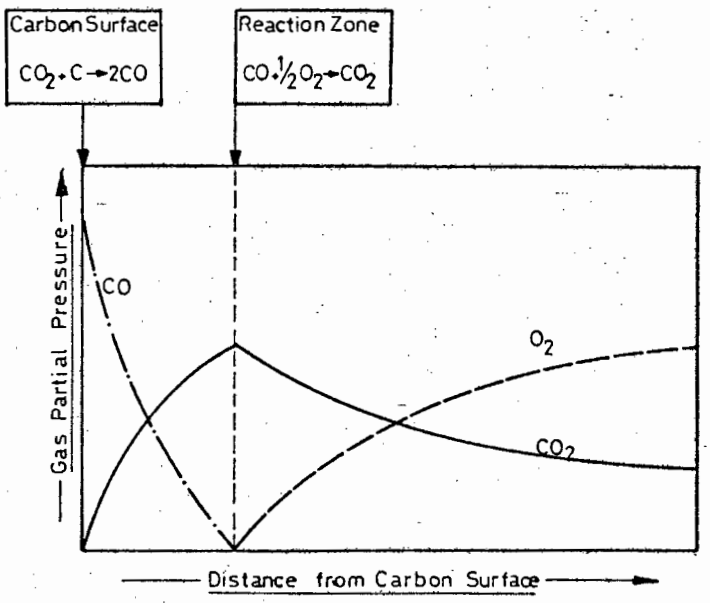

Figure 8 : Partial pressure profiles in the gas surrounding a particle burning according to Model 2.

In any model of the combustion process occurring in a fluidized bed, some indication of the rate controlling process is required. Avedesian and Davidson (66) studied the mechanism of combustion of batches of carbon in fluidized beds with a view to establishing whether the combustion of the fixed carbon component of coal is controlled by chemical kinetics, mass transfer or a combination of both. They applied the two phase theory of fluidization (22) with the combustion mechanism described by Model 2 to describe their results. Combustion is assumed to take place in the particulate phase, while the bubble phase is completely devoid of particulates. Avedesian and Davidson (66) cite the findings of various authors who have shown that the burning rate of pulverized particles, i.e. having diameters of less than 50 microns, is controlled by chemical kinetics whilst the combustion of particles greater than 100 microns is diffusion controlled. The transition from kinetics to diffusion control takes place over the particle size range from 50 to 100 micron. They (66) established from both theory and experiment that the combustion of coal in a fluidized bed of inert particles could be assumed to be controlled by two diffusional resistances, viz. the interphase transfer of oxygen from the bubbles of air to the surrounding ash particles, and the diffusion of oxygen through the ash phase of each burning carbon particle.

Campbell and Davidson (68) have extended the work of Avedesian and Davidson (66) to allow for a finite concentration of carbon dioxide in the particulate phase and have applied the model to allow for the continuous feeding of the coal. Basu et al (67) have further refined the model by determining a varying voidage function in the particulate phase which alters the Sherwood number. The accuracy of this work is questioned by Pyle (69) who further considers that the refinement to allow for varying voidage is unnecessary when much of the process is still not fully understood.

More recent investigations (70), (71) have indicated that the rate controlling step may not be one described simply by diffusion, but a combination of chemical kinetics and diffusion. Chakraborty and Howard (71) found this to be particularly true of large coal particles. They studied the combustion of coal particles of 6 mm and 12 mm in size and found the combustion rate to be significantly affected by bed operating conditions and design parameters. They found that the highest combustion rates occurred with the largest carbon and inert particle sizes, the highest fluidizing velocities and with the shallowest beds (12,5 mm static bed depth). This would indicate that combustion models based on the diffusion of oxygen to the carbon surface are inadequate.

The reactivity of the fuel can be considered as another parameter in determining the rate of combustion of solid fuel in a fluidized bed. Leung and Smith (72) have represented the reactivity of the fuel by the ratio of the unit rate of carbon combustion to the rate coefficient for the mass transfer of oxygen through the dense phase to the fuel particle. These parameters are related by equations (25) and (26).

$$\psi = R_t / R_m \qquad (25)$$

$$1 / R_t = 1 / R_m + 1 / R_c \qquad (26)$$

From their (72) theoretical analysis they found that reactivity does not play an important role up to about 730°C. However, the diffusion of oxygen through the particulate phase was found to have the greatest effect on the rate of burning when considering coal sizes normally encountered in practical fluidized beds. They (72) also emphasized the importance of carbon concentration, bubble size and size of particles forming the bed.

It is evident that the combustion of coal is a complex phenomenon. When applied to fluidized bed combustion,

further unknowns are introduced, and in summary the combustion process could best be described as follows:

Once a coal particle has been introduced into a bubbling fluidized-bed of inert particles at a temperature of the order of 800°C, the volatile fraction will be liberated within the first two to three seconds, to burn partially within the bed and partially above the bed, dependent upon the prevailing conditions. The remaining char particle burns within the particulate phase at a rate determined partially by chemical kinetics and partially by oxygen diffusion which in turn is dependent upon the bed operating conditions as well as on the type of coal being burnt. The carbon particle steadily reduces in size through the combined action of combustion and attrition until it is small enough to be entrained in the fluidizing gas as a result of splashing or elutriation. On leaving the fluidized bed, further combustion of the entrained particle may take place in the freeboard.

1.5 A REVIEW OF THE DEVELOPMENT OF ATMOSPHERIC FLUIDIZED BED COMBUSTION FOR STEAM RAISING

The Winkler gasification process developed in the early 1920's is recognised as representing the first application of fluidized bed combustion. By 1929 five Winkler gasifiers were operating at Leuna, East Germany, producing power gas to fuel gas-engines driving ammonia synthesis compressors (73). A total shaft power of 130 MW was developed. In the Winkler process fine coal particles are gasified in a fluidized bed with steam and air to form hydrogen and carbon monoxide.

In the United States, pioneering work into fluidized bed combustion was initiated by Odell, who filed a patent for fluidized bed cat cracking in 1929 (5). Subsequent to these initial processes the development of fluidized bed combustion has passed through three phases, and represents fluidized bed combustion in the generally accepted sense. The first phase

was initiated in Britain in the early 1950's and was characterized by processes in which the main aim was the use of fluidized bed combustion as a means of burning low grade coals without incurring coal preparation costs associated with pulverized fuel firing. A further characteristic of the initial phase, was that no attempt was made to extract heat directly from the bed. This was followed by investigations into the extraction of heat from surfaces immersed within the bed. The final stage of development has seen the use of the fluidized bed as a means of reducing atmospheric pollution.

1.5.1 Development Trends and Application of Fluidized Bed Combustion

The potential advantages of fluidized bed combustion, in particular the ability to utilize poor grade fuels and inherent high heat transfer rates to surfaces immersed within the bed, have been well documented. Teague and Wright (74) produced an early literature survey on the subject, whilst most of the work up to the end of 1969 has been well covered in the review by Skinner (64). Naudé (75) has reviewed much of the literature up to mid 1977 with particular reference to the application of fluidized bed combustion of coal in South Africa. Since then the development of this technology has been rapid with vast amounts of capital being expended into the research effort with the ultimate objective being the commercial exploitation of the technique.

At present, five main avenues of the development of coal fired fluidized bed combustion, excluding gasification can be discerned:

(i) special small scale applications,

(ii) atmospheric fluidized bed combustion for industrial steam raising,

(iii) atmospheric fluidized bed combustion for power generation,

(iv) pressurized fluidized bed combustion,

(v) centrifugal fluidized bed combustion.

Although pressurized fluidized bed combustion, or gasifiers coupled with utility type power plant, represents a long term solution for the efficient utilization of coal for the production of power, atmospheric fluidized combustion is suited for the combustion of poor quality coals for industrial steam raising (76). This is particularly true of duff coal (i.e. coal of size less than 6,3 mm) which is not readily burnt on traditional forms of coal burning equipment.

In view of the work undertaken in this thesis being concentrated towards atmospheric fluidized bed combustion for steam raising, only a brief survey of the development of the remaining three avenues will be made in this section, whilst a more comprehensive survey of atmospheric fluidized bed combustion relating to the more recent developments following the earlier review (75) is included in section 1.5.2.

a) Special Small Scale Applications of Fluidized Bed Combustion

The British National Coal Board (NCB) has utilized fluidized bed combustion for the incineration of wet 'tailings' from coal washing (77), (78), (79). The tailings consist of a slurry of very fine particulates, 40% of which are less than 5 microns in size. A granulated ash product is formed as a result of agglomeration of the fine particles during combustion. The NCB has applied this technology for the drying of cattle fodder as well as for the combustion of sewage. Work in Australia (80), (81), (82) has shown that the fluidized bed combustion of wastes from coal mining provides not only the means for lessening the impact on the environment but can also provide considerable quantities of useful heat. Poersch and Zabeschek (83) have investigated the combustion of flotation tailings (having 40% by weight of fine particles below 10 microns) in a fluidized bed with the

view to obtaining a relatively carbon-free product for use in the production of masonry cement.

Thring et al (84) has reported on the use of coal fired fluidized beds for use on steam locomotives, whilst a fluidized bed heat exchanger (85) has been installed on board a super tanker for extracting heat from the exhaust of the diesel engines. With the increasing price of oil, fluidized beds have been considered as a means of burning coal for raising steam on ships (86), however the logistics would appear to rule out this possibility in the immediate future.

b) Pressurized Fluidized Bed Combustion

Pioneering work was conducted by the British Coal Utilization Research Association (BCURA) into the pressurized fluidized bed combustion of coal (87). Indeed, until the mid-seventies the only research of any significance into this aspect of fluidized bed combustion had been conducted on the BCURA test facility which has an output of 2 MW_t and is capable of being operated at pressures up to 6 bar.

The increase in complexity and capital cost of equipment associated with pressurized fluidized bed combustion has resulted in this technology being developed mainly for utility power generation utilizing coal as the combustor fuel. Two main cycles have emerged, the first utilizes a combined gas and steam cycle in which the boiler is pressurized on the gas side whilst the second incorporates an air cycle (88). In the former, a pressurized fluidized bed steam generator provides steam for a conventional turbine-generator set. The gases leave the steam generator at a temperature of about 900°C and are expanded through a gas turbine before being finally cooled in a heat recovery system forming an integral part of the main steam generator. Dependent upon the excess air utilized, the gas turbine generates about 15 to 33% of the total output. Five systems incorporating a 60 MW_e gas turbine are mentioned (88) as employing the concept of the

pressurized boiler and associated combined gas and steam cycles.

A number of air cycles can be distinguished. However, the cycle most commonly proposed for power generation incorporates a system in which air is heated in tubes immersed in the fluidized bed before being mixed with the products of combustion. The resulting gases are cleaned prior to expansion through a gas turbine. The gases are finally cooled in a waste heat boiler which produces steam for a steam turbine-generator set. Bergbau Forschung GmbH in association with the Vereinigte Kesselwerke AG (89) have built a small demonstration plant incorporating a 13 MW_e gas turbine. A considerable amount of work has been performed by Curtiss Wright (90), (91), (92) into the development of an air cycle for use in a 500 MW_e coal fired modular type plant which would be feasible by the beginning of the 1990's. At present much preliminary work on air heater tubes has been undertaken on a pressurized fluidized bed technology rig some 20m high and incorporating a 1,5 m diameter pressure vessel. Work is presently in hand (1980) on the construction of demonstration plant utilizing a 13 MW_e gas turbine.

Valuable work is also being undertaken into pressurized fluidized bed combustion in South Africa at Natal University on a fairly large scale (92), (93). They have investigated the use of a three staged fluidized bed contained in a single pressure vessel. The fluidized beds are 450 mm in diameter and the unit is capable of an output of some 1 MW_t. In view of the fly ash having to percolate through three stages, a novel tuyere type distributor was developed which provides swirl to the incoming gases to enable high loads of ash to be transmitted whilst providing adequate fluidization characteristics. Considerable development has also taken place into the design of recirculating bed material downcomers. The main objective, i.e. the combustion in staged fluidized beds has been demonstrated, whilst exceptionally high combustion efficiencies have been obtained in a two stage system with very low excess air levels (93).

c) The Centrifugal Fluidized Bed Combustor

The centrifugal fluidized bed combustor can be considered after atmospheric and pressurized fluidized bed combustion as a third generation of fluidized combustion technology. Many difficulties associated with atmospheric and pressurized beds have still to be overcome, and it is thus to be expected that the commercial realization of the centrifugal combustor is a long way off. The fluidized bed is housed in a cylindrical vessel which is rotated at about 1000 rpm causing the bed to be thrown to the sides by the centrifugal force resulting in a loading of from 10 to 100 g. The bed is then fluidized by passing air through the walls of the cylinder, thus enabling exceptionally high combustion intensities of the order of 100 MW/m^3 whilst the output can easily be controlled by varying the rotational speed. Early work was reported by Elliot (95) and this has been followed by investigations at the universities of Aston (96) and Sheffield (97) in Britain and Lehigh (98) in the United States.

1.5.2 The Recent Development of the Coal Fired Atmospheric Fluidized Bed Combustor for Steam Raising

Since the survey conducted up to the middle of 1977 (75) the development of the atmospheric fluidized bed boiler has accelerated with a number of commercial and semi-commercial projects having been undertaken. Most of the work has taken place in Britain and the United States and to a lesser extent in West Germany. Smaller scale, but by no means insignificant research has taken place in Australia, India and Brazil. Work in Japan has been concentrated towards gasification of coal rather than combustion, whilst small laboratory scale work has been reported in New Zealand (99).

Work in Britain has concentrated on the smaller scale industrial application of fluidized bed combustion, and in particular in the retrofitting of existing oil-fired shell-boilers to enable the combustion of coal in a fluidized bed. Whereas research in Britain into fluidized bed combustion was begun for its potential as a coal burning technique, work in the United States

has been conducted primarily as a means of reducing air pollutants. The United States Department of Energy (DOE), formerly the Energy Research and Development Administration (ERDA), heads the effort in the United States with the Environment Pollution Agency (EPA) playing a supporting role in assessing the environmental impact of fluidized bed combustion (100). The Electric Power Research Institute (EPRI), a non-profit organization, is backing investigations for its member utility firms who supply the funding to the Institute so that sufficient funds are available to enable work and development on a large enough scale to be meaningful for utility applications.

Work into fluidized bed combustion is being conducted in various other parts of the world. However the scale of this research is small when compared to that in either the United Kingdom, the United States or West Germany. It is clear that any major developments are likely to come from these three countries. However, countries such as India and South Africa with very large reserves of coal, and Brazil with a substantial amount of poor quality coal represent regions where the development of the technology may be the most fruitful. The development of the atmospheric fluidized bed combustor with its particular application to industrial steam raising in each of these countries is discussed in more detail in the following sections.

a) United Kingdom

In Britain, the major incentive for the application of fluidized bed technology has been in the retrofit market. The spiralling cost of oil has made coal burning equipment attractive once again. However the large number of oil fired shell boilers which were sold during those times when oil was relatively cheap, represents a substantial capital investment. The high heat transfer rates associated with fluidized bed combustion enables the fitting of a fluidized bed to an existing oil fired unit without incurring the penalty of reduced boiler ratings. A number of British companies are

therefore actively engaged in the retrofit market.

Energy Equipment (101) have developed a fluidized bed boiler in which the coal is partially gasified within the bed with the combustion reaction being completed above the bed and in the horizontal flue leading from the bed. After initially retrofitting a boiler at Stirling with a fluidized bed, they obtained a contract to adapt two boilers at Cadbury's Bourneville plant (102). More recently a contract was awarded to this company for the supply of three shell type hot water boilers rated at about 1,5 MW each (103).

Work by the NCB in collaboration with a number of manufacturers has resulted in a number of different types of fluidized bed boilers being installed in industrial environments (88), (104), (105), (106). These include a large 14 000 kg/h unit installed at Rist's Wires and Cables at Newcastle under Lyme. The unit was commissioned in March 1978 and by September about 100 hours operation had been recorded at efficiencies ranging from 80 to 85%. The coal burnt ranged from 12 mm to 25 mm in size. A vertical shell type unit capable of generating 3500 kg/h of steam was installed for Antlers luggage factory at Bury. A similar vertical type unit was constructed at Mardon for the generation of hot water and is rated at about 3 MW_t. A large 30 MW_t fluidized bed coil type boiler was built by M.E. Boilers in collaboration with the NCB for British Steele's River Donne Works.

Northern Engineering Industries embarked on an extensive development programme which culminated in the launching of a coal fired fluidized bed boiler by Thompson Cochrane, an NEI subsidiary in the middle of 1979 (107). A particular feature of the NEI design is the mechanical ash recycling system.

A number of designs have incorporated various concepts to improve the combustion of fines which normally are entrained from the bed without contributing significantly to the

combustion process. Highley has patented one concept (108) in which circulation of the solids ensures that particles are drawn down the sides and forced up the centre of the bed by combining features of fluidized and spouted beds. Virr (109) incorporates a parabolic type distributor made up of ceramic tiles to induce a similar type of motion on the solid particles, whilst yet a further design (110) incorporates a number of windboxes sloping away from the horizontal to induce a circulatory pattern on the bed material by regulating the flow to each of the windboxes.

The largest industrial fluidized bed boiler on which a considerable amount of testing has been undertaken to date is the boiler at Babcock and Wilcox's Renfrew Works (111), (112). The boiler is essentially a Babcock cross-type unit with the stoker replaced by a distributor plate and windbox. The unit is capable of generating steam at a rate of about 22 000 kg/h.

Whilst a considerable amount of work is being directed towards developing units for use in Britain, Thurlow (113) has reported on a number of design and feasibility studies undertaken by the NCB on behalf of clients in the United States and Canada. Further, Butler (114) reports that one British manufacturer sees the packaged water tube boiler market in the United States as offering the greatest potential for the development of atmospheric fluidized bed boilers, whilst another views India and South Africa with their large indigenous coal reserves as offering the greatest potential for development of the technology.

b) The United States

The largest operational fluidized bed boiler is the 135 000 kg/h unit required for a 30 MW_e demonstration unit at Rivesville, West Virginia (115). The research and development contract which led to the design of this plant was awarded to the consultants, Pope, Evans and Robbins in 1965. The development led to the design of the Rivesville boiler which was constructed by Foster Wheeler Corporation with a

substantial proportion of the capital being supplied by ERDA. After a number of minor difficulties the plant was commissioned towards the end of 1976. Following the experience gained at Rivesville, Foster Wheeler and Pope, Evans and Robbins were awarded a contract for the construction of a 45 000 kg/h fluidized bed boiler at Georgetown University. A major departure from the Rivesville design, is the use of two spreader stokers for evenly distributing the fuel across the boiler, whereas fifty feed points were provided at Rivesville. The Georgetown University boiler was first lit on the 9th July 1979 and by November 1979 about 650 hours of operation had been logged (116).

During 1979, Combustion Engineering commenced with construction of a 22 000 kg/h package water tube boiler at the US Navy's Great Lakes Training Station in Illinois. Although an atmospheric unit, the boiler utilizes a relatively deep bed of some 500 mm to 700 mm (static bed depth) (117). Other features of the demonstration unit include the use of natural circulation, in-bed cooling tubes and a novel windbox arrangement which allows higher windbox pressure differentials during start-up.

In a joint development programme with the EPRI, Babcock and Wilcox Co. (US) have built a 1,8 m square test facility for obtaining more comprehensive design data relating to the utilization of fluidized bed combustion for industrial steam raising (118). In particular, information relating to the heat transfer to immersed tubes, limestone utilization and combustion efficiency will be obtained. Babcock and Wilcox Co. (US) have produced designs for a package type concept as well as for a field erected type of fluidized bed water tube boiler (118).

In the smaller ranges of industrial boilers, Johnston Boiler Co. has developed a line of packaged fire tube boilers built under licence from Combustion Systems Ltd. in Britain (119). The capacities of this boiler range are from about 1 000 kg/h

to 22 000 kg/h. In another joint venture illustrating co-operation between companies in Britain and the United States (119), Babcock Contractors Inc., an affiliate of Babcock and Wilcox (UK), and Riley Stoker have announced that they will jointly manufacture atmospheric fluidized bed boilers in the range from about 20 000 kg/h to 200 000 kg/h. They have obtained a contract for retrofitting of a 27 000 kg/h boiler at the Central Ohio Psychiatric Hospital with a fluidized bed combustion system for burning Ohio coals, which typically have a high sulphur content, within existing clean-air laws (120).

In an effort to improve the combustion of fines, Keairns et al (121) have introduced the use of a draught tube within the fluidized bed normally associated with the Westinghouse gasifier system. The concept has considerable potential if relatively deep beds can be tolerated.

c) West Germany

The original development of fluidization technology took place in Germany during the twenties with the development of the Winkler gasification process. It was only in the fifties, however, that development took place along the more familiar lines apparent today. Up to the early seventies, development in Germany was in the field of special types of equipment incorporating fluidized bed combustion. Reh (122) reports on the Lurgi fluidized bed roasting process for the roasting of sulphide ores with steam generation. In one particular application, a fluidized bed roaster having a diameter of 12,5 m and with a maximum steam generation capacity of some 40 000 kg/h is described.

More recently Schilling (123) has described fluidized bed combustion as an economic means of utilizing coal for power and heat generation. Four main areas are distinguished where fluidized bed combustion can be applied (123). The combustion of wastes is described as the first area of application in

which the combustion of slurries, oil shale, used oil, roasting etc. can be undertaken. A 35 MW_t plant built by Ruhrkohle AG near Dortmund for the combustion of flotation tailings in which 10 MW_t is extracted by "in-bed" cooling tubes and the remaining 25 MW_t is extracted in a waste heat boiler is also described (123).

The second application is in the field of small industrial steam generation or the production of hot water for industrial or large blocks of flats. A design concept for a 0,4 MW_t unit has been developed. A 6 MW_t plant is in operation at Recklinghausen and is operated by a subsidiary of Ruhrkohle AG.

Electricity generation and large scale generation of heat for district heating is considered as the third potential application of fluidized bed combustion of coal. Indeed, the Federal Minister for Research and Technology of the West German government has initiated five projects relating to fluidized bed combustion (124).

These projects include the conversion of the chain-grate boiler for operation as a fluidized bed unit with a thermal output of 35 MW_t at the Düsseldorf-Flingern plant. Another plant combines a conventional pulverized fuel-fired furnace with six fluidized bed furnaces. The fluidized bed furnaces are located around the periphery of the main boiler and we ducted into the boiler above the burner zone. The unit is being built for Saarbergwerke AG at Völklingen and will have a total output of 200 MW_e of which about 40 MW_e is supplied by the fluidized beds. In order to burn a coal with a high ash and sulphur content, the Wesertal electricity supply utility has planned a 125 MW_t fluidized bed power plant to be built by the Vereinigte Kesselwerke. The remaining two projects relate to pressurized fluidized bed combustion. They include the demonstration plant at Bottrop built by Bergbauforschung and the Vereinigte Kesselwerke AG, and the involvement of German companies in the International Energy Agencies pressurized fluidized bed combustor at Grimethorpe in England.

d) India

India has a total coal reserve, proved, indicated and inferred, of about 82 million tons (125). However, one of the major problems with Indian coals is their high ash content and their abrasiveness. Tests conducted on a 590 mm square refractory lined combustor (126) indicated that these coals are amenable to combustion in a fluidized bed, and that screened coal could be burnt without any further coal preparation. Abbi et al (127) have described the work of a number of national laboratories and of Bharat Heavy Electricals Ltd. in the development of fluidized combustion boilers for burning Indian coals.

An atmospheric-pressure fluidized bed package boiler capable of generating 10 000 kg/h of steam was installed at Bharat Heavy Electricals Ltd. test site. This unit has been in operation since March 1977. A smaller 2 000 kg/h was commissioned in April 1976 at the Central Fuel Research Institute, Dhanbad with a view to establishing scale effects in the design equations of fluidized beds. Work is also being conducted into pressurized fluidized bed combustion and a design of a prototype unit for the generation of hot water has been developed.

e) Brazil

Brazil has vast reserves of high ash and relatively high sulphur coal (about 35-55% ash and 3% sulphur on a dry basis). A recent study by Saddy and Szego (128) has indicated that fluidized bed combustion would be slightly more expensive than stoker firing for industrial steam generation. Both these systems though more capital intensive than oil fired or electric boilers presently utilized were substantially cheaper to operate. The potential of the fluidized bed to reduce the sulphur emissions would favour the development of a fluidized bed boiler for industrial steam raising in Brazil. A project has been initiated for the development of Brazil's first fluidized bed combustion system. The prototype unit will generate steam and/or hot gases at a rating equivalent

to 8 000 kg/h of steam and is being financed by the Brazilian government coal marketing company (129). The objective is the replacement of a large number of small fuel oil plants required for brick manufacture, tobacco drying, industrial boilers etc with coal fired fluidized bed combustors.

f) South Africa

Excluding the work done by Natal University, cf Section 1.5.1 (b), all the research and development in South Africa has been related to atmospheric fluidized bed combustion. The Fuel Research Institute commenced work into the fluidized bed combustion of large coal in December 1975 on a small 210 mm diameter test rig (130). Research is presently being conducted on a larger 500 mm square refractory lined combustor into the evaluation of the potential of a number of South African coals for combustion in a fluidized bed of inert particles (131). Work at Cape Town University in collaboration with John Thompson Africa (Pty.) Ltd. and on which this thesis is based, has been towards the development of an atmospheric fluidized bed combustor capable of utilizing poor quality South African coals, and in particular the high fines content duff coal (i.e. coal having a top size of 6,3 mm) of which there is an abundant supply.

Holsteyn (132) has reported on the design and construction of a 4 000 kg/h boiler built under a licence agreement negotiated with Combustion Systems Ltd. at the beginning of 1975. The most recent development in South Africa, was the announcement of the official firing of the World Energy Resources Consultancy Service vertical fluidized bed coal fired steam boiler at the end of August 1980. The boiler is located at Ngwelezana Hospital, Empangeni in Natal.

1.6 OBJECTIVES OF THIS THESIS

Research into fluidized bed combustion is continuing at an increasingly rapid pace and a large volume of work is being

produced. However, the complex and inter-related nature of the subject has resulted in it being difficult, if not impossible, to produce a unifying theory. This is compounded by the lack of a fundamental understanding of many of the basic parameters affecting the process. Much of the information has been obtained on small scale rigs and the extrapolation to large scale plant has to be made with some caution. Further, the original development of fluidization stems from the chemical and process industries which utilized relatively fine particles and deep beds.

In South Africa the development of fluidized bed combustion for industrial steam generation and for possible small scale electricity generation, will in the short to medium term be along the lines of atmospheric fluidized bed combustion. It is evident that such a unit is on the threshold of becoming commercially available from overseas suppliers who have based their designs on conditions peculiar to the country of origin. In any event, the designs by and large have developed as a result of 'engineering experience' and many lack a fundamental understanding or description of the heat transfer and combustion processes taking place. This is particularly true of the development of the shallow fluidized bed combustor.

The main objectives of this thesis are therefore to obtain a better understanding of the heat transfer and combustion processes taking place in an industrial sized atmospheric fluidized bed combustion unit. This implies an investigation into both the in-bed and above-bed reactions associated with the unit. In view of the increased fan power associated with deep beds, only shallow beds of relatively coarse particles are to be investigated.

In view of the importance of coal distribution which has been highlighted by the literature survey, an assessment of both under-bed and above-bed feeding of the coal is to be evaluated. The effect of these means of feeding on the basic processes occurring in the combustor unit are to be evaluated on a

qualitative basis to facilitate scale-up to larger industrial plants. A final objective is the development of a sound theoretical basis for the heat transfer and combustion phenomena studied.

The thesis therefore covers the mechanism of heat transfer from the bed to a peripheral enclosing surface, to a horizontal tube immersed within the bed and to the freeboard zone above the bed. Combustion both within and above the bed is considered and the shallow fluidized bed and freeboard zone is considered as a single furnace entity.

CHAPTER 2

EXPERIMENTAL EQUIPMENT

As the prime objective of the research is the assessment of the combustion, entrainment and heat transfer phenomena on an industrial scale, a shallow fluidized bed combustor furnace was built which would be representative of a small industrial unit. Further the flue gases on leaving the combustion chamber are exhausted to atmosphere at some 600 to 800°C depending on the operating conditions and are not cooled in a convective section as this technology has been well researched and is readily described by fundamental heat transfer relationships. The exhaust gases are ducted away from the test facility by means of an uncooled duct to an existing stack.

2.1 GENERAL ARRANGEMENT

The test rig is located at the Bellville works of John Thompson Africa (Pty.) Ltd. and is housed in a separate building to accommodate the test facility with its associated instrumentation and controls. The test rig comprises the flue of a vertical flue fluidized bed shell boiler having a diameter of 1 000 mm. A sectional representation of the test rig is illustrated in Figure 9, while a diagramatic flow diagram is presented in Figure 10.

Air is supplied to the test rig as primary air via a windbox situated at the base of the fluidized bed, and as secondary air through nozzles situated in the freeboard zone above the fluidized bed. Coal can be introduced into the side of the bed by means of a screw feeder or from above the bed by means of a rotary drum-type feeder. A pneumatic spreader is utilized for distributing the coal across the width of the bed. The spreader consists of an air jet which is located

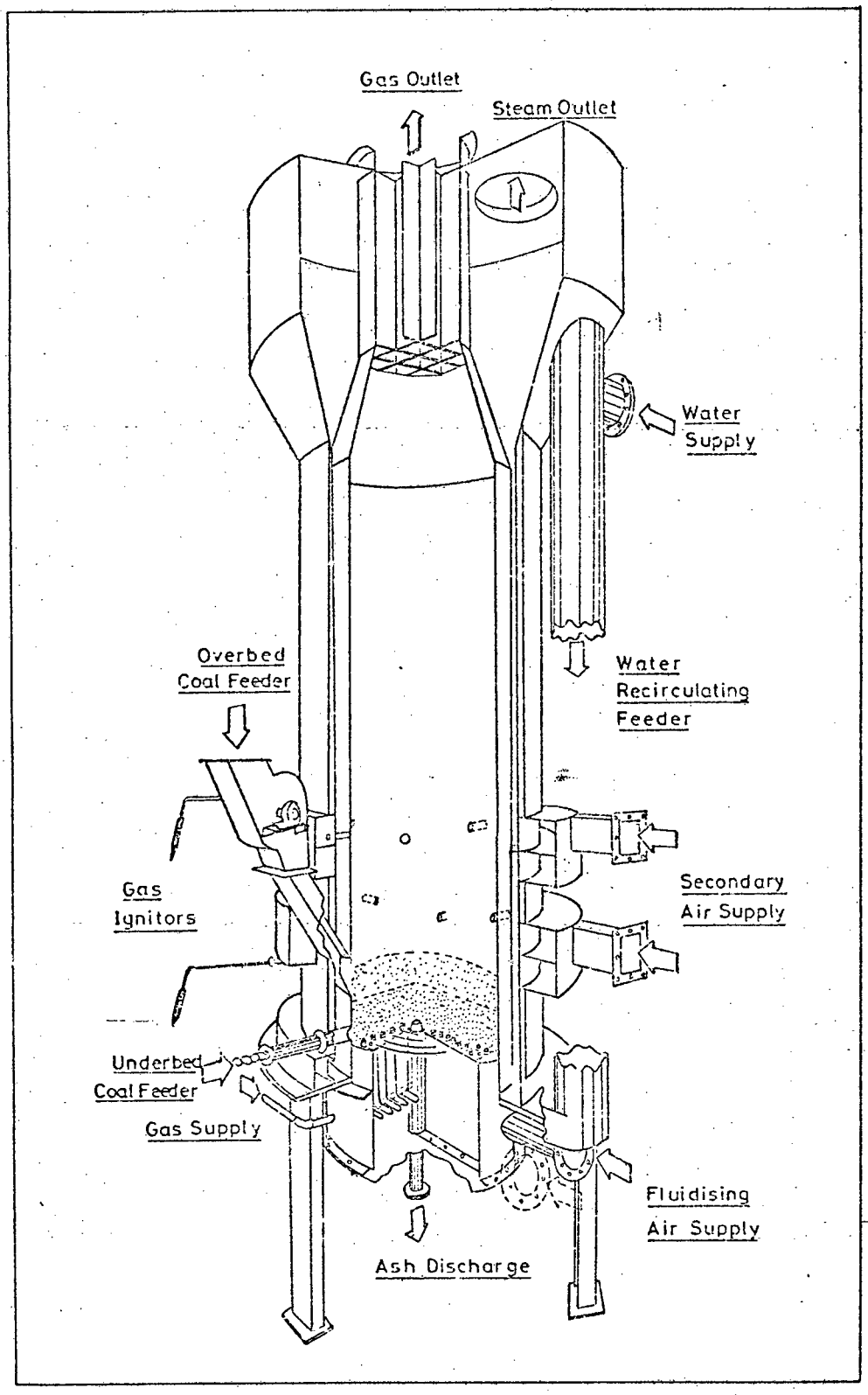

Figure 9 : Sectional representation of the 1000 mm diameter water cooled Fluidized Bed Combustion Test Facility (Immersed cooling tube not shown).

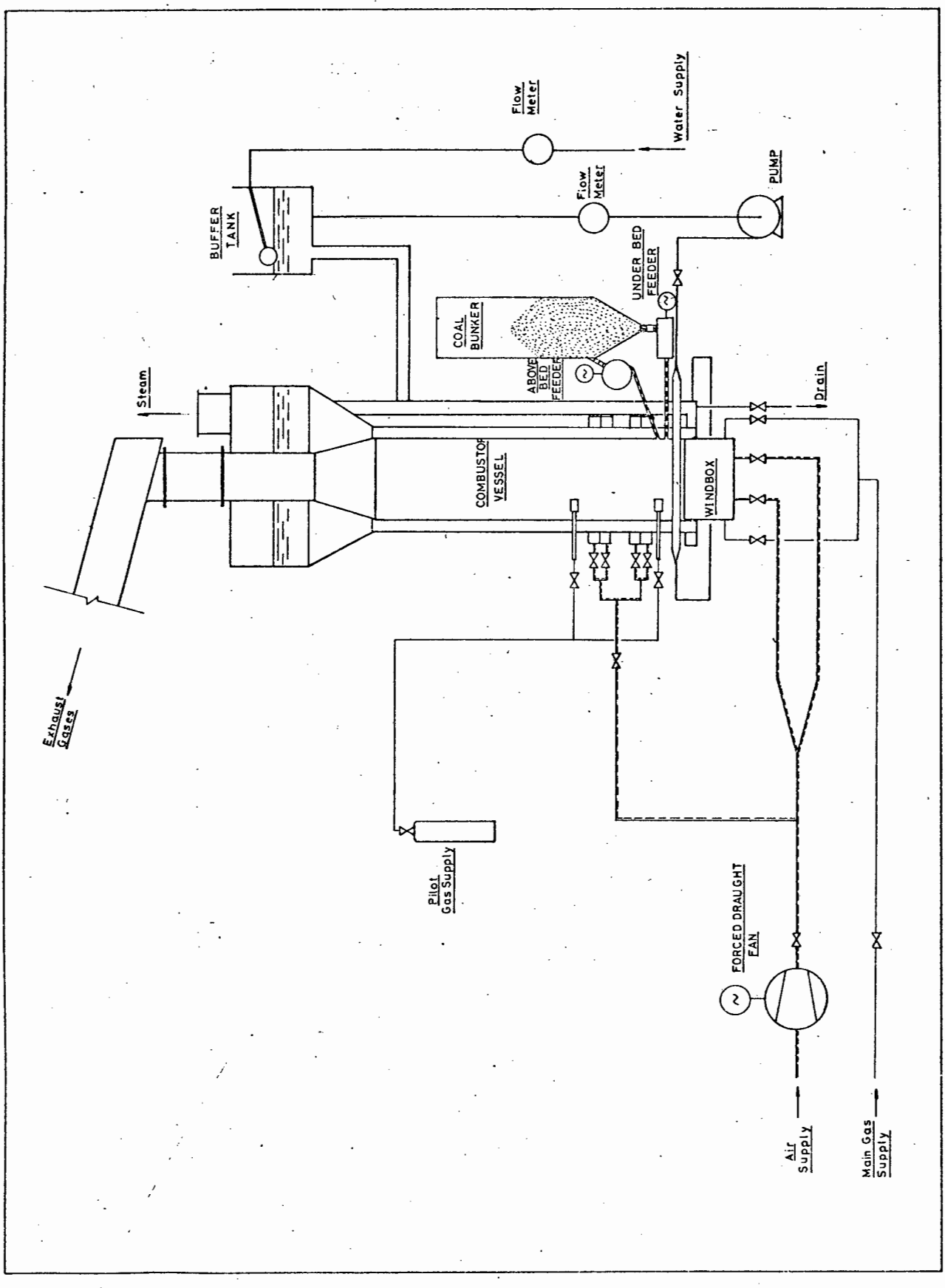

Figure 10 : Flow diagram of the 1000 mm diameter test rig.

at the base of the above bed feed chute. Details of the arrangement of the two feeders are contained in Figure 11.

The vertical flue is surrounded by a water jacket in which the water and steam mixture is forced upwards by natural circulation which is effected by means of an external 200 mm ID downcomer pipe. The jacket is expanded at its upper end to provide an adequate surface area for the release of the steam. The freeboard extends some 4 metres above the fluidized bed providing sufficient time for the completion of a secondary combustion reaction and further enabling the entrainment of particles from the bed to be largely devoid of splashed material as a consequence of bubbles bursting at the surface of the bed. A horizontal cooling tube can be immersed in the fluidized bed by introducing a secondary cooling circuit. The tube does not form a fixed part of the test rig, and can easily be removed or replaced by tubes of different diameters. Tests have however only been conducted with a tube of 76,2 mm OD in the secondary cooling circuit.

Gas is used as a means of raising the bed temperature to the ignition temperature of the coal during start-up. The gas is introduced by means of an elaborate distribution system at the base of the fluidized bed, and ignited by means of pilot gas burners located in the freeboard as illustrated in Figure 9.

The test facility has been extensively instrumented. Heat flux pads have been attached at some eleven levels in three vertical planes of the flue. Gas temperatures can be monitored by means of suction pyrometers at various levels in the flue whilst the exhaust gases can be sampled isokinetically to establish the dust burden. An adjustable water cooled heat transfer probe has been fabricated for introduction via the ash discharge port in the centre of the bed. This probe enables the measurement of the bed-to-probe heat-transfer coefficients at various levels within the bed and the region immediately above the bed.

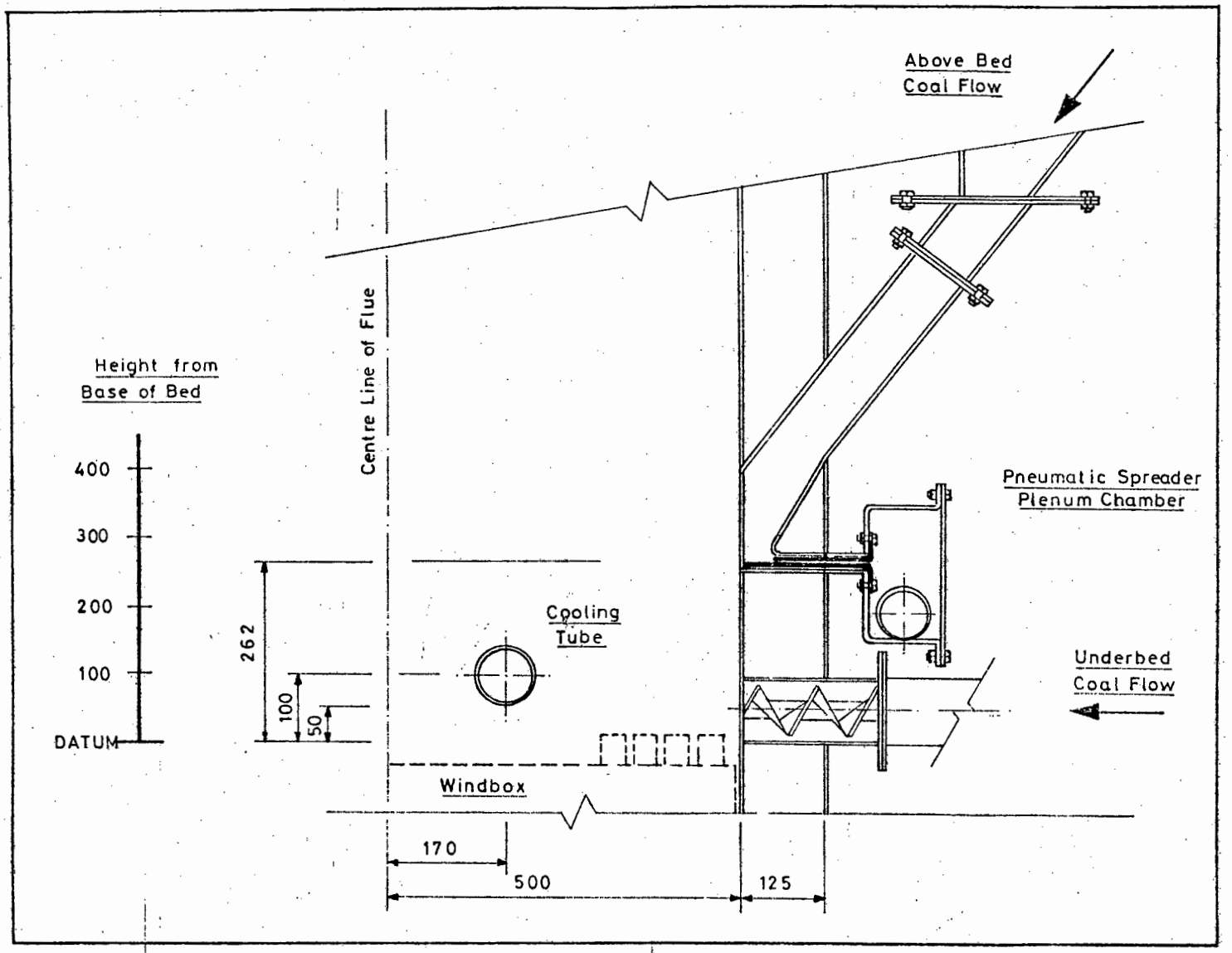

Figure 11 : Sectional elevation of the fluidized bed to illustrate the arrangement of the coal feeders and the cooling water tube.

2.2 INDIVIDUAL COMPONENTS AND SUB-SYSTEMS

As is evident from the preceding section, the fluidized bed combustor test facility is made up of a number of individual components and sub-systems. These include the air and fuel supply systems, the cooling water circuits and the gas ignition equipment required for start-up. A number of safety features have been incorporated concerning the gas ignition and for ensuring an adequate flow of water through the secondary cooling circuit. A general description of the components making up each of these sub-systems is included below, whilst diagrams and the detailed design of the components are to be found in Appendix A.

2.2.1 The Combustor Vessel

The combustor vessel is made up of the vertical flue which contains the fluidized bed at its base with a freeboard of some 4 metres. The freeboard acts as a radiant furnace chamber for the transfer of heat and the completion of the combustion reaction. A 125 mm water jacket surrounds the flue providing adequate cooling by means of natural circulation, the circulation circuit being completed by means of a 200 mm downcomer pipe. The steam produced is vented directly to atmosphere. The feed flow is monitored by means of an integrating type of water feed flow meter from which the evaporation rate is determined. It is imperative, therefore, to ensure that no water droplets are carried over with the steam as this would seriously affect the results. As a result, the steam release area had to be increased and this has been accommodated by expanding the vessel jacket to a diameter of some 2 200 mm. In view of the steam space being at about atmospheric pressure, large volumes of steam are generated resulting in high circulation rates which have been calculated to be of the order of one hundred times the evaporation rate.

The primary air windbox extends some 200 mm into the combustor vessel, thus providing the water jacket with a mixing zone

immediately prior to the fluidized bed where exceptionally high heat flux rates exist. Access to the interior of the vessel can only be made after unbolting and removal of the primary air windbox from the base.

Two secondary air windboxes are located at about 500 mm and 1 000 mm above the base of the primary air windbox. Each windbox is split along a horizontal plane, thereby effectively forming four windboxes, each having four 38 mm diameter nozzles. Details of the combustor vessel are illustrated in Figure A1 of Appendix A.

2.2.2 The Primary Air Windbox

The primary air windbox is 600 mm deep and divided into two parts to enable tests to be performed with half the bed active and the remainder slumped. A number of standpipes or 'bubble caps' are located on top of the windbox to form the distributor. Each bubble cap has been individually machined and screws down onto a socket welded to the windbox. Thus different pressure drop characteristics can be obtained by changing a complete set of bubble caps.

In designing the distributor, a number of various types were considered viz, a perforated plate type, a sintered metal or porous ceramic, sparge tubes and finally bubble caps. The latter were chosen as

(i) They are easily replaced,

(ii) they are not susceptible to warping as are sparge tubes in contact with the hot fluidized bed,

(iii) they result in a distributor of high mechanical strength and are not susceptible to failure as a result of thermal shock,

(iv) provided the nozzle is sufficiently tall, a 'dead' layer of sand forms between adjacent nozzles which does not form part of the active bed. This layer insulates the top of the windbox from the hot fluidized bed.

A further consideration is the relatively unstable nature of the fluidized bed which can result in channelling if the distributor is poorly designed leading to uneven fluidization. This is "because the pressure drop of a fluidized bed depends only on the weight of the bed per unit area and is independent of the fluidizing gas flow rate...., there are no self-regulating properties to help maintain a uniform flow rate across the bed" (8, p.80). The major functior of the distributor is to promote uniform fluidization by stabilizing the effect of gas distribution. The distributor must support the defluidized bed and prevent the backflow of material during normal operation or when the bed is shut down. A further characteristic of the bubble cap type of distributor is its ability to maintain uniform fluidization at lower loads even when the distributor to bed pressure drop ratio is small.

The windbox was designed with 312 bubble caps which are located on concentric circles separated radially from each other by 50 mm. The arrangement of the bubble caps on the windbox is illustrated in Figure A2. The bubble caps were designed using simple orifice plate type calculations and a sample of twelve nozzles were initially fabricated. The design of these nozzles and the associated stub is illustrated in Figure A3. The nozzle was manufactured from hexagonal bar and contained a 4 mm diameter hole drilled into each of the six faces. The pressure drop to volume characteristics of this initial sample of twelve nozzles was obtained for each of the nozzles on a special calibration test piece. The discharge coefficient for the sample was found to be 0,694. It was decided to decrease the diameter of the holes drilled into the nozzles to 3,5 mm thereby increasing the pressure

drop for a specific volume flow rate of fluidizing air. This implies a free area of 2,29%.

2.2.3 The Air Supply System

Air is supplied to the combustor vessel by means of a high pressure fan capable of delivering 1,4 kg/s of air at 860 mm Wg. The total flow rate from the fan is controlled by means of a set of contra-rotating dampers (133) which in turn are controlled by a modulating motor activated from the control panel. A separate manually adjustable flow control damper was fitted to the suction side of the fan to improve the control of the air flow at low ratings. A layout of the air supply system is presented in Figure A4.

After the total air control damper, the air is divided into primary and secondary air whilst a much smaller quantity is available for pneumatic spreading. The flow rate in each of these air streams is monitored by means of orifice plates located in the air pipework in strict adherence to BS 1042.

2.2.4 The Coal Feed System

Coal can be fed to the side of the fluidized bed by means of a screw feeder, or from above the bed by means of a rotary drum-type feeder. The flow from each feeder is controlled by varying the feeder speed. This is manually effected by making the necessary adjustment to an infinitely variable hydraulic gearbox.

In order to accommodate the high coal flow rates envisaged, a relatively large diameter rotor was required for the screw feeder. This in turn requires a large aperture in the water jacket which can have a disruptive effect on the flow characteristics of the fluidized bed in the vicinity of the coal feeder. The flighting of the screw is of 75 mm diameter having a pitch of 75 mm and is welded onto a 30 mm diameter shaft.

The overbed drum feeder incorporates a pneumatic spreader for distributing the coal more evenly over the furnace. The coal is led down a feed chute to a flat momentum breaking section at which point the pneumatic air projects the coal across the width of the furnace.

Coal is brought into the test rig building by means of a screw conveyor from a small hopper to the coal storage bunker from which both coal feeders obtain their coal supply. The coal bunker has a storage capacity of about 2 tons of coal. The layout of the coal feed system is illustrated in Figure A5 in Appendix A. Further details are illustrated in the photographs contained at the end of Appendix A.

2.2.5 The Secondary Cooling Circuit

In order to evaluate the heat transfer to horizontal tubes immersed within the bed, a secondary cooling circuit was installed. The flow has to be of such a rate as to prevent the formation of a saturated steam and water mixture to facilitate the measurement of the total heat transferred. A flow diagram of the secondary cooling circuit with its cooling tube and associated safety system is illustrated in Figure 12.

From Figure 12 it is seen that both the secondary cooling circuit and the combustor vessel are fed from a common float controlled buffer tank. The water to the buffer tank is metered, and thus measures the sum of the total amount of water evaporated and the quantity discharged via the drain should the drain be open. The cooling of the furnace flue by means of the water jacket is inherently safe as in the event of an interruption to the feed water flow rate or in the event of a power failure cooling will be provided as a consequence of natural circulation as previously described. However, the same inherent safety is not true of the horizontal cooling tube. In the event of a pump failure or any interruption of the water flow through the cooling tube, the

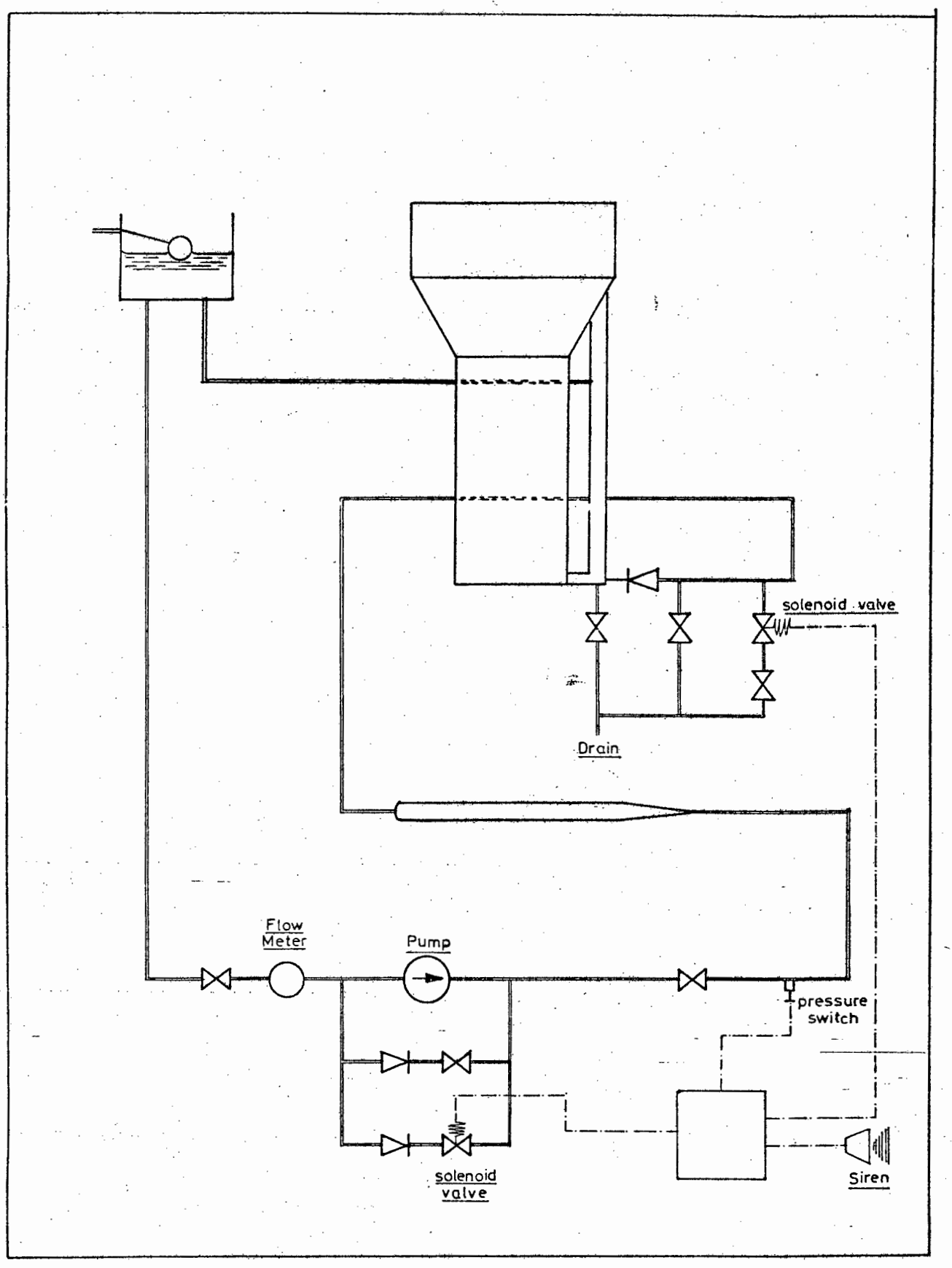

Figure 12 : Flow diagram of the secondary cooling circuit with its associated cooling tube and safety system.

water in the tube will stagnate leading to failure within seconds in view of the high heat transfer rates associated with the hot fluidized bed. The safety system for the immersed cooling tube is illustrated in Figure 12 and contains two solenoid valves which are deactivated should the pressure in the secondary circuit fall below a pre-set value. The solenoid valves open on de-activation, causing the water to flow from a head of about 7 metres through the cooling tube to waste via a drain after having by-passed the pump.

Although the secondary cooling circuit has been designed to enable the heat transfer to a number of different sized tubes to be evaluated, heat transfer studies were conducted on a 76,2 mm OD tube only. Grooves 2 mm deep and 1,6 mm wide were machined into the tube for the fitting of eight 1,5 mm diameter stainless steel sheathed chromel alumel thermocouples. These thermocouples were silver soldered into the grooves at two locations each having four thermocouples at 90^{o} from each other on the circumference of the tube. Details of the location and fitting of the thermocouples to the tube as well as details of the fitting of the tube to the combustor vessel are illustrated in the detailed drawings of Appendix A.

The thermocouples were silver soldered to the grooves in the tube so as to measure wall metal temperatures. These temperatures are required in order to evaluate heat transfer coefficients as opposed to total heat transfer rates. The water flow rate to the cooling tube is measured by means of an integrating type of flow meter whilst the inlet and outlet water temperatures are measured by means of mercury in glass thermometers with graduations reading $0,2^{o}C$. Although the cooling tube immersed within the bed has a diameter of 76,2 mm, the inlet and outlet pipes to this cooling tube have diameters of 25 mm and contain the thermometers. Thus Reynolds numbers at the thermometers are always well in excess of 25 000, thereby ensuring a well mixed fluid at the point of measurement.

Referring to the flow diagram of Figure 12, it is seen that the connecting pipe from the buffer tank to the combustor

vessel introduces the feed to the downcomer. This has specific advantages relating to the circulation; however, it should be noted that this pipe is made up of a 200 mm NB pipe and as such has a negligible pressure loss associated with it. The level in the combustor vessel is therefore very similar to that in the buffer tank, but can be slightly higher or lower than that in the buffer tank dependent on operating conditions. The flow through the cooling tube is dictated by the need to prevent the formation of a saturated steam water mixture at its exit whilst the feed flow rate is dictated by the rating of the unit and hence the evaporation rate. Both these criteria are essentially independent on each other, hence the condition can, and does, arise where the flow in the cooling water circuit exceeds that of the evaporation rate. In this instance water flows from the combustor vessel to the buffer tank. The buffer tank then becomes a mixing tank and the water enters the cooling tube at a temperature somewhat in excess of the feed water temperature. Figure 13 is a graphical representation of the effect of increasing the water mass flow rate in the secondary cooling circuit on the inlet and outlet cooling tube water temperatures for different tube heat absorption rates.

2.2.6 The Gas Ignition System

Before the combustion of coal will be self-supporting, the coal particle must be raised to a temperature in excess of the ignition temperature. For coal surrounded by a mass of inert particles as in a fluidized bed combustion system, the entire mass of coal and inerts must be raised to the temperature at which the combustion of the coal becomes self-sustaining. In the larger scale industrial type of equipment, this can generally be achieved by

(i) preheating the fluidizing air by means of a start-up burner located in the ducting immediately upsteam of the windbox,

(ii) use of above bed burners directed onto the fluidized bed,

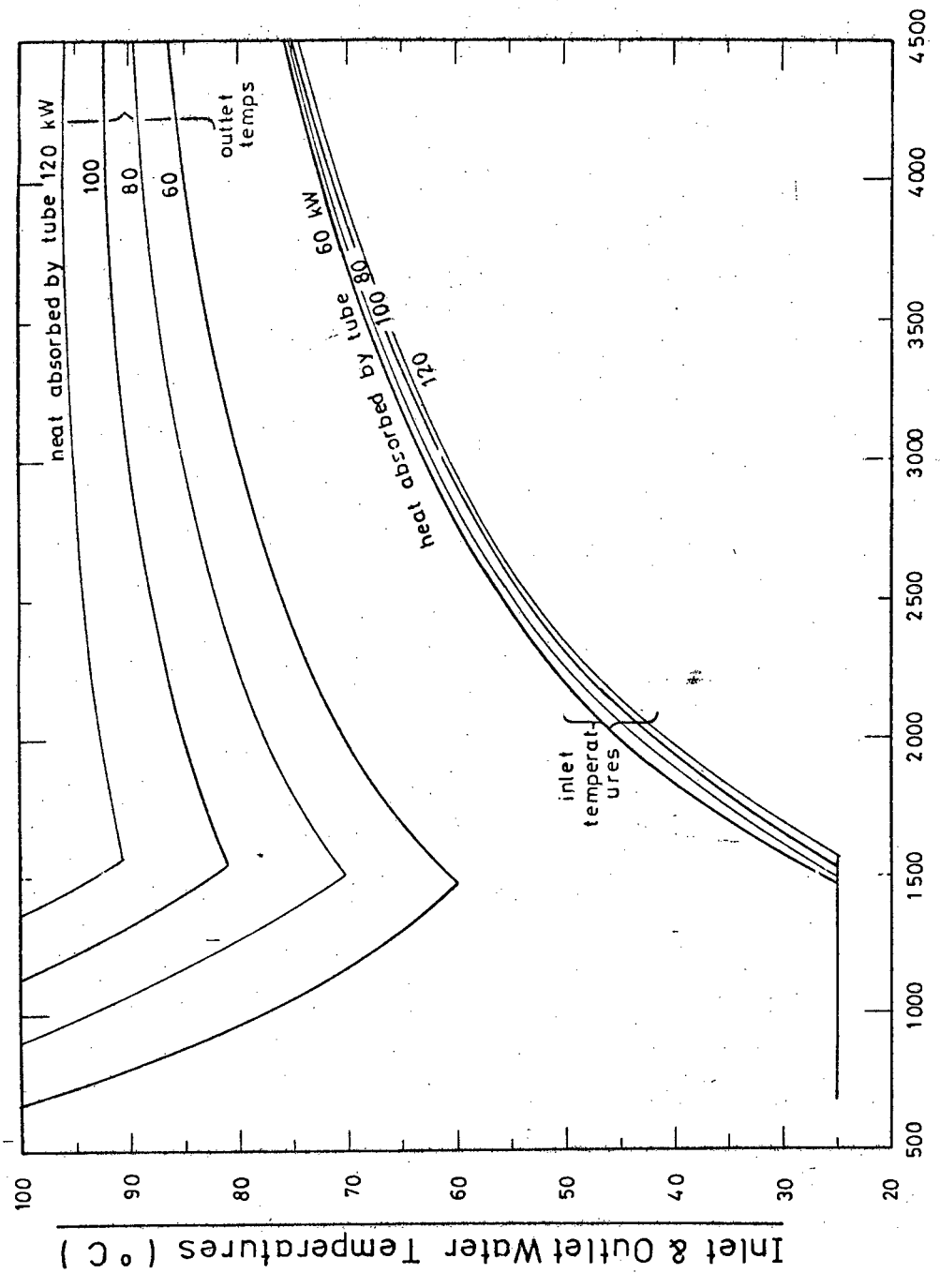

Figure 13 : Inlet and outlet cooling tube temperatures for various tube heat absorption rates at an evaporation rate equivalent to 1000 kW.

(iii) gas combustion within the bed.

It was decided to utilize gas as a means of raising the bed temperature, and a number of gas start-up systems were investigated. Inherent in any effective gas combustion system is the requirement of good mixing with the air. For a fluidized bed system this can best be achieved by pre-mixing the gas and the air in the plenum chamber or windbox providing the fluidizing medium. However, the resulting large explosive gas volume contained in the windbox constitutes a hazard and is industrially unacceptable. The nozzle-type of distributor would also result in the nozzles presenting high temperature surfaces from which ignition could be propagated.

A number of different gas ignition systems were considered. The concept of gas mixing in the nozzle developed by BCURA would require extensive safety features to enable its use with any degree of confidence. The system employed by NEI at Annan, in which the gas is introduced by means of a separate system of gas nozzles or bubble caps though inherently safe does not enable the satisfactory mixing of the gas and air. The mixing is determined by the rate at which gas diffuses from a bubble to the particulate phase. For shallow fluidized beds the bypassing of unburnt gases can be substantial.

Even in premixed gas and air mixtures, combustion in shallow fluidized beds may not always be accomplished (134). A lower particle size limit has been established below which stable combustion will in any event not occur. Cole and Essenhigh (135) have also emphasized the difficulties associated with the combustion of gases in fluidized beds which have resulted in start-up times of as much as 24 hours being cited for large units. The major problem stems from the bypassing of the combustible gas through the bed as bubbles with its subsequent combustion above the bed. Both Broughton (134) and Cole and Essenhigh (135) indicate that combustion takes place within

the particulate phase, whilst the explosive nature of the gas combustion observed (75) would indicate that under certain conditions the bubbles do ignite.

In view of the inadequacy of existing gas ignition systems concerning either their safety or their ability to form an adequate gas air mixture for combustion within the bed, a novel gas distribution system was developed. Two 19 mm diameter gas pipes are introduced into the windbox, where after distribution to smaller gas headers, the gas is finally distributed into a series of 4,76 mm diameter pipes each of which extend through the windbox before being arranged between the nozzles. Small diameter holes drilled into these 4,76 mm diameter pipes enable the distribution of gas above the windbox.

Figure 14 illustrates how the gas is effectively mixed with the air in the fluidized bed. From Figure 14 it is seen that the gas distribution pipework is situated in the defluidized section between the fluidizing air nozzles. The gas is readily distributed through this fixed bed layer and diffuses into the particulate zone. Air from the fluidizing air nozzles diffuses from the bubbles formed into the particulate zone. Thus combustion should take place in the particulate zone with at worst, air bypassing in the bubbles.

The overall gas start-up system and associated safety features are illustrated in Figure 15. Gas is supplied from the factory gas ring main to the main gas distribution system described previously whilst a separate gas source is used for the pilot burners. The pilot burners are used for igniting the gas and further provide an ignition source should the main gas be extinguished, thus preventing a large volume of an explosive gas mixture from being formed in the confined space of the combustor vessel. Further, the solenoid valve will only be activated if a predetermined pressure is measured in each half of the windbox, and further that the pilot burner is in operation. A gas detector is

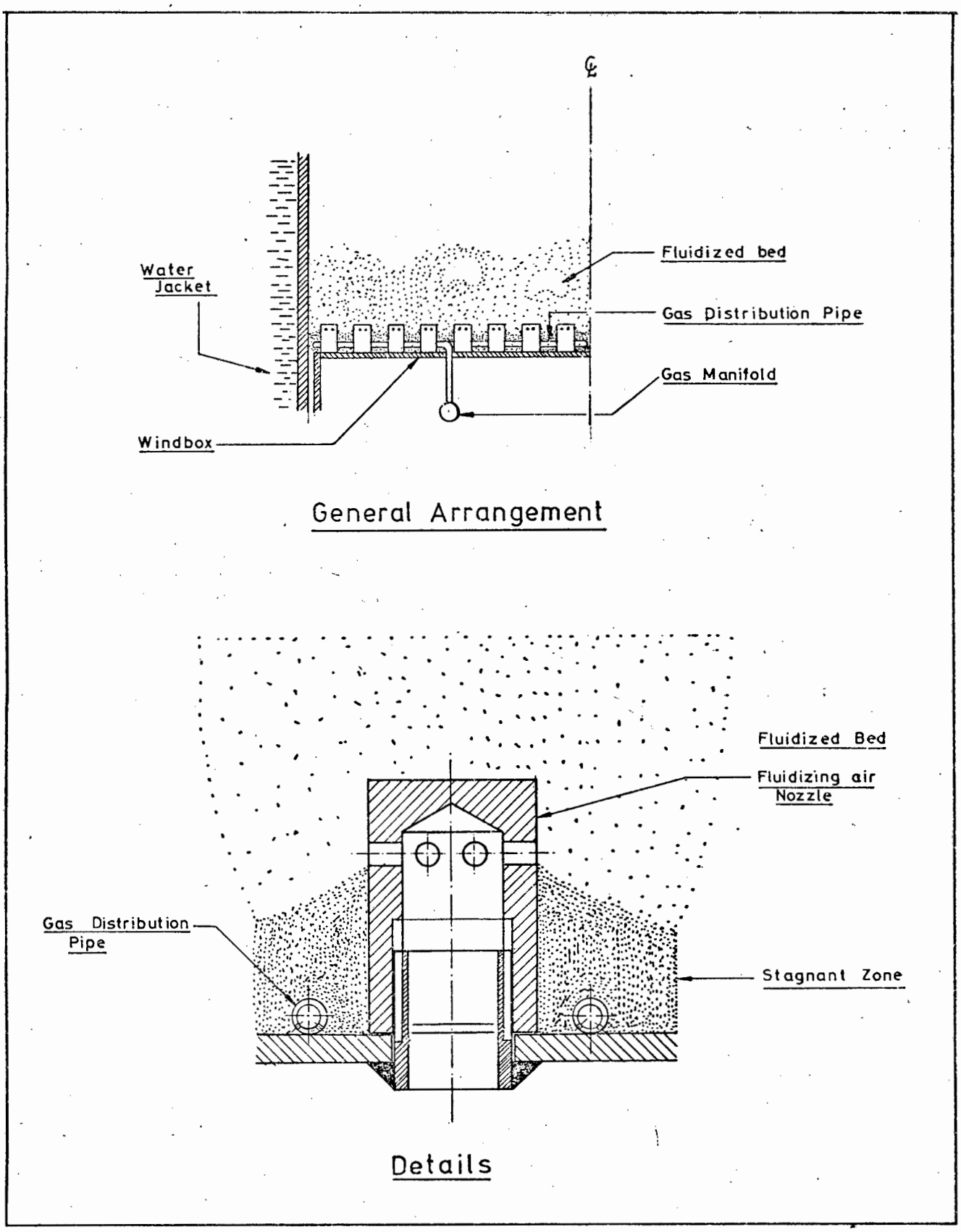

Figure 14 : Illustration of the gas distribution system.

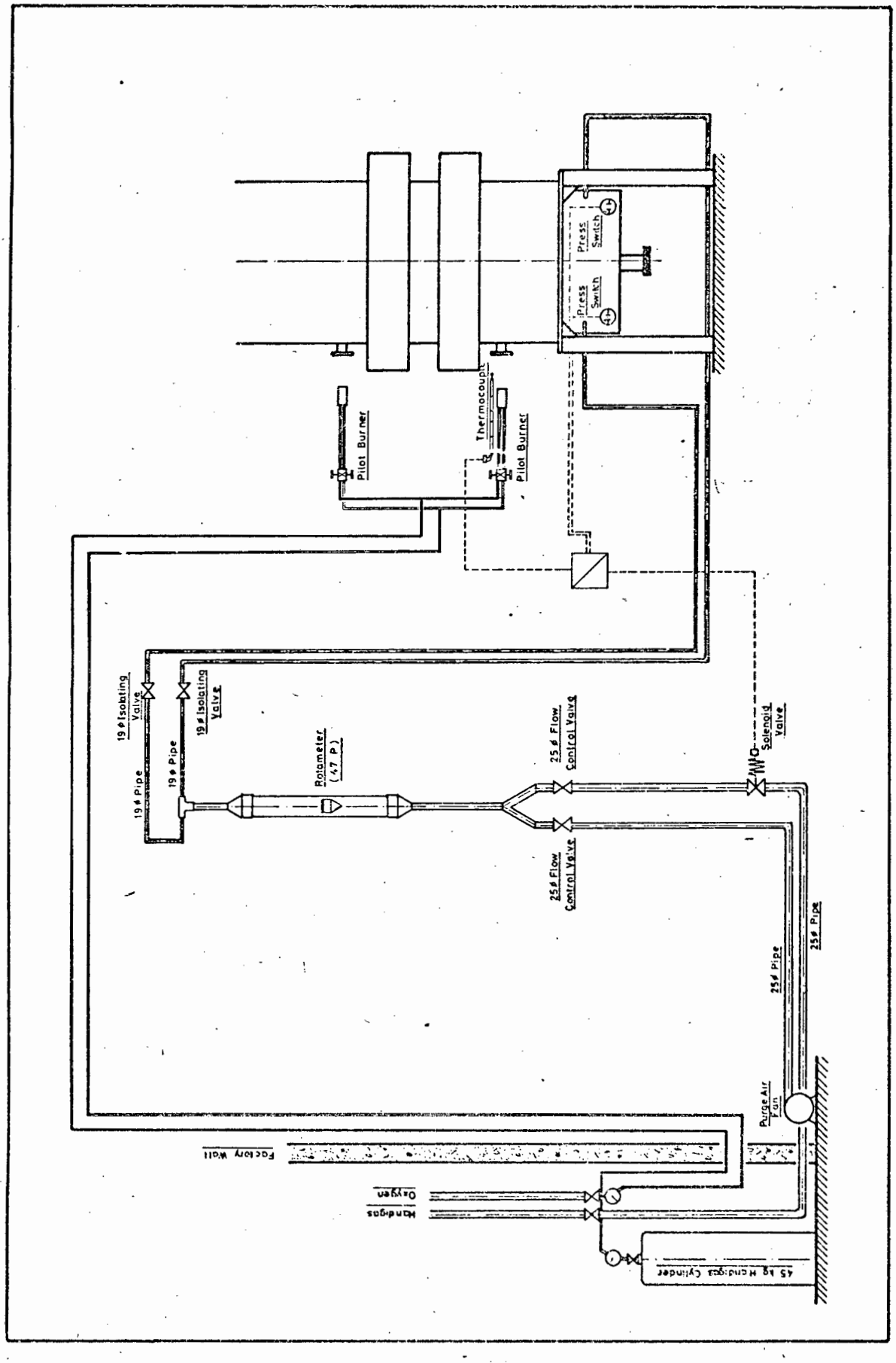

Figure 15 : Diagrammatic representation of the gas start up system.

contained in each half of the windbox to establish that no gas has leaked from the distributing gas manifolds.

2.2.7 Instrumentation

In order to obtain as much information as possible on both the combustion and heat transfer reactions taking place both within the fluidized bed and in the freeboard space above the bed, the test facility has been extensively instrumented. All the signals from thermocouples and other electrical outputs have been brought to a common control and monitoring panel. These signals have been monitored continuously by means of two twelve point Philips recorders and a further thirty points can be monitored intermittently on a Fluke data logger. The majority of the pressure tappings have been connected to a manometer board on the control panel, whilst others specific to the suction pyrometers have been connected to a separate manometer board. Continuous recording gas analysers are housed in the control panel. Most of the motors and auxiliary equipment such as the high pressure fan, cooling water pump, coal feeders and coal conveyor are operated from the control panel. A photograph of the control panel is included with the photographs at the end of Appendix A.

The variables which are to be monitored can be divided into six main categories:

(i) temperature measurements,
(ii) heat flux measurements,
(iii) pressure measurements,
(iv) flue gas analysis,
(v) particulate sampling, and
(vi) ancillary and special measurements.

A detailed flow diagram of the instrumentation related to electrical signals is illustrated in Figure 16 whilst the

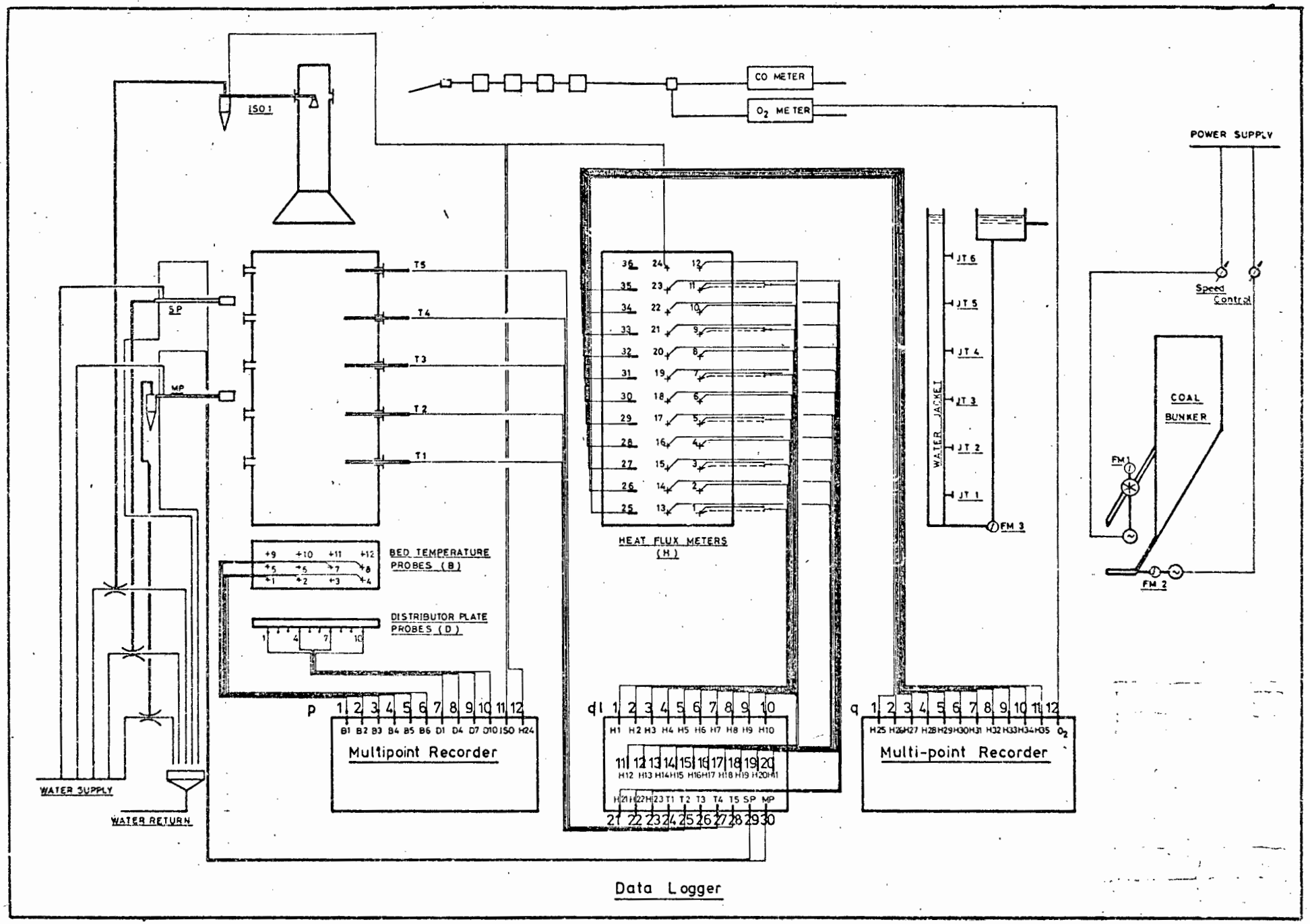

Figure 16 : Diagram illustrating instrumentation with electrical outputs and probe service requirements.

flow diagram for pressure measurements is illustrated in Figure 17. Much effort has been spent in designing the instrumentation, details of which are presented in Appendix B. The general instrumentation philosophy is included in the following sections whilst reference to detail is made to Appendix B.

a) General Temperature Measurements

The bed temperature is measured by means of eight stainless steel sheathed chromel-alumel thermocouples situated at various points in the bed as illustrated in Figure 18. Iron-constantan thermocouples have been silver soldered to five of the fluidizing air nozzles and to five different points on the distributor plate. These temperatures are measured in order to ensure that the plate or nozzles do not become too hot. The monitoring of these temperatures is of particular importance during start-up when flow disturbances could result in localized slumping or channelling in the fluidized bed.

b) Gas Temperature Measurements

Gas temperatures are measured by means of two types of suction pyrometers, details of the design and construction of which are contained in Section B.1 of Appendix B. The first type is a ceramic low efficiency type of pyrometer which is used to obtain the temperature of the gas flow at more frequent intervals than from the second type of pyrometer. This latter type is a portable high efficiency suction pyrometer having three concentric Incolloy shields. Two of these pyrometers were manufactured and were used to take temperature measurements at the end of the combustion chamber and at the measuring station immediately above the secondary air windboxes as illustrated in the Figures of Appendix B.

c) Heat Flux Measurements

The heat flow from the furnace to the water jacket can be measured by means of some thirty-one heat flux pads which

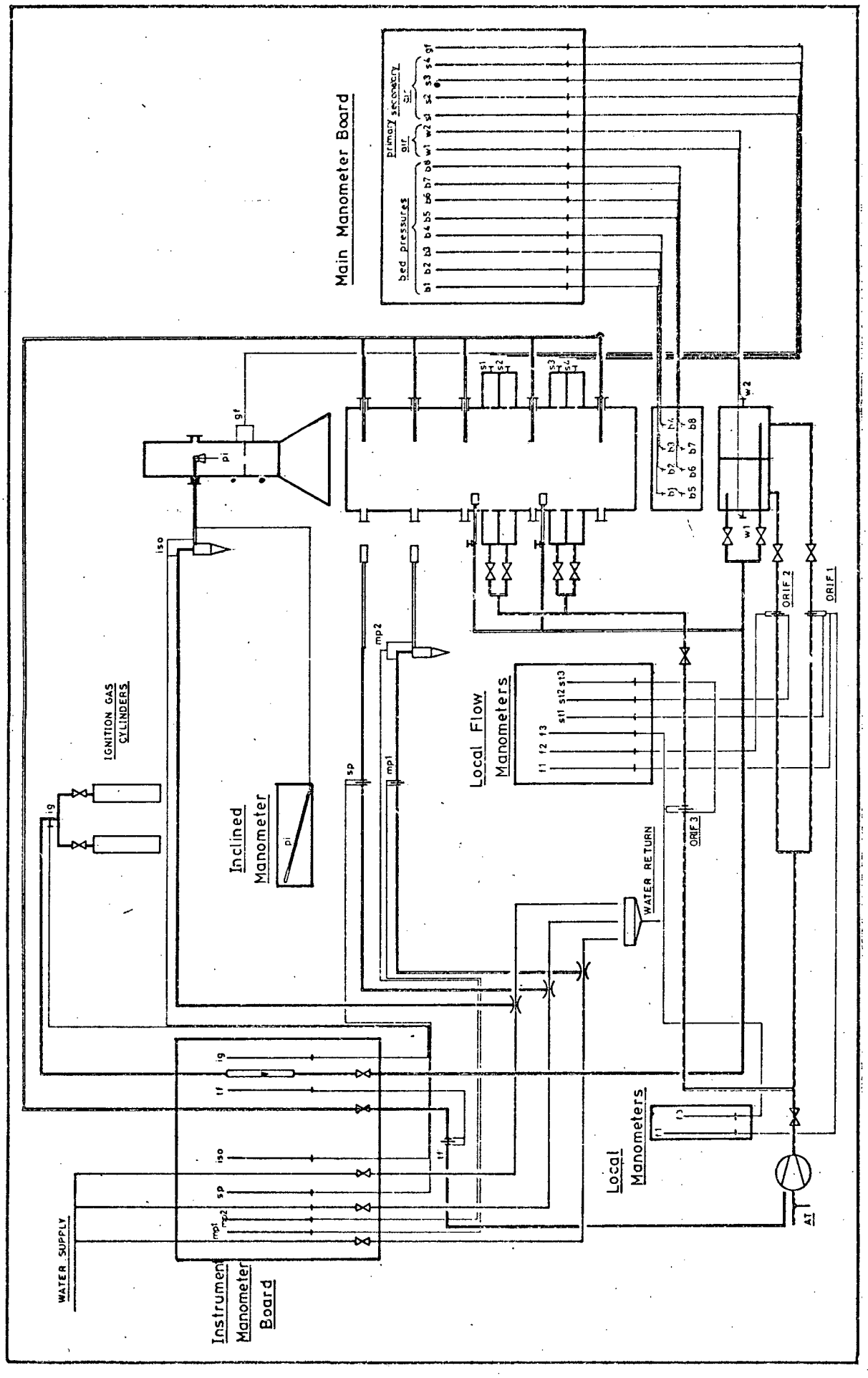

Figure 17 : Diagram illustrating pressure measurements and the relevant groupings on the respective manometer boards.

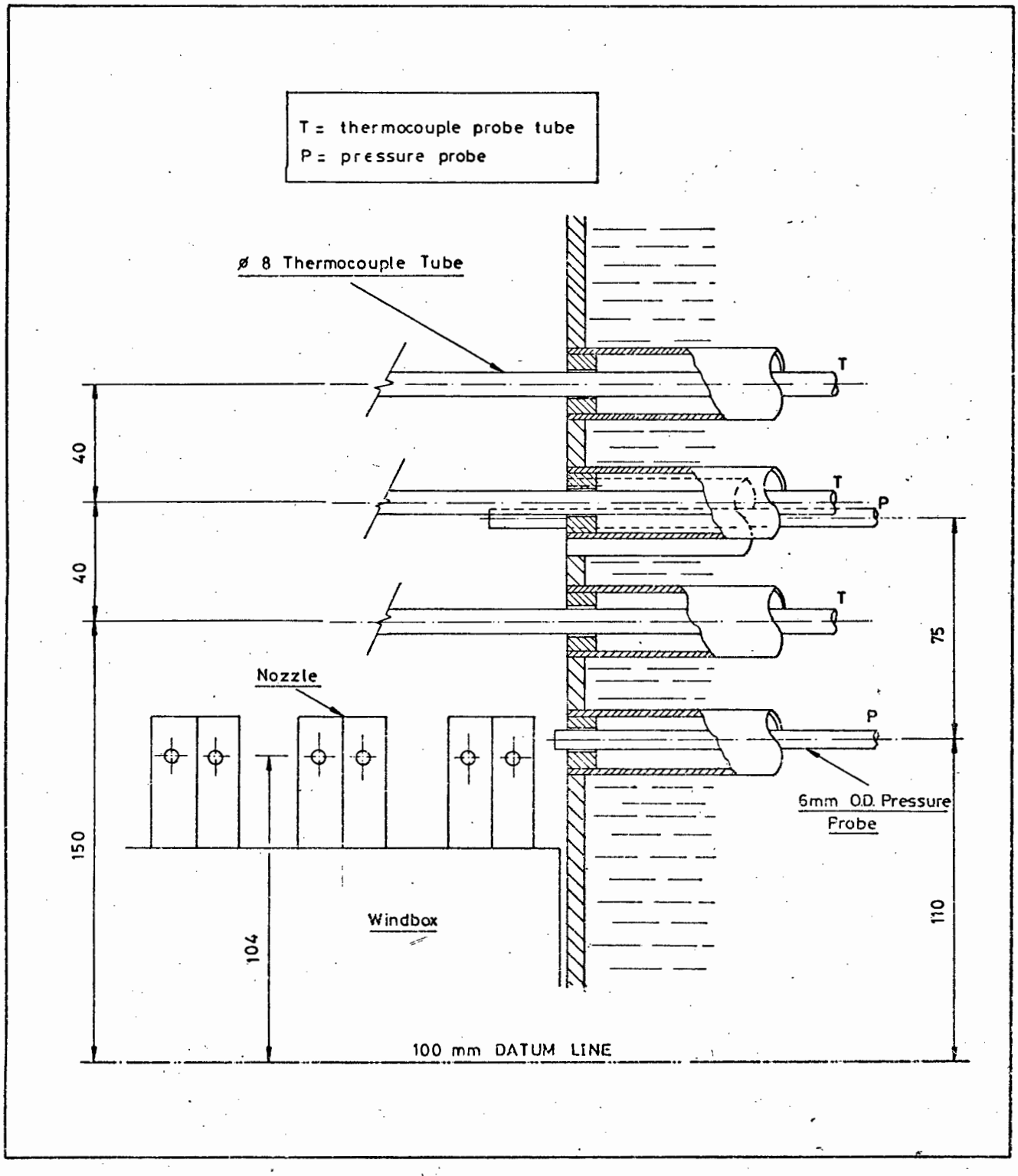

Figure 18 : Section through the combustor vessel to illustrate the location of the bed temperature and pressure probes.

have been attached at eleven levels in three vertical planes in the flue. These pads are located both within and above the fluidized bed. The design of the heat flux pads is similar to that proposed by Anson and Godridge (136), manufacturing details of which are illustrated in Figure 19. The heat flux is assumed to be proportional to the temperature difference monitored by means of two thermocouples which have been accurately positioned on the pad. Each of the pads was machined from flat bar on a numerically controlled milling machine of the Mechanical Engineering Department of Cape Town University. This ensured that the close tolerances required by the machining drawing of Figure 19 were met, and further that each of the heat flux pads were identical with each other within the machining capability of the particular milling machine. The welding of the pads to the combustor vessel flue was carefully supervised to further ensure that there were no deviations in the welding technique from pad to pad. Details of the development of the design, and actual design details of the heat flux pads are presented in Section B.2 of Appendix B.

d) Pressure Measurements

Water manometers have been adopted for the monitoring of the bed pressure at eight different locations, whilst provision has been made for the measurement of the static pressures associated with the primary and secondary windboxes. In addition those pressure values associated with the respective orifices were also monitored.

The bed pressure probes are, however, worth special note. The cooling jacket wall is penetrated by means of a 25 mm NB tube which is welded into the cooling jacket. A welded plug with a 7 mm diameter hole is fitted to the pipe on the bed side and ground flush with the jacket wall. The pipe which protrudes towards the outside of the combustor vessel is fitted with an end cap having a 6 mm diameter hole at its end. A 6 mm diameter stainless steel pipe is fitted through both the holes to extend some 25 mm into the fluidized bed.

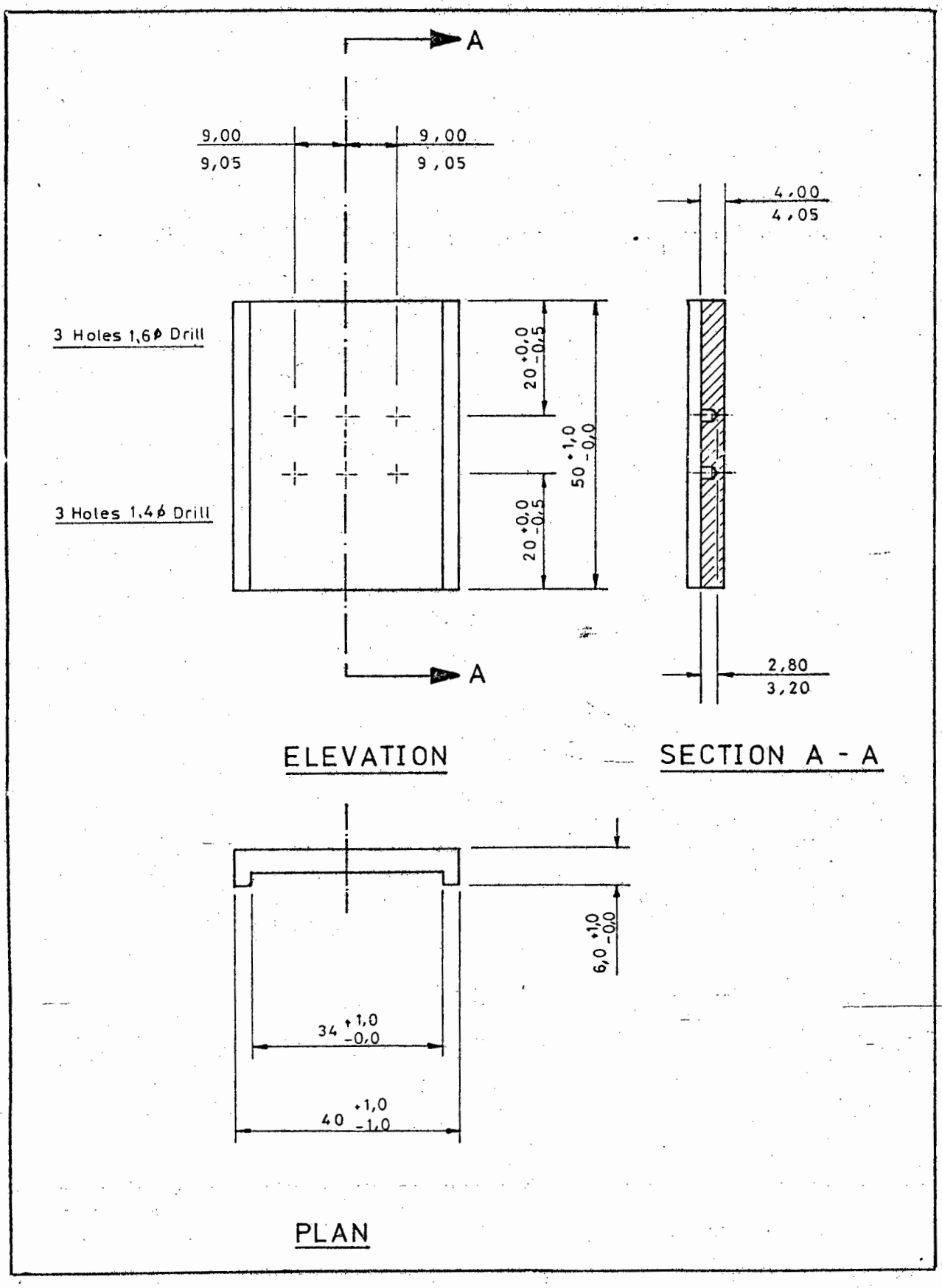

Figure 19 : Heat flux pad machining details

This pipe acts as the bed pressure probe. It was decided to project this pipe a short length into the bed to overcome any wall effects the combustor vessel might have on the bed static pressure measurements.

e) Flue Gas Analysis

A Bosch non-dispersive infra-red type carbon monoxide analyser and a Beckman polarographic oxygen analyser were utilized to monitor these two gases in the exhaust gas stream on a continuous basis. A flow diagram of the flue gas sampling system is illustrated in Figure 20.

Periodically an Orsat analyser was utilized to measure carbon dioxide and oxygen concentrations to act as a final check on the oxygen analyser.

f) Particulate Sampling

The BCURA type isokinetic dust sampling probe was selected as a means of obtaining a representative dust sample from the test rig. The background to and the design of the sampling probe are contained in Section B.3 of Appendix B. Strict adherence to isokinetic sampling conditions in accordance with the relevant standard were conducted in the duct above the combustion chamber. The location of the isokinetic sampling point is illustrated in Figure 21.

The BCURA isokinetic dust sampling probe comprises a nozzle, a probe tube and a cyclone for metering the gas flow and removing the solids. Although the pitot traverse is recommended to be performed prior to gas sampling, the design described in Appendix B has the pitot tube attached some 50 mm from the sampling nozzle to enable simultaneous measurements of the pitot tube to be taken whilst sampling. Flow straighteners and an orifice plate are located upstream of the sampling point to ensure uniform flow and a uniform solids concentration in the sampling plane.

The main function of the isokinetic sampling probe is to establish the carbon content of the entrained dust and so

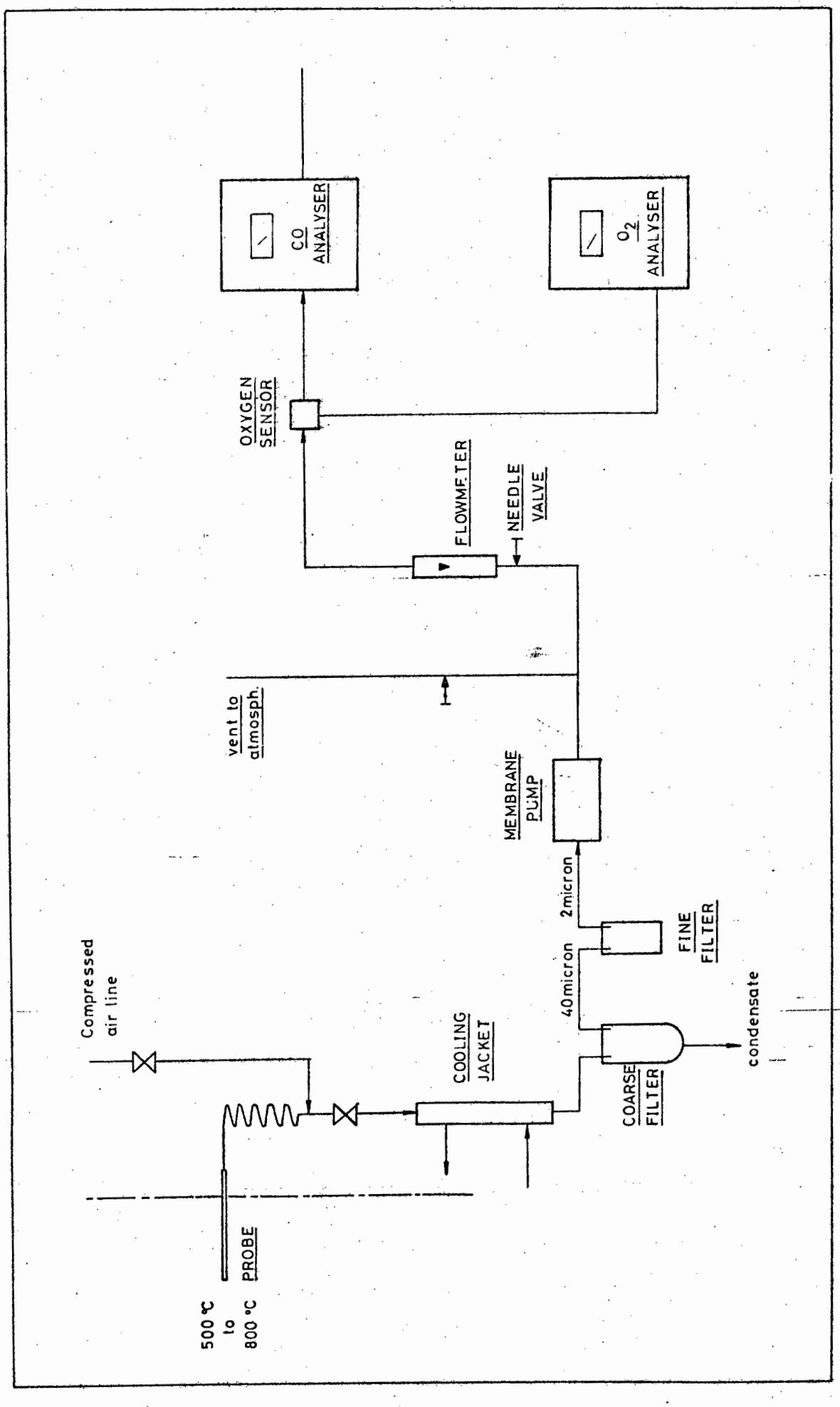

Figure 20 : Flow diagram of the flue gas sampling system.

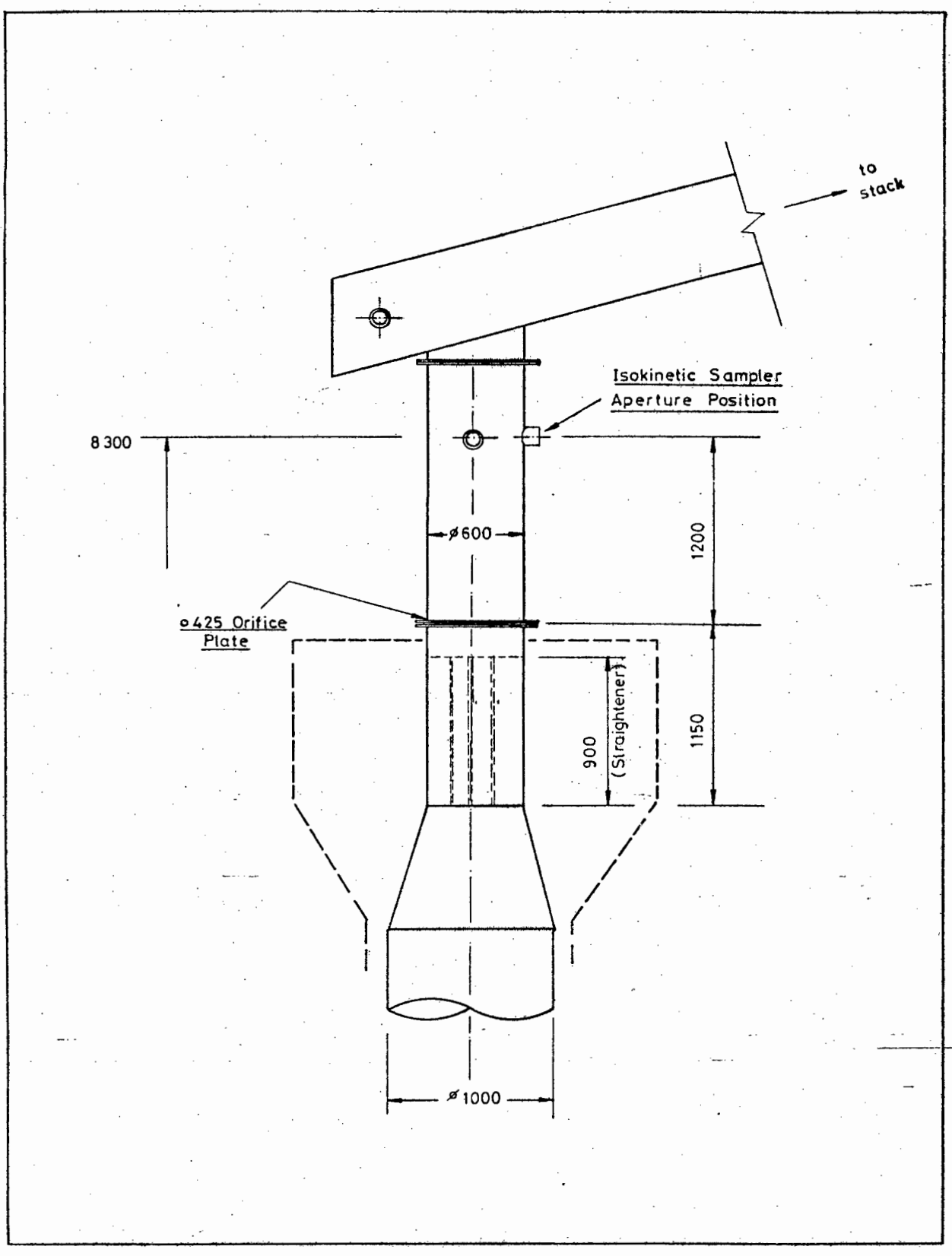

Figure 21 : Location of the isokinetic sampling points.

establish the carbon loss of the combustor under differing operating parameters.

g) Ancillary and Special Measurements

In addition to the measurements taken in the previous sections, monitoring of water flow rates, air temperatures, barometric pressure and so on have to be undertaken. However, of special note is a heat flux probe which is introduced via the ash part. Details of the design of this probe are contained in Section B.4 of Appendix B. This probe is used to measure bed to probe heat transfer coefficients and though not affecting the overall process, it can provide information on the heat transfer mechanism from the bed to an immersed surface. Furthermore, associated with the shallow fluidized bed is a cloud zone (50) which can have important heat transfer characteristics. An adjustable heat flux probe will enable the relative heat transfer coefficients between the probe and the bed, and the probe and the cloud zone to be investigated.

The design of the heat flux probe is based on the principle of measuring the difference in temperature between two points in a conductor having a well defined geometric configuration. The probe is introduced via the central ash pipe. Seals have been designed and fitted to the ash pipe to prevent sand wedging between the probe and the ash pipe. The probe itself is located at the end of a cooling jacket section and is made up of an 1,5 mm thick stainless steel cylindrical section that enables water to be introduced into the core of the cylinder. The cylinder has a diameter of 38 mm with an effective length of 25 mm. A sketch to illustrate the operation of the probe is presented in Figure 22.

The probe was designed to ensure a high velocity of the cooling water on the inner surface of the probe thereby ensuring a high internal heat transfer coefficient. A recess on the upper surface allows a stagnant layer of sand

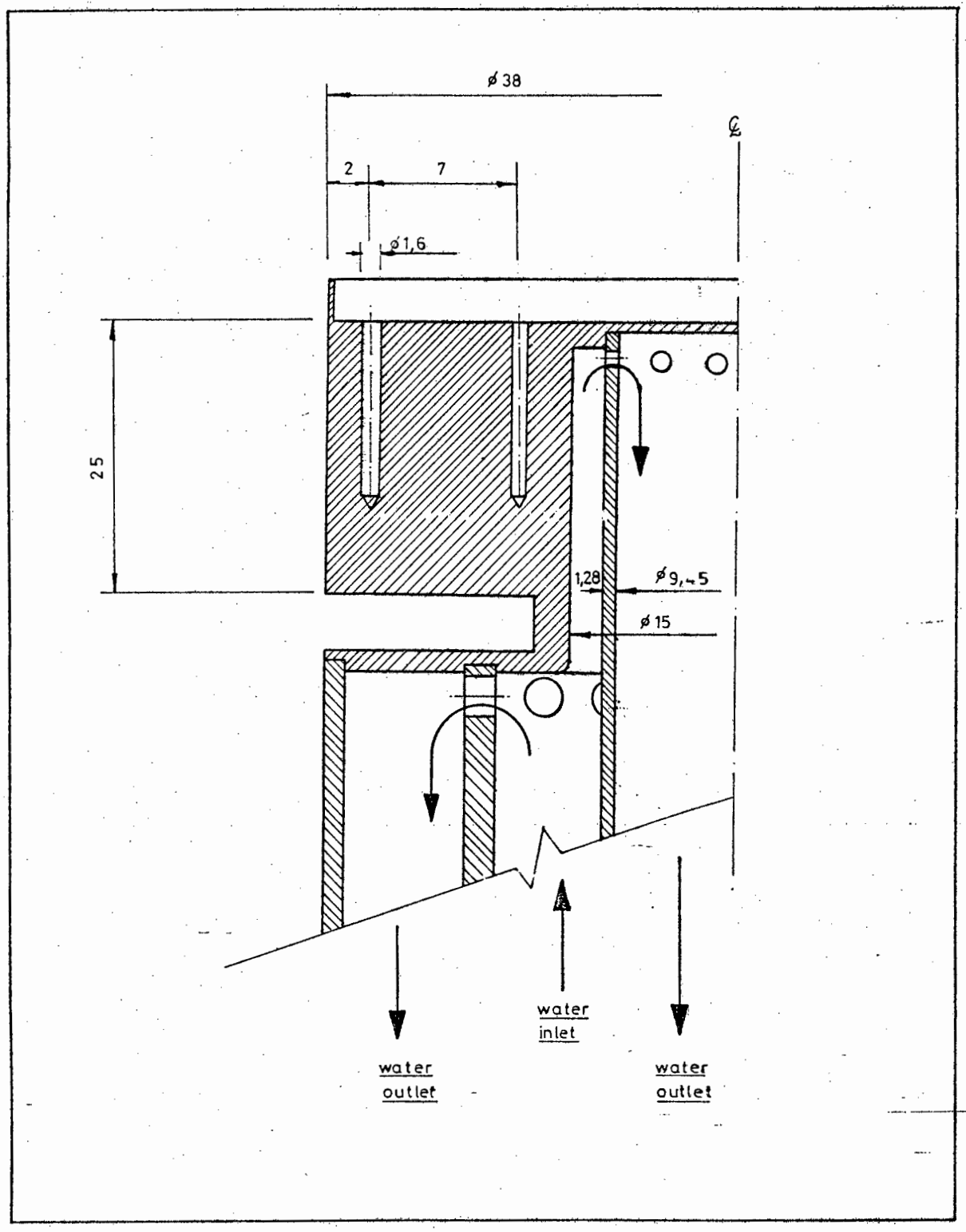

Figure 22 : Sketch to illustrate the operation of the heat transfer probe.

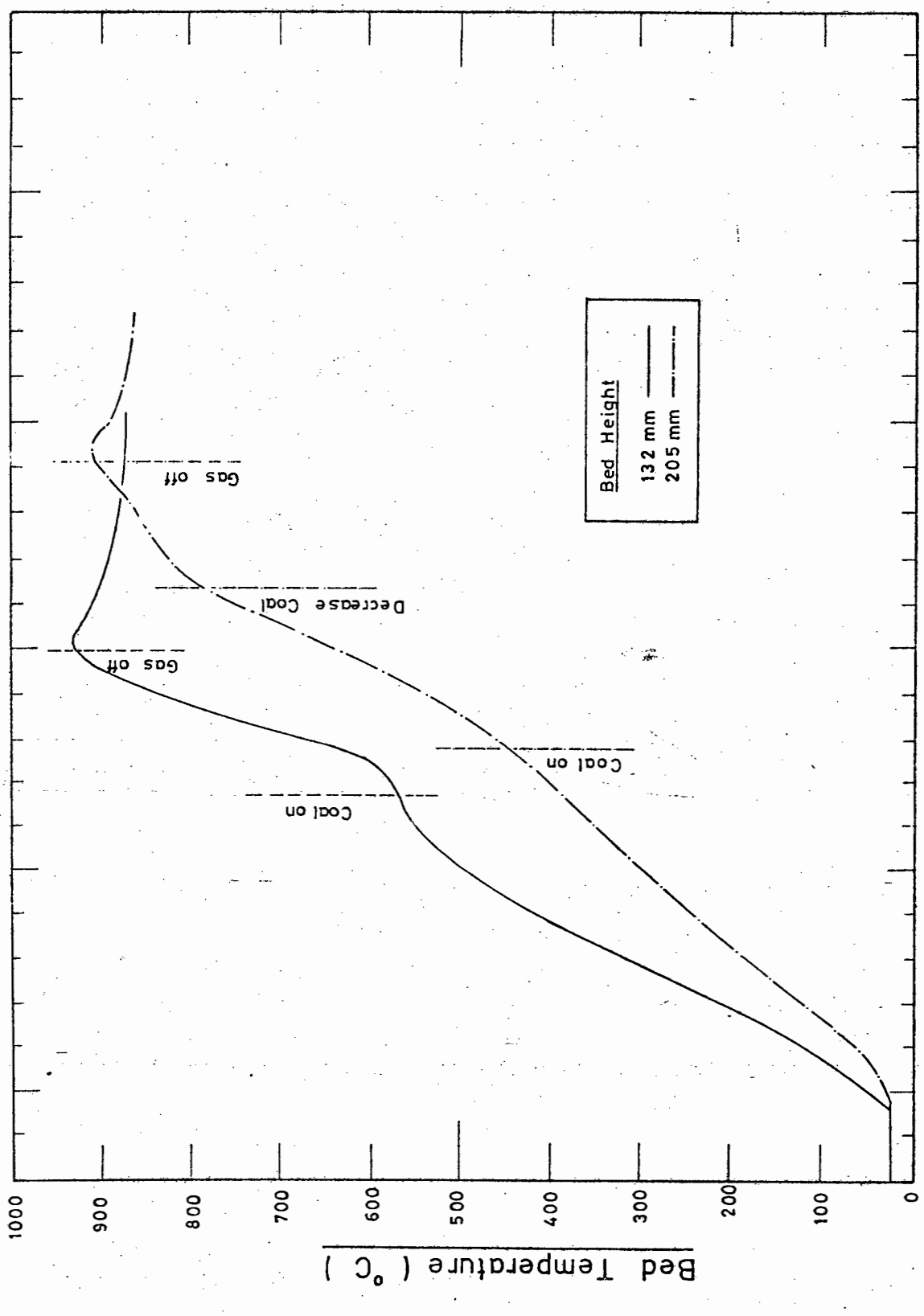

Figure 23 : Typical start-up curves for a deep bed and a shallow bed.

2.3.2 General Operation

Once steady coal combustion has been established and the gas isolated from the rig, the air and coal flow rates are simultaneously adjusted until the bed temperature approximates that at which the test is to be performed. The air flow is then adjusted to obtain an approximate bed velocity condition. Finally, with the air flow fixed, the coal flow is adjusted until the oxygen level in the flue gas is about 4%. This corresponds to an excess air factor of about 1,2 which would represent a desired operating condition in an industrial environment. Details of the relationships between the flue gas components, the excess air factor and so on are contained in Appendix D.

On maintaining steady operating conditions for at least fifteen minutes, the test is commenced. About 90 minutes of steady operation is required in order to obtain a complete set of results. If only one particular parameter is to be investigated, eg carbon loss, or only the heat transfer to the immersed cooling tube, then the duration of the test can be much shorter.

2.4 EXPERIMENTAL PROCEDURE

2.4.1 Calibration of Ecuipment

Prior to the performance of any tests, the test equipment must be adequately calibrated. The calibration of various items of plant is discussed below, whilst the calibration of the instrumentation has been covered in Appendix B.

a) The Primary Air Windbox

The pressure drop to volume characteristic of the primary air windbox was established prior to any fluidization tests. The flow characteristic was compared with that obtained from the tests performed on the individual nozzles where the discharge

coefficient of the nozzle was evaluated as 0,694, cf Section 2.2.2. The characteristic for one half of the windbox containing 156 fluidizing air nozzles has been derived from a least squares analysis as:

$$M_{\frac{1}{2}} = 0{,}0298 \cdot \sqrt{\rho_f \cdot p_w \cdot / \, g} \qquad (27)$$

This relationship is illustrated in Figure 24. The pressure drop is lower for the complete windbox than for the single nozzle for an equivalent gas mass flow rate, this implies a higher coefficient of discharge than that obtained for the single nozzle test. Indeed, the coefficient of discharge is found from equation (27) to be 0,746. This would imply some form of pressure recovery with the nozzles acting as a distributor on top of the windbox.

b) The Underbed Coal Feeder

The screw feeder was calibrated using the duff coal having the size analysis represented in Appendix C. The experimental points illustrated in Figure 25 have been fitted by a least squares analysis by equation (28)

$$M_{fu} = 1{,}96 \cdot 10^{-3} \cdot n \qquad (28)$$

The flow rate using the low fines coal is also found to be related by equation (28) corrected by a factor equivalent to the ratio of the bulk densities of the two coals. Values for these bulk densities are to be found in Appendix C.

c) The Overbed Feed System

The overbed feed system is made up of a rotary drum type feeder and a pneumatic spreader. Details of the flow and spreading characteristics of this spreader are contained in Appendix E together with details of the flow calibration of the drum feeder. This feeder was also calibrated using the duff coal, the results of which were fitted by a least squares analysis represented by equation (29).

$$M_{fo} = 1{,}32 \cdot 10^{-3} + 0{,}0416 \cdot n \qquad (29)$$

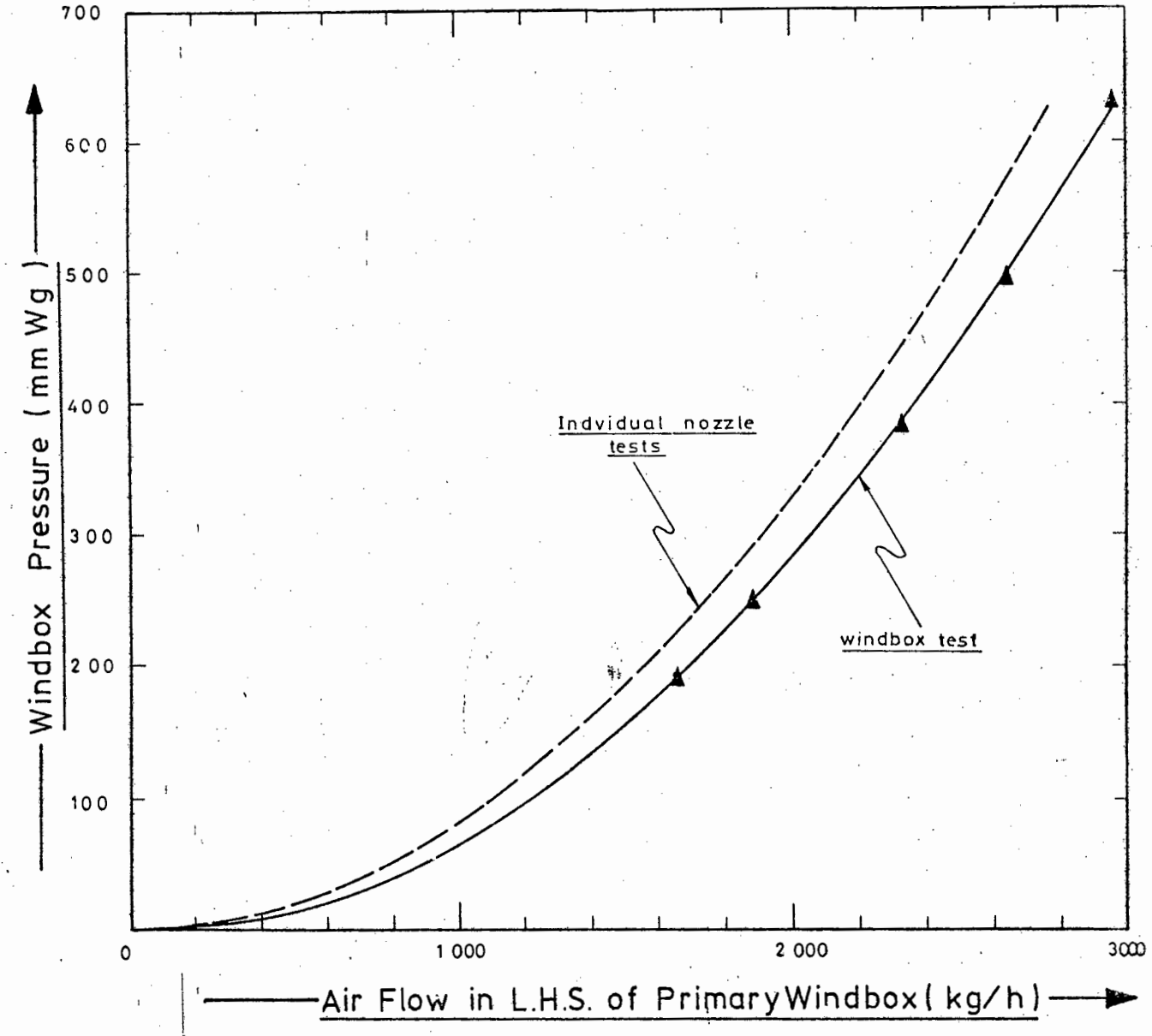

Figure 24 : Primary air windbox pressure to flow characteristic.

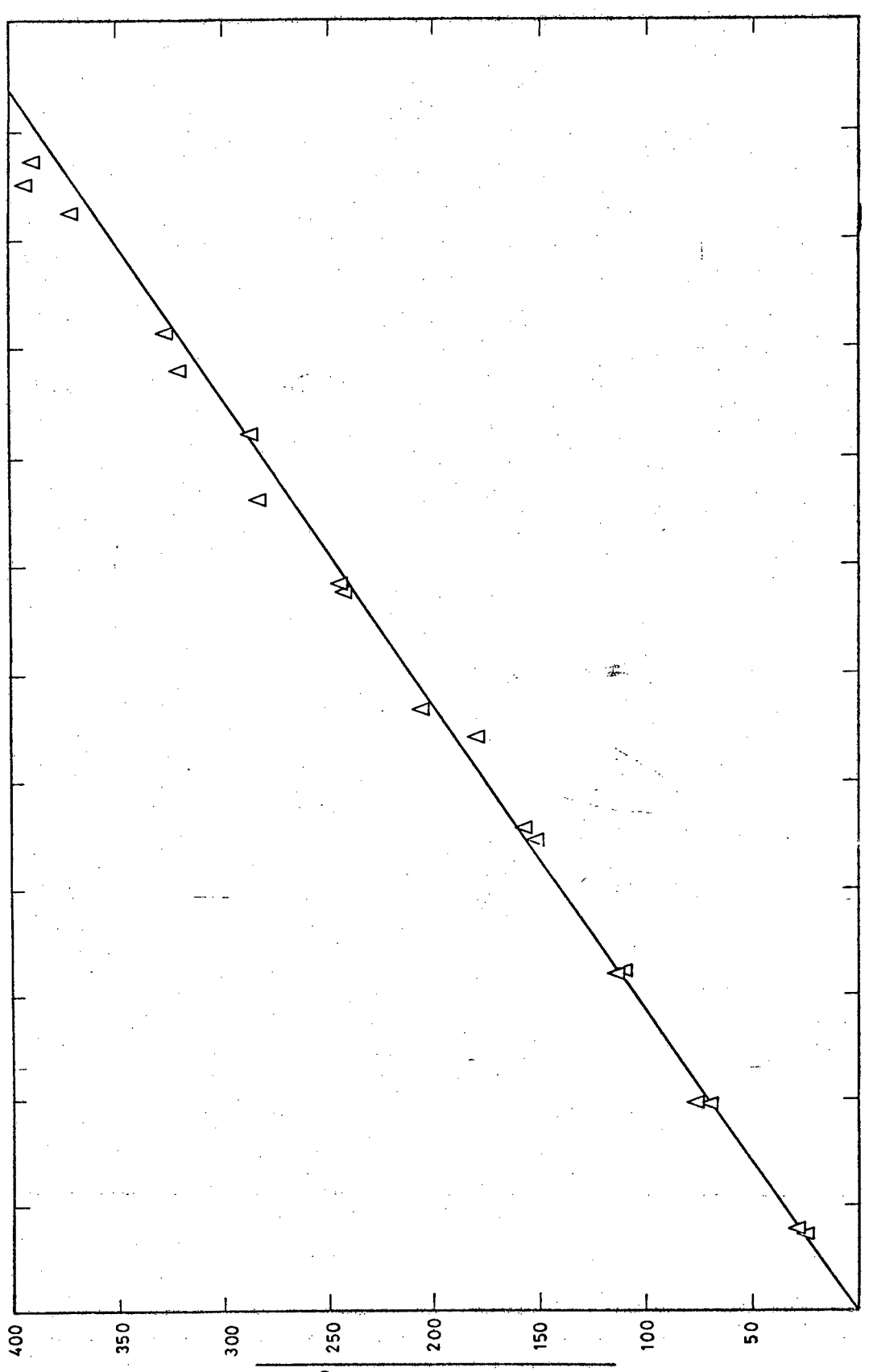

Figure 25 : Screw feeder calibration curve using duff coal.

After having obtained the relationship given by equation (29), the maximum flow delivered by the feeder was reduced to about 0,100 kg/s by increasing the gear ratio between the feeder and drive.

2.4.2 Outline of Tests Performed

A total of fifty three test runs were undertaken. In some instances it was possible to undertake a number of individual tests during each test run, however in others due to poor operation of individual components or instrumentation no tests were completed or only limited results were obtained. In particular, considerable difficulties were experienced in feeding wet coal having a high content of fine material. Complete results were therefore only possible when burning relatively dry coal as indicated by the analyses of Appendix C. The duration of each test run never exceeded twelve hours due to operational and staffing requirements. In particular, after testing for this length of time, the various filters on the high efficiency suction pyrometer and to a lesser extent on the gas cleaning system required attention in order to continue obtaining good results.

The grading of the bed material changed during operation as a result of the coarser ash fraction remaining in the bed. This tended to bring about an increase in the mean particle size of the inert bed material. However, periodic replacement of the material with fresh silica sand prevented there being any significant variation in the bed material size grading from one test to another.

During the test series two coal types were utilized. The first is a coal having a high content of relatively fine material and referred to as "the duff coal"; and a second coal being relatively free of fines and referred to as "the low fines content coal". Other than grading, the two coals have very similar properties. Details of the properties of these two coals are included in Appendix C.

In addition to the two types of coal, the test results are further distinguished by the coal feed system utilized; i.e. above-bed or under-bed feeding of the coal. In summary, the following can be written:

Test Runs 1-39 and 51-53 undertaken with duff coal
Test Runs 40-50 undertaken with low fines coal

and

Test Runs 1-43 undertaken with under-bed feeder
Test Runs 44-53 undertaken with over-bed feeder.

These tests can be divided into three main sections:

(i) Heat transfer within the bed.

(ii) Heat transfer and combustion above the bed.

(iii) The overall plant performance.

a) Heat Transfer within the Bed

Heat from the fluidized bed can be transferred to the surrounding cooling water jacket, to an immersed horizontal tube, to a heat transfer probe introduced via the ash port and finally from the top surface of the bed to the gas and enclosure of the freeboard. This latter element of the total heat transferred from the bed has not been specifically measured, though it is considered in the theoretical analysis.

The heat transferred from the bed to the water jacket has been monitored by means of heat flux pads. These measurements are undertaken for all of the tests and averaged over the duration of the test. However, from Test Run 47 onwards, a measure of the instantaneous heat transfer coefficient was obtained by monitoring the instantaneous heat flux rate at a faster recorder speed.

The horizontal tube was only installed in the bed after Test Run 43, whilst measurements to the heat transfer probe were monitored from Test Run 45 onwards. This latter probe was used to obtain information on the mechanism of heat transfer

within the fluidized bed. None of the three heat transfer measurements should be affected by the change from under-bed to above-bed feeding, nor by the size grading of the coal feed.

b) Heat Transfer and Combustion above the Bed

The measurement of heat flux by means of heat flux meters at various levels in the freeboard provides a measure of the heat transferred in this region. In addition, flue gas temperatures are monitored by means of the ceramic temperature probes as well as the high efficiency shielded pyrometers. The heat transfer in this zone can clearly be affected by the means of coal feeding, the grading of the coal and the operating conditions due to the variations in the heat released. Of particular interest is the monitoring of the heat transfer when the combustor acts as a gasifier, i.e. with the introduction of secondary air above the bed with substoichiometric combustion of the coal within the fluidized bed. A complete set of results was obtained for eight tests incorporating the use of secondary air. These tests are tests 35b, 38b, 40b, 41b, 41c, 47d, 50b and 50c.

c) The Overall Plant Performance

The carbon content of the entrained ash is measured to assess the overall combustion efficiency under different operating conditions. The size gradings of the entrained ash have been obtained to evaluate the elutriation for different coals and methods of feeding the coal. For all but one test in which secondary air was employed, the secondary air represented about 30% of the total air flow. Efforts were made during most of the tests to maintain the excess air level at about 20% excess over stoichiometric. The bed operating parameters were varied between the following general limits:

static bed height	120 - 230 mm
superficial gas velocity	1,0 - 3,3 m/s
bed temperature	780 - 990°C

CHAPTER 3

EXPERIMENTAL RESULTS

The major objectives of the experimental work are to establish the nature and extent of the combustion phenomenon, and to evaluate the heat transfer in various regions of the shallow fluidized bed combustor furnace under different operating conditions. The operating parameters were maintained at those levels likely to be utilized commercially. The bed height was therefore restricted to relatively shallow depths to limit the fan power consumption whilst the lower velocity limit is maintained well above the minimum fluidizing velocity whilst the maximum velocity is restricted to limit the carry-over of unburnt carbon.

In the previous chapter, the tests were divided into three main sections. However, further subdivision into six main groupings is necessary in order to describe the results. These six groups are:

(i) Heat transfer to the immersed tube.
(ii) Heat transfer to the peripheral wall.
(iii) Heat transfer to an adjustable probe.
(iv) Heat exchange in the freeboard.
(v) Combustion.
(vi) Entrainment.

Some of these groupings are completely independent of each other, for instance the heat transferred to an immersed tube and the entrainment, whilst combustion and entrainment are very much inter-related. The groupings have further been necessitated in view of their dependence on different input parameters, since while combustion and entrainment are markedly affected by the size grading of the incoming coal, the same cannot be said for the heat transfer within the bed.

Previous work (75) indicated the dependence of the combustion efficiency upon the temperature, velocity and bed height. This is considered as a good approximation under similar excess air conditions and the work has been expanded in this thesis to incorporate the simultaneous extraction of heat by heat exchange surfaces whilst burning the coal at relatively low excess air levels. Empirical correlations have been established for some of the heat transfer studies. Statistical analysis of the data has enabled the use of only those parameters which significantly affect the heat transfer coefficient to be employed in the correlations. A brief description of the more important statistical relationships used in this thesis are contained in Appendix F.

Prior to a description of the results given by the six groupings, the results pertaining to some of the fundamental parameters are described. Of particular importance to shallow fluidized bed combustors is the bed expansion and the determination of this parameter is discussed at length. The results for all the tests have been included as tables in Appendix G. A summary of the conditions prevailing during each of the tests is given in Table G1 of Appendix G.

3.1 EXPERIMENTAL DETERMINATION OF THE MAIN PARAMETERS

3.1.1 The Fluidization Diagram

In order to obtain information on a multiple component particle system, some form of fluidization diagram is useful. Reh (11), (137), (138) has proposed the use of a diagram in which a Reynolds number is plotted against a modified Froude number. A modified form of the diagram is represented in Figure 26. The diagram represented by Figure 26 is similar to that proposed by Zenz and Othmer (9) as the ordinate may be represented by the reciprocal of the drag coefficient for a single particle. The lower boundary line represents the transition from the fixed bed to a fluidized bed flow regime

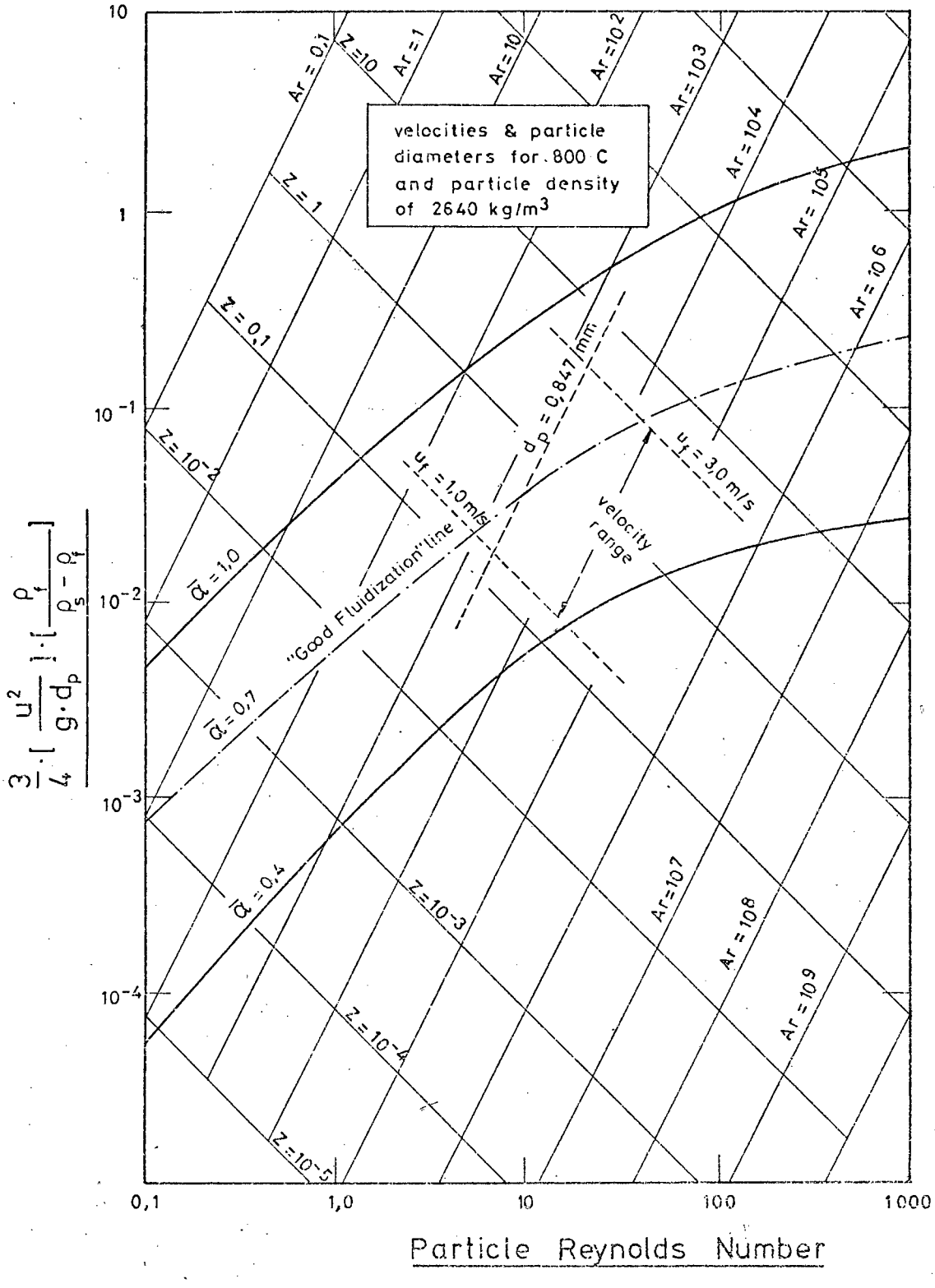

Figure 26 : Fluidization diagram as proposed in Reference (11) with superimposed particle diameters and velocities referring to conditions at 800°C.

whilst the upper boundary line represents the relationship defining the particle terminal velocity. The two boundary lines have been obtained from equations (4) and (8). Superimposed on the diagram are lines of constant Archimedes number and lines representing constant values of the dimensionless parameter Z which is defined by equation (30):

$$Z = \frac{\mu_f}{\rho_s - \rho_f} \cdot u_f^3 \qquad (30)$$

Clearly from the definition of the Archimedes number and equation (30), the Archimedes number is a function of the particle diameter, the particle density and the operating temperature, whilst the parameter Z is a function of the particle density, the bed temperature and the velocity. These two relationships are represented below:

$$Ar = f(\rho_s, T, d_p)$$

$$Z = f(\rho_s, T, d_p)$$

Thus for a particular particle density, lines of constant velocity and constant particle diameter can be superimposed onto the fluidization diagram for a particular bed temperature. As opposed to Figure 26 which has general application, a similar diagram can be drawn at a specific temperature relating the various flow regimes as a function of velocity and particle diameter. This is illustrated by Figure 27 which has been drawn for a fluidized bed at 1000°C.

Battock and Pillai (139), have defined a region of "good fluidization" on a similar fluidization diagram which they have developed. This "good fluidization" line has been drawn on both Figures 26 and 27 together with the operating ranges of velocities and bed material particle sizes. Although the particle size range varies from zero to about 9 mm, the mean particle diameter was never very different from that of the original sand i.e. 0,847 mm. It is clear therefore from both Figures 26 and 27 that the bed was operated at values very different from those recommended for good fluidization

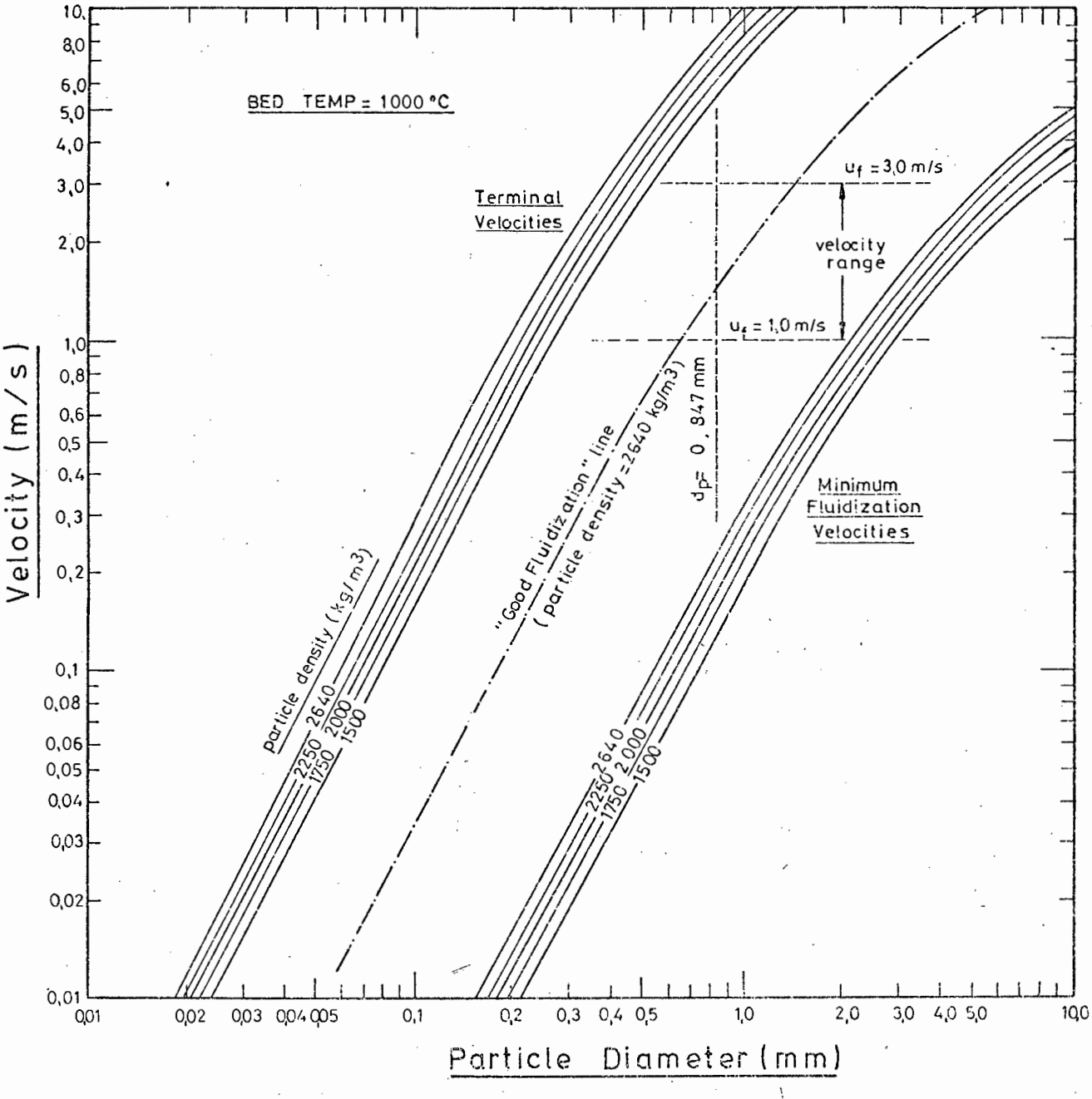

Figure 27 : Presentation of the variation of both the minimum fluidizing and particle terminal velocities at different particle diameters when fluidized by air at 1 000°C.

(139). This will lead to higher elutriation rates than anticipated and a possible decrease in the combustion performance i.e. combustion efficiency.

3.1.2 The Minimum Fluidizing Velocity

Figure 28 illustrates the bed pressure to velocity relationship for two different bed heights. The curve has been drawn on logarithmic paper. The slope of the curves in the fixed bed region is about 1,5 which is between a value of unity for laminar flow and two for turbulent flow. The intersection of this line with the constant pressure lines yields a minimum fluidization velocity of 0,38 m/s. This value compares well with the 0,376 m/s obtained from the use of equation (4). As the temperatures at which the test rig is operated are well in excess of the 40°C at which the fluidization studies were performed, equation (4) has been used to evaluate the minimum fluidization velocities at these higher temperatures without experimental verification.

3.1.3 Correlation of the Dynamic Bed Height

The pressure measurements associated with the combustor plenum chamber (or windbox) and the bed sections fluctuated continuously during the tests as a result of bubbles bursting at the surface. This made accurate measurement of these readings difficult. Four pressure probes are contained at two levels, one at the base of the fluidized bed and the second some 75 mm above the base of the bed. A mean value for each of the four readings at each level yields a value for the bed pressure as well as a value for a pressure midway along the bed from which an assessment of the dynamic bed height is possible. Further measurements, which relate to the effective bed height, have been made utilizing the adjustable heat transfer probe and are discussed in section 3.4. A diagram to indicate the precise positioning of the bed pressure probes and illustrating their connection to the water manometers is given in Figure 29. The bed density is

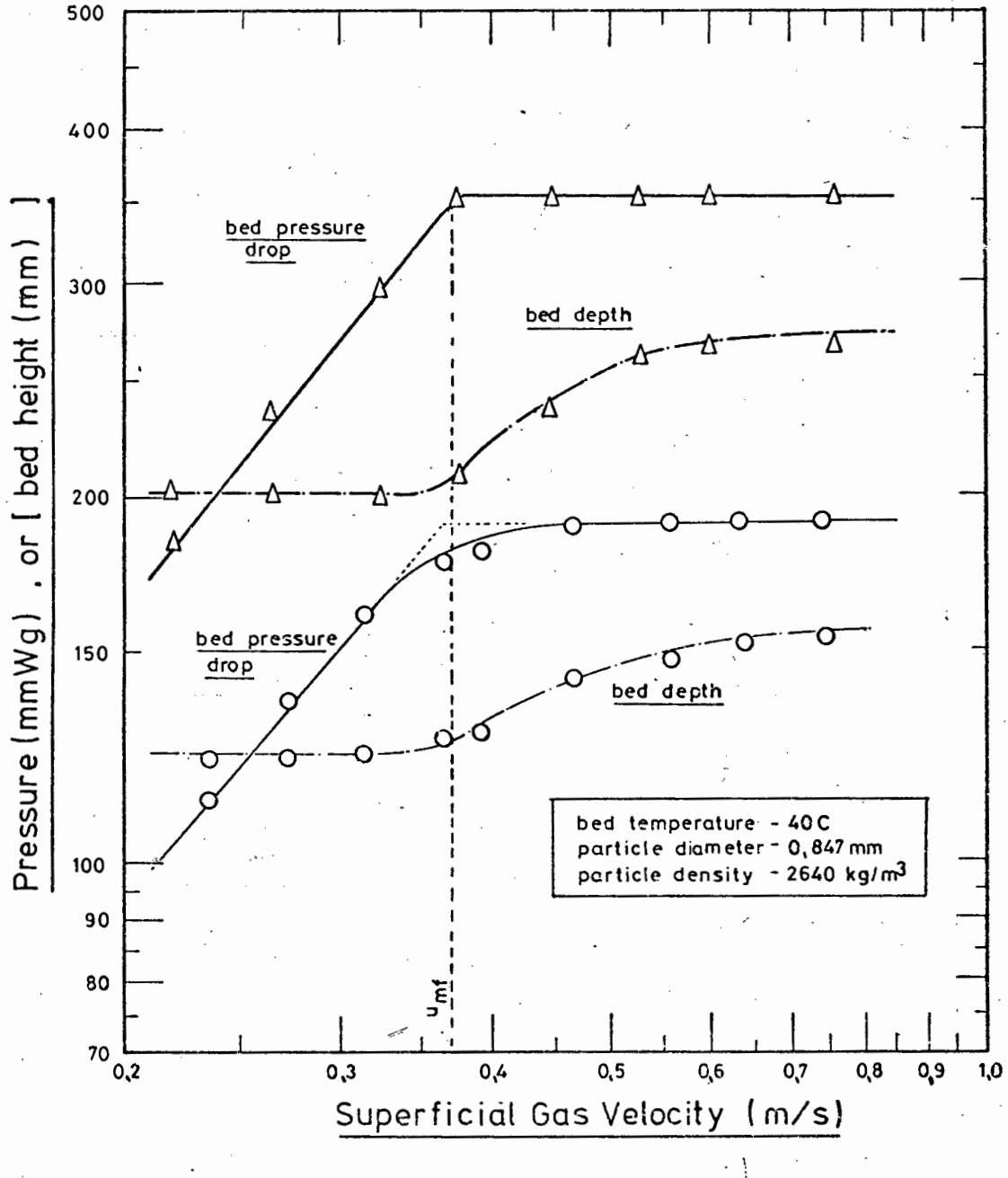

Figure 28 : Pressure-drop velocity characteristic for a typical fluidization study with a bed of 230 mm deep and a second characteristic for a shallower bed 120 mm deep.

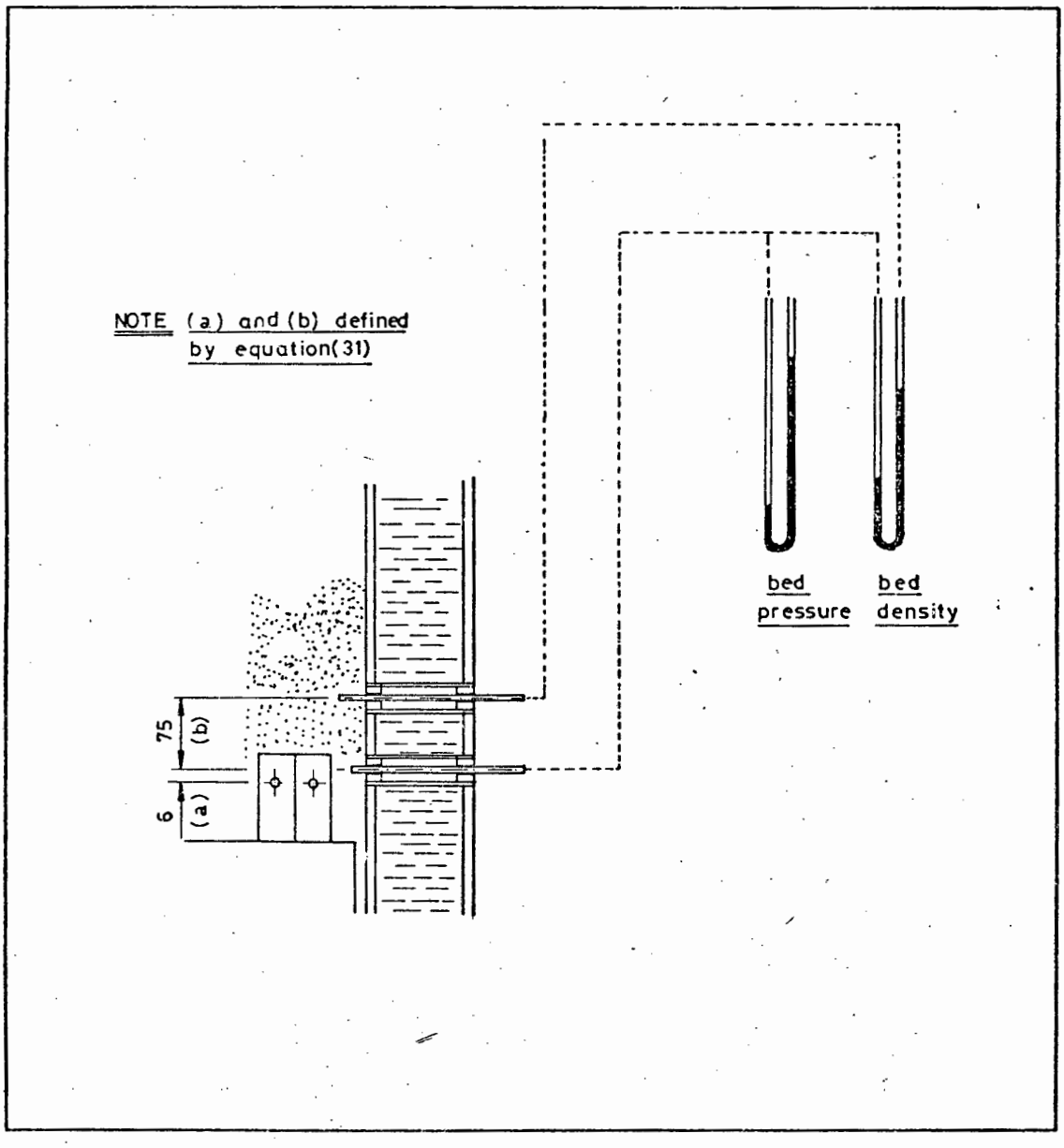

Figure 29 : Diagram to illustrate the use of the bed pressure probes for evaluating the dynamic bed height.

defined as the pressure differential between the two levels of pressure measurement. The dynamic bed height can therefore be estimated by equation (31), where the constants 'a' and 'b' are defined in Figure 29.

$$H_f = a + b \cdot \frac{(bed\ pressure\ )}{(bed\ density\ )} \qquad (31)$$

On increasing the gas velocity through a fluidized bed, the bed expands as a result of the increased formation of bubbles which in turn causes an increase in the mean bed voidage. However, the bubble velocity is significant in that this parameter determines the bubble residence time and hence the volume occupied by the bubbles in the bed. The mean bed voidage therefore incorporates the space occupied by the bubbles as one component together with the voidage of the particulate phase, which is assumed to be similar to the bed voidage which exists at the minimum fluidization condition, forming the second component. The mean voidage fraction can be related to the dynamic bed height by equation (32).

$$\bar{\alpha} = 1 - \frac{H_{st}}{H_f} \cdot (1 - \alpha_{mf}) \qquad (32)$$

For reasonably spherical particles a voidage of 0,4 is normally assumed at the minimum fluidization velocity. Using this value the mean voidage during each of the tests can be obtained from the bed pressure measurements and by making use of equations (31) and (32). The results of these calculations are contained in Table G2 of Appendix G. The value of the dynamic bed height included in the table has been evaluated from equation (31).

Staub and Canada (140) have introduced a method which has been widely used for gas-liquid systems for describing the bed expansion of large particle shallow fluidized beds. The same method has been employed in correlating the data of Table G2 in Figure 30. This figure incorporates a plot of the ratio of the mean voidage to the velocity against this superficial gas velocity. The points have been correlated by a

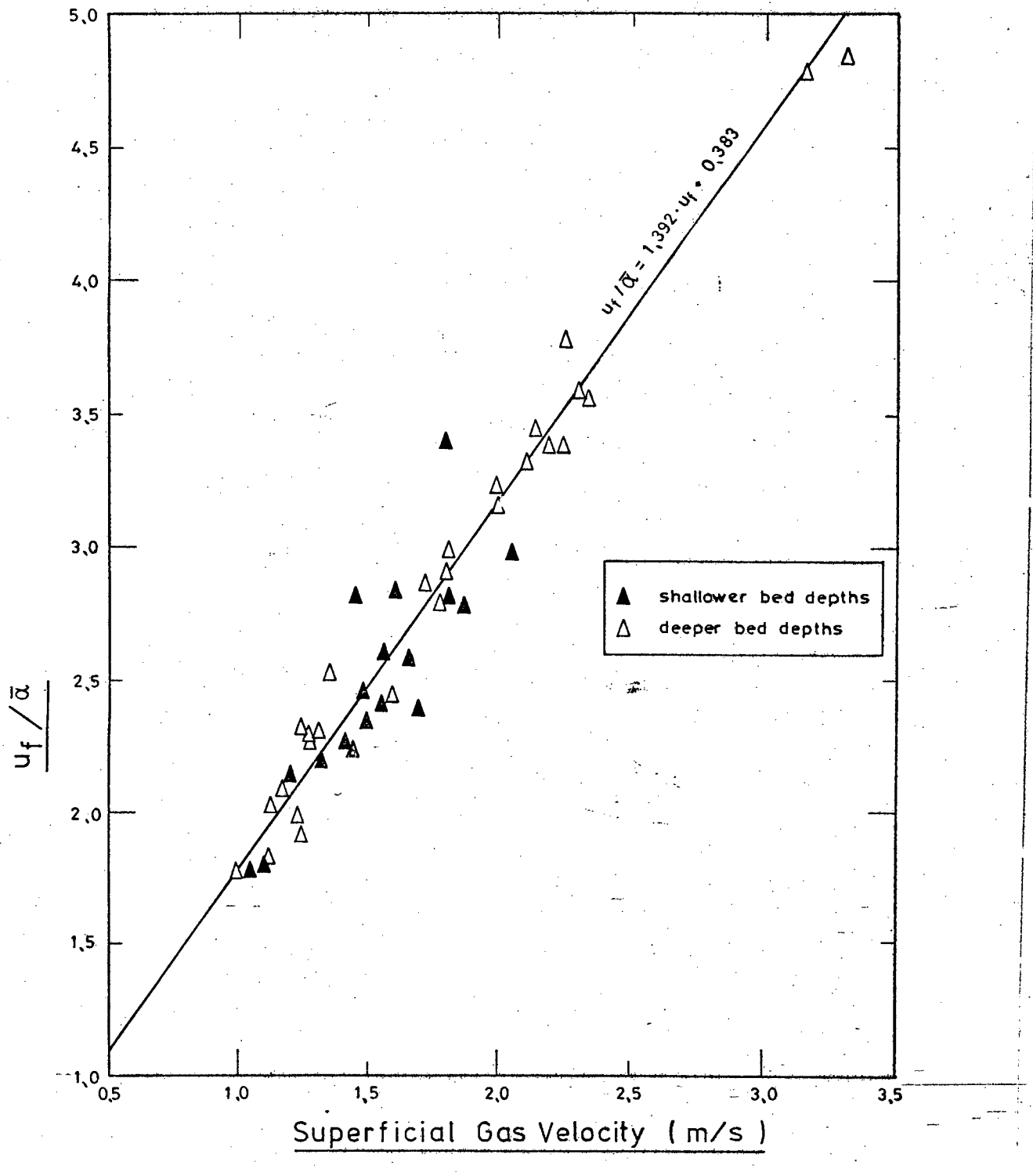

Figure 30 : Bed voidage to superficial gas velocity characteristic.

least squares method resulting in the straight line given by equation (33)

$$u_f / \bar{\alpha} = 1{,}392 \cdot u_f + 0{,}383 \qquad (33)$$

The coefficient of correlation is 0,976 which indicates a particularly good fit. The dynamic bed height is easily obtained from the bed expansion by utilizing equations (32) and (33). This value of dynamic bed height has been adopted in all further calculations in preference to that obtained from measurement in view of equation (33) effectively smoothing the errors resulting from bed pressure measurements. Figure 31 has been drawn to illustrate the variation of the voidage fraction with the superficial gas velocity, whilst the variation of the dynamic bed height with gas velocity is illustrated in Figure 32. Also included in Figure 32 is the relationship derived by Kolenko and Collin (141). From the figure, it is seen that both curves predict bed expansions which do not differ by more than 15% of each other for all velocities up to about 2,5 m/s. At higher velocities the bed expands rapidly according to Kolenko and Collin (141) as is to be expected for deep fluidized beds, whilst equation (33) predicts a maximum bed expansion of 2,13. Such a maximum is to be expected for shallow beds with low aspect ratios, i.e. where the bed height is very much less than the vessel diameter. Clearly, under the range of test conditions employed, the combination of equations (32) and (33) yields representative information on the bed expansion.

A further point to note from Figures 30 and 31 is the greater scatter of the data obtained when using the shallower (i.e. those about 120 mm deep) as opposed to the deeper (i.e. those about 230 mm deep) fluidized beds. This is probably due to the pressure fluctuations, though smaller in the case of the shallower beds, being relatively larger when considered in relation to the mean value of the pressure reading. This relatively larger fluctuation will incur a larger error in the bed pressure measurements thus accounting for the greater scatter of these results.

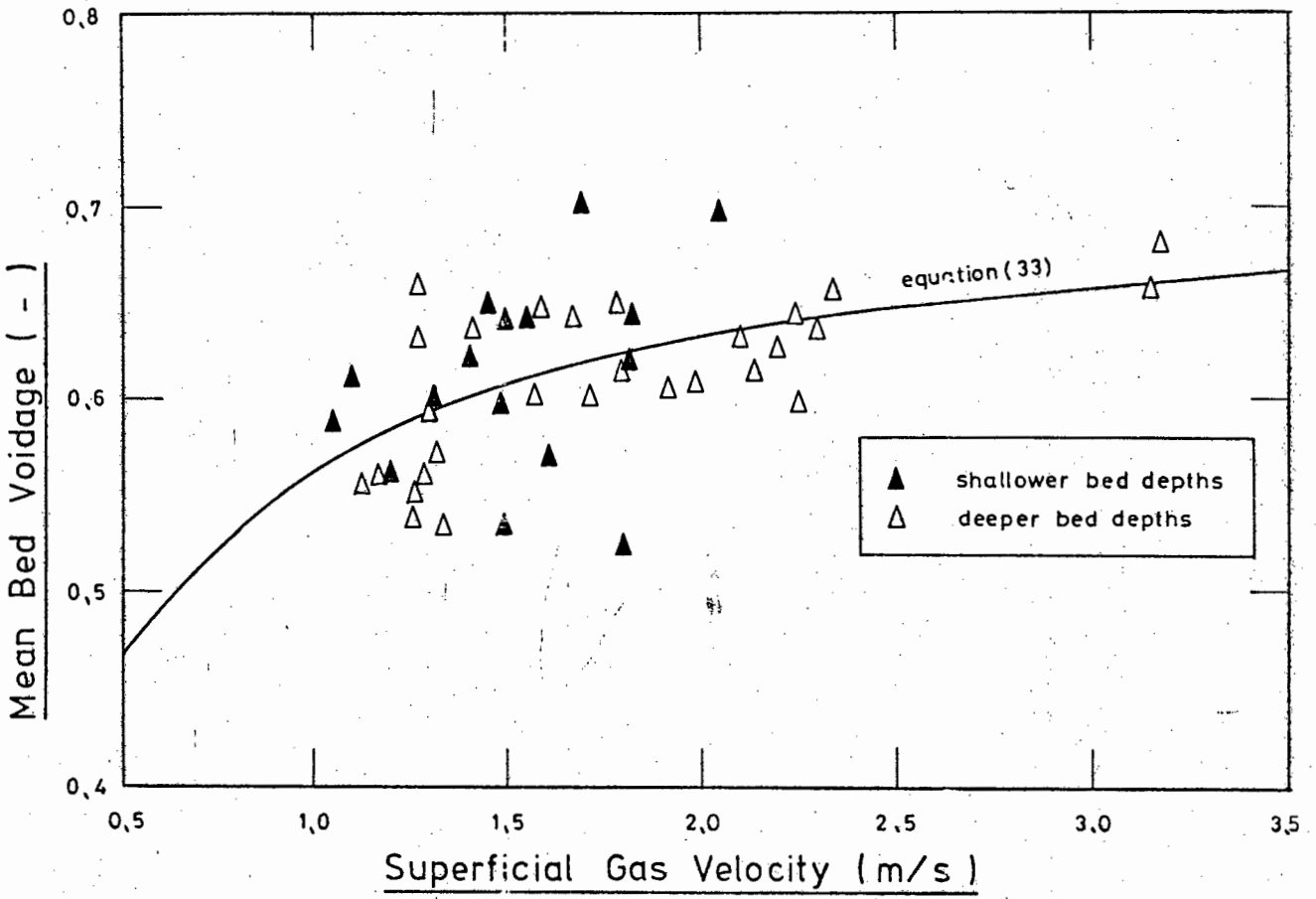

Figure 31 : Graph to illustrate the variation of the bed voidage with superficial gas velocity.

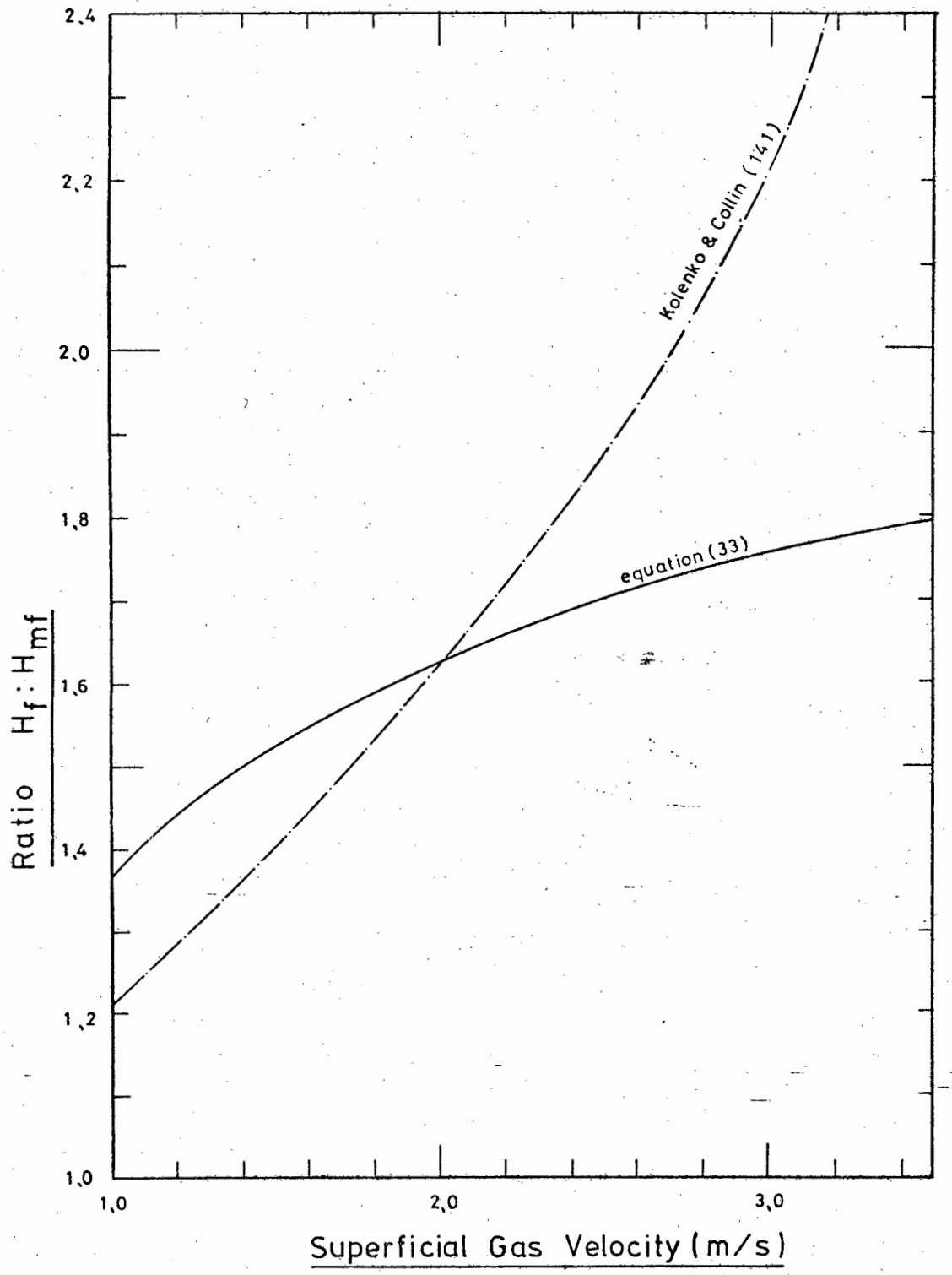

Figure 32 : Relationships between the bed expansion and the superficial gas velocity.

3.2 HEAT TRANSFER TO A HORIZONTAL IMMERSED TUBE

The horizontal immersed tube is located in the secondary cooling circuit. The general arrangement of the tube has been described in Section 2.2.5. Thermometers at inlet to and at the outlet from the tube, together with an integrating flow meter permit an accurate assessment of the total heat transferred to the tube to be made. The measurement of the tube wall metal temperature is necessary in order to evaluate the heat transfer coefficient in contrast to the heat flux or the overall heat transfer rate. These thermocouples have been imbedded in the upper, lower and mid-positions at 90^{o} from each other in two vertical planes through the tube as detailed in Section 2.2.5. Figure 33 illustrates the dependence of the heat flux rate upon the bed temperature. From the figure it is evident that a very high heat flux rate is attained in the bed and rises steadily as the bed temperature increases.

This high heat flux rate results in the tube metal temperature exceeding the boiling point of the cooling medium and as a consequence the mechanism of heat transfer at the inner tube surface is that of sub-cooled boiling. This sub-cooled boiling heat transfer coefficient will be higher than the corresponding convective coefficient which would have prevailed had the tube metal temperature not exceeded the boiling point of the water. This further enhances the measurement of the bed to tube heat transfer coefficient as this external coefficient therefore becomes the controlling parameter in the overall heat transferred. Thus, fairly large variations in the internal heat transfer coefficient will have only a rather small effect on the overall heat transferred. This is illustrated by Test 50e represented in Table G3 of Appendix G where a 33% variation in the cooling water mass flow rate (and hence a 28% increase in the internal heat transfer coefficient in absence of subcooled boiling) results in only a 4% increase in the total heat absorbed.

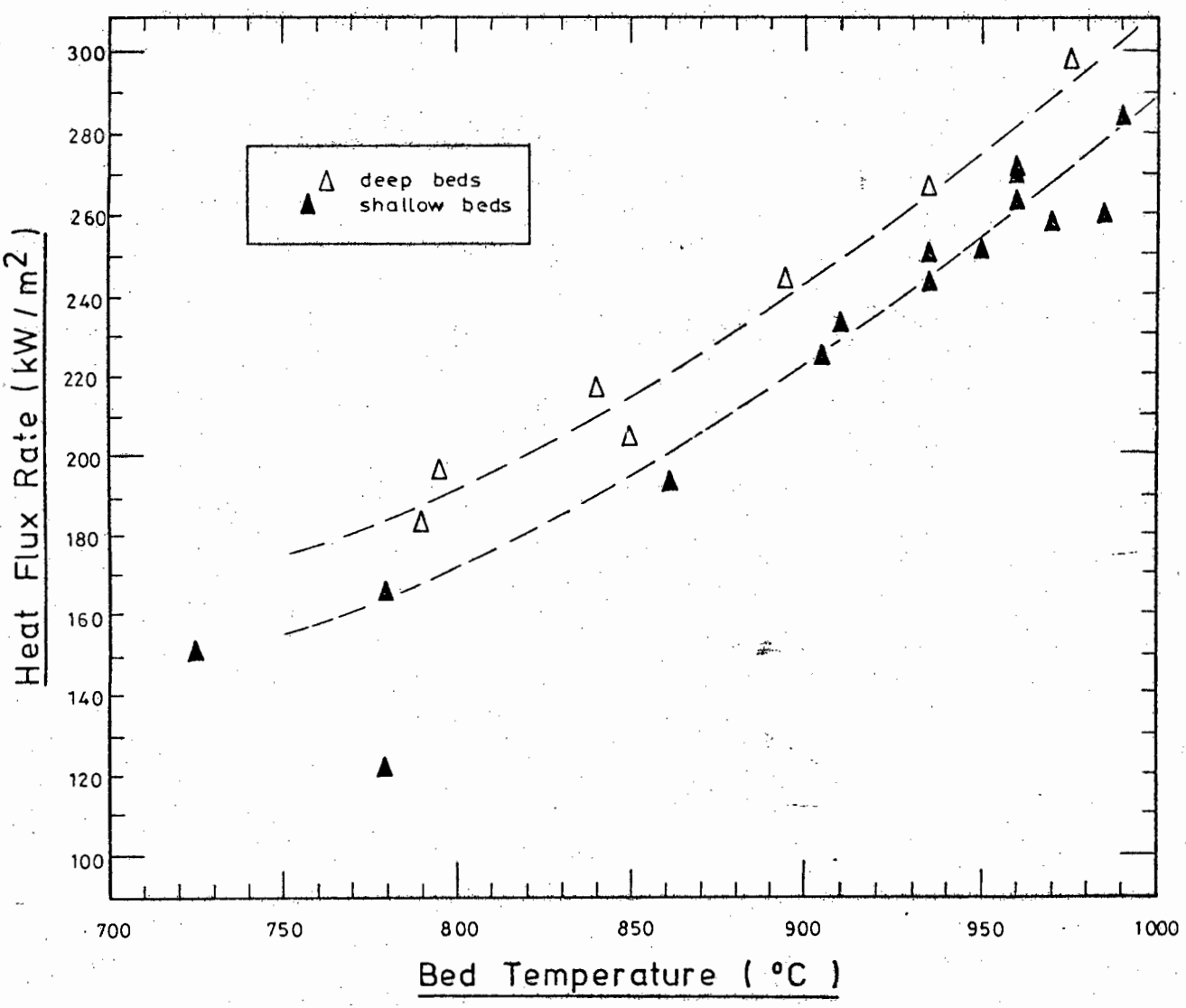

Figure 33 : The total heat flux rate to the 76,2 mm OD immersed cooling tube as a function of the bed temperature.

A further point to note from Figure 33 is the consistently higher heat flux rates obtained from the deeper beds in contrast to the shallower beds. The reason for this has been proposed as being due to the correspondingly higher gas velocities associated with the deeper bed at a similar bed temperature in view of the higher bed rating (136b). However, further investigations described in Section 3.4 using the adjustable heat transfer probe indicate that the cause of this difference may be of a more fundamental nature. In particular the frequency of variation of the instantaneous heat transfer coefficient is found to differ for the two bed heights employed.

Reference to Table G3 of Appendix G indicates that the inlet water temperature is significantly lower at the equivalent flow rate than would be predicted by Figure 13. This is due to the opening of the drain so as to increase the water flow to the buffer tank thereby reducing the final temperature leaving this tank. This was undertaken to limit the sub-cooled boiling phenomenon which resulted in widely varying tube metal temperatures and at times caused fluctuations in the water outlet temperature (of the order of $0,5^{o}C$).

3.2.1 Heat Transferred by Radiation

The total external heat transfer coefficient has been described as the sum of that due to the particle and gas convective components and the radiative component, cf Section 1.3.1 (a). In view of the relative ease with which the radiative component can be described, it is assumed for the purpose of this thesis that

(i) the radiative and convective components are purely additive

(ii) particle and gas convective components are considered as a single component

(iii) the contribution to heat transfer when the surface is contacted by a bubble is assumed to be small.

Thus equation (13) reduces to

$$h_t = h_c + h_r \qquad (34)$$

Now the radiative component h_r is dependent on the total interchange area between the bed and the tube. Assuming the exchange to be between the tube and a surrounding cylinder of bed material and further that the gas between the two cylinders is transparent to radiation then the following relationships can be derived for grey surfaces:

$$Q_{b=t} = \overline{S_b S_t} \cdot \sigma \cdot (T_b^4 - T_t^4) \qquad (35)$$

where

$$\overline{S_b S_t} = \frac{1}{(1 / \varepsilon_b A_b) + (1 / \varepsilon_{to} - 1) / A_t} \qquad (36)$$

The emissivity of an entire bed of silica sand with a particle emissivity of 0,6 has been found to be 0,85 (41), (46), whilst for boiler tube an emissivity of 0,70 (58) can be assumed. Substituting these two emissivity values into equation (36) the following can be derived:

$$\overline{S_b S_t} = 0{,}62 \cdot A_t$$

$$(\textit{since } A_t \simeq A_b)$$

the radiative heat transfer coefficient

$$h_r = \frac{\overline{S_b S_t} \cdot \sigma \cdot (T_b^4 - T_t^4)}{A_b \cdot (T_b - T_t)} \qquad (37)$$

Equation (35) yields the amount of the total heat transferred which can be attributed to the radiative component. By subtracting this from the total heat transferred, the heat transfer due to the convective component is obtained. Indeed, in view of the low pressures, gas convection is small and the total convective component approximates the particle convective component.

3.2.2 Statistical Analysis of Results

In order to relate the data to the different operating conditions it is of value to form some empirical correlation. In view of the ease with which the radiative component can

be evaluated, the resulting convective component of the heat transfer coefficient will be utilized in formulating the empirical relation. A large number of correlations exist, and these have been reviewed in Section 1.3. However these have generally been obtained utilizing deeper beds of fine particles at relatively low temperatures. A large number of these correlations utilize a combination of Nusselt, Reynolds, Archimedes and Prandtl numbers and it is of value particularly for the sake of comparison to utilize similar forms of dimensionless numbers. The Archimedes number has previously been shown to be a function of the prevailing temperature, the particle diameter and the particle density. The particle diameter which is raised to the third power, clearly has the major effect on the Archimedes number whilst temperature and particle have only a secondary influence. It was therefore decided to utilize a relationship similar to equation (19). The product of the Nusselt number and Archimedes number raised to the power of 0,3 was considered as a single parameter in view of only one particle diameter being utilized. A number of preliminary investigations indicated that the correlation could be improved by incorporating the mean bed voidage into this parameter as suggested by Andeen et al (52). The resulting parameter has the form

$$P = Nu_{to} \cdot Ar^{0,3} / (1 - \bar{\alpha})$$

It was therefore decided to utilize the parameter 'P' as the dependent variable, and to evaluate the variation in 'P' and hence the heat transfer coefficient as defined by the Nusselt number in terms of the operating parameters designated by specific groupings and forming the independent variables. A list of the independent variables considered is quoted below:

(i) the tube Reynolds number

(ii) ratio of the dynamic bed height (as evaluated from equation (33) to the static bed height

(iii) the dimensionless reduced static bed height which is defined as the ratio of the prevailing static bed height to a height of 100 mm

TABLE 1 : Bivariate Correlation Coefficients for the Parameters utilized for the 76,2 mm OD Tube and listed in Table G5 of Appendix G

	$\ln(Re_{to})$ r_{i1}	$\ln\frac{(Hdyn)}{(Hst)}$ r_{i2}	$\ln(H_{st,r})$ r_{i3}	$\ln(\theta)$ r_{i4}	$\ln(N)$ r_{i5}	$\ln(P)$ r_{iy}
$\ln(Re_{to})$ r_{1j}	1,0000	0,5740	-0,0728	-0,1570	0,5184	0,1471
$\ln\frac{(Hdn)}{(Hst)}$ r_{2j}	0,5740	1,0000	-0,1503	0,4640	0,9900	0,0841
$\ln(H_{st,r})$ r_{3j}	-0,0728	-0,1503	1,0000	-0,3910	-0,1965	0,7859
$\ln(\theta)$ r_{4j}	-0,1570	0,4640	-0,3910	1,0000	0,5834	-0,4612
$\ln(N)$ r_{5j}	0,5184	0,9900	-0,1965	0,5834	1,0000	0,0042
$\ln(P)$ r_{6j}	0,1471	0,0841	0,7859	-0,4612	0,0042	1,0000

or for there to be no significant correlation between any two parameters, the following inequality must be satisfied:

$$-2{,}09 < r_{ij}\sqrt{\frac{20}{1 - r_{ij}^2}} < 2{,}09 \qquad (39)$$

or

$$|r_{ij}| < 0{,}423 \qquad (40)$$

Reference to equation (40) and Table 1 indicates that a significant correlation exists between the following parameters:

Reynolds Number	: and H_{dyn}/H_{st} , N
The Height Ratio (H_{dyn}/H_{st})	: and Re_{to} , θ , N
Temperature Ratio	: and H_{dyn}/H_{st} , N
Fluidization Index	: and Re_{to} , H_{dyn}/H_{st} , θ

From Table 1 it is evident that the static bed height has a very significant effect on the dependent variable whilst the fluidization index, the temperature ratio and height ratio appear to be largely interrelated. In order to determine the significance of each of the dependent variables on the combustion efficiency, the standard normal correlation coefficient B_i, for each of these parameters must be determined. These are found from the components of the inverted matrix formed from the bivariate correlation coefficient matrix of all the components between the independent variables, i.e. excluding the sixth row and sixth column of Table 1. This inverted matrix or g- matrix is given in Table 2.

TABLE 2 : Inverted Matrix of the Bivariate Correlation Coefficients between the Independent Variables

	g_{i1}	g_{i2}	g_{i3}	g_{i4}	g_{i5}
g_{1j}	6,990	89,689	1,6915	20,966	-104,27
g_{2j}	89,689	1846,4	24,346	389,47	-2096,0
g_{3j}	1,6915	24,346	1,602	6,026	-28,167
g_{4j}	20,966	389,47	6,026	85,468	-444,9
g_{5j}	-104,27	-2096,0	-28,167	-444,9	2383,1

From Table 2, the following standard normal correlation coefficients are determined:

1)	Reynolds number	:	B_1	= -0,2038
2)	Ratio of bed heights (H_{dyn}/H_{st})	:	B_2	= -0,7583
3)	Reduced static bed height, $H_{st,r}$	:	B_3	= 0,6844
4)	Temperature ratio	:	B_4	= 0,6987
5)	Fluidization index	:	B_5	= 0,3950

The multiple correlation coefficient has been calculated as:

$$R = 0,8671$$

indicating that the regression equation which could be determined from the five independent variables fits the data moderately well. However the contribution of some of the independent variables may not be significantly different from zero. By taking 95% confidence limits the interval estimates, B^1, for each of the standard partial correlation coefficients can be determined from equations (F11) and (F12) of Appendix F. The calculated interval estimates are given below:

$$-0,8496 < B_1' < 0,4420$$
$$-11,2533 < B_2' < 9,7367$$
$$0,3753 < B_3' < 0,9935$$
$$-2,9658 < B_4' < 1,5594$$
$$-10,530 < B_5' < 13,3130$$

From the interval estimates for the partial correlation coefficients it would appear that only the reduced static bed height (B_3) has any major significance in the regression analysis in view of its interval estimate not containing the zero point. In view of the possible inter-relationship between parameters, the Reynolds number (B_1) may provide some influence in an empirical relationship.

The remaining three variables have been eliminated and the regression analysis based on a least squares method undertaken to correlate the parameter P in terms of the reduced

bed height and the tube Reynolds number. By rearranging equation (38) the resulting correlation for the convective heat transfer coefficient is given by:

$$Nu_{to} = 1705 \cdot (1 - \bar{\alpha}) \cdot Ar^{-0,3} \cdot Re_{to}^{0,17} \cdot H_{st,r}^{0,26} \qquad (41)$$

The multiple correlation coefficient is evaluated as

$$R = 0,8067$$

The elimination of three of the original five variables has resulted in a decrease in the multiple correlation coefficient from 0,8671 to 0,8067. In order to establish whether the coefficient has been lowered significantly by the elimination of the three variables, the test as presented in Appendix F.2 is applied. From equation (F13) the following value is obtained:

$$F = 2,139$$

and

$$F_{0,95}(16,3) = 3,24$$

$$F_{0,05}(16,3) = 0,309$$

And since the value of F lies between 0,309 and 3,24 the multiple correlation coefficient has not been significantly reduced. Equation (41) can therefore be taken as the best estimate of the Nusselt number from which the convective component of the heat transfer coefficient is easily established. In the determination of equation (41) the following regression table given by Table 3 was generated:

TABLE 3 : Regression Table from the Analysis resulting in the formation of Equation (41)

	Sum of Squares	Degrees of Freedom	Mean Squares
Regression	0,1497	2	0,07486
Residual	0,0798	19	0,00420
Total	0,2295	21	

With the following statistical values:

Coefficient of Determination	:	0,6522
Standard Error of Estimate	:	0,0648
Multiple Correlation Coefficient	:	0,8076

The results of the heat transfer studies performed on the horizontal cooling tube have been plotted in Figure 34 to illustrate the variation of the data points. The parameter has been plotted as a function of the Reynolds number resulting in the distinction in the results obtained for deeper (about 230 mm) and shallower (about 120 mm) bed depths being clearly evident.

3.3 HEAT TRANSFER TO THE PERIPHERAL WALL

As illustrated in Figure B7 of Appendix B, three heat flux pads are located at a level some 65 mm above the base of the bed. A further three are situated 290 mm above the base of the bed. These latter three at the higher bed level were not always covered by the bed material, particularly when utilizing the shallower fluidized beds. However, the meters at the shallower bed level were always covered by bed material. By monitoring the mean metal temperature and the temperature differential between two points in the pad, both the heat flux rate and the bed to wall heat transfer coefficient can be established. Only the results from one of the lower three heat flux pads has been utilized in analysing the heat transfer data in order to enhance the comparison from test to test.

The results from some forty five tests of the measured heat flux rate as a function of the bed temperature are illustrated in Figure 35. The heat flux rate includes both that due to radiation and that due to convection and has been evaluated by using the heat flux meter coefficient of 88,98 $kW/m^2/mV$ established in Section B2 of Appendix B. The operating

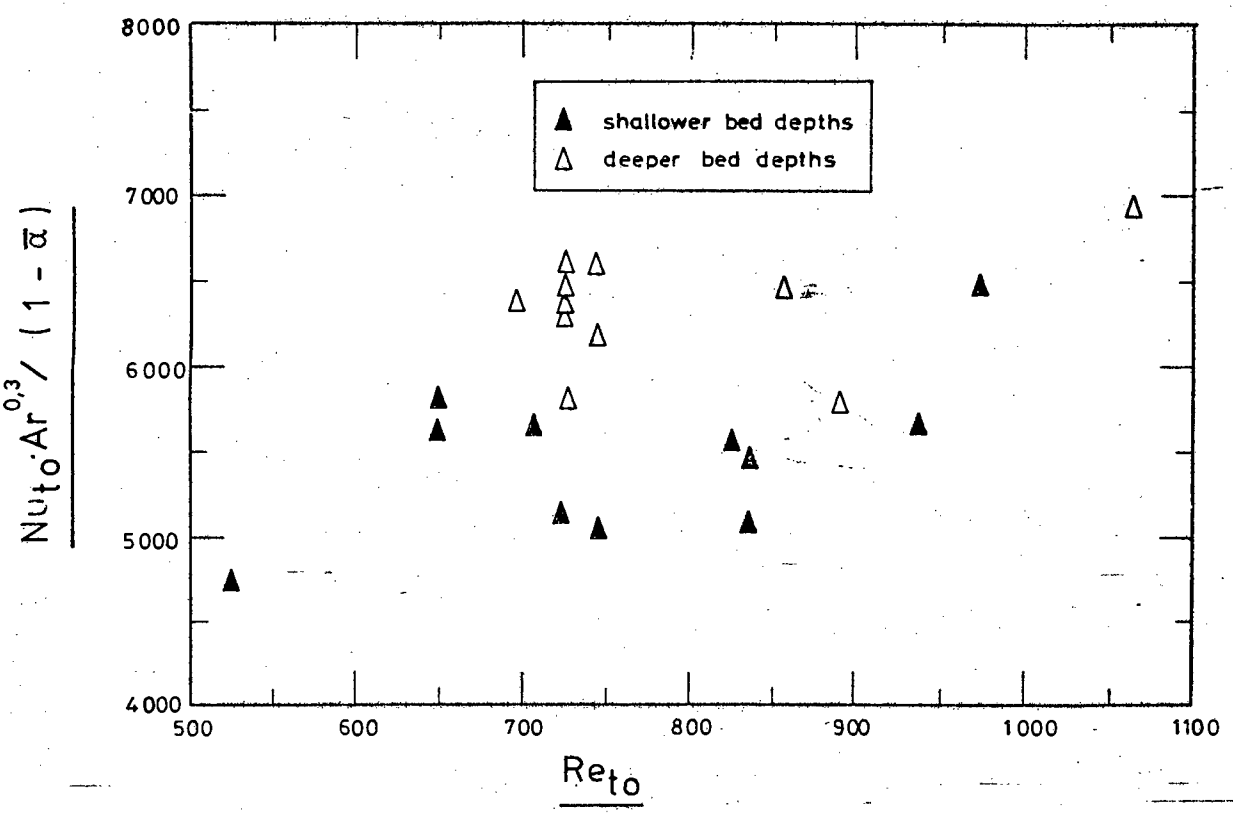

Figure 34 : Plot of the results obtained from the heat transferred to the 76,2 mm OD immersed cooling tube.

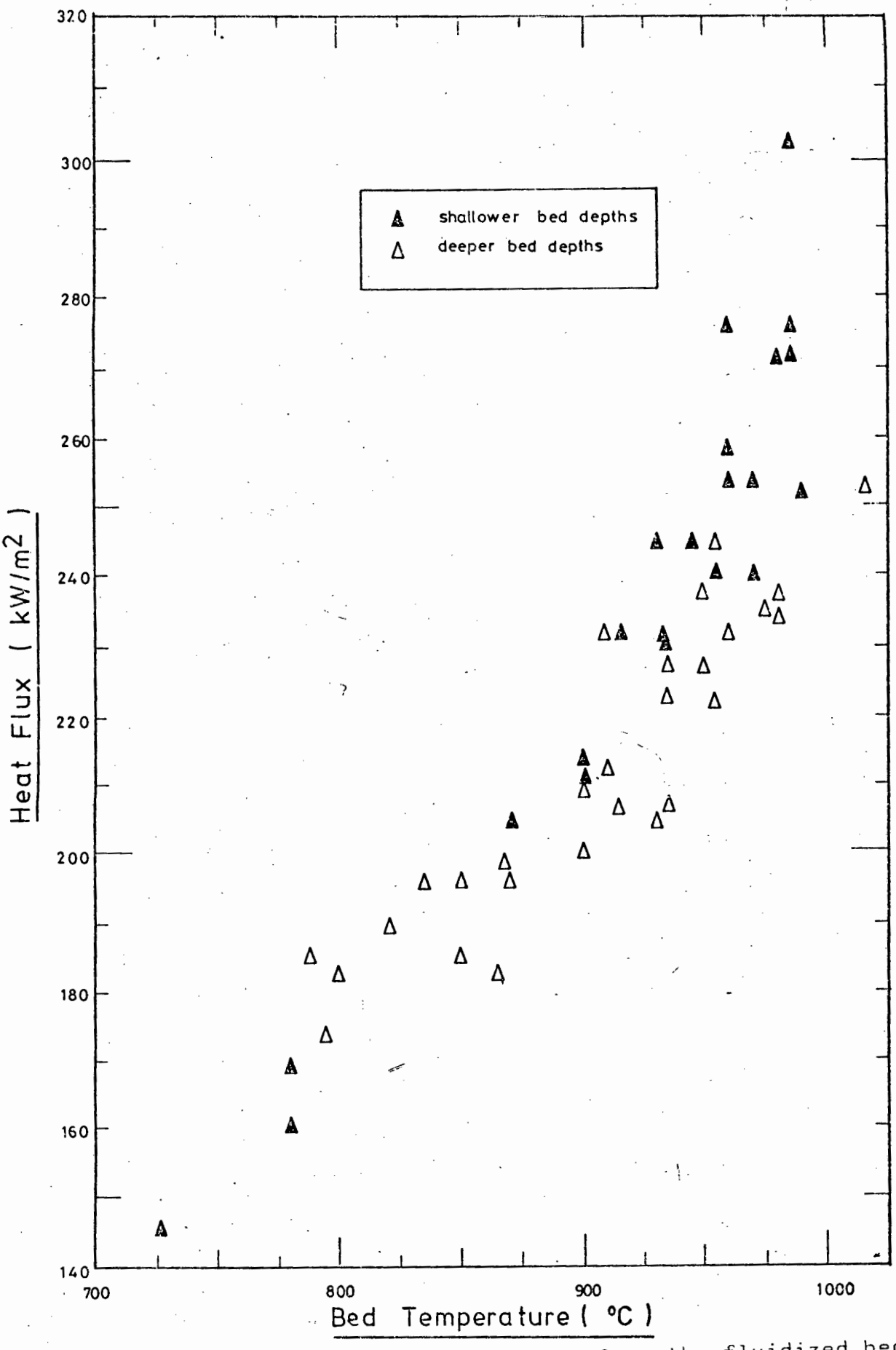

Figure 35 : Total heat flux rate from the fluidized bed to the peripheral wall as a function of the bed temperature.

conditions for the results of the heat transferred to the surface as well as the calculated values of some dimensionless numbers have been tabulated in Table G6 of Appendix G. The radiative component of the heat transferred has been considered to be additive to the convective component to form the total heat transferred. This radiative component has therefore been obtained in a very similar manner to that described in Section 3.2.1 and utilizing the same emissivity values for the surrounding surface of 0,70 and for the bed of 0,85.

The forty five test results can be divided into two groups, those related to the shallower bed depths (ranging from 97 to 148 mm) and those related to the deeper beds (ranging from 188 to 226 mm). From Figure 35 no clear distinction is immediately obvious regarding the difference in heat flux rate between shallower and deeper beds as was reported for the immersed tube. However closer investigation would tend to indicate that the heat flux rate to the shallower beds is marginally higher than to the deeper beds, which is contrary to observations concerning the immersed cooling tube. A statistical evaluation of the results has therefore been undertaken.

3.3.1 Analysis of the Test Results

The statistical analysis of the results obtained from the measurement of the heat transfer by a submerged heat flux meter has been conducted in a similar manner as was employed for the immersed cooling tube. In view of this similarity, only the more important points have been highlighted in the description of the analysis.

The convective heat transfer coefficient has been plotted as a function of bed temperature in Figure 36. From the figure, it is seen that the results obtained from the deeper bed tests appear to have convective heat transfer coefficients almost independent of the bed temperature, whilst the heat transfer

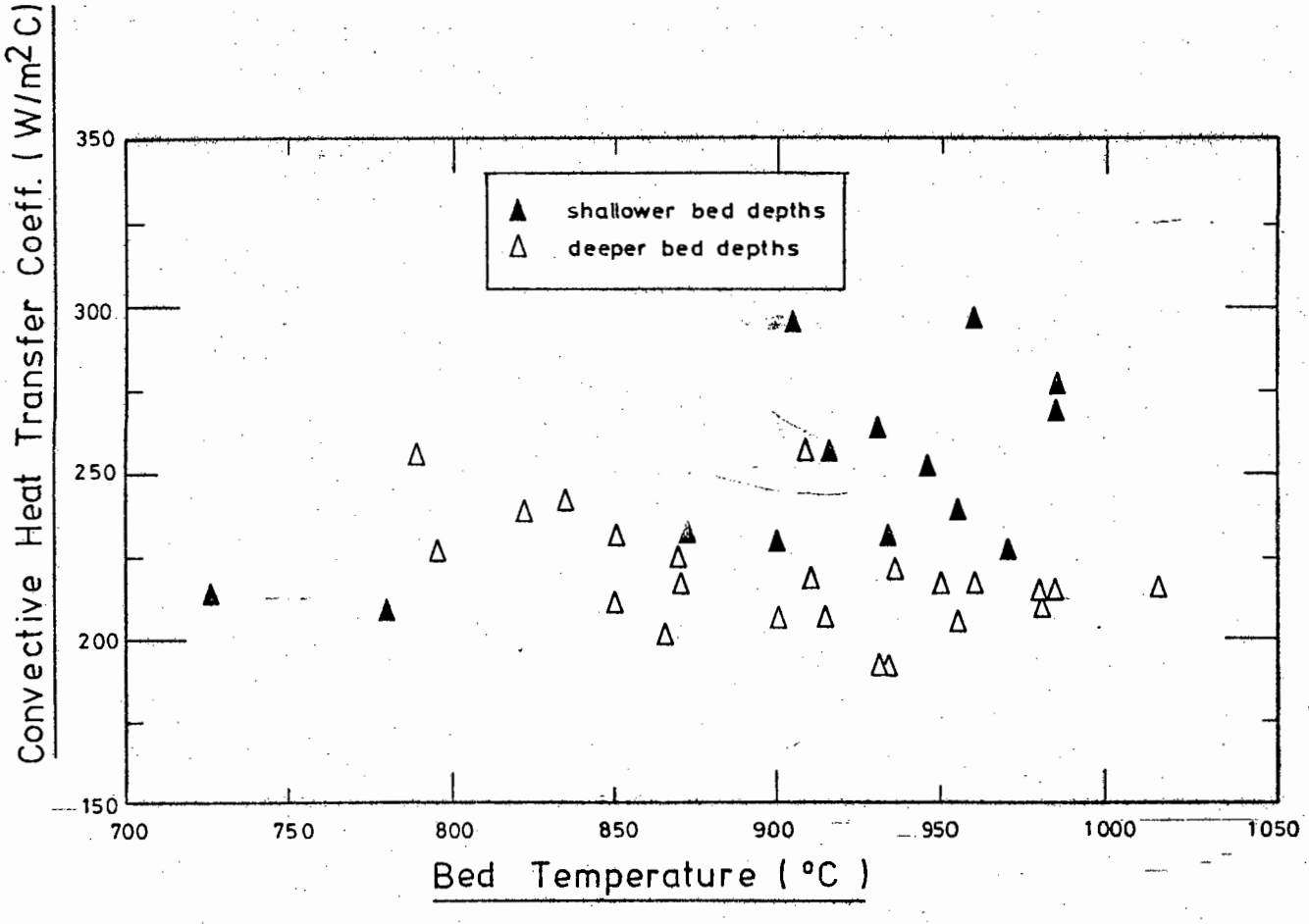

Figure 36 : The convective heat transfer coefficient as a function of the bed temperature.

coefficient for the shallow bed test series appears to increase marginally as the temperature increases. On the whole, the shallow beds result in slightly higher heat transfer coefficients than the deeper beds. The results have further been illustrated by plotting the Nusselt number formed from the convective heat transfer coefficient and the particle diameter as a function of the bed temperature. These results have been represented in Figure 37. They indicate that the Nusselt number is only slightly affected by the bed temperature. The use of a parameter incorporating the bed voidage as was employed for the immersed cooling tube studies cf equation (41), did not result in a significant improvement in the correlation.

3.3.2 The Regression Analysis

The convective heat transfer coefficient is contained in the particle Nusselt number. This dimensionless number is considered as the function of the following independent variables in a multiple regression analysis:

(i) the ratio of the dynamic to static bed heights,

(ii) the reduced static bed height,

(iii) the temperature ratio defined as $\theta=T_b/273$,

(iv) the fluidization index defined as $N=(u_f-u_{mf})/u_{mf}$,

(v) the particle Reynolds number, and

(vi) the Archimedes number.

The regression analysis was performed by considering the logarithm of the Nusselt number as the dependent variable, in terms of the sum of the logarithms of each of the six independent variables multiplied by a constant determined from a least squares analysis. The logarithms of all the parameters utilized in the regression analysis are given in Table G7 of Appendix G, whilst the resulting bivariate correlation coefficients r_{ij} are presented in Table 4 overleaf.

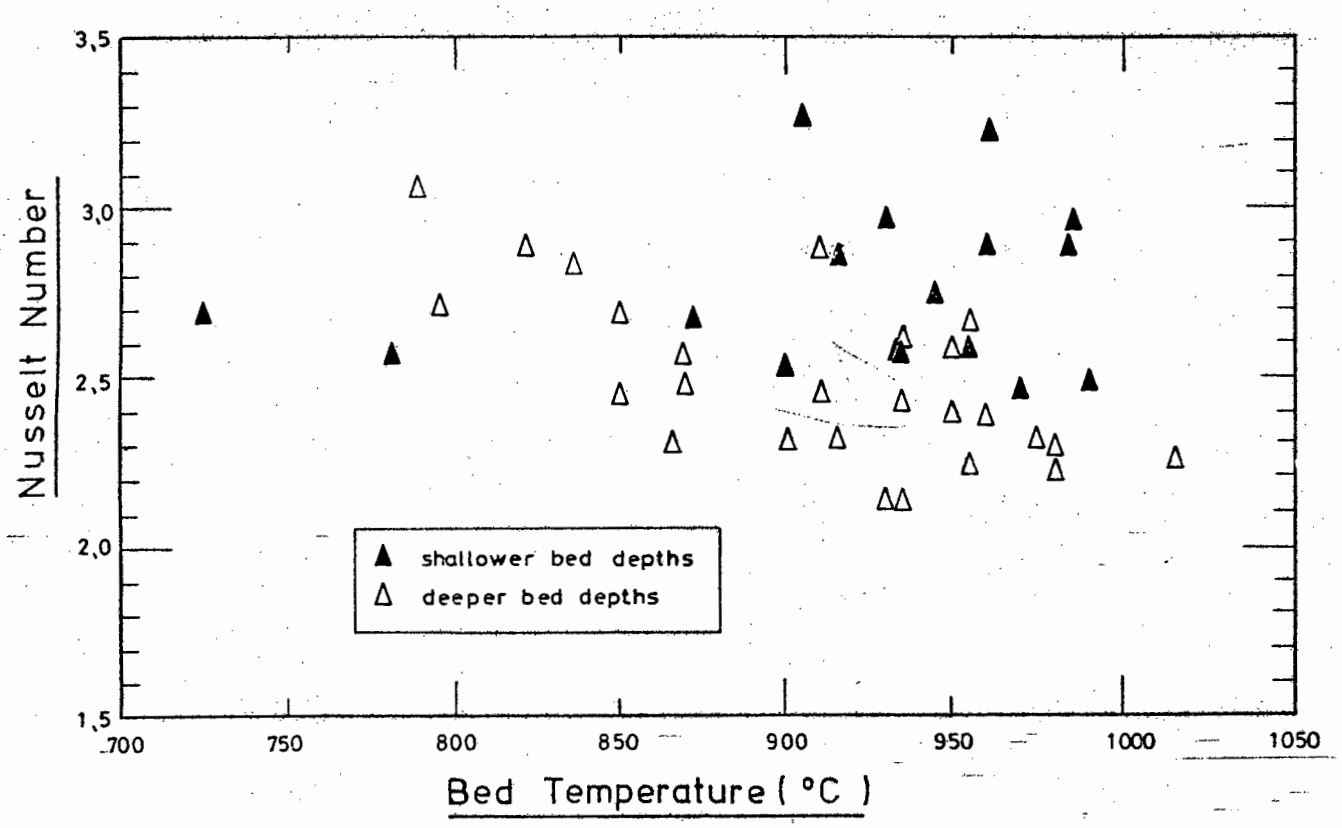

Figure 37 : The particle Nusselt number as a function of the bed temperature.

TABLE 4 : Bivariate Correlation Coefficients for the Parameters utilized for correlating the bed to Peripheral Surface Heat Transfer Coefficient and listed in Table G7 of Appendix G.

		$\ln \left(\frac{Hdyn}{Hst}\right)$ r_{i1}	$\ln (H_{st,r})$ r_{i2}	$\ln (\theta)$ r_{i3}	$\ln (N)$ r_{i4}	$\ln (Re_p)$ r_{i5}	$\ln Ar$ r_{i6}	$\ln Nu_p$ r_{iy}
$\ln \left(\frac{Hdyn}{Hst}\right)$	r_{1j}	1,0000	0,0458	0,4968	0,9960	0,9381	0,4964	-0,4302
$\ln (H_{st,r})$	r_{2j}	0,0458	1,0000	-0,1774	0,0433	0,1462	0,1766	-0,4367
$\ln (\theta)$	r_{3j}	0,4968	-0,1774	1,0000	0,5566	0,1770	-0,99999	-0,2415
$\ln (N)$	r_{4j}	0,9960	0,0433	0,5566	1,0000	0,9157	0,5563	-0,4350
$\ln (Re_p)$	r_{5j}	0,9381	0,1462	0,1770	0,9157	0,0000	-0,1767	-0,3980
$\ln (Ar)$	r_{6j}	-0,4964	0,1766	-0,99999	0,5563	-0,1767	1,0000	0,2417
$\ln (Nu_p)$	r_{yj}	-0,4302	-0,4367	-0,2415	-0,4350	-0,3980	0,2417	1,0000

Using all forty five points, the data is found to be correlated by equation (44).

$$Nu_p = 0,616 \cdot Ar^{0,23} \cdot Re_p^{-0,13} \cdot H_{st,r}^{-0,15} \qquad (44)$$

with a multiple correlation coefficient of 0,610.

It is evident that with a multiple correlation coefficient of only 0,610, the data have not been fitted too well. From an analysis of the effect of each of the three independent variables on the Nusselt number, it was evident that each contributes significantly in the prediction of the Nusselt number. In this analysis the standard normal correlation coefficients were evaluated as

B_1 (refers to Ar) = 0,269
B_2 (refers to Re) = - 0,286
B_3 (refers to $H_{st,r}$) = - 0,443

From each of these three standard normal correlation coefficients it is evident that the static bed height has the major influence on the prediction of the Nusselt number, whilst the Archimedes and Reynolds numbers have a secondary influence.

In considering only those data obtained from the deeper bed tests the following relationship was obtained.

$$Nu_p = 0,0260\ Ar^{0,58}\ Re^{0,012}\ H_{st,r}^{0,033} \qquad (45)$$

with a multiple correlation coefficient = 0,680

The effect of the Reynolds number and the reduced static bed height is easily shown to be insignificant with the resulting expression for the deeper bed being represented by equation (46).

$$Nu_p = 0,0295\ Ar^{0,57} \qquad (46)$$

with a multiple correlation coefficient = 0,676

A similar analysis performed on the shallower beds utilized resulted in a poorer correlation of the data than that given by equation (44). The correlation resulted in the Nusselt number being represented in terms of the Archimedes and Reynolds numbers.

It is therefore apparent that two relationships relating to different bed heights do not best describe the results obtained for the heat transferred from the bed to a peripheral cooling surface. Equation (44) therefore best describes the heat transferred by the mechanism of convection from the bed to a vertical peripheral cooling surface.

3.4 RESULTS OBTAINED FROM THE HEAT FLUX PROBE

The design of the heat flux probe is presented in Section B4 of Appendix B and has been discussed in Section 2.2.7 (g). The probe is made up of a 38 mm diameter stainless steel cylinder with an effective height of 25 mm. This probe is mounted on top of a system of concentric tubes forming a cooling jacket, which enables the probe to be introduced via the ash port. Vertical movement of the probe enables it to measure the heat transfer coefficient at various levels within the bed. Although this will only provide information concerning the heat transferred from the bed to an immersed probe, the relative value of the results will provide information which could be applied to other immersed surfaces.

Originally the probe was designed to establish the extent to which heat transfer from the expanded bed is effective as well as to monitor the nature of the heat transferred in the cloud zone which exists above the surface of shallow fluidized beds. However, the maximum depth to which the probe was able to extend into the bed was some 350 mm from the base of the bed. This proved to be too short to monitor the expansion of the deeper beds. Thus measurements of the effective bed heights were only possible for the shallower fluidized beds.

Two series of tests can be distinguished from measurements obtained from its immersion in the fluidized bed. The first are related to the mean value of the heat transfer coefficients at various levels within the bed, whilst the second relate to instantaneous heat transfer coefficients at a particular bed height.

3.4.1 Mean Heat Transfer Coefficients

Mean heat transfer coefficients between the probe and the bed were obtained at various levels within and immediately above the bed for the shallow bed tests 45, 47a, 47b, 47c, 47d, 53a, 53b and 53c. The position of the probe was varied during test 50a without the detection of any significant variation in the mean heat transfer coefficient. Test 50a represents a deep bed test. Further tests were carried out with the probe at a single depth for tests 50b, 50c and 50d. The results of these tests, together with some calculated values are contained in Table G8 of Appendix G.

From the table, it is evident that insufficient data have been obtained to derive an empirical correlation for the heat transfer coefficient between the bed and the immersed probe. In any event, the absolute value of the heat transfer coefficient thus obtained is not of much significance. However the relative value of the heat transfer coefficient is of particular interest as the probe height is varied. The heat transfer coefficients obtained for the four tests of Run 47 have been plotted in Figure 38 as a function of the bed depth. Curves obtained from Tests 47a, 47b and 47c tend to illustrate the same general trend of a relatively constant heat transfer coefficient which decreases rapidly from the top of the expanded bed of some 180 to 200 mm. These values compare well with the values obtained for the expanded bed height from equations (32) and (33). The values obtained when utilizing these two equations are indicated in Figure 38.

However, in the case in which the bed is operated substoichiometrically, represented by test 47d, the heat transfer

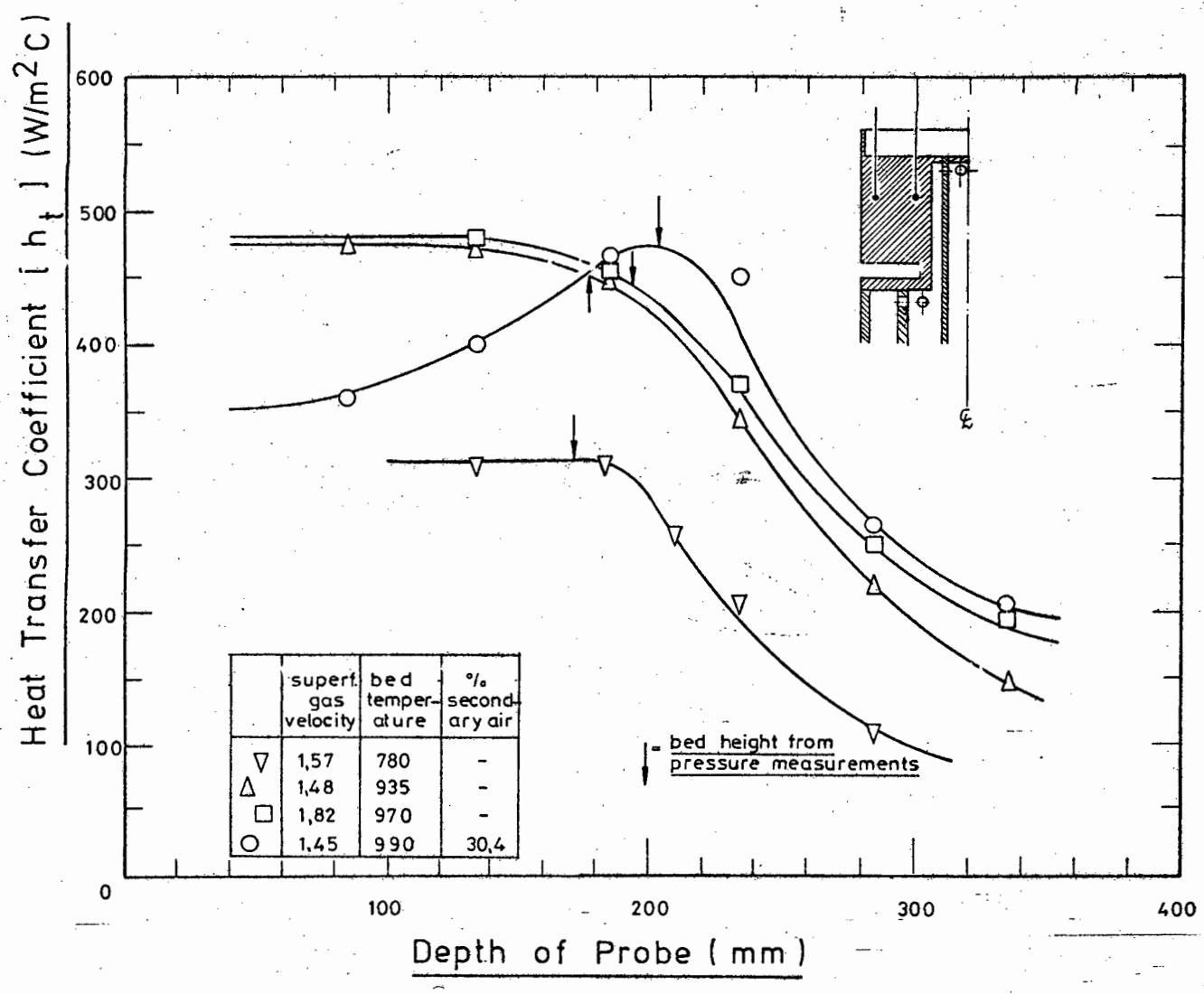

Figure 38 : Heat transfer coefficient from the fluidized bed to the heat transfer probe for the four tests of Run 47.

coefficient tends to increase and shows a marked rise near the top of the expanded bed. This is explained by the more intense homogeneous gas combustion taking place in the very dispersed particulate phase existing at the top of the expanded bed. The heat generated by this combustion is more easily transferred to a cooled surface such as a probe or surrounding cooling surface than to the bed material, as the sand bed shows no variation in the temperature throughout its height. Indeed temperature variations of some 15°C between extreme thermocouples were usually monitored during normal combustion, whereas on operating as a partial gasifier the difference decreases to below 10°C. This decrease is due to an increase in the temperature of the thermocouples at the lowest level in the bed indicating a more intense combustion in the region closest to the nozzles.

A further point to note from Figure 38 is the difference between the bed height predicted from pressure probe readings (i.e. as given by equations (32) and (33)) and that indicated by the heat transfer readings from the heat transfer probe. It is clear that in the normal combustion case, the predicted bed height is very similar to effective heat transfer height indicated by the heat transfer probe studies. However when operating the bed substoichiometrically, the heat transferred at the higher heat transfer coefficient extends some 25% beyond the expanded bed height predicted from the pressure probe readings. This phenomenon is described by the heat transfer in the cloud zone. Similar results are obtained when plotting the results of tests 45 and 53 represented in Table G8 of Appendix G.

3.4.2 Instantaneous Heat Transfer Coefficients

The heat transfer coefficients measured by both the heat flux probe and the heat flux pads vary continuously during the tests, and as such mean values have had to be obtained. However, useful information relating to the mechanism of heat transfer can be established by monitoring the variation of the heat transfer coefficient over short time intervals.

The measurement of the heat transfer coefficient in both instruments is evaluated from the monitoring of the temperature difference between two well defined points in a solid material. In the case of the heat transfer probe, two thermocouples are used. The centre of the outer thermocouple is located 2 mm from the edge of the probe and hence the bed, whilst the inner thermocouple is positioned 7 mm away from the outer thermocouple and 2,5 mm from the inner cooled surface of the probe. A diagram illustrating the operation of the heat transfer probe was presented in Figure 22.

The heat transfer coefficient between the inner wall of the probe and the cooling water is very much higher than the external heat transfer coefficient and further, this inner coefficient remains relatively constant. In contrast to this steady internal coefficient, the external heat transfer coefficient fluctuates rapidly with a frequency of the order of 1 H_z (142).

The outer thermocouple responds very rapidly to changes in the heat transfer coefficient in view of the low thermal inertia of the outer layer of the probe. On the other hand, temperature fluctuations of the inner thermocouple are relatively well damped due to the thick cylinder, and temperature at this point shows only slow and small variations from the mean value. Figures 39 and 40 illustrate these temperature fluctuations as a function of time for a shallow and deep bed respectively.

From observation of the two figures, it is evident that both the frequency, and to a lesser extent, the amplitude of the variation of the outer temperature of the probe is greater in the deeper than in the shallower fluidized bed. In view of the relatively steady temperature of the inner thermocouple, cf Figure 39 (a), the outer temperature provides an indication of the variation of the heat transfer coefficient.

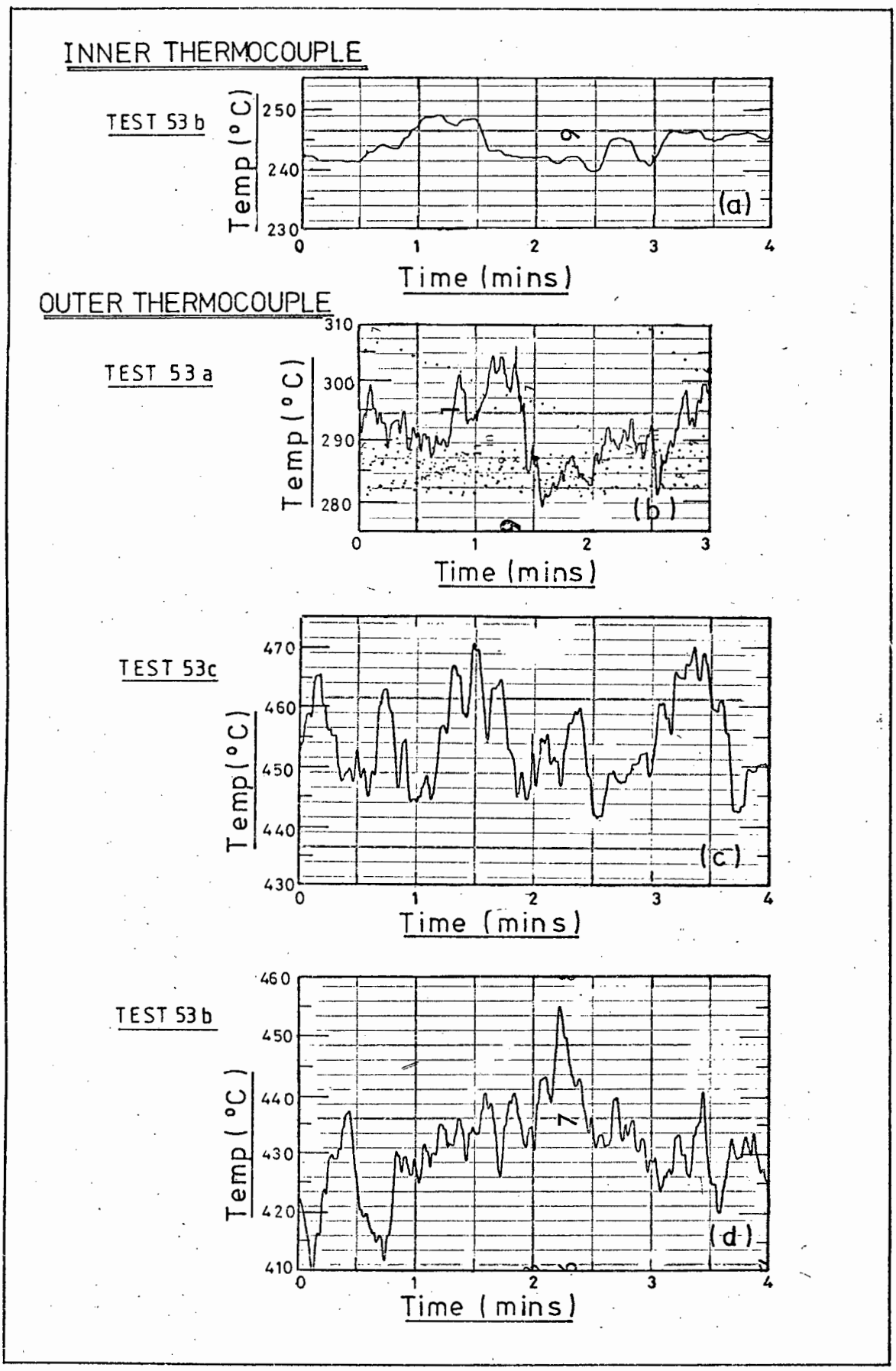

Figure 39 : Temperature traces of the inner and outer thermocouples of the heat flux probe for a bed of 132 mm deep, i.e. Test 53.

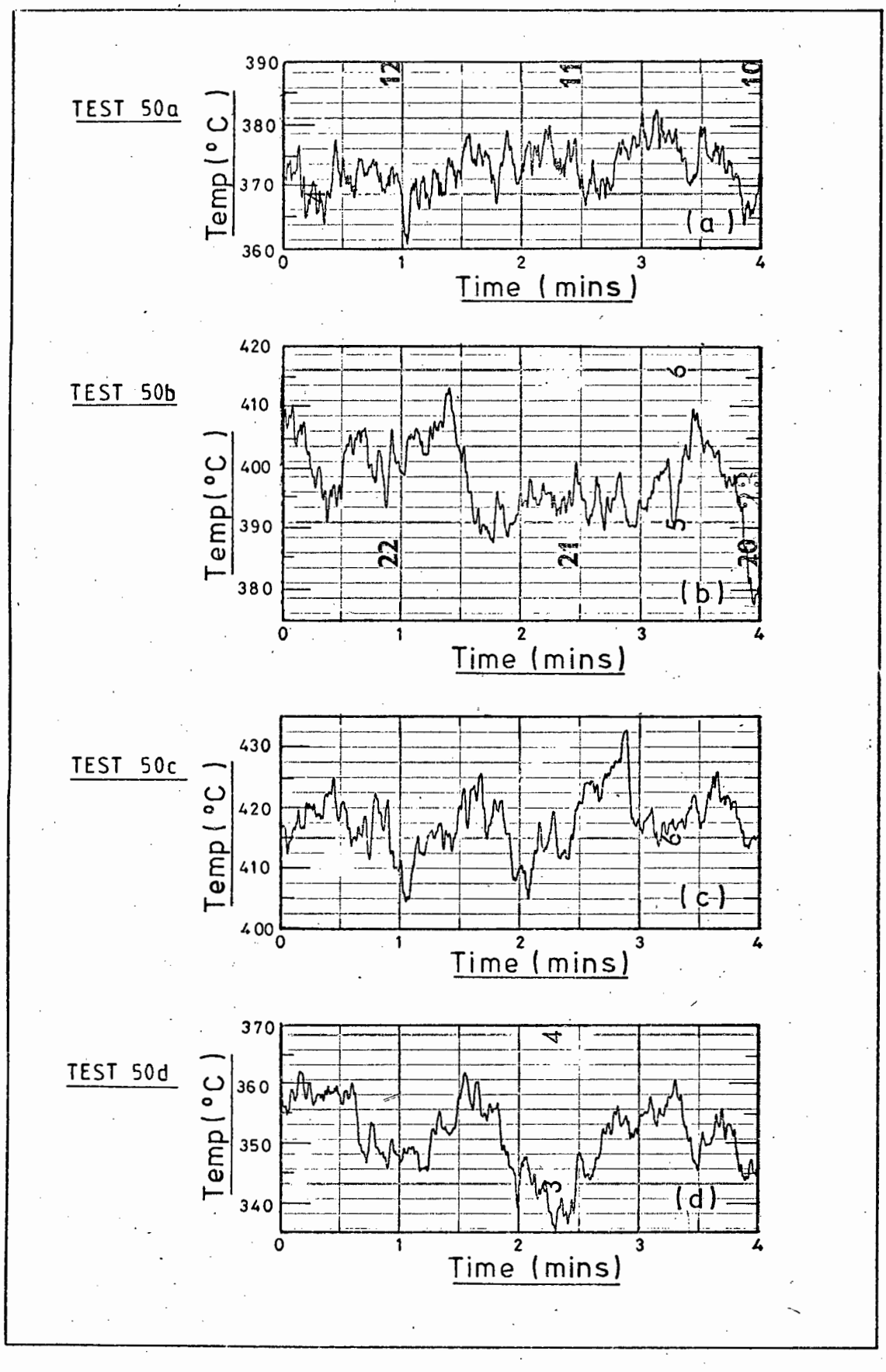

Figure 40 : Temperature traces of the outer thermocouple of the heat flux probe for a bed of 210 mm deep, i.e. Test 50.

This is evident from equation (47)

$$Q = k \cdot A_t \frac{\Delta T}{t \Delta x} = h_o \cdot A_o \cdot \Delta T_o$$

hence

$$h_o = \frac{k \cdot A_t}{A_o \cdot \Delta x} \cdot \frac{(T_{to} - T_{ti})}{(T_b - T_w)} \qquad (47)$$

Now the term incorporating the thermal conductivity of the material and the dimensions of the probe can be considered to be constant. Further, for those cases in which the bed temperature is much greater than the outer wall temperature, the variation in the temperature term in the denominator will be small. The small variation in the inner thermocouple temperature results in almost all of the fluctuation in the probe external heat transfer coefficient being accommodated by variations in the temperature of the outer probe thermocouple.

The fluctuations in the outer thermocouple temperature represented in Figures 39 and 40 can therefore be regarded as being equivalent to the nature of the fluctuation in the bed to probe heat transfer coefficient. In view of the almost non-uniform nature of this fluctuation, a simplified analysis has been undertaken in order to analyse the data. The results of this analysis are contained in Table G9 of Appendix G.

The amplitude has been measured between each peak and trough, including the minor peaks and troughs which occur, and the frequency has been taken as the reciprocal of the interval between each of these peaks and troughs. It is clear that the values would not be very accurate in view of it being difficult to establish the existence of either a peak or a trough in many instances. However, by taking the results over a period of at least two minutes, these difficulties are largely overcome.

From Table G9, it is evident that the frequency of the variation in temperature is always larger for the deeper

than the shallower beds. The amplitude of the change is not clearly different in either whilst the range of change between the maximum recorded value and the minimum value is very much the same for both the deeper and shallower beds investigated.

The frequency of the variation in temperature indicates that the variation can be attributed to the alternate movement of bubbles and particulate phase across the heat transfer probe. The greater the frequency, the greater the resulting heat transfer. From Table G9 it is evident that this frequency alone, and not amplitude or the product of the frequency and amplitude result in a distinction between the heat transferred to an isolated probe for beds of different heights. Taking the mean of the frequencies obtained from the tests at the two bed heights, the square root of the ratio of these two mean values yields the following

$$\sqrt{\bar{\nu}_d / \bar{\nu}_s} = 1{,}151 \qquad (48)$$

where $\bar{\nu}_d$ = mean frequency for tests in which the static bed height was 210 mm

$\bar{\nu}_s$ = mean frequency for tests in which the static bed height was 132 mm.

A similar analysis was performed for the heat flux pads by monitoring the fluctuation in the heat flux rate. These results are contained in Table G10 of Appendix G. No apparent distinction between the results of the deeper and shallower bed tests is evident from either the tabulated results or the traces, some of which have been reproduced in Figure 41 for reference.

3.5 HEAT EXCHANGE IN THE FREEBOARD

On leaving the fluidized bed, the gases and particulates are further cooled in the freeboard by the surrounding water jacket. The gases are assumed to leave the bed at the bed

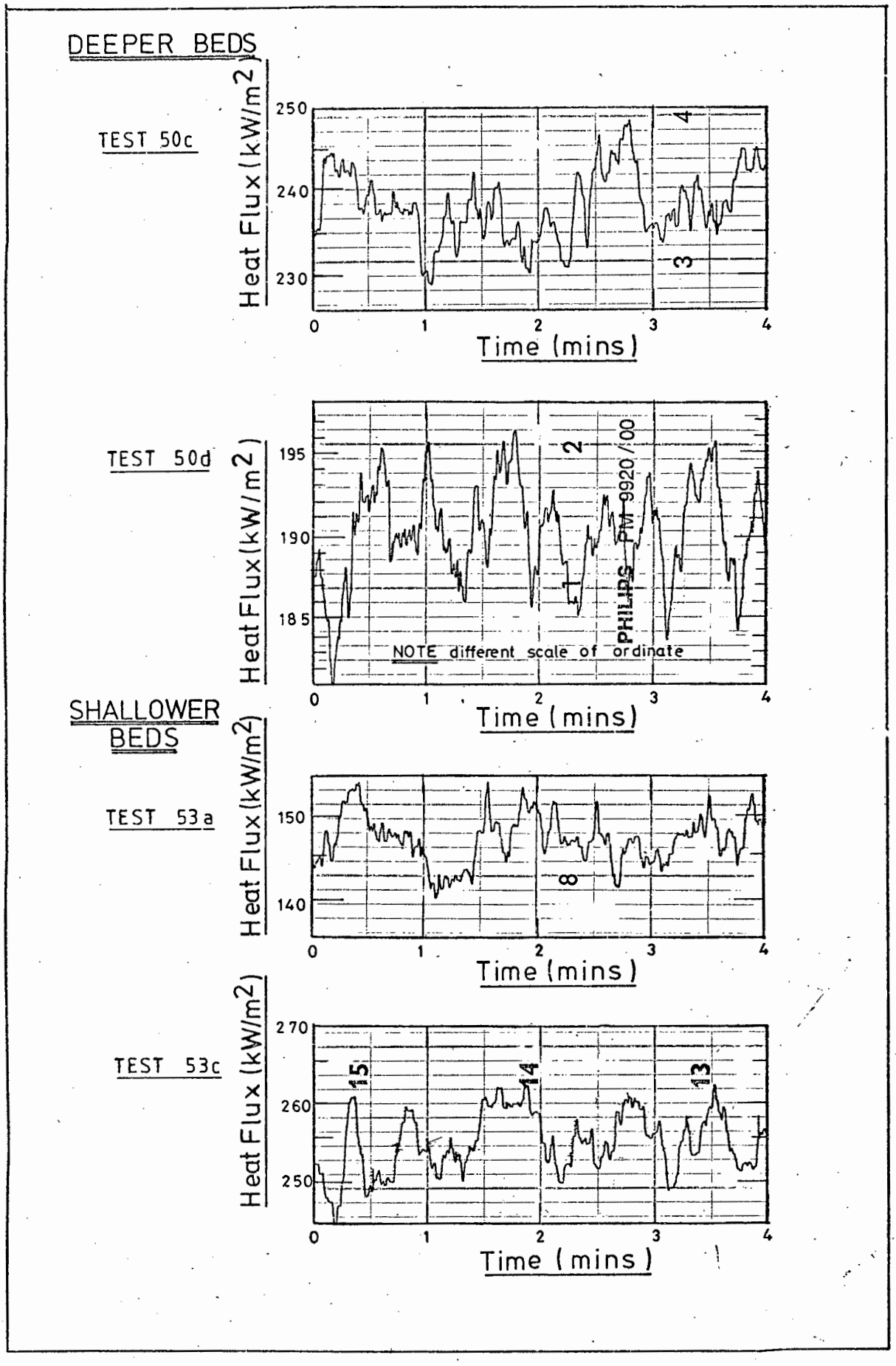

Figure 41 : Temperature traces of the heat flux pad for both the deeper (210 mm deep) and the shallower (132 mm deep) bed depths.

temperature and comprise the major source of heat input to the freeboard. In addition, unburnt particulates, unburnt volatile matter and other combustible gases may burn in the freeboard providing a second source of heat. This is particularly true in those tests in which the bed was operated substoichiometrically with secondary air being added above the bed to complete the combustion process. The freeboard therefore acts as a secondary combustion chamber in which the processes of heat transfer, combustion and the entrainment of particulates takes place. Each of these three phenomena are inter-linked. It is prudent to consider each of these parameters separately in this chapter, and to combine them in a unifying theoretical model which is proposed as an extension of Hottel's (57) single gas zone model in Chapter 4.

3.5.1 Graphical Interpretation of the Heat Transferred in the Freeboard

In order to correlate the results, the data have been reduced to a reduced firing density and a reduced furnace efficiency. These terms are similar to those originally proposed by Hottel (143). The pseudo flame temperature (T_F) is defined below as:

$$(T_F - T_o) = Q_F / m_g \cdot c_{pg} \qquad (49)$$

where for the case of zero combustion above the bed

$$T_F = T_b$$

For the case in which secondary air is introduced above the bed, it is assumed that the heat liberated above the bed is only that required to complete the combustion process. In other words, for an excess air factor 'λ' and a secondary air fraction 'S' the fraction of heat released above the bed is given by:

$$\left[\frac{\text{fraction heat released}}{\text{above bed}}\right] = s - (1 - \lambda)$$

Or in the case of combustion due to the introduction of secondary air in the freeboard, the total heat input to the freeboard is given by:

$$Q_F = m_g \cdot c_{pg} \cdot (T_b - T_o) + \{ s - (1 - \lambda) \} \cdot Q_{lib,f} \qquad (50)$$

which on substituting into equation (49) yields an increased pseudo flame temperature. The furnace efficiency and the reduced firing density are defined as

$$\eta_f = (Q_F - Q_g) / Q_F \qquad (51)$$

$$D' = Q_F / (\sigma \cdot GW \cdot T_F^4 \{ 1 - \theta_o \}) \qquad (52)$$

where

$$\theta_o = T_o / T_F$$

The effective sink area of equation (52) is a characteristic of the furnace. By multiplying the reduced firing density by this area, the right hand side of equation (52) is readily obtained from data obtained on the test rig. A complete set of results is contained in Table G11 of Appendix G.

The results of Table G11 have been plotted in Figure 42 together with the characteristic curve of the furnace derived in Chapter 4. The abscissa of Figure 42 is given by the reduced firing density D^1 for the characteristic curve, whilst for the individual points the abscissa has been established as the product $D^1.GW$. Since the plot is based on logarithmic co-ordinates, each of the points is shifted a distance log (GW) to the left to be related to the characteristic curve.

3.5.2 Combustion in the Freeboard

It is evident from Figure 42 that the data points can be approximated by a straight line. However the slope of the line is much steeper than would be anticipated from the characteristic curve shifted to the right a distance log (GW). This is due to the evaluation of the heat input given by equation (50) omitting to take into account the heat release

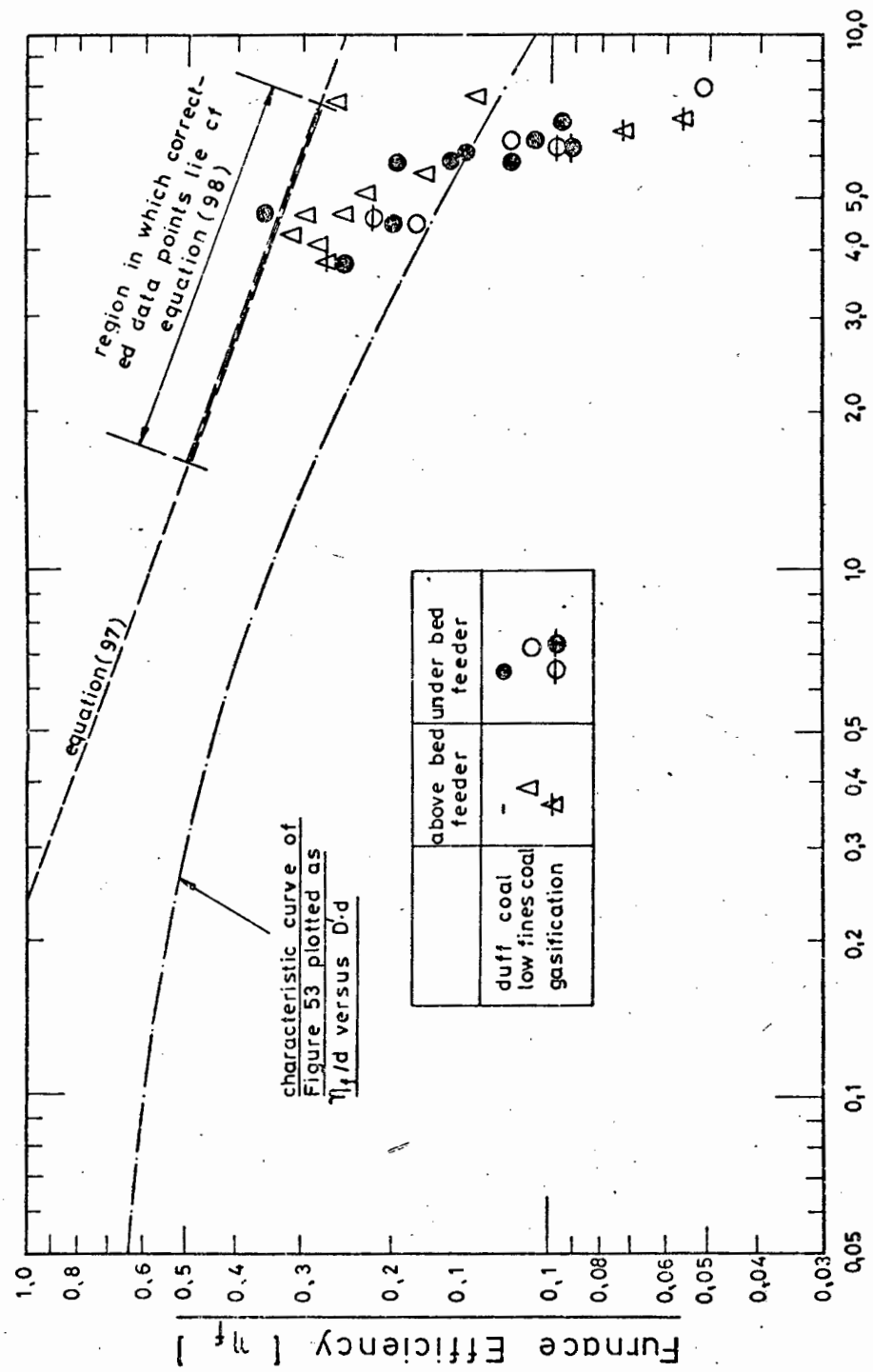

Figure 42 : Graphical representation of the combustion chamber performance.

in the freeboard due to the combustion of volatiles and unburnt gases as well as the combustion of some of the particulates. This is particularly true for the higher gas velocities and hence higher bed ratings where the volatiles may leave the bed to burn in the freeboard. More heat will therefore be added to the freeboard at the higher bed ratings than at the lower ratings. Thus the low furnace efficiencies predicted by the data points in Figure 42 at the higher firing densities will be increased somewhat more than those at the lower firing densities resulting in a shallow curve. The method of deriving this increased intensity of combustion in the freeboard is presented in the theoretical analysis of Chapter 4 which further links the phenomena of heat transfer, combustion and entrainment in the freeboard zone.

A further point to note from Figure 42 is the relative groupings of the data obtained from operation using the above bed feeder, and those when utilizing the underbed feeder. It is seen that with exception of those tests making use of secondary air, in which the combustion in the freeboard represents an appreciable contribution of the heat input to the region above the bed, the measured reduced furnace efficiencies are in general higher for the above bed feeder than for the underbed feeder when burning the low fines coal. This difference is clearly due only to the combustion taking place in the freeboard. In relating all the points to a characteristic curve, it is evident that the greater freeboard combustion takes place when employing the underbed feeder for burning the low fines coal.

This is due to only a small fraction of the low fines coal having a size which is small enough for it to be entrained in the gas stream without entering the bed when utilizing the above bed feed system. The major portion of the coal therefore enters the bed, and is evenly distributed cf Appendix E, resulting in there being relatively few regions devoid of oxygen. As a consequence, the major fraction of

the volatile matter burns within the bed whilst the absence of reducing regions results in almost no carbon monoxide formation for subsequent combustion above the bed. In contrast to this, the poor mixing characteristics of the underbed feeder results in regions of high carbon concentrations occurring near the feeder whilst those areas away from the feeder are relatively devoid of combustible matter and result in high oxygen levels. There is insufficient oxygen near the feeder to enable adequate combustion of the volatile component and as a result this is released and is burnt together with carbon monoxide above the bed.

3.6 THE COMBUSTION EFFICIENCY

Complete combustion of coal is assumed to have taken place when all of the coal is burnt in the presence of oxygen to form carbon dioxide, sulphur dioxide and water vapour. The reactions taking place during the formation of these products are all exothermic, resulting in a corresponding release of heat.

The combustion efficiency of the fluidized bed combustion chamber can therefore be defined as the ratio of the rate of heat liberated to the rate of heat input. This ratio can be shown to be equal to the rate at which the coal is burnt to the rate of coal fed into the rig, or:

$$\eta_c = M_f / M_{fo} \qquad (53)$$

Which can also be written as

$$\eta_c = 1 - h_c \qquad (54)$$

where h_c is the unburnt carbon loss defined by a boiler acceptance test standard eg, BS 2885 of 1974.

The rate of heat input is the rate at which the heat could be generated should complete combustion of the entire coal feed

be effected. The rate of heat liberated is less than this quantity as a result of

a) incomplete combustion resulting in carbon monoxide formation, and

b) unburnt carbon remaining in the ash.

Incomplete combustion of the coal generally refers to the combustion of the carbon component of the coal to carbon monoxide instead of carbon dioxide which is accompanied by a reduction in the heat released due to the smaller heat of formation of carbon monoxide. Although substantial amounts of carbon monoxide are generated in the fluidized bed section during combustion with secondary air above the bed, the completion of the combustion reaction in the freeboard ensures that the final carbon monoxide content of the exhaust gases is low. Reference to Table G11 of Appendix G indicates that for above bed feeding of coal in all but two tests the carbon monoxide content of the flue gases is less than 0,5%. It should be noted that these two tests represent conditions in which secondary air was introduced above the bed to enable relatively high bed ratings to be achieved. On the other hand, tests undertaken utilizing the underbed screw feeder resulted in correspondingly higher carbon monoxide levels being monitored.

However the unburnt carbon loss is significantly higher than the loss due to incomplete combustion referred to above, even when employing the underbed feeder, and as a consequence only the unburnt carbon loss has been considered in establishing the combustion efficiency.

As no provision was made during the tests for removal of bed material from the ash pipe, ash and bed material can only be removed from the test rig as a result of the entrainment process. The unburnt carbon loss is therefore limited to the carbon entrained in the off gases. The proportion of carbon contained in the ash collected by isokinetic sampling

can be utilized in order to determine the unburnt carbon loss. In fact, this represents the entire unburnt carbon loss and the combustion efficiency can be determined directly from it as given by equation (54).

3.6.1 Methods of Evaluating the Combustion Efficiency

If the loss due to incomplete combustion is small compared to the unburnt carbon loss, and further, if this unburnt carbon loss can be considered to be due only to the unburnt carbon in the entrained ash, then the combustion efficiency may be determined by one of two methods:

a) by means of a heat balance, or

b) by determination of the carbon loss from the unburnt carbon in the entrained ash.

The heat balance method relies on the measurement of a number of different parameters and in particular, the coal flow rate. In view of coal feeding difficulties the required degree of accuracy in the measurement of the coal flow rate cannot be attained. Therefore the combustion efficiency has been determined by the second method; i.e. the determination of the carbon loss from the unburnt carbon in the entrained ash. This loss can be shown to be related to the carbon content of the entrained ash by equation (55).

$$h_c = \frac{c_c}{1 - c_c} \cdot a \cdot \frac{33\,820}{GCV} \qquad (55)$$

Or the combustion efficiency can be determined in terms of the carbon content of the entrained ash and the ash content and calorific value of the coal i.e.

$$\eta_c = f(GCV, a, c_c) \qquad (56)$$

From equation (56) it is clear that the combustion efficiency is independent of the direct measurement of any of the main operating variables during each individual test. Provided a representative ash sample is analysed, and that the main

operating variables remain within acceptable limits, a good assessment of the combustion efficiency as defined by equation (56) can be obtained. The resulting values are contained in Table G11 of Appendix G.

3.6.2 Test Results

The results of the combustion and gasification (i.e. when the bed is operated sub-stoichiometrically) tests are illustrated in Figure 43 in which the carbon loss has been plotted against the heat liberated in the test rig per unit of bed plan area. During the tests referred to as gasification tests, the bed is operated sub-stoichiometrically, whilst secondary air is introduced via the secondary air nozzle to promote a secondary combustion reaction above the bed. In the data points of Figure 43 which refer to secondary air operation, this secondary air flow rate represented about 30% of the total air flow.

Referring to Figure 43 it is evident that no trend can be established for the tests conducted with the underbed coal feeder. The two tests for which the carbon loss was less than 20% were conducted at excess air levels of 41% and 78% for the lower and higher bed ratings respectively. The remaining underbed feeding tests represented in Figure 43 were conducted at excess air levels between 16% and 25%. A further point to note with the underbed feeding tests is the high carbon loss when operating the bed sub-stoichiometrically. It is evident that under these conditions only a small amount of carbon is burnt in the secondary combustion zone above the bed.

The results when using the overbed feeder and pneumatic spreader are also included in Figure 43. Here, all but one of the tests were conducted at excess air levels between 16% and 25%, and a trend can be distinguished for the shallower of the two bed heights employed. The carbon loss tends to decrease as the bed rating increases. This is due

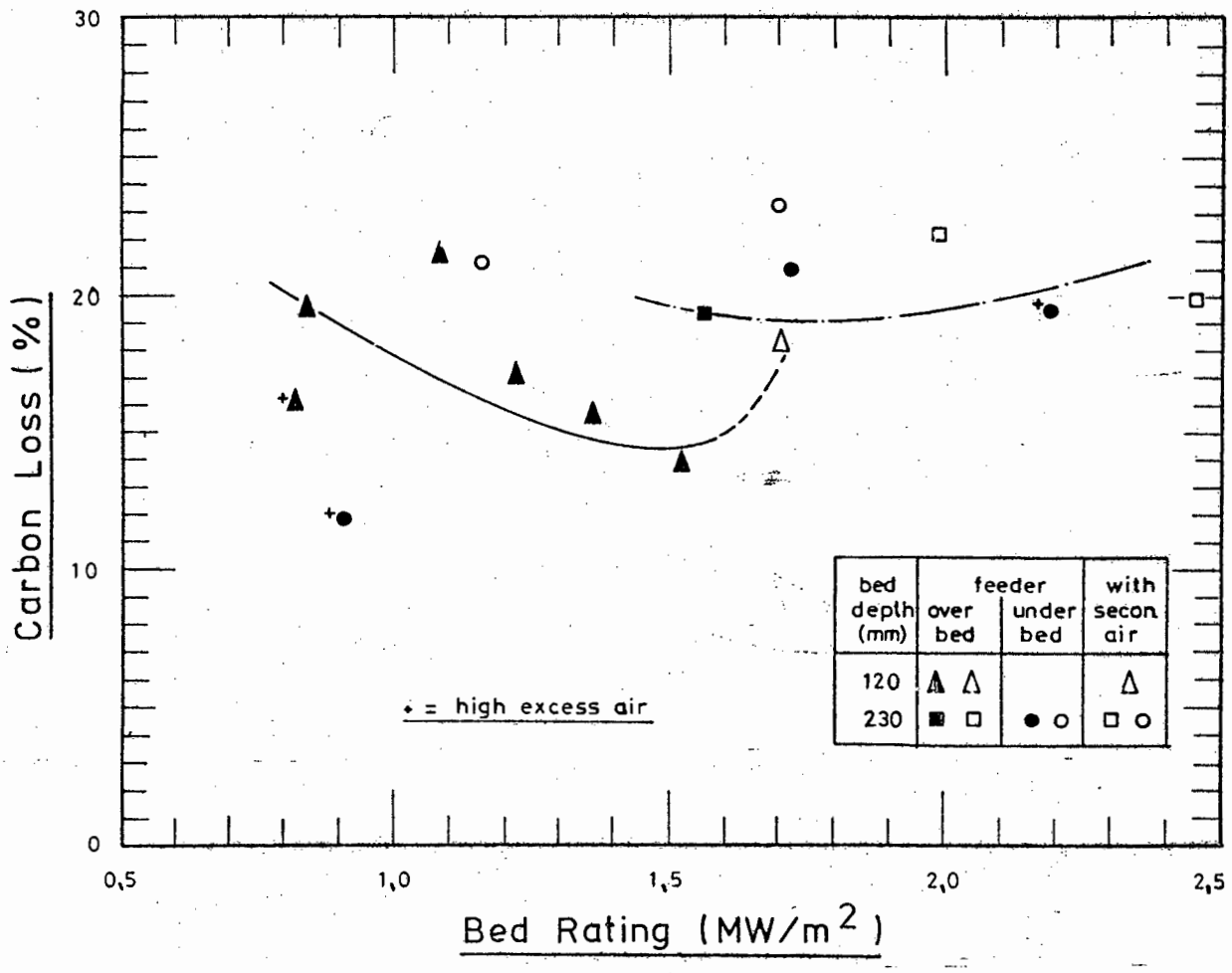

Figure 43 : Carbon loss as a function of the bed rating.

to an increase in bed rating being accompanied by a simultaneous increase in velocity and bed temperature. Clearly the effect of the improved combustion efficiency at higher temperatures is greater than the decrease caused by the higher entrainment rates associated with increases in velocity. Gasification once again results in increased carbon losses. However, the increase is of the order of 2% which would indicate that a substantial amount of heat is liberated as a result of combustion taking place above the bed.

The tests conducted with a bed having a static bed depth of some 230 mm with the overbed feed system does not yield the same defined trend as the shallow bed. This is partially due to the lack of sufficient data points and partially due to the expanded bed covering the feeder discharge aperture. The expanded bed height of these deeper beds exceeded 400 mm which clearly from Figure 11 submerges the pneumatic spreader. However, the pneumatic air stream did appear to result in improved distribution over that when operating with the underbed screw feeder since low excess air levels could be achieved without resulting in high levels of carbon monoxide in the exhaust gases. Of interest are the high bed ratings which were achieved with the fluidized bed operating sub-stoichiometrically and with the combustion process being completed above the bed.

Unlike the previous work into combustion (75), or as with the heat transfer studies of this thesis a correlation relating the combustion efficiency to the operating parameters has not been possible. This is due to the increase in the number of variables introduced such as the different types of coal feed systems employed, the variation in the fines content of the coal, the extraction of heat, operation at low excess air levels, and so on. However, it is evident that a larger proportion of heat is released above the bed during underbed feeding due to the poor distribution characteristics of the screw feeder cf Figure 42 and Section

3.5.2 whilst the improved distribution of the above bed feeder results in improved combustion efficiencies.

3.7 THE ENTRAINMENT OF PARTICULATES

Particles are entrained from the combustor vessel of the fluidized bed combustion rig and sampled isokinetically in the 600 mm diameter duct at the end of the combustor vessel cf Figure 21. The collected ash was graded and the carbon content of specific size fractions as well as for the sample as a whole were measured. The results of the grading analyses are presented in Table G12 of Appendix G.

All the ash gradings of Table G12 can be represented by three distinct bands as illustrated in Figure 44. These bands demonstrate that the grading of the resulting ash is affected by the fuel feed system, i.e. whether the above bed or underbed coal feeder is utilized, and further whether the duff coal or low fines coal is burnt. Included in Table G12 are the mass fractions of material which would be collected in the size intervals:

greater than 300 microns
from 150 to 300 microns
from 75 to 150 microns
and less than 75 microns.

The results can be approximated by the mean size grading curves for each of the bands as represented in Table 5.

TABLE 5 : Representative Size Gradings for each of the Bands Illustrated in Figure 44

Size Interval (microns)	Material Contained in Interval		
	Duff Coal	Low Fines Coal	
	Underbed Feed %	Overbed Feed %	Underbed Feed %
300	0	21	32
150 to 300	21	22	26
75 to 150	31	15	14
75	48	42	28

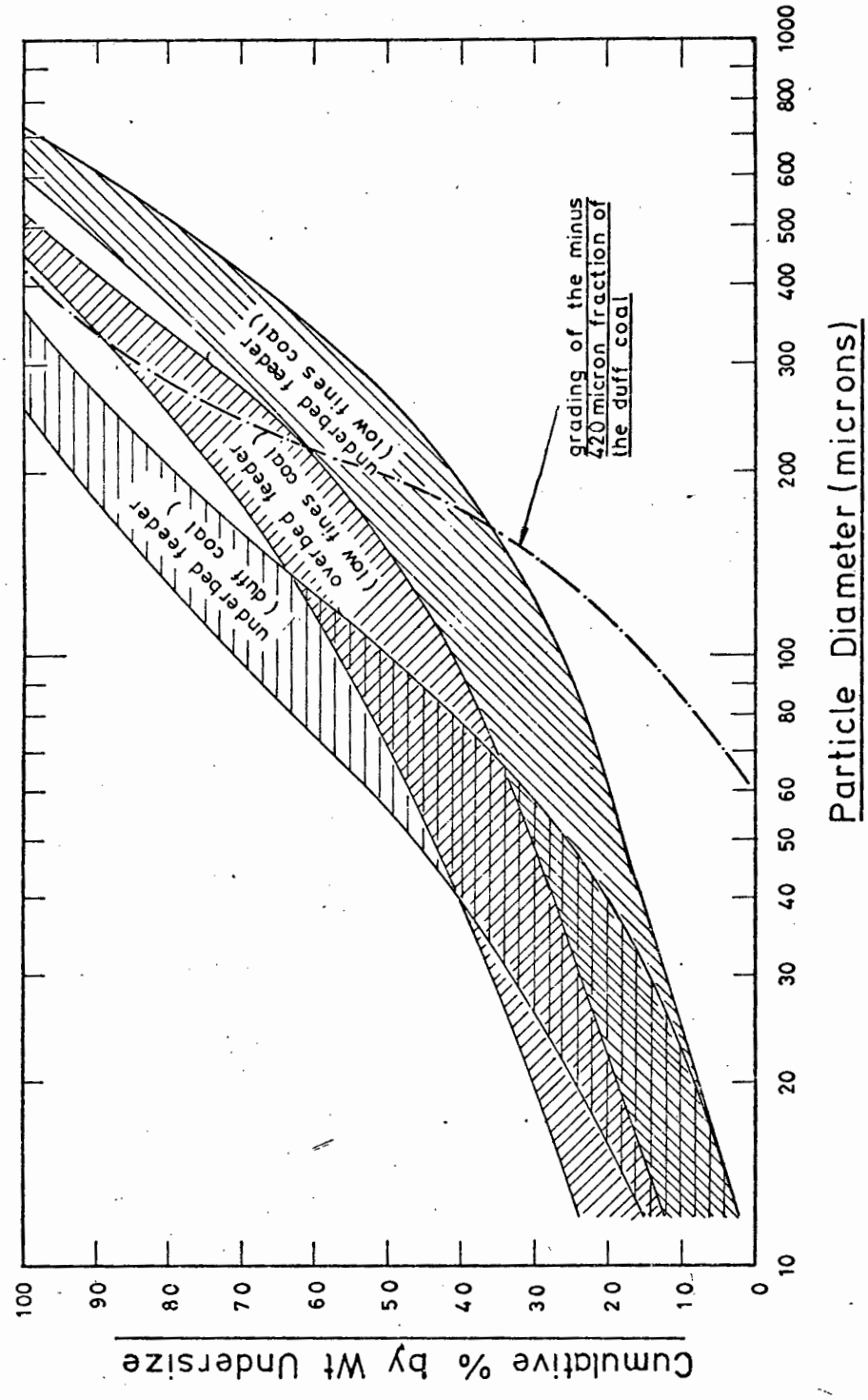

Figure 44 : Size gradings of the entrained ash.

It is evident from both Table 5 and Figure 44, that the combustion of the duff coal leads to the finest ash size grading. Further the form of the curve obtained when burning this coal is different to that obtained when burning the low fines coal utilizing either of the two coal feed systems. Clearly the grading of the incoming fuel causes this change. Examining the fuel gradings as represented in Figure C1 of Appendix C, it is seen that whilst less than 10% of the low fines coal is of a size of less than 1 mm, more than 50% of the duff coal passes through a 1 mm sieve. In addition, 29,5% of the duff coal is of size less than 420 microns and would therefore be readily entrained from the fluidized bed. The resulting size grading of the minus 420 micron size fraction of the duff coal has been drawn on Figure 44. It is seen that this grading curve is somewhat similar to the band obtained for the resulting ash when burning the duff coal.

It is clear, that when burning the duff coal, a large proportion of the fuel leaves the bed after releasing only a very small proportion of the energy associated with it. Considering the ash gradings obtained when burning the low fines coal by introducing the fuel by either the overbed or underbed coal feed system, it is seen that though the curves are of similar shape, the resulting particulates obtained from overbed feeding are significantly smaller than those obtained when utilizing the underbed screw feeder.

This difference is explained by the combination of the initial fuel size grading and the better distribution characteristics of the above bed pneumatic feed system. Considering the grading of the fuel, with only 3,3% of size less than 420 microns, almost all of the fuel enters the bed even when utilizing the above bed feed system. Whereas the pneumatic spreading of the coal leads to a uniform concentration of the fuel over the width of the combustor cf Appendix E, the underbed screw feeder results in an increased concentration of fuel in the area immediately adjacent to the coal feeder. An inadequate supply of oxygen in this region results in a

decrease in the combustion rate and consequently a decrease in the particle shrinkage. Therefore a larger concentration of larger particles are present in the inert bed material when utilizing the screw feeder than when employing the above bed feed system. Although these particles are concentrated in a reduced area when using the screw feeder, the ratio of the bed weight in this region to the effective entrainment area remains the same for both feed systems. Considering equation (5) reproduced below:

$$-\frac{1}{A}\cdot\frac{dm_i}{d\tau} = K'\frac{m_i}{M} \qquad (5)$$

it is evident that for the 'i th' size fraction, the rate of removal of material in this size fraction is dependent on the mass 'm_i' of this size fraction contained in the bed. Clearly the entrainment rate constant K^1 for a particular set of operating conditions is independent of the fuel feed system, and therefore the higher concentrations of the larger size fractions associated with the underbed feeder lead to coarser ash gradings.

A further consequence is the high carbon content of the coarse ash fraction and the low carbon content of the minus 75 micron fraction as illustrated in Table G12 of Appendix G. Clearly better combustion efficiencies are anticipated with the coal feed system resulting in a finer ash. This is true with the low fines coal, however, the high proportion of fines in the duff coal results in the production of a relatively fine ash with a higher carbon content.

CHAPTER 4

THEORETICAL MODEL

The extension of results obtained from an experimental or pilot plant for use in large scale equipment or even the comparison of results from one particular arrangement to another requires the formulation of a model to describe the process. Models are particularly useful in establishing the effect of individual parameters on the overall system whilst they can further be utilized in a description of the mechanism of the particular process. However the combustion of solid fuels within and above a shallow fluidized bed and the subsequent transfer of heat to cooling surfaces represents a complex system which is difficult to describe analytically in view of the large number of unknown parameters. Indeed, when considering the combustion phenomenon alone, Pyle (69) reports that models are quite often qualitative or at best semi-quantitative, whilst when some form of correlation is required to predict the performance in some other situation, the model may be empirical.

The theoretical analysis pertaining to the description of the shallow fluidized bed coal-fired fluidized bed combustor furnace has therefore been divided into three main sections. The first describes the heat transfer and combustion in the freeboard. A comprehensive model is presented based on the zone method of analysis (55) and is extended to a simplified analysis from which a characteristic equation is developed and presented to explain the heat transfer phenomenon occurring in the freeboard region above a shallow fluidized bed. The simplified analysis is further utilized as a means of establishing the combustion in the freeboard from the results obtained in Chapter 3. A description of the mechanism of the heat transfer to surfaces contained within the bed is presented in the second section. In particular, the packet theory of Mickley and Fairbanks (31) with the introduction of

a contact resistance as employed by Baskakov (34) is extended to formulate a description of the mechanism of the convective component of the heat transfer from a fluidized bed to an immersed surface. Finally an explanation of both combustion and entrainment is presented based largely on previous work (75) performed on a 300 mm diameter combustor.

4.1 HEAT TRANSFER AND COMBUSTION IN THE FREEBOARD

The freeboard region above the fluidized bed forms the second component of the shallow fluidized bed combustor furnace. This region can therefore be considered as a separate furnace deriving its heat input from the hot gases leaving the fluidized bed at the bed temperature as well as from the combustion of gases and particulates above the fluidized bed. The enclosing water cooled walls of the furnace present an effective heat sink for cooling the gases whilst the upper surface of the fluidized bed forms a further heat source transferring heat to the volume of gas in the region above as well as to the enclosing walls after partial heat absorption by the gas. These basic processes occurring in a fluidized bed combustor furnace have been illustrated in Figure 1.

4.1.1 The Zone Method of Analysis

The different methods of furnace analysis have been discussed in Section 1.3.2. The symmetry of the vertical flue fluidized bed test facility, however, lends itself to the application of the zone method of analysis as originally presented by Hottel and Cohen (55). The method has further been developed by Hottel and Sarofim (56) and the nomenclature devised by these authors to describe the radiant heat transfer has been adopted. Prior to the development of the zone method of analysis a description of the fundamental processes is described.

a) A Description of the Fundamental Radiative Heat Transfer Relationships

Although much of the information presented in this sub-section is fundamental to radiative heat transfer it is useful to present these concepts with a view to obtaining a clear understanding of the final model. The enclosing surface and upper surface of the bed have been assumed to behave as grey bodies, i.e. they absorb and emit radiation monochromatically. Therefore the total absorptivity and hence the total emissivity will be independent of the spectral energy distribution of the incident radiation. This enables the emissivity to be used in substitution for the absorptivity even though the emitted and absorbed radiation does not take place at the same temperatures. Although the body of gas may be considered to be grey for most of the relationships, an allowance has been made to enable a difference in the absorbed and emitted radiation to be made where these take place at different temperature levels.

The direct radiative exchange between a pair of surfaces A_i and A_j separated by a non-absorbing or reflecting medium can be represented by

$$Q_{i-j} - Q_{j-i} = Q_{i\rightleftharpoons j} = \overline{s_i s_j} \cdot \sigma \cdot (T_i^4 - T_j^4)$$

where $\overline{s_i s_j}$ is the direct radiative exchange area. In the event of radiative exchange being between two black bodies, the direct radiative exchange area is simply the product of one of the areas and the form factor as described in other texts. However this approach will not be adopted in this thesis.

Should reflection from other surfaces contribute to the transport of radiant energy to surface A_j originating from A_i, then the use of a simple direct radiative exchange area is no longer valid. The radiative heat transfer between two surfaces can however be similarly represented by defining the total exchange area $S_i S_j$ such that

$$Q_{i-j} - Q_{j-i} = Q_{i\rightleftharpoons j} = \overrightarrow{S_i S_j} \cdot \sigma \cdot T_i^4 - \overrightarrow{S_j S_i} \cdot \sigma \cdot T_j^4$$

but since each surface is assumed to be grey with its greyness independent of temperature, we can write

$$Q_{i \rightleftharpoons j} = \overline{S_i S_j} \cdot \sigma \cdot (T_i^4 - T_j^4)$$

However, in order to evaluate the total exchange areas, the radiation from each surface must now be considered as the sum of the emitted radiation and the reflected radiation. This is illustrated in Figure 45.

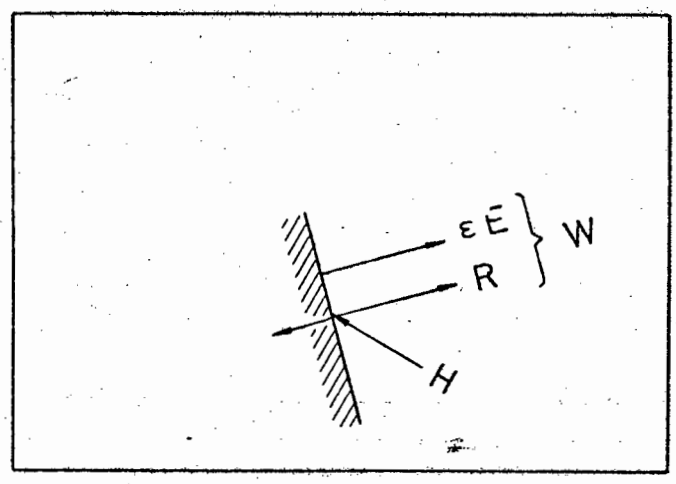

Figure 45 : Radiant flux densities at a surface element.

From Figure 45 it is seen that the leaving flux density, W, is composed of two parts. The first includes the black body emissive power, E, (or $E=\sigma T^4$) and the reflected flux density R which is due to partial reflection of the incident flux density H. From Figure 45 it is evident that

$$W = \varepsilon \cdot E + R \qquad (57a)$$

$$= \varepsilon \cdot E + \rho \cdot H \qquad (57b)$$

From equation (57), Hottel and Sarofim (56, p 75) derive the integral equation of radiative exchange for the total incident flux density arriving at surface A_j as :

$$\frac{W_j - \varepsilon_j \cdot E_j}{\rho_j} = \int_{A_i} W_i \cdot \frac{\partial^2 s_i s_j}{\partial A_i \cdot \partial A_j} \cdot dA_i \qquad (58)$$

For a system of finite areas or zones, equation (58) becomes

$$A_j \cdot \frac{W_j - \varepsilon_j \cdot E_j}{\rho_j} = \sum_i W_i \cdot \overline{s_i s_j} \qquad (59)$$

For a system of 'n' zones, 'n' equations such as that given by equation (59) may then be solved simultaneously for the 'n' leaving flux densities i.e. the W_i's. In order to do this, equation (59) is written in the more convenient form given by equation (60).

$$\sum_i \left(\overline{s_i s_j} - \delta_{ij} \cdot A_j / \rho_j \right) \cdot W_i = - \frac{A_j \varepsilon_j}{\rho_j} \cdot E_j \qquad (60)$$

where δ_{ij} is the Kronecker delta and is defined as :

$$\delta_{ij} = 0 \qquad \text{if } i \neq j$$

$$\delta_{ij} = 1 \qquad \text{if } i = j$$

Once equation (60) has been solved for the leaving flux densities (W_i's) the total exchange areas can be determined from equation (61)

$$\overline{S_i S_j} = \frac{A_i \varepsilon_i}{\rho_i} \cdot \left({}_jW_i / E_j - \delta_{ij} \cdot \varepsilon_j \right) \qquad (61)$$

Now in a furnace system, which is made up of a number of surface zones, enclosing a number of gas zones, the radiative properties and in particular the absorption and emittance of the gas body have to be considered in evaluating the surface leaving flux densities.

In a similar manner, total gas-to-surface, and total gas-to-gas exchange areas may be defined. The system of 'n' simultaneous equations represented by equation (60) then becomes

$$\sum_i \left(\overline{s_i s_j} - \delta_{ij} \cdot A_j / \rho_j \right) \cdot W_i = - \frac{A_j \cdot \varepsilon_j}{\rho_j} \cdot E_j - \overline{g s_i} \cdot E_g \qquad (62)$$

where only a single gas zone has been considered. For a system made up of a number of gas zones, equation (62)

becomes (56 p. 369)

$$\sum_i \left(\overline{s_i s_j} - \delta_{ij} \cdot A_j / \rho_j \right) \cdot W_i = - \frac{A_j \cdot \varepsilon_j}{\rho_j} \cdot E_{s,j} - \sum_i \overline{g_i s_j} \cdot E_{g,i} \qquad (63)$$

Equations (62) and (63) have employed the use of direct gas-to-surface (gs) and gas-to-gas (gg) exchange areas. These exchange areas are dependent upon both the relative orientation of the surface and gas zones as well as on the gas absorption coefficient.

In general, the gas temperatures are unknown, whilst some or all of the surface temperatures may be known. The problem is solved by combining the radiative interchange with an energy balance on each volume element which results in the unknown temperatures being evaluated. Equation (63) can be solved for the leaving flux densities (W_i's) from which the relevant gas and surface total exchange areas (SS's, GS's and GG's) can be evaluated. Once the relevant temperatures and exchange areas have been evaluated, an energy balance on each surface element yields the total heat transferred at each of these surface zones.

However, prior to evaluating these energy balances means must be obtained for describing the gas absorption coefficients as well as the definition of the effective radiating gas volume.

b) <u>The Radiative Properties of the Enclosed Gas</u>

The emissivity of a real gas containing substantial amounts of water vapour and carbon dioxide is usually represented by a grey gas model made up of one clear gas and a number of grey gas components (56), (59), (62), (143). The method represents an exponential curve fitting technique with the number of grey gas components being dependent upon the optical thickness, i.e. the product of the partial pressure and mean beam length ($p \cdot L$). The emissivity is also dependent upon the temperature of the gas and the ratio of water vapour to carbon dioxide partial pressures

(i.e. p_w/p_c). Almost all of the overall performance test results have been obtained when burning the coal in an air dried condition. Assuming a surface moisture content of 2,5%, the combustion of both the duff and the low fines coal result in a low p_w/p_c ratio of about 0,5. In zoning the test facility the maximum path length will not be greater than 1,0 m and the resulting product of the total partial pressure and the mean beam length will not exceed a value of about 0,2 m.atm.

A one clear and two grey gas model was found to adequately represent the gas emissivity over the temperature, partial pressures and mean beam lengths anticipated. The derivation of the compound grey gas model from the emissivity charts originally presented by Hottel (58) is presented ir Appendix H and is represented by equation (64).

$$\varepsilon_g = \sum_{i=1}^{3} a_{g,i}\left(1 - exp \{ - k_i \cdot (p_w + p_c) \cdot L \} \right) \qquad (64)$$

where

$$a_{g,i} = b_{o,i} + b_{1,i}\, t_g \qquad (65)$$

for which Table 6 is presented for determining the coefficient of equations 64 and 65.

TABLE 6 : Table of coefficients for the determination of the gas emissivity represented as a compound grey gas model

i	gas absorption coefficient (k) 1/(atm.m)	b_o	$-b_1$ 1/°C
1	0,00	0,417	$0,168.10^{-3}$
2	1,405	0,416	$-0,102.10^{-3}$
3	22,49	0,167	$-0,0664.10^{-3}$

From equations (64) and (65) it is seen that the temperature dependence of the gas emissivity is accommodated by the weighting factors, a_i, whilst the gas absorption coefficients are assumed to be constant. This is particularly useful when applying the zone method of analysis, as the total exchange areas need be determined only once, i.e. for the specific absorption coefficient. This results in a considerable reduction in computing time.

c) Characterization of the Particulates

The greater proportion of the ash and the unburned carbon is entrained in the gases leaving the bed, with a small fraction accumulating in the fluidized bed. Isokinetic sampling for particulates in the flue gases indicated that at all times the entrained ash represents over 90% of the total ash flow with only a very small fraction remaining in the bed. The radiative contribution of this dispersed cloud of solids can be significant. The formation of soot is assumed to be low, and hence only radiation from the entrained particulates is considered. These particles can be regarded as grey radiators (59) (61, ch. 3), (62) with an absorption coefficient given in terms of the particle size and concentration by equation (66).

$$k_p = \frac{1}{4} C_p \cdot S_p \qquad (66)$$

In addition to the absorption coefficient, allowance can be made for the ability of the particle to scatter radiation. However this complication has not been included in the radiative model developed in this thesis. Therefore an absorption coefficient for the cloud of particles can be evaluated from a knowledge of the particle concentration in the flue gas and the mean harmonic diameter obtained from the particle size analysis. It is normal to assume that the radiation from these particulates can be approximated by a three grey-gas model, and further that the weighting factors employed for the gas radiation model apply for particulate radiation.

Therefore the emissivity of a cloud of particles can be written as:

$$\varepsilon_p = \sum_i a_{p,i}(t_g)\cdot(1 - exp\{ - k_{p,i}\cdot L \}) \qquad (67)$$

and assuming

$$a_{p,i} = a_{g,i}$$

then the combined emissivity of a gas-particulate system is given by

$$\varepsilon_{g,p} = \sum_{i=1}^{3} (b_{o,i} + b_{1,i}\cdot t_g)\cdot(1 - exp\{ - K_i\cdot L \}) \qquad (68)$$

where

$$K_i = k_{p,i} + k_{g,i}\cdot(p_w + p_c) \qquad (69)$$

Equations (68) and (69) model the flue gas emissivity of the resulting gas and particulate system in the freeboard of a fluidized bed combustor burning the duff or low fines coal having the analyses presented in Appendix C. The effect of introducing an absorption coefficient for the particulates by addition to the gas absorption coefficient results in the one-clear-gas two-grey-gas model being replaced by a three-grey-gas model. Thus the radiation 'window' afforded by the clear gas, i.e. one in which the absorption coefficient is zero, no longer exists.

d) Formulation of the Gas and Surface Zones

The freeboard area of the fluidized bed combustion test rig has been divided into nine surface zones and seven gas zones as represented in Figure 46. The seven gas zones are formed as cylinders having a height of 500 mm and a diameter of 1 000 mm. Each of these in turn is surrounded by a cylindrical surface zone of similar dimensions. The upper surface of the fluidized bed forms one boundary of the freeboard and has been modelled as a flat circular surface zone having an emissivity of 0,85 cf Section 3.2.1 whilst the conical surface at the upper end of the flue is considered as a similar flat water cooled surface of 1 000 mm diameter. The water cooled surfaces

enclosing the gas zones are assumed to have an emissivity of 0,70 (58). Tables H3, H4 and H5 contain the direct exchange factors, i.e. assuming a non absorbing medium within the freeboard, whilst Tables H6, H7 and H8 contain the total exchange factors for an absorption coefficient of 0,5 m^{-1}.

e) The Energy Balance

In the furnace defined by Figure 46, all the surface zone temperatures are specified and the gas zone temperatures and heat transfer rates at the surface zones have to be predicted. This requires the solution of the energy balance over each of the seven gas volume zones. A total energy balance over the seven volume zones is then required which results in an iterative procedure having to be employed to evaluate the gas temperatures in each of the volume zones. The energy balance on the i th gas zone can be represented by equation (70).

$$\begin{bmatrix}\text{radiated}\\ \text{heat from}\\ \text{all gas zns}\\ \text{to gas}\\ \text{zone } i\end{bmatrix} + \begin{bmatrix}\text{radiated}\\ \text{heat from}\\ \text{all surface}\\ \text{zns to gas}\\ \text{zone } i\end{bmatrix} + \begin{bmatrix}\text{net}\\ \text{decrease}\\ \text{in sens-}\\ \text{ible ht}\\ \text{in gas}\end{bmatrix} + \begin{bmatrix}\text{heat}\\ \text{release}\\ \text{in}\\ \text{zone } i\end{bmatrix} = \begin{bmatrix}\text{heat}\\ \text{rad-}\\ \text{iated}\\ \text{from}\\ \text{zn } i\end{bmatrix} + \begin{bmatrix}\text{convec-}\\ \text{tive}\\ \text{ht loss}\\ \text{in}\\ \text{zone } i\end{bmatrix} \qquad (70)$$

Which for the i th gas zone can be represented by :

$$\sum_{j=1}^{7} \overline{G_j G_i} \cdot \sigma \cdot T_{g,j}^4 + \sum_{j=1}^{9} \overline{S_j G_i} \cdot \sigma \cdot T_{s,j}^4 + \dot{m}_g \cdot c_p(T) \cdot (T_{g,i+1} - T_{g,i-1})$$

$$+ Q_{lib,i} = \sum_{n=1}^{3} 4\, a_{g,n}(T) \cdot K_n \cdot V_i \cdot \sigma \cdot T_{g,i}^4 + h_i \cdot A_i \cdot (T_{g,i} - T_{s,i}) \qquad (71)$$

Seven simultaneous equations representing the seven heat balances each similar to equation (71) can be formed. By evaluating the various known quantities, and grouping the required unknown temperatures a system of equations represented in matrix format as equation (72) is formed.

$$\begin{bmatrix} a_{11} & a_{12} & \cdots & a_{17} \\ a_{21} & a_{22} & \cdots & a_{27} \\ \vdots & \vdots & & \vdots \\ a_{71} & a_{72} & \cdots & a_{77} \end{bmatrix} \cdot \begin{bmatrix} T_{g1}^4 \\ T_{g2}^4 \\ \vdots \\ T_{g7}^4 \end{bmatrix} + \begin{bmatrix} b_{11} & b_{12} & \cdots & b_{17} \\ b_{21} & b_{22} & \cdots & b_{27} \\ \vdots & \vdots & & \vdots \\ b_{71} & b_{72} & \cdots & b_{77} \end{bmatrix} \cdot \begin{bmatrix} T_{g1} \\ T_{g2} \\ \vdots \\ T_{g7} \end{bmatrix} + \begin{bmatrix} c_1 \\ c_2 \\ \vdots \\ c_7 \end{bmatrix} = 0 \qquad (72)$$

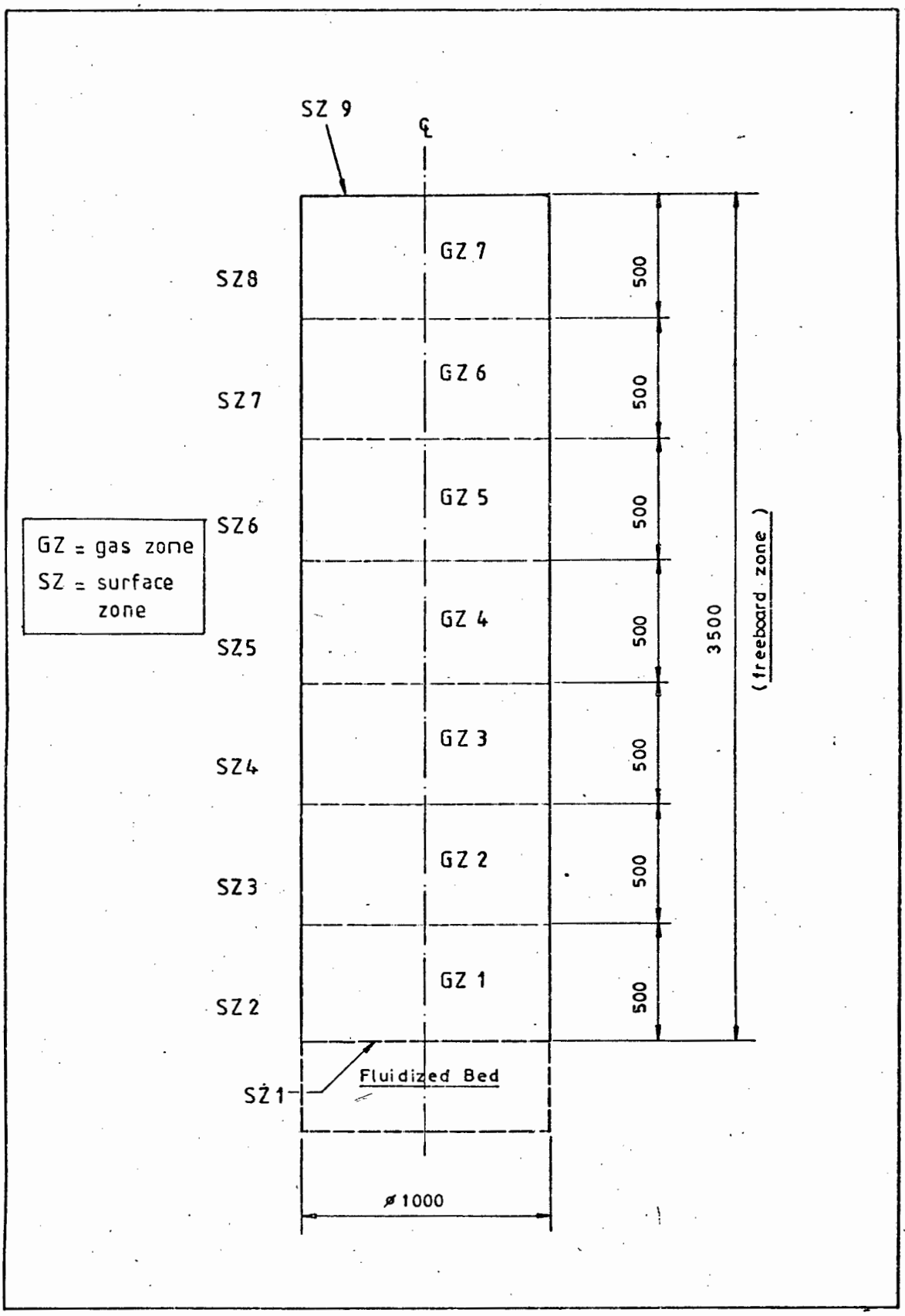

Figure 46 : Diagram to illustrate the zoning of the freeboard zone of the 1000 mm diameter test rig into nine surface and seven gas zones.

Each of the terms of the coefficients matrices i.e. a_{11}, b_{53}, c_7 and so on, have no real physical significance but consist of the relevant total exchange areas, convective heat transfer coefficients etc. pertaining to the particular operating conditions.

Once the gas temperatures have been evaluated, a heat balance is performed on each of the surface zones to evaluate the net heat flow. In a similar manner to that used for determining the heat balance over the gas zone, the heat balance over the surface zone i can be represented by :

$$\left[\begin{array}{c}\text{radiated heat from all gas zns to surface zone } i\end{array}\right] + \left[\begin{array}{c}\text{radiated heat from all surface zns to surf zone } i\end{array}\right] + \left[\begin{array}{c}\text{heat absorpn by convection to zone } i\end{array}\right] - \left[\begin{array}{c}\text{heat radiated from surface zone } i\end{array}\right] = \left[\begin{array}{c}\text{net heat absorbed by surface zone } i\end{array}\right] \qquad (73)$$

which for the i th surface zone can be represented by :

$$\sum_{j=1}^{7} \overline{G_j S_i} \cdot \sigma \cdot T_{g,j}^4 + \sum_{j=1}^{9} \overline{S_j S_i} \cdot \sigma \cdot T_{s,j}^4 + h_i \cdot A_i \cdot (T_{g,i} - T_{s,i}) - A_i \, \varepsilon_i \cdot \sigma \cdot T_{s,i}^4 = Q_{s,i} \qquad (74)$$

f) Design of the Computer Programme

The heat transfer and combustion model for the freeboard is based on the zone method of analysis with seven gas zones and nine surface zones. Although resort has to be made to a high speed computer, the storage and calculation requirements are fairly moderate and therefore the use of a small desk top computer with a 16 K memory was utilized rather than the larger UNIVAC computer at the university. However in view of the fairly large matrix requirements and data manipulation, the core space of the smaller machine was rapidly consumed and chaining of the programmes had to be adopted. A total of ten chained programmes had to be employed in which the relevant programmes contained on a tape are sequentially introduced and deleted with only those details required for further use being retained in the memory. This results in a rather cumbersome system in which the tape is continually being loaded and rewound. However the easier access to and use of the smaller

machine outweighed the simpler programming techniques which could have been employed on the larger computer.

A summary of the basic chained computer modules is illustrated in Figure 47. Direct and total exchange areas are determined for two absorption coefficients defined by the three-grey-gas model utilized for evaluating the gas emissivity. The third absorption coefficient is so large that the radiation can be considered to take place as a diffusion process as the optical thickness i.e. the product of the absorption coefficient and the mean beam length of the zone exceeds 3,0 (56 p. 356). With this optically dense component of the three-grey-gas model, total exchange areas need not be evaluated as the radiation exchange takes place between adjacent zones within a small layer common to the two zones.

From Figure 47 it is seen that the first six chained modules are utilized for evaluating the exchange areas associated with the smaller two absorption coefficients. The advantage of accommodating the temperature dependence of the emissivity in the weighting factors rather than in the absorption coefficients is evident from the large computational effort required in evaluating the exchange areas for the absorption coefficients. Once these have been determined, the first six modules need not be accessed again, unless changes in the absorption coefficients are envisaged. Referring to Figure 47 it is seen that the input manipulation, the heat balance and iterative procedure, and output manipulation are contained in the following three modules whilst the overall control of the entire suite of programmes is contained in the final programme module.

The flow diagram of the entire suite of programmes is presented in Figure 48. Details of the general calculations undertaken are presented in Appendix D, whilst more details relating specifically to the combustion and radiation are included in Appendix H.

Referring to Figure 48, it is seen that in the preliminary programme module the geometry of the furnace is defined. Gas

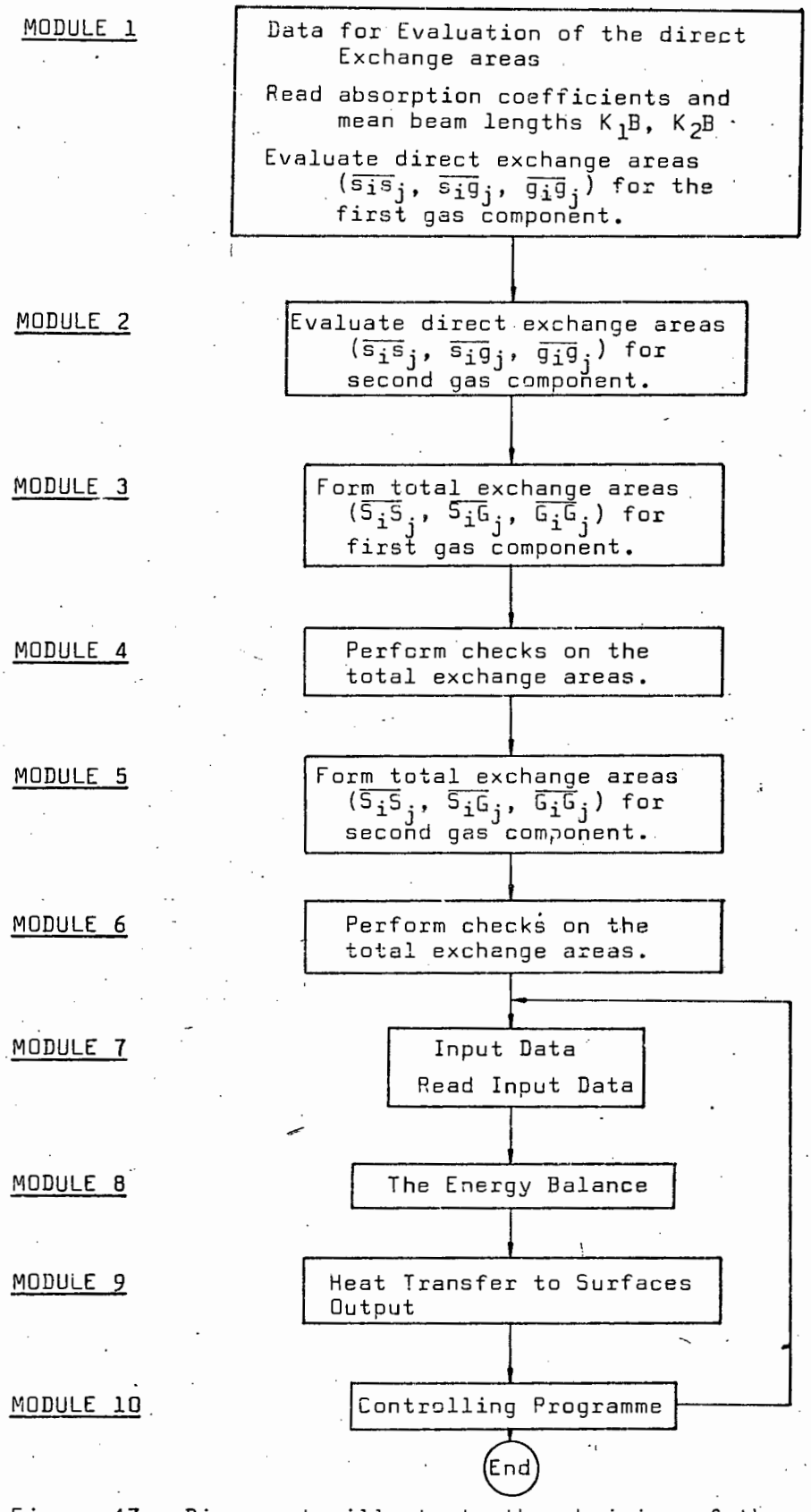

Figure 47 : Diagram to illustrate the chaining of the programmes to enable the above bed heat transfer and combustion model to be performed on a computer with a small memory core.

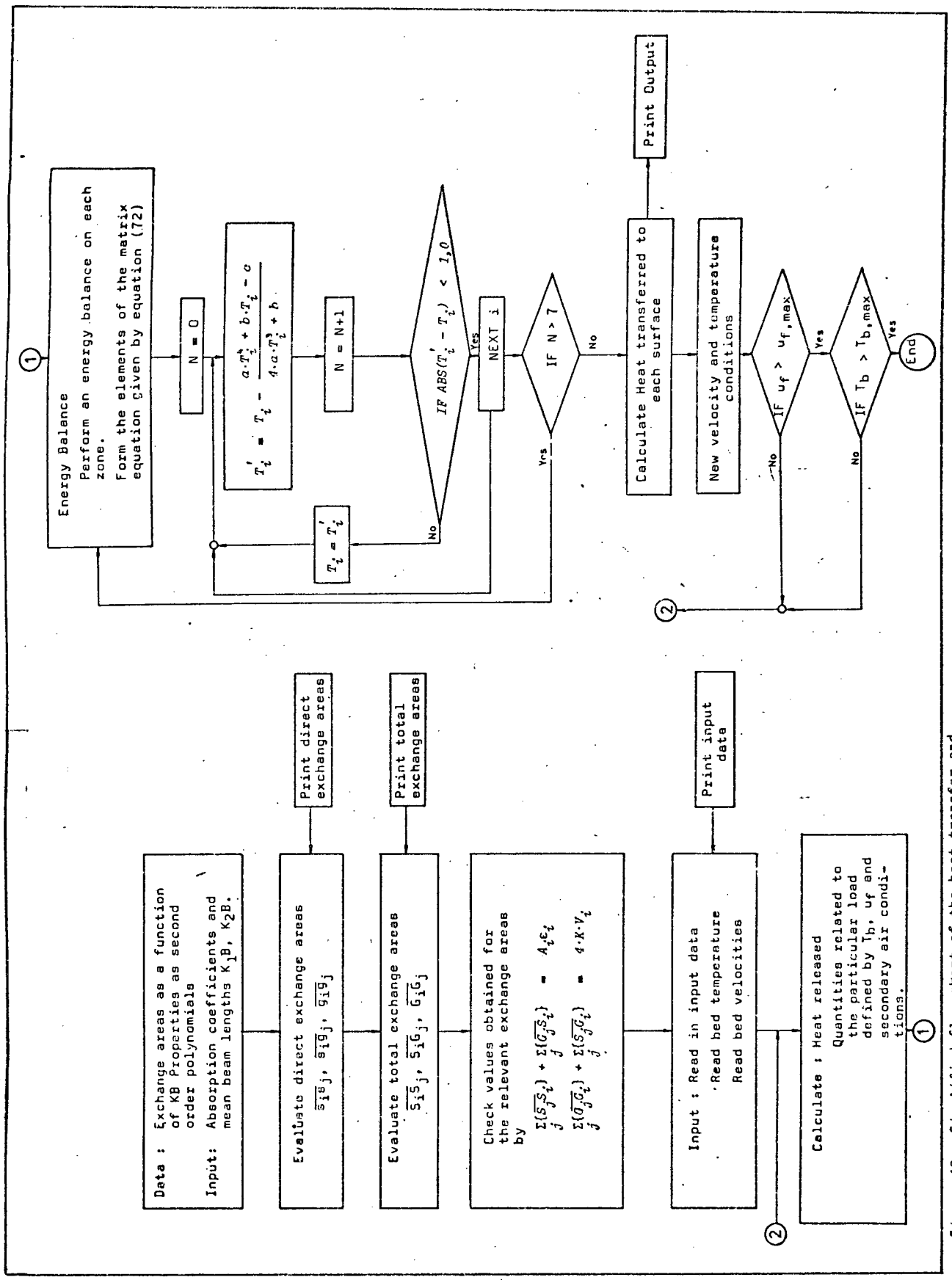

Figure 48 : Simplified flow chart of the heat transfer and combustion model to predict the performance in the freeboard.

properties have been evaluated for the gas composition which would arise from the combustion of the coal when burning with 25% excess air. The resulting gas components are contained in Table D1 of Appendix D. The flue gas properties have been approximated by second order polynomials for a range in temperature from 400°C to 1400°C. The polynomials are all in a form given by equation (75) which refers to the mean specific heat of the gas

$$c_{p_m} = a + b \cdot T + c \cdot T^2 \qquad (75)$$

The direct interchange areas for cylindrical enclosures have been tabulated as a function of the optical thickness (56, ch 7). These relationships have been approximated by a combined exponential, and polynomial curve fitting technique to yield a direct exchange area in the form of equation (76) which is based on a least squares analysis

$$(\overline{s_i s_j} / B^2) = exp \{ a + b \cdot (KB) + c \cdot (KB)^2 \} \qquad (76a)$$

$$(\overline{g_i g_j} / (KB)^2 \cdot B^2) = exp \{ a + b \cdot (KB) + c \cdot (KB)^2 \} \qquad (76b)$$

$$(\overline{g_i s_j} / KB \cdot B^2) = exp \{ a + b \cdot (KB) + c \cdot (KB)^2 \} \qquad (76c)$$

Thirty six relationships similar to the equations represented above had to be generated to define the direct exchange areas. On supplying the three absorption coefficients as input data, the total exchange areas can be established from equation (61) for each of the two smaller coefficients and by considering the radiation to take place by diffusion for the substantially larger third absorption coefficient. The three total exchange areas are then combined in accordance with the weighting factors given in Table 6 to establish the gas emissivity at the particular temperature.

A shortcoming of the procedure lies in the system not taking into account local variations in the absorption coefficient. However, a higher absorption coefficient immediately above the bed should exist in view of the higher concentration of particles in this region. Stott and Garrod (144) used varying radiation intensities to overcome this, whilst Johnston and Beer (145)

suggest that the emissivity weighting factors (a_{gi}) could be adjusted. Hottel and Sarofim (56, p 374) proposed the use of an average absorption coefficient based on the attenuation between zones and embodying the respective direct exchange areas and allowing for the absorption coefficients in the emitting and absorbing zones. In view of the absorption coefficient differing in the first gas zone only, it was decided to allow for this variation by adjustments to the resulting gas emissivity in a manner similar to that proposed by Johnston and Beer (145).

Once the total exchange factors have been evaluated the remaining input data is supplied. In Appendix D, a relationship has been derived between the heat liberated in the bed and the superficial gas velocity and gas density. For the duff and low fines coal this relationship can be represented by equation (77).

$$\bar{Q}_{lib,b} = 3020 \cdot \rho_f \cdot u_f / (\lambda + 0,0909) \qquad (77)$$

As the density of the gas is directly related to the bed temperature, it is evident that the heat liberated in the bed is dependent upon the superficial gas velocity, the bed temperature and the excess air factor. Thus by specifying these three parameters, the output of the furnace can be determined.

Different conditions can therefore be specified by varying the superficial gas velocity and the bed temperature for constant excess air conditions. These two parameters have therefore been included in two loops in the programme to enable complete furnace performance details to be evaluated under the different bed operating conditions. In particular various gas emissivities can be provided as input as well as varying degrees of secondary combustion above the bed.

For each bed operating condition i.e. bed temperature and velocity, the resulting gas temperatures are obtained by solving the system of equations represented by equations (70)

to (72). From the equations containing seven unknown temperatures, each equation is seen to contain each temperature in two forms i.e. raised to the fourth power, and as a simple temperature multiplied by a constant coefficient. An iterative technique has to be employed. Hottel and Sarofim (56 p. 105) suggest the use of a Gauss-Seidel iterative procedure for solving the equations. It is evident that the diagonal element in each row is dominant, and by assuming temperatures for the remaining elements, the temperature of the i th row is solved iteratively (146). The iterative equation has the form given by equation (78) which is effectively a modified Newton-Raphson approach to speed up the convergence.

$$T_i = T_i - \frac{a_{ii} \cdot T_i^4 + b_{ii} \cdot T_i - c'}{4 \cdot a_{ii} \cdot T_i^3 + b_{ii}} \qquad (78)$$

The iteration for each temperature is stopped when the difference between the current (T_i) and the revised (T_i') temperature do not differ by more than $1^{o}C$. After each of the seven temperatures has been evaluated by equation (78) the procedure is repeated until no further iteration is necessary. This calculation procedure is illustrated in Figure 48.

Once the gas temperatures have been evaluated the heat flow to the various surface elements can be determined from equation (74).

g) Application of the Model

The model enables the combustion and heat transfer in the above bed freeboard region to be studied as a function of :

(i) the absorption coefficient

(ii) the extent of combustion above the bed.

Although a number of other parameters can be investigated, it is the effect of the above two which have the most significance in the description of shallow fluidized bed combustors. Clearly,

the excess air factor will have an effect, however in most practical systems it is of importance to operate at as low an excess air level as is possible. Indeed, the most usual level of excess air which would be employed in a shallow fluidized bed steam generator would be of the order of 25%.

Initially the gas emissivity in the first gas zone was increased by 10% over the remaining gas zones. This was undertaken in order to assess the effect on the entire freeboard zone as a result of the increased particle density in this region. However the overall result was not materially affected and in view of the rather arbitrary increase in emissivity this was dispensed with for the further analyses. Indeed, the increased emissivity in this region could easily be described as a "microscopic" as opposed to a "global" phenomenon when related to the upper freeboard region.

A series of curves presenting the exhaust gas temperature as a function of the superficial gas velocity in the bed at constant bed temperature levels is illustrated in Figures 49 and 50. Both have been drawn for excess air levels of 25%. However the relationships of Figure 49 have been drawn assuming no contribution to the radiative heat transfer due to the particulates in the freeboard gases. This results in higher freeboard gas temperatures than those obtained from Figure 50 where a fairly substantial contribution to the gas absorption coefficient due to heat transfer from the particulates has been assumed.

In order to illustrate the effect of secondary air combustion, the exhaust gas temperature has once again been drawn as a function of the superficial gas velocity in Figure 51 but for the case in which 30% of the total heat released takes place in the freeboard and at a bed temperature of 950^{o}C. A number of test results obtained from Table G11 of Appendix G have also been plotted in Figure 51. These data points correspond to conditions similar to those for which the curves in Figure 51 have been drawn. Clearly, for similar fractional combustion rates in the freeboard,

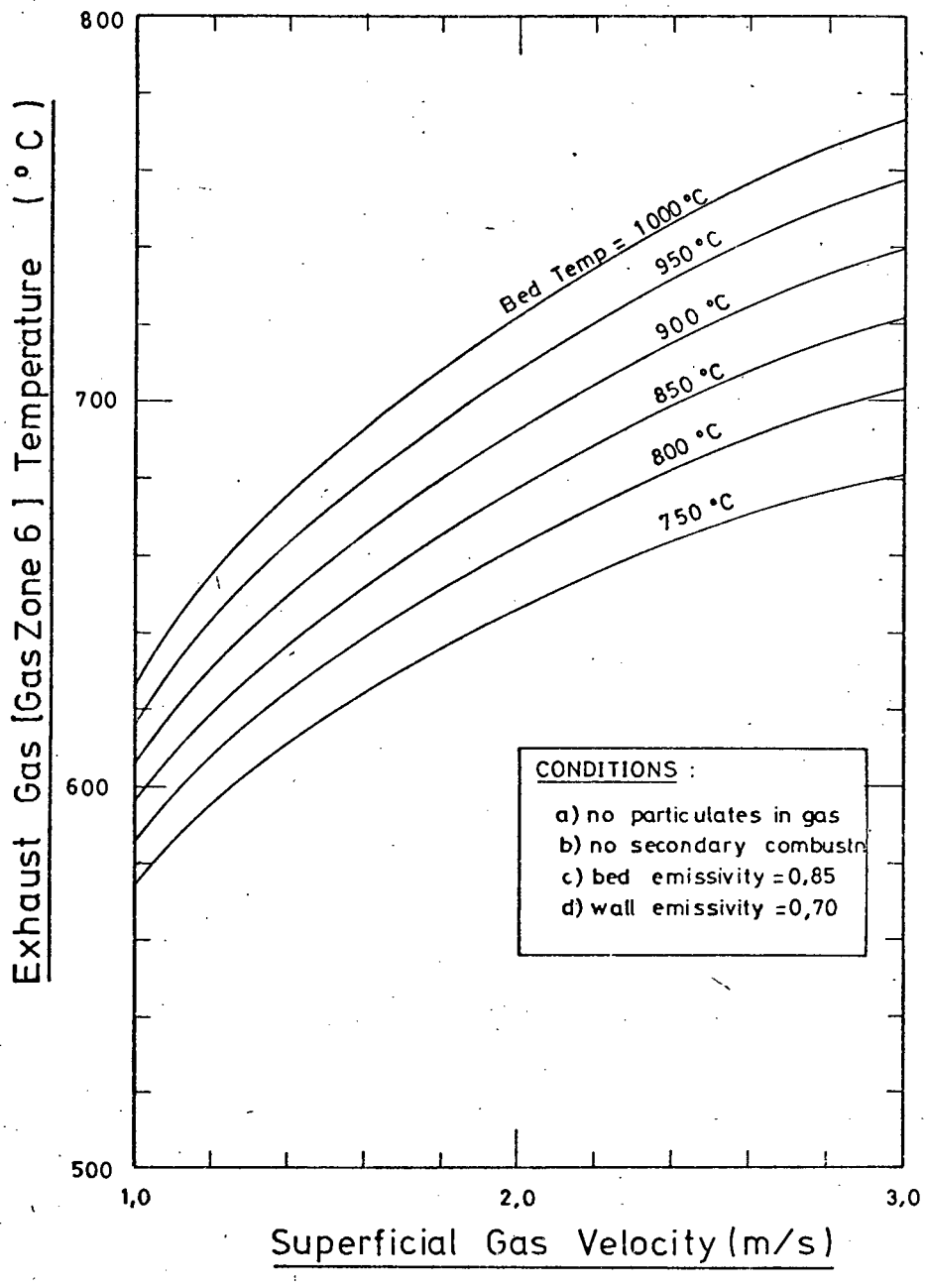

Figure 49 : Exhaust gas temperature as a function of the bed superficial gas velocity for constant bed temperatures at an excess air level of 25% and neglecting the contribution to the heat transfer due to the particulates in the freeboard gases.

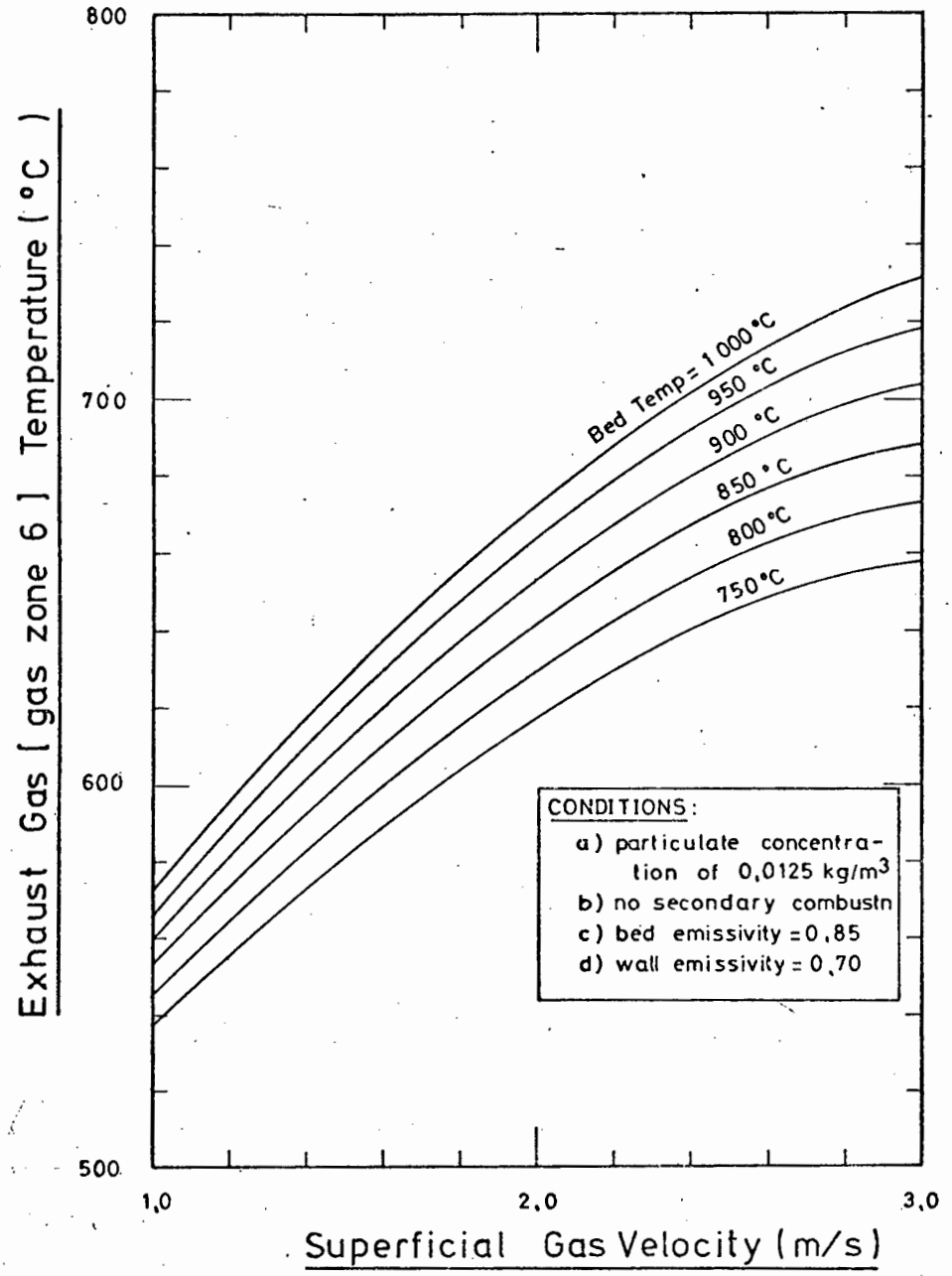

Figure 50 : Exhaust gas temperature as a function of the bed superficial gas velocity for constant bed temperatures at an excess air level of 25% and including a substantial contribution to the radiant heat transfer by the particulates in the freeboard gases.

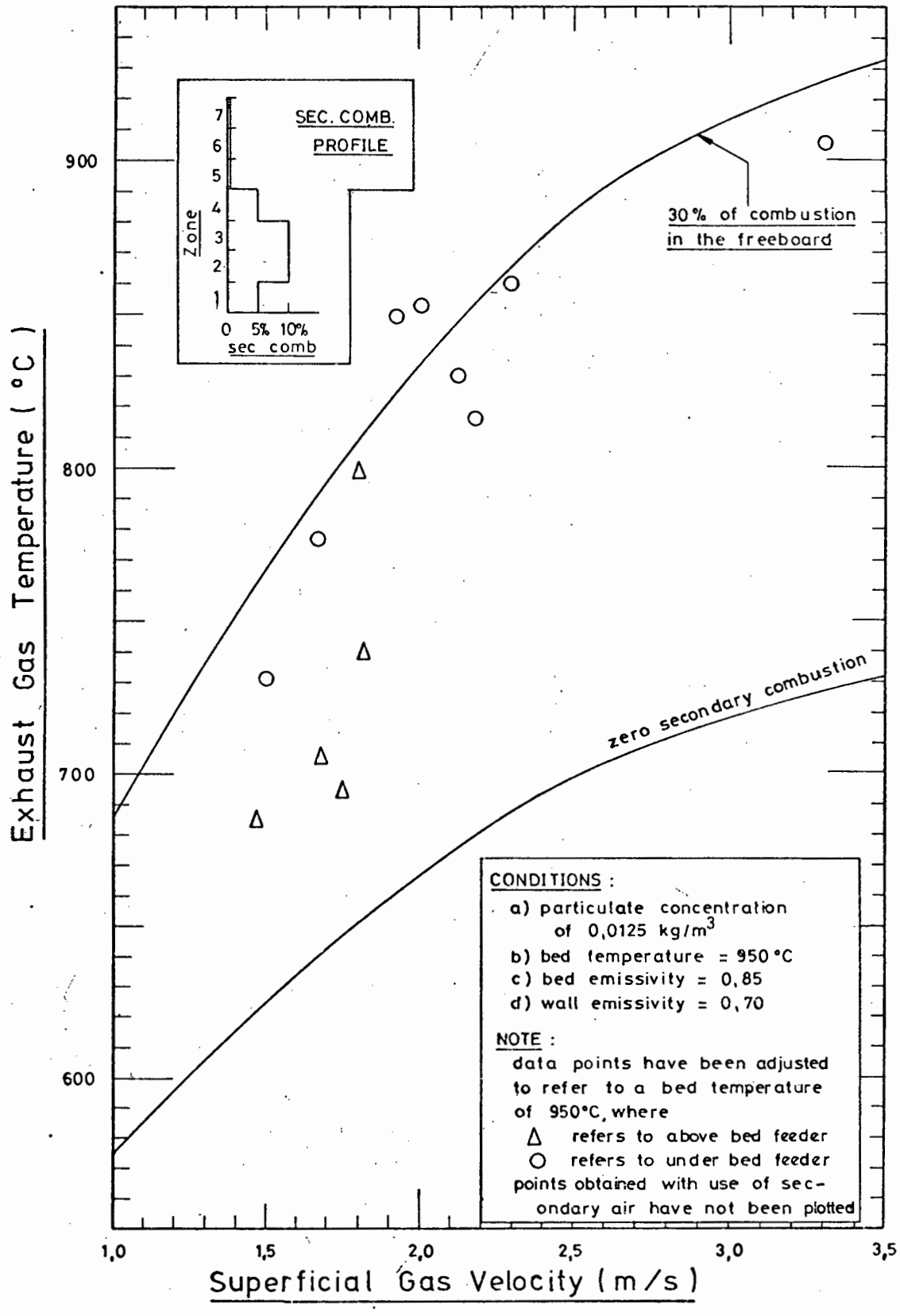

Figure 51 : The effect of combustion in the freeboard on the exhaust gas temperature and a comparison of data obtained on the test rig under similar bed operating conditions.

i.e. the ratio of the heat released in the freeboard to the total heat liberated, increasing the fluidizing velocity at a constant bed temperature will result in an increase in the entrained particulates. This in turn will lead to higher heat transfer rates and a subsequent decrease in the predicted exhaust gas temperature from the curves of Figures 49 to 50. This implies a shallower characteristic. However the data points in Figure 51 imply a steeper characteristic than that predicted by the model. For this to be so, the rate of combustion above the bed must increase as the superficial gas velocity increases. The nature of this increase and the effect of overbed and underbed feeding is discussed in more detail in section 4.1.2.

However, another objective in performing a detailed analysis on the freeboard region of the furnace of a fluidized bed combustor is to be able to assess the heat flux rates in this region. The predicted heat flux profiles together with measured data points under similar operating conditions are illustrated in Figure 52 both with and without combustion above the bed. From both the theoretical curves and the empirical curves, it is evident that the heat flux in the freeboard is substantially lower than the heat flux rates in the bed zone. From the experimental results illustrated in Figure 52 a small difference in the heat flux is noted between the two curves in the fluidized bed due primarily to the difference in bed temperature. The difference between the two curves in the above bed region is more marked than in the fluidized bed zone in view of the secondary combustion reaction taking place in the freeboard in the one case. The difference between the theoretical and empirical curves could be accommodated by increasing the particulate absorption coefficient, however the difference is attributed to higher heat release rates in the freeboard zone than those anticipated of section 4.1.2. Thus the difference between the theoretical and empirical curves of Figure 52 is the result of a significant amount of combustion taking place in the freeboard of the furnace.

4.1.2 Development of a Characteristic Equation for the Shallow Fluidized Bed Combustor Furnace

As is evident from the preceding section; the flow, combustion and heat transfer phenomena occurring in the freeboard above the

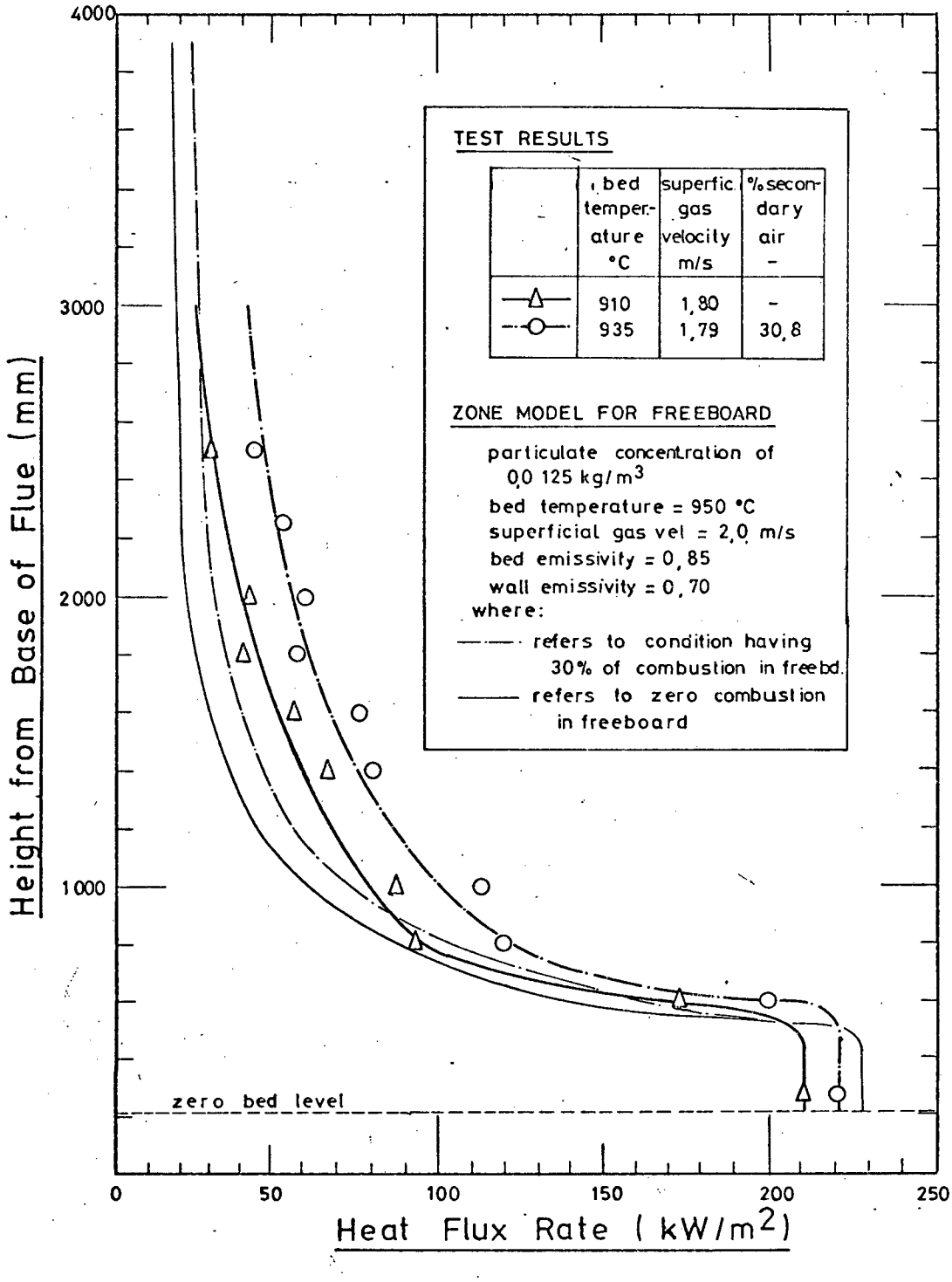

Figure 52 : Heat Flux profiles during normal combustion and substoichiometric combustion in the fluidized bed.

fluidized bed, besides being interrelated are extremely complex and difficult to describe. Indeed, refining of the zoning grid to approach a continuous type system results in the complexity increasing as a power type relationship. Further, the more complex the system, the more one has to question the validity of the basic assumptions as well as the accuracy of the input data. This is particularly true of a coal fired furnace configuration where for example wall emissivities are not accurately known and even in the event of an accurate value being obtained this may change during operation. Further, in view of the radiative heat transfer taking place in proportion to the fourth power of the temperature this does permit a less rigorous approach when considering the effects of other parameters. One of the advantages of the detailed approach is that it enables the prediction of the magnitude and region in which the peak heat flux will occur. It is evident from both the experimental work and the preceding detailed analysis that such a peak flux does not occur in the freeboard zone. Indeed heat transfer rates in the bed zone are significantly larger than those obtained above the bed. Therefore a simpler approach has been devised which enables the prediction of the final gas temperature whilst allowing for the effect of the radiating bed surface and the enclosing water cooled surface. This leads to the formation of an equation which can be described as a one-gas zone two-surface zone model and can be considered as a characteristic equation of the fluidized bed furnace.

Hottel (56, ch 14), (57), (143) has developed the one-gas zone model for the prediction of industrial furnace performance. This model has been used as a basis and then extended to formulate an equation which can be considered as characterizing the performance in the freeboard of a fluidized bed.

The furnace is therefore described by a single gas zone which behaves as an intimately stirred tank reactor having a uniform radiating temperature. This temperature is assumed to exceed the exhaust gas temperature by an amount Δ. The single gas zone is surrounded by a sink formed by cooling walls and a

second surface, the bed surface which is in fact a radiation source. The description of this latter surface zone is clearly different from the refractory surface zones generally included in furnace analysis and employed by Hottel (57) in the development of his one-gas-zone model. The bed surface radiates heat to the gas and the surrounding wall, whilst the refractory surfaces are considered as no flux surfaces and only assist in the transfer of heat from a source to a sink. In other words, they result in an increase in the total exchange area as compared to the direct exchange areas utilized in the previous section.

Temperatures have all been reduced to a dimensionless form by dividing by a pseudo adiabatic flame temperature. This temperature is defined by the heat input to the furnace such that this pseudo flame temperature is given by:

$$(T_F - T_o) = Q_F / m_g \cdot c_{p_m} \qquad (79)$$

where the heat input Q_F includes the chemical heat of combustion released above the bed as well as the heat content of the gases entering the freeboard region from the surface of the bed. It is evident therefore that in the event of there being no heat released above the bed, the pseudo flame temperature will be equal to the bed temperature. The heat input can therefore be represented by equation (80) :

$$Q_F = Q_{lib,f} + m_g \cdot c_{p_m} \cdot (T_b - T_o) + (\text{heat content of the secondary air}) \qquad (80)$$

In-order to develop the characteristic equation for the fluidized bed freeboard zone, the following assumptions are made

(i) the gas is well stirred and at a temperature T_g

(ii) the heat transfer by convection is neglected

(iii) the loss through refractory walls and radiation openings is small

(iv) the flue gases leave the furnace at a temperature $(T_g - \Delta)$

Three total exchange areas can be defined

(i) from the gas to the sink (cooling surface) - GW

(ii) from the gas to the source (fluidized bed) - GB

(iii) from the fluidized bed to the cooling surface - BW

From the assumptions and the definitions of the various total exchange areas, the rate of heat transfer from the gas to the surrounding surfaces can be written as

$$Q_G = GW \cdot \sigma \cdot (T_g^4 - T_w^4) - GB \cdot \sigma \cdot (T_b^4 - T_g^4) \qquad (81)$$

The energy balance on the gas equates the heat transferred from the gas given by equation (81) to the difference in heat input to the resulting enthalpy of the leaving gas stream. Assuming this gas stream to leave the bed at a temperate Δ below the exhaust gas temperature the heat balance can be given by equation (82).

$$Q_G = Q_F - m_g \cdot c_{p_m} \cdot (T_g - \Delta - T_o) \qquad (82)$$

If no dissociation of the gas takes place at the higher temperatures the value for the mean specific heat used in equations (79) and (82) will be very similar and the two equations can be combined to form

$$\frac{Q_F - Q_G}{Q_F} = \frac{T_g - \Delta - T_o}{T_F - T_o} \qquad (83)$$

Now the furnace efficiency is defined as

$$\eta_f = \frac{Q_G + losses}{Q_F} \qquad (84)$$

and assuming no losses this becomes

$$\eta_f = Q_G / Q_F \qquad (85)$$

Provided that the total exchange areas can be established, then we have two equations, (81) and (83), containing two unknowns viz the mean gas temperature and the heat transferred from the gas Q_G. Equation (81) has been made dimensionless by dividing by $GW \cdot \sigma \cdot T_F^4$ and the resulting dimensionless temperatures are

given by an equation of the form of equation (86) with the subscripts having the same designations as before

$$\theta_g = T_g / T_F \qquad (86)$$

Thus equations (81) and (83) become

$$\frac{Q_G}{GW \cdot \sigma \cdot T_F^4} = (\theta_g^4 - \theta_w^4) - \frac{GB}{GW} \cdot (\theta_b^4 - \theta_g^4) \qquad (87)$$

$$\frac{Q_G}{Q_F} \cdot (1 - \theta_o) = 1 - \theta_g - \theta_\Delta \qquad (88)$$

By defining a reduced firing density D' and a reduced rate of heat transfer from the gases Q' by equations (89) and (90)

$$Q' = \frac{Q_G}{Q_F} (1 - \theta_o) \qquad (89)$$

$$D' = \frac{Q_F}{GW \cdot \sigma \cdot T_F^4 \cdot (1 - \theta_o)} \qquad (90)$$

Equation (91) can be formed:

$$Q' : D' = (\theta_g^4 - \theta_w^4) - \frac{GB}{GW} \cdot (\theta_b^4 - \theta_g^4) \qquad (91)$$

For industrial furnaces, Hottel (143) has established that the reduced temperature difference is approximately proportional to the reduced heat transfer from the gases Q'. The relationship between these two parameters can be represented by the following relationship :

$$\theta_\Delta = (1 - 1/d) Q' \qquad (92)$$

Which on substitution into equations (85) and (91) yields the following equations

$$(Q'/d) \cdot (d D') = \{ (1 - Q'/d)^4 - \theta_w^4 \} - \frac{GB}{GW} \cdot \{ \theta_b^4 - (1 - Q'/d)^4 \} \qquad (93)$$

$$\eta_{f/d} = \frac{Q'/d}{(1 - \theta_o)} \qquad (94)$$

Equations (93) and (94) are parametric equations in (Q'/d) and can be considered to characterize the freeboard region of a fluidized bed combustor furnace. The form of the equations is similar to that presented by Hottel (56, ch 14), (57), (143) but can be considered as an extension by inclusion of the second term on the right hand side of equation (93). This term, in view of the ratio of exchange areas, takes into account differences which occur from one furnace to another with regard to the relative position and arrangement of the upper surface of the fluidized bed and the surrounding cooled surfaces or sink. It should be noted, however, that though the equations do not make allowance for losses through refractory sections and openings in the furnace these can be allowed for by introducing more terms into equations (93) and (94). In any event, their effect is very small and in view of the simplicity of the relationship given by equations (93) and (94), they should be neglected. A further point to note, is that convection can be allowed for by modifying the gas to wall total exchange area GW.

The total exchange factors are easily obtained from a table of interchange areas in a cylindrical enclosure (56, ch 7), a knowledge of the absorption coefficient and a relation of the form of equation (95)

$$\overline{GS}_i = A_i \cdot \varepsilon_i - \sum_{j=1}^{2} \overline{S_i S_j} \qquad (95)$$

The ratio of the total exchange areas was determined assuming the emissivity of the bed to be 0,5, and the surrounding wall to be 0,7 with an absorption coefficient of 0,5 m^{-1}. The resulting ratio was found to be 0,0415.

Using this value the parametric equations (93) and (94) were solved. The resulting relationship between the reduced furnace efficiency and the reduced firing density have been illustrated in Figure 53. The use of these equations as represented in Figure 53 is presented in Section 4.1.3 where the extent of combustion in the freeboard zone has been evaluated.

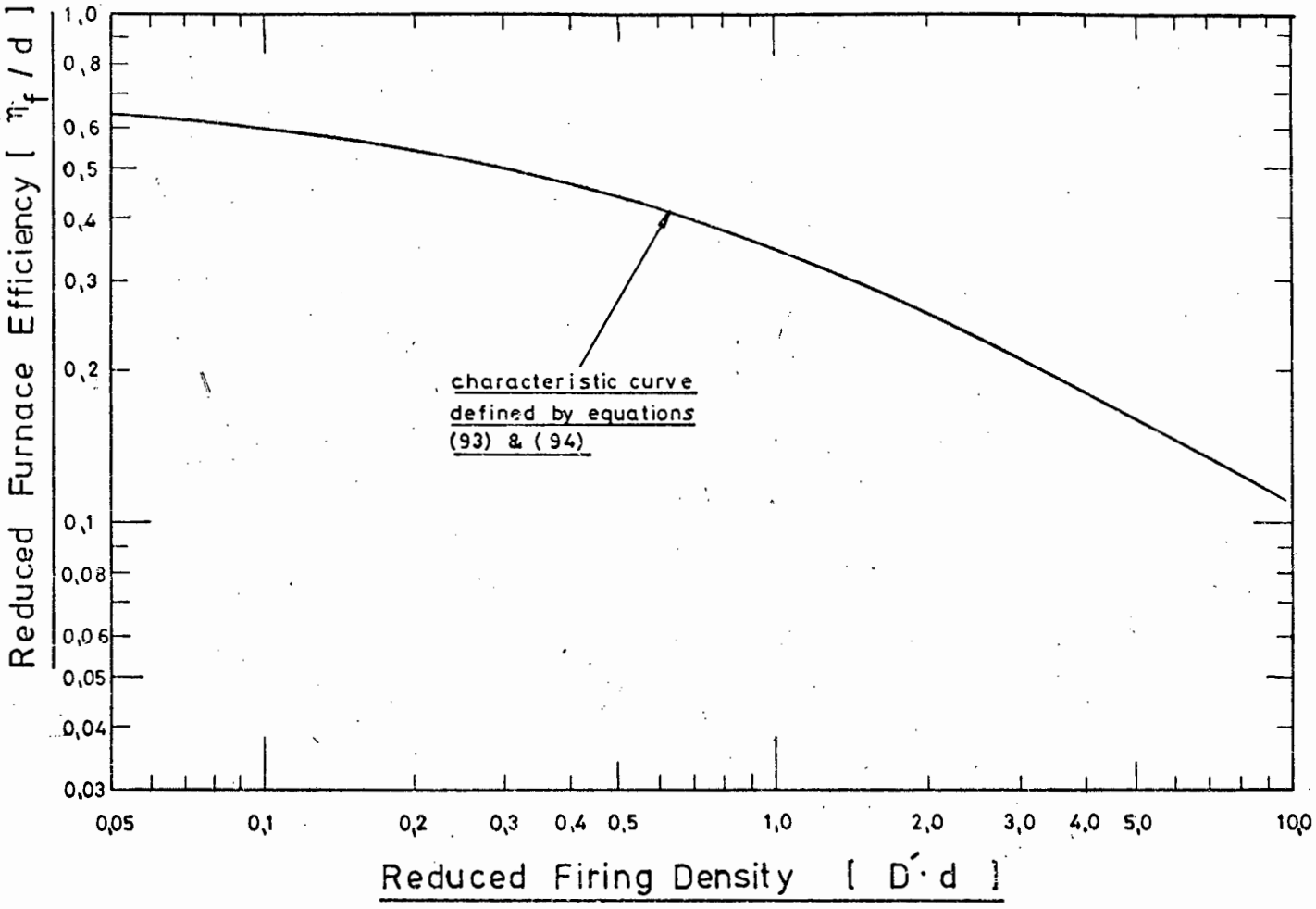

Figure 53 : Representation of the thermal performance of a well stirred freeboard zone above a fluidized bed with a total exchange area ratio of 0,0415.

4.1.3 Combustion in the Freeboard

The characteristic curve of Figure 53 has been plotted together with a number of data points obtained from tests in Figure 42. Although the points have been plotted as the relationship between the furnace efficiency and the product of the reduced firing density, the characteristic curve and the points should have the same slope as they have been drawn on logarithmic paper. The points should be displaced a distance (ln d - ln GW) along the abscissa and a distance -ln(d) along the ordinate.

From Figure 42 it is seen that the points lie on a much steeper line than would be predicted by the characteristic line. Although the points tend to lie on the same general line, groupings of points related to the different feed systemsemployed can be distinguished. A further grouping, relating to the combustion of the duff coal as opposed to the low fines coal is also evident.

Although values for the parameter 'd' and the total exchange area could be utilized to further correct the data points, this will have no affect on the slope. Examination of the points in relation to the characteristic curve indicates a far more rapid decrease in the furnace efficiency obtained from the experimental results than from the characteristic curve as the firing intensity is increased. In many instances the furnace efficiency is very low. Clearly heat must be released in the freeboard which has not been accounted for. This is particularly true of the high velocity conditions where volatiles and indeed burning carbon particles will burn in the freeboard even in the absence of secondary air introduction above the bed.

A further point to note is the apparent lower efficiencies obtained when utilizing the underbed screw feeder as opposed to the above bed feeder when burning the low fines coal. More combustion takes place in the freeboard when using the underbed feeder than when using the above bed feeder. This would also explain the lower apparent furnace efficiencies obtained for the underbed feeder at corresponding firing densities.

In order to obtain the experimental points on a line parallel to the characteristic curve presented in Figure 42, the data points must be adjusted to accommodate the apparent combustion in the freeboard. Although the characteristic line is in fact a curve, this can be represented by a straight line on the logarithmic co-ordinates of Figure 42 or 53. This straight line can be represented by equation (96).

$$(\eta_f / d) = 0,5811 \; (D' \cdot d)^{-0,3727} \qquad (96)$$

or for the relevant data points as

$$(\eta_f) = 0,5811 \; \left(\frac{Q_F}{\sigma \cdot T_F \cdot (1 - \theta_o)} \right)^{-0,3727} \qquad (97)$$

In order to adjust the data points of Figure 42 so that they lie on the straight line given by equation (97), the heat liberated in the freeboard must be evaluated from a solution of equations (98) and (99).

$$\eta_f = \frac{Q_G}{Q_F + Q_{lib,f}} = 0,5811 \left\{ \frac{Q_F + Q_{lib,f}}{\sigma \cdot T_F^4 \cdot (1 - \theta_o)} \right\}^{-0,3727} \qquad (98)$$

$$\eta_f = 1 - \frac{Q_g}{Q_F + Q_{lib,f}} \qquad (99)$$

An iterative procedure had to be adopted in order to solve for the apparent heat liberated in the freeboard for each of the test points. The results of the calculation are illustrated in Figure 54 which is a plot of the fraction of the heat released above bed as a function of the superficial gas velocity for those tests in which all the air for combustion was supplied as fluidizing air, i.e. substoichiometric bed combustion with the introduction of secondary air above the bed has not been included in the figure.

From Figure 54 it is seen that with the increase in velocity, the fraction of heat liberated above the bed steadily increases until about 25% of the heat is released in the freeboard at a

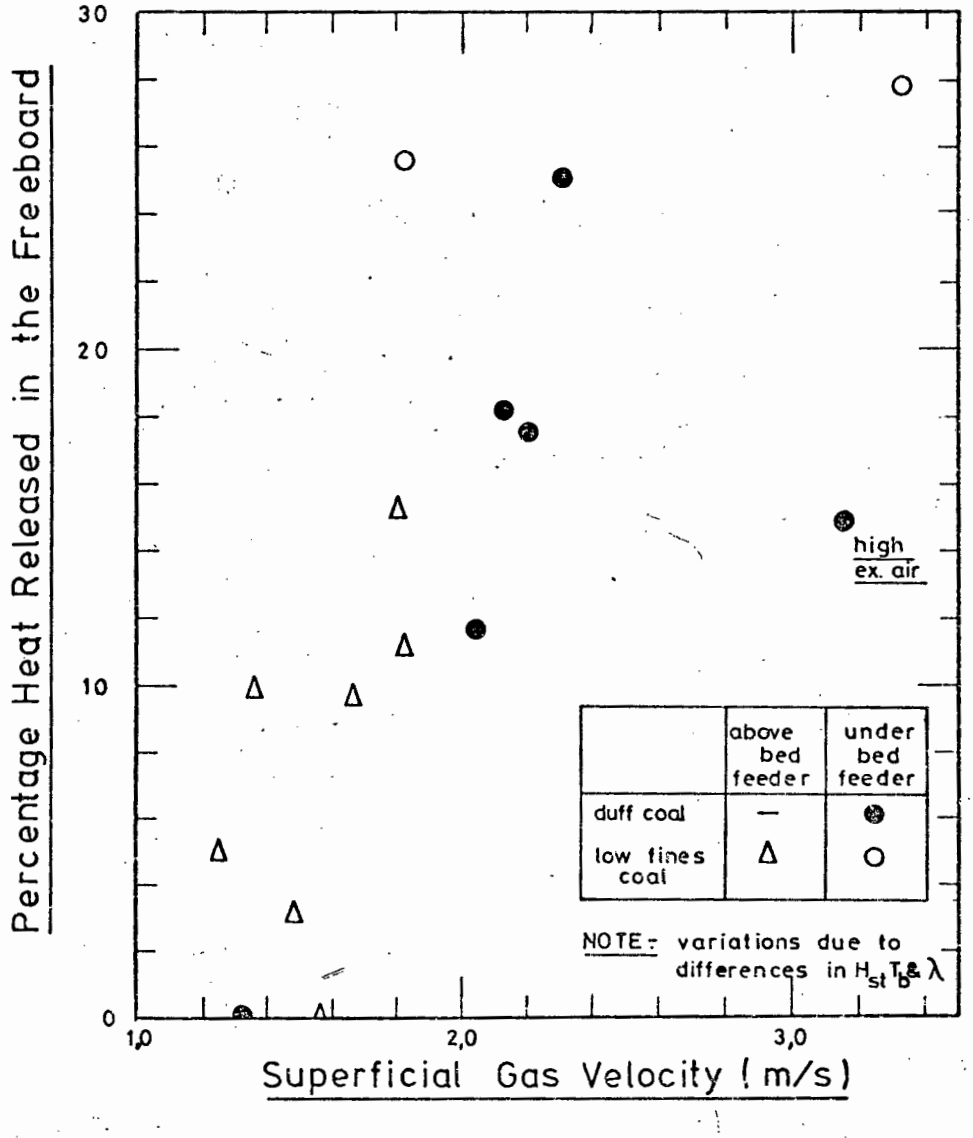

Figure 54 : Heat release in the freeboard as a function of the bed superficial gas velocity for conditions in which all of the combustion air is supplied as fluidizing air.

velocity of 3,0 m/s. The development of the characteristic equation for the freeboard of a fluidized bed combustor besides providing a simple description of this region has enabled a better estimate of the combustion taking place above the bed to be made.

4.2 THE MECHANISM OF HEAT TRANSFER WITHIN THE BED

When considering the heat transferred from the fluidized bed a distinction is made between the heat transferred to the peripheral walls and to an immersed horizontal tube. Heat transfer studies have also been conducted by means of a small heat transfer probe which can be immersed at various levels within the bed. This probe has been utilized in establishing instantaneous heat transfer coefficients. Since the major objective is to establish the heat transfer coefficient between the bed and the peripheral surface or an immersed surface the absolute value of the heat transfer coefficient between the bed and an isolated probe is not of primary interest. However, the relative values of heat transfer between such a probe and the bed provide an insight into the mechanism of the heat transfer. As a consequence, sufficient data were obtained from the experimental investigations to permit the formulation of empirical equations for predicting the heat transfer from the bed to both the peripheral walls and the immersed horizontal tube whilst no correlation was formed for the heat transfer to the small heat transfer probe.

The heat transfer mechanism, and the correlations for heat transfer established in Chapter 3 refer only to the particulate convective heat transfer component. The gas convective component is small and can be neglected in atmospheric systems, whilst the radiative component has been considered as being additive to the convective component in forming the total heat transfer coefficient. The particle convective component can therefore easily be obtained from total heat transfer data, as presented in Section 1.3.1.

The well ordered bubble formation in deep beds is not apparent in the shallow fluidized beds studied. The basic models for fluidized bed heat transfer have been discussed in Section 1.3.1. Although no new fundamental approach is presented the mechanism of the observed heat transfer as presented in Chapter 3 is discussed in the following sections with the aid of a theoretical model. In view of the apparent differences in the heat transfer mechanism for peripheral as opposed to immersed surfaces the mechanism of heat transfer to each of these surfaces is considered separately.

4.2.1 Bed to Wall Heat Transfer

The correlation of the particle convective heat transfer coefficient between the fluidized bed and the surrounding cooling surface did not fit the data as well as that obtained for the immersed horizontal tube. However, examination of the resulting correlation for the surrounding surface indicates a slight dependence on the bed height cf equation (44). The heat transfer coefficient therefore decreases as the bed height increases. This decrease is not very large, and is proportional to the bed height raised to a power of 0,15.

Considering the packet theory of Mickley and Fairbanks (31) it was seen in equation (14) that the particle convective coefficient is proportional to the square root of a stirring factor. However this stirring factor can be defined in terms of the velocity of solids movement along the cooling surface of length L. Hence the local stirring factor can be written as

$$S_l = \frac{(u/L)}{\pi} \qquad (100)$$

or the relationship given by equation (14) can be written as

$$h_{p,c} = 2\cdot\sqrt{k_m\cdot\rho_m\cdot c_{p_s}}\cdot(u/H_{dyn})^{0,5} \qquad (101)$$

It is clear from equation (101) that increases in the dynamic bed height will result in a decrease in the particulate convective heat transfer coefficient. However, the decrease

predicted from the experimental work, cf equation (44), is not as large as that proposed by equation (101). This could be overcome by introducing a contact resistance as suggested by Baskakov (34). A further point to note, was the absence of any significant variation in the frequency of the change in the heat transfer coefficient for different bed heights, cf Section 3.4.2. Thus the frequency of bubble contact with the peripheral wall is not affected by the change in bed height.

Hence if the packet theory is considered as describing the heat transfer from the fluidized bed to the surrounding wall in a shallow fluidized bed, it appears that the bubble flow has little effect on the stirring factor which arises solely as the result of the movement of the packet along the length of the cooling surface. Therefore, in the shallow fluidized beds utilized in the 1 000 mm diameter test rig, the solids movement is evident as a continuous downflow of solids along the vessel wall with bubble producing an overall upflow of solids in the central bed region. Clearly this is an over-simplification as solids movement would tend to be random, however the mechanism of heat transfer would tend to indicate that on average there is an upflow of solids in the central region due to the transport of solids in the bubble wake and a downflow of solids along the walls. A contact resistance is easily incorporated to obtain the reduced sensitivity of the heat transfer coefficient predicted by the empirical relationship.

4.2.2 Heat Transfer to an Immersed Surface

In contrast to the correlation obtained for the bed to surrounding surface heat transfer, the heat transfer coefficient between the bed and a horizontal immersed tube increases as the bed height is increased. Further the effect on bed height is more significant for the immersed tube, cf equation (41) than for the evaluation of the heat transfer coefficient from the bed to a surrounding wall.

It would appear that the packet theory of Mickley and Fairbanks (31) could not effectively be employed. However, closer

investigation indicates that the immersed tube does not represent a deviation from the basic mechanism presented in the preceding section. Consideration of equation (101) would indicate that in its application to an immersed horizontal tube, the dynamic bed height cannot be utilized in formulating the stirring factor as the heat transfer does not take place along this length but only over the tube diameter which is independent of the height. Clearly, if a relationship similar to equation (101) is employed, the variation in heat transfer coefficient will have to be accommodated by the velocity.

However tests conducted utilizing the small heat transfer probe indicated a significant variation in the frequency of oscillation of the instantaneous heat transfer coefficient for different values of the static bed height, cf Section 3.4.2. This frequency is found to increase as the bed height increases. The bubble phase is associated with a low heat transfer coefficient as opposed to the high heat transfer coefficient associated with the particulate phase. This gives rise to the fluctuations in the instantaneous heat transfer coefficient. The bubble movement within the bed will affect the heat transfer to the immersed heat transfer probe and the horizontal cooling tube in a similar manner. Therefore the frequency of variation in heat transfer coefficient associated with the probe can be related to the immersed tube. Clearly the stirring factor of equation (101) is none other than a frequency or the reciprocal of the period, thus the packet model is utilized by defining the stirring factor in terms of the frequency as given by equations (102) and (103)

$$S_l = C^2 \cdot \nu \qquad (102)$$

$$h_{p,c} = 2 \cdot C \cdot \sqrt{k_m \cdot \rho_m \cdot c_{p_s}} \cdot \nu^{0,5} \qquad (103)$$

From equation (48) the ratio of the root of the frequencies obtained when operating the bed at two different static bed levels is found to be 1,151. In other words, the heat transfer coefficient of the deeper bed should be 1,151 times that obtained from the shallower bed.

Using equation (41) for both bed depths results in a ratio of 1,13. Although very similar to the value obtained when using equation (103), this latter equation could be further modified by incorporating a contact resistance. This is similar to the approach employed for the bed to surrounding wall heat transfer coefficient, however, in view of the relatively small difference in the ratio of the heat transfer coefficients obtained using equations (103) and (41) the contact resistance used for the immersed surface will be less than that needed to complete the heat transfer model for the surrounding surface.

This contact resistance can be described by equation (104)

$$R_w = \delta_w / k_m \qquad (104)$$

Where δ_w is the thickness of the zone adjacent to the wall and has been assumed by a number of workers to take on values varying from $0,1\ d_p$ to as much as $0,5\ d_p$.

4.3 COMBUSTION AND ENTRAINMENT

The combustion and entrainment rate data of Chapter 3 are more of a qualitative than a quantitative nature, and it is therefore very difficult to be able to utilize a sophisticated model to predict results or establish a mechanism of combustion, attrition, elutriation and so on taking place in both the fluidized bed and freeboard of the test rig. However, a model was developed to describe the combustion and entrainment phenomena occurring during combustion at high excess air levels in a refractory lined 300 mm diameter combustor (75). The model developed was fairly complex and the justification of its application to the present work is doubtful in view of the difficulty of expressing attrition and combustion rate constants, as well as certain assumptions concerning the mixing of the fuel in the bed, etc. The model is therefore far too complex for the large scale 1 000 mm diameter test rig. However, for completeness, the basic outline of the model has been summarized in Appendix I. Clearly the model could be applied to the test rig and by

adjusting the attrition and splashing rate constants results similar to those obtained during the tests could be obtained, however, the artificial manipulation of rate constants is undesirable and renders questionable the use of such a model. However more work into defining the splashing, attrition and mixing phenomena, together with a description of the combustion process differentiating between heterogeneous carbon and homogeneous gas combustion would be necessary to obtain a better understanding of many of the fundamental processes. A further area in which work could be undertaken would be in the description of the combustion rates related to coals of differing apparent reactivities.

CHAPTER 5

DISCUSSION

The development of fluidized bed combustion has progressed beyond the small scale laboratory type experiments to the pilot and demonstration plant stage. Particularly with respect to atmospheric fluidized beds, the technology has reached commercial realization. However, although a number of industrial sized boilers have been operating in commercial environments for some time, work on these units has been directed at solving the numerous engineering problems which occur when a new technology is introduced. It is therefore difficult to relate the results obtained on bench scale equipment to commercial plant, whilst the results obtained from industrial equipment have not been conducive to detailed analysis. A further complication is due to the earlier fluidization studies having been undertaken with relatively deep beds of fine particles whilst the development of fluidized bed combustion, and in particular atmospheric fluidized bed combustion has resulted in the utilization of relatively shallow beds of coarse particles.

The 1 000 mm diameter test rig represents the vertical flue of a small industrial scale boiler which would be capable of evaporating about 3 000 kg/h of water to steam. Extensive instrumentation has enabled a study of heat transfer, combustion and entrainment phenomena to be undertaken on equipment of an industrial scale. Investigations have, however, been concerned with the study of these reactions in the fluidized bed and the freeboard zone situated immediately above the bed. The furnace of a fluidized bed boiler, which is effectively modelled by the test rig, has therefore been defined as being made up of two distinct zones, the fluidized bed itself and the disengaging radiant heat transfer zone forming the freebaord immediately above the bed. Whilst the two zones operate as a unit in forming the furnace, each has been

considered separately when evaluating the test results. However, it should be clear that operating conditions in the fluidized bed zone are inextricably linked with the freeboard particularly as the energy input to the freeboard originates from the fluidized bed.

Two coals have been utilized, the first having a high content of relatively fine particles, and the second being almost devoid of this fine component. Although having no effect on the heat transfer in the bed, and only a minor effect on the heat transfer in the freeboard region, the different coals give an indication of the effectiveness of the shallow fluidized bed combustor in burning fuels of different size gradings. Further, overbed and underbed means of feeding the coal to the bed have been employed. This has indicated the importance of the distribution of the fuel to the fluidized bed.

Considering the division of the shallow fluidized bed combustor furnace into two distinct zones, further discussion is presented with separate reference to the two zones. A final section on the combustion and entrainment phenomena has also been included.

5.1 THE FLUIDIZED BED ZONE

The fluidized bed can further be considered to be divided into a dispersed cloud zone at the upper portion of the bed, and lower dense zone made up of a particulate and bubble phase. Investigation into the heat transfer within the cloud zone and the extent of this zone was only possible for the shallower (about 120 mm deep) bed heights investigated. It was found that no distinction could be made on the basis of heat transfer between the two bed zones when all the air for combustion was supplied as fluidizing air. However, on operating the bed substoichiometrically, higher heat transfer rates to the heat transfer probe were measured in the cloud zone than in the lower more dense zone. It was therefore evident, that under

correlations are similar in form, however the heat transfer coefficient between the bed and the surrounding wall is found to decrease slightly as the bed height increases, whilst the reverse is true for the heat transferred to the horizontal immersed tube. Further, the correlation of the heat transfer data obtained from the immersed tube is improved by including data on the bed expansion. Although a difference exists in the effect of bed height on the heat transfer coefficients to the surrounding wall and the immersed tube, the same fundamental mechanism has been utilized in describing the heat transfer phenomena.

In both of the heat transfer studies undertaken within the bed zone, the packet theory of heat transfer incorporating a contact resistance has been employed to describe the phenomenon. In the case of the peripheral surface, the bed height is utilized as the characteristic dimension required in the stirring factor, whilst bubble frequencies have been used in the heat transfer mechanism describing the heat transfer to the immersed tube. The peripheral wall heat transfer coefficient is relatively unaffected by bubble frequencies whereas bubble motion appears to be largely responsible for the heat transfer to an immersed surface. It is therefore postulated that the heat transfer to immersed surfaces is by bubble motion whereas the particulate component of the heat transfer to the peripheral wall is as a result of a steady downflow of particles along the surrounding wall. This is supported by the empirical correlations. This is further emphasized by the improvement in the correlation obtained for the immersed tube by including a parameter related to the bed expansion which is a function of the bubble fraction contained in the bed. A further point is the smaller contact resistance associated with the immersed surface which clearly is a consequence of the more vigorous bubble motion in the centre of the bed than at the bed periphery.

5.2 THE FREEBOARD ZONE

A detailed heat transfer analysis of the freeboard was undertaken. The zone method of analysis was employed and the freeboard was divided into seven gas zones and nine surface zones. Although variation of the absorption coefficient in the different gas zones was originally allowed for, this was dispensed with, as though this largely effects the emitted radiation for the particular zone its effect on zones further away becomes insignificant. Heat flux profiles from the furnace analysis were similar to those obtained by measurements obtained using the heat flux pads. However, comparison with the overall performance data indicated that combustion was taking place in the freeboard even though sufficient air to complete the combustion in the bed was supplied as fluidizing air.

The zone method was simplified to form a single gas zone and two surface zone model. The model was developed and a characteristic equation for the freeboard zone of a fluidized bed combustor was developed. This equation relates the furnace efficiency to a firing density and a ratio of the total exchange areas describing the geometry of the particular furnace.

The overall analysis of the experimental results obtained from tests on the 1 000 mm diameter test rig indicated that particularly low furnace efficiencies were obtained at high firing densities. The results were modified by utilizing the characteristic equation to establish the heat released above the bed. This heat release was found to have a close relationship with the fluidizing velocity.

5.3 COMBUSTION AND ENTRAINMENT

Curves obtained from grading analyses of the entrained ash indicated that the size of this ash can be represented by three distinct bands, dependent on the fines content of the

original coal feed and whether above or underbed feeding of the fuel was employed. No relationship was derived for relating the entrained material size gradings to a particular entrainment mechanism but it was evident that the uniform distribution of the fuel to the bed is important in reducing entrainment rates and thereby increasing the burn-out of the carbon fraction within the bed. It was particularly noticeable when employing the above bed feeder as opposed to the underbed screw feeder with a similar coal, that the carbon content of the entrained ash decreased together with the carbon monoxide content of the flue gases. Clearly poor mixing associated with the underbed screw feeder resulted in carbon rich areas near the feeder causing carbon monoxide and hydrocarbon formation with significant quantities of oxygen bypassing the bed for combustion of these combustible gases above the bed.

The development of a characteristic equation for the freeboard of the fluidized bed combustor enabled an evaluation of the heat released by combustion in the above bed region. This further indicated higher heat release rates above the bed with the screw feeder due to its poor lateral mixing characteristic.

CHAPTER 6

CONCLUSIONS AND RECOMMENDATIONS FOR FURTHER WORK

Coal having a high fines content is in abundant supply as a result of the limited demand for this fuel. Such a coal has been successfully burned in a fluidized bed combustor which would be representative of the furnace section of an industrial scale fluidized-bed steam-generator. In order to enhance the commercial application of the fluidized-bed combustion process, the coal has been burnt in relatively shallow beds with a relatively low pressure drop across the distributor. A shallow bed, though reducing the combustion efficiency, results in a reduction of the fluidizing air fan power consumption which is normally considerably higher than the auxiliary power consumption of conventional solid fuel combustion equipment. Secondary air was introduced above the bed as a means of creating a secondary combustion reaction above the bed to increase the carbon burn-up as well as to increase the rating of the unit. The fluidized bed is surrounded by a water jacket which extends to the freeboard above the bed thus forming a furnace which has been considered as being made up of a fluidized bed zone and a freeboard zone. The work of this thesis is therefore concerned with the combustion and heat transfer phenomena taking place in each of these zones in a furnace of a size similar to that which could be utilized commercially. The following conslusions have been drawn :

6.1 CONCLUSIONS

Heat Transfer within the Fluidized Bed

a) The heat transfer coefficient from the bed to the surrounding wall has been correlated by means of dimensionless numbers incorporating the relevant operating parameters by the following relationship having a correlation

coefficient of 0,610 :

$$Nu_p = 0{,}616 \cdot Ar^{0{,}23} \cdot Re_p^{-0{,}13} \cdot H_{st,r}^{-0{,}15} \qquad (44)$$

The above relationship has been derived over the following approximate bed operating conditions :

Bed temperature	:	780 to 1000°C
Superficial gas velocity	:	1,0 to 3,0 m/s
Static bed height	:	100 to 250 mm

b) The heat transfer coefficient between the bed and an immersed horizontal tube has similarly been correlated by means of dimensionless numbers operating under conditions as utilized for the surrounding wall correlation. A far better correlation was obtained for the heat transfer coefficient from the bed to the immersed horizontal tube. The correlation, for which the multiple correlation coefficient was evaluated as 0,8067 is given by

$$Nu_{to} = 1705 \cdot (1 - \bar{\alpha}) \cdot Ar^{-0{,}3} \cdot Re_{to}^{0{,}17} \cdot H_{st,r}^{0{,}26} \qquad (41)$$

c) The mechanism of heat transfer from the bed to both the surrounding surface and the immersed cooling tube can be described by a packet theory of heat transfer modified by a contact resistance. The transfer of heat to the peripheral wall is affected by the residence times of the packets as they traverse the depth of the bed, whereas the heat transferred to the immersed tube is affected by bubble motion within the bed. The smaller contact resistance associated with the immersed tube compared to the peripheral surface suggests a more vigorous heat transfer within the bed in contrast with that at the peripheral surface. Further, even with shallow beds, a general pattern of solids movement is postulated with the general upward movement of solids in the central bubbling region and a general downflow of solids at the peripheral walls.

Heat Transfer in the Freeboard

d) The heat transfer in the freeboard was evaluated by dividing this region into seven gas zones and nine surface zones. Curves were established relating the bed operating parameters to the performance of the freeboard region.

e) A simplified single gas-zone two surface-zone model to describe the heat transfer in the freeboard region was formulated. This led to the development of a characteristic equation for describing the freeboard of a fluidized bed combustor. The equation is given by two parametric equations which are represented as

$$\left(\frac{Q'}{d}\right)(d \cdot D') = \left\{ (1 - \frac{Q'}{d})^4 - \theta_w^4 \right\} - \frac{GB}{GW} \cdot \left\{ \theta_b^4 - (1 - \frac{Q'}{d})^4 \right\} \qquad (93)$$

$$\frac{\eta_f}{d} = \frac{Q'/d}{(1 - \theta_o)} \qquad (94)$$

f) Use of the characteristic equation for the freeboard of the fluidized bed combustion furnace led to the evaluation of the quantity of heat released in the freeboard region of the bed. This heat released was found to be almost proportional to the fluidizing velocity.

Combustion and Entrainment

g) No correlation was possible regarding the combustion efficiency. However, it was established that the distribution of the fuel to the bed plays an important part in attaining good combustion efficiencies. The use of the overbed feed system resulted in significant improvements in the combustion efficiency compared to the underbed feeder due to the better distribution associated with the above bed feed system.

h) The carbon content of the coarser ash fraction was significantly higher than for the finer particles indicating the potential for improvement in separating and refiring this coarser fraction.

i) The entrained ash size gradings lie within three distinct bands, dependent upon the original grading of the fuel fired and the type of feed system employed.

General

j) The bed expansion data were correlated by a method normally utilized for gas-liquid systems. The data werecorrelated by a least squares analysis and having a correlation coefficient of 0,976 by the equation

$$u_f/\bar{\alpha} = 1{,}392 \cdot u_f + 0{,}383 \qquad (33)$$

k) The heat transfer coefficient at various levels in the bed was measured by means of an adjustable heat transfer probe. It was found that the heat transfer increased significantly in the cloud zone of the bed when the bed was operated sub-stoichiometrically.

6.2 RECOMMENDATIONS FOR FURTHER WORK

a) Laboratory scale testing to evaluate the fundamental combustion phenomena as well as the evaluation of attrition rate data for a number of South African coals should be undertaken. Although this information will not assist in the detailed design of industrial fluidized bed combustors, it would indicate trends and possibly highlight operating conditions where improvements in the plant performance could be obtained.

b) The combustion efficiency of the shallow atmospheric fluidized bed combustor utilizing a coal with a high

fines content is low. Potential improvements by recycling the entrained ash or by combustion of this ash in a separate bed should be investigated.

REFERENCES

1. BENNETT, K.F., "Energy Utilization in South Africa", PhD Thesis, University of Cape Town, 1977.

2. PETRICK, A.J., Chairman on "The Commission of Inquiry into the Coal Resources of South Africa", Department of Mines, RP63/1975.

3. HARRISON, G., "Coal quality - its effect on combustion and selection of equipment", Energy and the Environment Vol 3, No 2, March/April 1977.

4. NAUDÉ, D.P. AND DUTKIEWICZ, R.K. "Fluidized bed combustion of poor quality coal", Second Engineering Foundation Conference on Fluidization, Cambridge, England, 2-6 April 1978, p. 280-285.

5. EHRLICH, S. "History of the development of the fluidized-bed boiler", Fourth International Conference on Fluidized Bed Combustion, McLean (Virginia) USA, 9-11 December 1975.

6. DAVIDSON, J.F. AND HARRISON, D. "Fluidization", Academic Press, London and New York, 1971.

7. HARRISON, D., DAVIDSON, J.F. AND DE KOCK, J.W. "On the nature of aggregative and particulate fluidization", Trans. of the Institution of Chemical Engineers, Vol 39, 1961 p. 202-211.

8. KUNII, D. AND LEVENSPIEL, O. "Fluidization Engineering" John Wiley and Sons Inc., 1969.

9. ZENZ, F.A. AND OTHMER, D.F. "Fluidization and Fluid Particle Systems", Rheinhold Publishing Corporation, New York 1960.

10. BROUGHTON, J. "The influence of bed temperature and particle size distribution on incipient fluidization", Trans. of the Institution of Chemical Engineers, Vol 52, 1974, p. 105-107.

11. REH, L. "Verbrennung in der Wirbelschicht", Chemie Ingenieur Technik, Vol 40, No 11, 1968.

12. WEN, C.Y. AND YU, Y.H. "Mechanics of fluidization", AIChE Symposium Series No 62, Vol 62, 1966.

13. BARNEA, E. AND MEDNICK, R.L. "Correlation for minimum fluidization velocity", Trans. of the Institution of Chemical Engineers, Vol 53, No 4, October 1975, p. 278-281.

14. LEVA, M. "Fluidization", McGraw Hill Book Company Inc, 1959.

15. PATA, J. AND HARTMAN, M. "Minimum fluidization velocities of lime and limestone particles", Ind. Eng. Chem. Process Des. Dev., Vol 17, No 3, 1978, p. 231-236.

16. WEN, C. AND HASHINGER, R.F. "Elutriation of solid particles from a dense phase fluidized bed", AIChE Journal, Vol 6, No 2, June 1960, p. 220-226.

17. MERRICK, D. AND HIGHLEY, J. "Particle size reduction and elutriation in a fluidized-bed process", AIChE Symposium Series No 137, Vol 70, 1974.

18. GELDART, D., CULLINAN, J., GEORGHIADES, S., GILVRAY, D. AND POPE, D.J. "The effect of fines on the entrainment from gas fluidized beds", Trans. of the Institution of Chemical Engineers, Vol 57, 1979, p. 270-275.

19. GIBBS, B.M. "A mechanistic model for predicting the performance of a fluidized bed coal combustor", Fluidized Combustion Conference, Vol 1, Institute of Fuel, Symposium Series No 1, London, September 1975.

20. PATA, J. AND HARTMAN, M. "Operating region of fluidized bed of lime and limestone particles", Ind. Eng. Chem. Proc. Des. Dev. Vol 19, No 1, 1980 p. 98-103.

21. BOTTERILL, J.S.M. "Fluid-Bed Heat Transfer", Academic Press, London, 1975.

22. DAVIDSON, J.F. AND HARRISON, D. "Fluidized Particles", Cambridge University Press, 1963.

23. YERUSHALMI, J. AND CANKURT, N.T. "Further Studies of the regimes of fluidization", Powder Technology, Vol 24, 1979, p. 187-205.

24. LANNEAU, K.P. "Gas-solids contacting in fluidized beds", Trans. of the Institution of Chemical Engineers, Vol 38, 1960.

25. CANADA, G.S., McLAUGHLIN, M.H. AND STAUB, F.W. "Flow regimes and void fraction distribution in gas fluidization of large particles in beds without tube banks" AIChE Symposium Series No 176, Vol 74, 1978, p. 14-26.

26. TAMARIN, A.I. "The origin of self excited oscillations in fluidized beds", Int. Chemical Engineering Vol 4, No 1, January 1964 p. 50-54.

27. VERLOOP, J. AND HEERTJES, P.M. "Periodic pressure fluctuations in fluidized beds", Chemical Engineering Science, Vol 29, 1974 p. 1035-1042.

28. CATIPOVIC, N.M., JOVANOVIC, G.N. AND FITZGERALD, T.J. "Regimes of fluidization for large particles", AIChE Journal, Vol 24, No 3, May 1978 p. 543-547.

29. BOTTERILL, J.S.M. AND J.R. "The mechanism of heat transfer to gas fluidized beds", Trans. Institution of Chemical Engineers, Vol 41, 1963 p. 217-230.

30. GABOR, J.D. "Wall-to-bed heat transfer in fluidized and packed beds", Chemical Engineering Progress, Symposium Series Vol 66, No 105, 1970 p. 76-86.

31. MICKLEY, H.S. AND FAIRBANKS, D.F. "Mechanism of heat transfer to fluidized beds", AIChE Journal, Vol 1, No 3, Sept. 1955, p. 374-384.

32. BOTTERILL, J.S.M. AND DENLOYE, A.O.O. "Gas convective heat transfer to packed and fluidized beds", AIChE Symposium Series, Vol 176, No 74, 1978 p. 194-202.

33. BASKAKOV, A.P. AND SUPRUN, V.M. International Chemical Engineering Vol 12, 1972 p. 374.

34. BASKAKOV, A.P. "The mechanism of heat transfer between a fluidized bed and a surface", International Chemical Engineering, Vol 4, No 2, April 1964, p. 320-324.

35. XAVIER, A.M. AND DAVIDSON, J.F. "Heat transfer to surfaces in fluidized beds, particularly tube arrays", Second Engineering Foundation Conference on Fluidization, Cambridge, England, 2-6 April 1978, p. 333-338.

36. VEDAMURTHY, V.N. AND SASTRI, V.M.K. "An analysis of conductive and radiation heat transfer to the walls of fluidized bed combustors", Int. Journal of Heat and Mass Transfer, Vol 17, 1974, p. 1-9.

37. KUBIE, J. AND BROUGHTON, J. "A model of heat transfer in gas fluidized beds", Int. Journal of Heat and Mass Transfer, Vol.18, Feb. 1975, p. 259-299.

38. YOSHIDE, K., KUNII, D. AND LEVENSPIEL, O. "Heat transfer mechanisms between wall surface and fluidized bed", Int. Journal of Heat and Mass Transfer, Vol 12, 1969, p. 529-536.

39. WICKE, E. AND FETTING, F. "Wärmeübertragung in Gaswirbelschichten", Chemie Ingenieur Technik, Vol 26, No 6, June 1954, p. 301-309.

40. WRIGHT, S.J., HICKMAN, R. AND KETLEY, H.C., "Heat transfer in fluidized beds of wide size spectrum at elevated temperatures", British Chemical Engineering, Vol 15, No 12, December 1970, p. 1551-1554.

41. ZABRODSKY, S.S. "Compound heat exchange between a high temperature gas fluidized bed and a solid surface", Int. Journal of Heat and Mass Transfer, Vol 16, 1973, p. 241-248.

42. KARCHENKO, N.V. AND MAKHORIN, K.E., "The rate of heat transfer between a fluidized bed and an immersed body at high temperatures", International Chemical Engineering, Vol 4, No 4, October 1964, p. 650-654.

43. SZEKELY, J. AND FISHER, R.J., "Bed to wall radiation heat transfer in a gas-solid fluidized bed," Chemical Engineering Science, Vol 24, 1969, p. 833-849.

44. BOTTERILL, J.S.M. AND SEALEY, C.J., "Radiative heat transfer between a gas fluidized bed and an exchange surface", British Chemical Engineering, Vo. 15, No 9, September 1970, p. 1167-1168.

45. YOSHIDA, K., UENO, T. AND KUNII, D., "Mechanism of bed wall heat transfer in fluidized bed at high

temperatures", Chemical Engineering Science, Vol 29, 1974, p. 77-82.

46. SAWARKAR, S.K., SASI, K. AND SEN, P. "Heat transport in fluidized bed combustors", Journal of Mines, Metals and Fuels, September 1977, p. 269-276.

47. EINSTEIN, V.G. AND GELPERIN, N.I., "Heat transfer between a fluidized bed and a surface", Int. Chemical Engineering, Vol 6, No 1, January 1966, p. 67-74.

48. HOEBINK, J.H.B.J. AND RIETEMA, K., "Wall to bed heat transfer in a fluidized bed", Second Engineering Foundation Conference on Fluidization, Cambridge, England, 2-6 April 1978, p. 333-338.

49. VREEDENBERG, H.A., "Heat transfer between a fluidized bed and a horizontal tube", Chemical Engineering Science, Vol 9, No 1, 1958, p. 52-60.

50. AL ALI, B.M.A. AND BROUGHTON, J., "Shallow fluidized bed heat transfer", Applied Energy Vol 3, 1977, p. 101-114.

51. BORODULYA, V.A., GANZHA, V.L., ZHELTOV, A.I., UPADHYAY, S.N. AND SAXENA, S.C., "Heat transfer between gas solid fluidized beds and horizontal tubes bundles", Letters in Heat and Mass Transfer, Vol 7, 1980, p. 83-95.

52. ANDEEN, B.R., GLICKSMAN, L.R. AND BOWMAN, R., "Heat transfer from flattened horizontal tubes", Second Engineering Foundation Conference on Fluidization, Cambridge England, 2-6 April 1978 p. 345-350.

53. ELLIOT, D.E., "Exploiting fluidized bed combustion", Second International Symposium on Fluidized Bed Combustion, Heuston Woods, Ohio, 1970.

54. LIHOU, D.A. "Review of furnace design methods", Trans. of the Institution of Chemical Engineers, Vol 55, 1977, p. 225-242.

55. HOTTEL, H.C. AND COHEN, E.S. "Radiant heat exchange in a gas-filled enclosure : Allowance for non-uniformity of gas temperature", AIChE Journal, Vol 4, No 1, March 1958, p. 3-14.

56. HOTTEL, H.C. AND SAROFIM, A.F., "Radiative Heat Transfer", McGraw Hill Book Company, New York, 1967.

57. HOTTEL, H.C., "First estimates of industrial furnace performance : The one-gas-zone model reexamined", from Heat Transfer in Flames, Afgan, N.H. and Beer, J.M. (Editors), Scripta Book Co, Washington D.C., 1974.

58. HOTTEL, H.C., "Radiant heat transmission", Chapter 3 of Heat Transmission (W.H. McAdams), Third Edition, McGraw Hill Book Co, 1954.

59. JOHNSON, T.R., LOWES, T.M. AND BEER, J.M. "Comparison of calculated temperatures and heat flux distributions with measurements in the IJmuiden furnace", Journal of the Inst. of Fuel, March 1974, p. 39-51.

60. BEER, J.M. AND CLAUS, J. "The traversing method of radiation measurement in luminous flames", Journal of the Inst. of Fuel, 1962, p. 437-443.

61. FIELD, M.A., GILL, G.W., MORGAN, B.B. AND HAWKESLY, P.G.W., "Combustion of Pulverized Coal", British Coal Utilization Research Association, Leatherhead (Surrey), Great Britain, 1967.

62. BECKER, H.B., JUNIPER, L.A. AND JOHNSON, T.R., "A mathematical model of combustion and heat transfer in brown coal fired furnaces", Paper presented to the 5th Members Conference of the International Flame Research Foundation, Nordwijkerhout, The Netherlands, 8-10 May 1978.

63. PITT, G.J. "The kinetics of the evolution of volatile products from coal", Fuel, Vol 41, 1962, p. 267-274.

64. SKINNER, D.G. "The Fluidized Combustion of Coal", National Coal Board Research and Development Department, 1970.

65. BISHOP, J.W., ROBINSON, E.B., EHRLICH, S., JAIN, A.K. AND CHEN, P.M. "Status of the direct contact heat transferring boiler", Fuels Division of the ASME, ASME Winter Annual General Meeting and Energy Systems Exposition, New York, 1-5 December, 1968.

66. AVEDESIAN, M.M. AND DAVIDSON, J.F. "Combustion of carbon particles in a fluidized bed", Trans. of the Institution of Chemical Engineers, Vol 51, 1973, p. 121-131.

67. BASU, J., BROUGHTON, J. AND ELLIOT, D.E. "Combustion of single coal particles in fluidized beds", Fluidized Combustion, Vol 1, Institute of Fuel Symposium Series No 1, London, September 1975.

68. CAMPBELL, E.K. AND DAVIDSON, J.F. "The combustion of coal in fluidized beds", Fluidized Combustion, Vol 1, Institute of Fuel Symposium Series No 1, London, September 1975.

69. PYLE, D.L. "Fluidized Combustion Models: Rapporteur's Report", Fluidized Combustion, Vol 2, Institute of Fuel Symposium Series No 1, London, September 1975.

70. ROSS, I.B. AND DAVIDSON, J.F. Correspondence : Transactions of the Institute of Chemical Engineers, Vol 57, No 3, July 1979, p. 215-216.

71. CHAKRABORTY, R.K. AND HOWARD, J.R. "Burning rates and temperatures of carbon particles in a shallow fluidized bed combustor", Journal of the Institute of Fuel, December 1978, p. 220-224.

72. LEUNG, L.S. AND SMITH, I.W. "The role of fuel reactivity in fluidized bed combustion", Fuel, Vol 58, May 1979, p. 354-360.

73. SQUIRES, A.M. "Clean fuels from coal gasification", Science, Vol 184, April 1974.

74. TEAGUE, D.S. AND WRIGHT, S.J., "Fluidized combustion : A preliminary appraisal of fluidization data and the possibilities of further development", BCURA, Document No R16/7, August 1963.

75. NAUDÉ, D.P. "The Fluidized-Bed Combustion of Coal", MSc Thesis, University of Cape Town, 1977.

76. NAUDÉ, D.P. "The potential of fluidized bed combustion for industrial steam raising in South Africa", The South African Mechanical Engineer, Vol 29, No 7, July 1979, p. 243-250.

77. COOKE, M.J. AND HODGKINSON, N. "The fluidized combustion of low grade materials", Fluidized Combustion, Vol 1, The Institute of Fuel Symposium Series No 1, London, September 1975.

78. HODGKINSON, N. AND THURLOW, G.G. "Combustion of low grade materials in fluidized beds", AIChE Symposium Series, Vol 73, No 161, 1977, p. 108-114.

79. RANDALL, A.A., GAULD, D.W., DANDO, R.L. AND LA NAUZE, R.D., "Disposal of colliery tailings by fluidized bed combustion", Second Engineering Foundation Conference on Fluidization, Cambridge, England, 2-6 April 1978, p. 286-291.

80. WATERS, P.L., "Factors influencing the fluidized combustion of low grade solid and liquid fuels", Fluidized Combustion, Vol 1, The Institute of Fuel Symposium Series No 1, London, September 1975.

81. LA NAUZE, R.D., DUFFY, G.J. AND SANDERSON, R., "Burn before burying : An assessment of the utilization of coal wastes to produce power", Eighth National Chemical Engineering Conference, Melbourne, Australia, 24-27 August 1980 (to be presented).

82. LA NAUZE, R.D., DUFFY, G.J., POTTER, E.C. AND BRADSHAW, A.V., "Fluidized combustion of coal washery washes", Third Engineering Foundation Conference on Fluidization, Hennicker, USA, September 1980 (to be presented).

83. POERSCH, W. AND ZABESCHEK, G., "Fluidized bed combustion of flotation tailings", Second Engineering Foundation Conference on Fluidization, Cambridge, England, 2-6 April 1978, p. 292-296.

84. THRING, M.W., SHARP, J.E. AND LE SUER, P.K., "British ideas for a new kind of locomotive with fluidized bed combustion", Spectrum No 153, 1978.

85. CUSDIN, D.R. AND VIRR, M.J., "A marine fluidized bed waste heat boiler : Design and operating experience", Transactions of the Institute of Marine Engineers, Vol 91, 1979.

86. McNAIR, E.J., "Future fuels for the Royal Navy", Energy World, March 1979, p. 4-8.

87. HOY, H.R. AND ROBERTS, A.G., "Fluidized combustion of coal at high pressures", AIChE Symposium Series, Vol 68, No 126, 1972, p. 225-230.

88. HOY, H.R., "Work by the NCB on the development of atmospheric and pressurized fluidized bed combustion", I Mech E Conference : Power from Coal, 10 April 1979, p. 1-10.

89. SCHILLING, H.D., SCHRECKENBERG, H. AND WIED, E., "A new concept for the development of coal burning gas turbines", Gas Turbine Conference and Products Show, ASME Paper 78-GT-40, London, England, 9-13 April 1978.

90. MOSKOWITZ, S. AND WETH, G., "Design of a pressurized fluid bed coal fired combined cycle electric power generation plant", Gas Turbine Conference and Products Show, ASME Paper 78-GT-135, London, England, 9-13 April 1978.

91. MOSKOWITZ, S., WETH, G. AND LEON, A., "Development of a coal fired pressurized fluidized bed for combined cycle power generation", Gas Turbine Conference and Products Show, ASME Paper 80-GT-189, New Orleans, USA, 10-13 March 1980.

92. MOGUL, J., MOSKOWITZ, S. AND WOLOSIN, S.M., "Materials for pressurized fluidized bed air-heater system", Sixth International Fluidized Bed Conference, Atlanta, Georgia, USA, April 1980.

93. JUDD, M.R. AND ELEFTHERIADES, C.M., "Multistage fluidized bed coal combustor", 14th IECEC Conference, Boston, USA, 5-10 August 1979.

94. JUDD, M.R., ELEFTHERIADES, C.M. AND DAWSON, M.F., "Combustion of coal in a multistaged pressurized fluidized bed", Institute of Energy Conference : Fluidized Combustion, Systems and Applications, London, England, November 1980, (to be presented).

95. ELLIOTT, D.E., "Exploiting fluidized-bed combustion", Second International Conference on Fluidized bed Combustion, Hueston Woods, USA, 4-7 October 1970.

96. METCALFE, C.I. AND HOWARD, J.R., "Towards higher intensity combustion : Rotating fluidized beds", Second Engineering Foundation Conference on Fluidization, Cambridge, England, 2-6 April 1978, p. 276-279.

97. DEMIRCAN, N., GIBBS, B.M., SWITHENBANK, J. AND TAYLOR, D.S. "Rotating fluidized bed combustor", Second Engineering Foundation Conference on Fluidization, Cambridge, England, 2-6 April 1978, p. 270-275.

98. LEVY, E.K., REZA HASHEMI, S.M., LONDON, E.J., TABATABIE-RAISSI, A. AND CHEN, J.C., "Operation of a centrifugal fluidized bed with continuous feed and removal of bed material", 14th IECEC Conference, Boston, USA, 5-10 August 1979.

99. GILMOUR, I.A., "Fluidized-bed combustion of coal", New Zealand Engineering, 15 June 1975.

100. IAMMARTINO, N.R. "Fluidized-bed combustion : A better way to burn coal", Chemical Engineering, Vol 83, No 12, 7th June 1976.

101. CAPLIN, P.B., "The practical and commercial application of fluidized bed combustion", Energy Digest, Vol 7, No 5, October 1978.

102. KNOTT, C.M., "Introduction to industrial boiler firing by fluidized combustion : Investing in future technology", Annual Conference of the Combustion Engineering Association; Energy, Today and Tomorrow ; Eastbourne, 1977.

103. CHUTER, A., "NCB chooses fluid bed to fire three pit boilers", The Engineer, 26 July 1979.

104. BUTLER, P. "Fluid bed is proving a hot number at 80% efficiency", The Engineer, 7 September 1978.

105. BUTLER, P., "The NCB pushes for increased use of coal fired fluid beds", The Engineer, 21 June 1979.

106. BUTLER, P., "Final test bed for fluid bed boilers", The Engineer, 20 September 1979.

107. BUTLER, P. "Shell boilers will burn cheap and nasty fuels on a fluid bed", The Engineer, 13 July 1978.

108. HIGHLEY, J. British Patent 2006 942 A, Fluidized Bed Apparatus, 10 May 1979.

109. VIRR, M.J. "Commercialization of small scale fluidized combustion techniques", Fourth International Conference on Fluidized Bed Combustion, McLean, Virginia, 9-11 December 1975.

110. ANONYMOUS, "Flameless furnace produces cheap power from garbage and other refuse", Aircraft Engineering, March 1979, p. 17-20.

111. McKENZIE, E.C., "Fluidized bed firing boilers", The Heating and Air Conditioning Journal, Vol 47, No 542, March 1977, p. 28-32.

112. BEACHAM, B. AND MARSHALL, A.R. "Experiences and results of fluidized bed combustion plant at Renfrew", Journal of the Institute of Energy, June 1979, p. 59-64.

113. THURLOW, G.G., "The combustion of coal in fluidized beds", Proceedings of the Institution of Mechanical Engineers, Vol 192, No 15, 1978, p. 145-156.

114. BUTLER, P. "Coal fired fluidized beds will soon be raising steam for industry", The Engineer, 27 March 1980.

115. GAMBLE, R.L. AND WARSHANY, F.R., "Commercial development of atmospheric fluidized bed utility steam generators", Joint Power Generation Conference, sponsored by ASME Power and Fuels Division and IEEE Power Engineering Society, Portland, Oregon, USA, 28 September - 2 October 1975.

116. ANONYMOUS, "Fluidized bed combustion unit operational", Chemical and Engineering News, Vol 57, No 48, 26 November 1979, p. 24-25.

117. ANDERSON, J.B. AND NORCROSS, W.R. "Fluidized bed industrial boiler", Combustion, February 1979, p. 9-14.

118. WALKER, D.J., McILROY, R.A. AND LANGE, H.B., "Fluidized bed combustion technology for industrial boilers of the future : A progress report", Combustion, February 1979, p. 26-32.

119. BERRY, R.I., "Fluid-bed gets the nod", Chemical Engineering, 8 October 1979, p. 60, 62, 64.

120. SCHWIEGER, B. "Commercializing fluidized bed boilers", Power, July 1979, p. 79.

121. KEAIRNS, D.L., YANG, W.C., NEWBY, R.A., HAMM, J.R. AND ARCHER, D.H. "Circulating bed boiler concepts for steam and power generation", Proceedings 13th IECEC Conference, San Diego, California, 20-25 August 1978, p. 540-547.

122. REH, L., "Einsatzmöglichkeiten der Wirbelschichtfeuerung als Kraftwerksfeuerung", VGB Kraftwerkstechnik, Vol 56, No 8, August 1976, p. 509-518.

123. SCHILLING, H.-D., "Technischer Stand und Wirtschaftlicher Chancen der Wirbelschichtfeuerung zur Strom- und Wärmeerzeugung aus Kohle", Chemie Ingenieur Technik, Vol 51, No 3, 1979, p. 184-191.

124. SCHILLING, H.-D., "New technologies for coal based electricity generation", Proceedings 4th International Conference on Coal Research, Vol III, Vancouver, Canada, October 1978, p. 1137-1157.

125. SHARAN, H.N., "Research, development, demonstration and commercialization programmes for better utilization of coal", Bharat Heavy Electricals Ltd., New Delhi, September, 1977.

126. RAMA PRASAD, V.R., "Combustion of high ash, Indian coals", Fluidized Combustion Conference, Vol 1, The Institute of Fuel Symposium Series No 1, London, September 1975.

127. ABBI, Y.P., BANERJI, M., GHOSH, M.K., MALLIAH, K.T.U. AND SHARAN, H.N., "Development of fluidized combustion boilers for Indian coals", AIChE Symposium Series Vol 74, No 176, 1978, p. 162-169.

128. SADDY, M. AND SZEGO, J., "Economics and concepts of industrial coal fluidized bed combustion in Brazil", Second Miami International Conference on Alternative Energy Sources", Miami Beach, Florida, 10-13 December 1979.

129. CENTRO DE TECNOLOGIA PROMON "First Brasilian F.B.C. prototype in development by CTP", CTP Newsletter, Vol 4, No 1, February 1979.

130. DU TOIT, P., "A progress report on preliminary investigations into the fluidized-bed combustion of large coal, Fuel Research Institute of South Africa, Report No 33 of 1976, 6 May 1976.

131. FUEL RESEARCH INSTITUTE OF SOUTH AFRICA, "Forty-eighth annual report of the Fuel Research Board for the year ended 31st December 1978".

132. HOLSTEYN, H.W., "Fluidized combustion", The Clean Air Journal, Vol 3, No 1, November 1976.

133. MAGASINER, N., "Development of a coal-fired packaged boiler designed specifically for operation in Southern Africa", The South African Mechanical Engineer, Vol 25, No 2, February 1975, p. 52.

134. BROUGHTON, J., "Gas combustion in shallow fluidized beds", Applied Energy, Vol 1, 1975, p. 61-79.

135. COLE, W.E. AND ESSENHIGH, R.H., "Fluid bed combustion of natural gas", Second Conference on Natural Gas Research and Technology, American Gas Association and Institution of Gas Technology, Atlanta, Georgia, 5-7 June 1972.

136. ANSON, D. AND GODRIDGE, A.M., "A simple method for measuring heat flux", Journal of Scientific Instruments, Vol 44, 1967, p. 541-544.

137. REH, L. "Fluidized bed processing", Chemical Engineering Progress, Vol 67, No 2, February 1971.

138. JANSEN, K., SCHILLING, H.-D. AND PETERS, W., "Wesentliche Merkmale der Wirbelbettverbrennung unter besondere Berücksichtigung der Wärmeübergangskoeffizienten", VDI-Berichte 211, Verbrennung und Feuerungen, VDI Verlag, 1973.

139. BATTOCK, W.V. AND PILLAI, K.K., "Particle size in pressurized combustors", Fifth International Conference on Fluidized Bed Combustion, Washington, USA, December 1977.

140. STAUB, F.W. AND CANADA, G.S., "Effect of tube bank and gas density on flow behaviour and heat transfer in fluidized beds", Second Engineering Foundation Conference on Fluidization, Cambridge, England, 2-6 April 1978.

141. KOLENKO, T. AND COLLIN, R. "Combustion of coal in a fluidized bed", Second Engineering Foundation Conference on Fluidization", Cambridge, England, 2-6 April 1978.

142. RICHARDSON, J.F. AND SHAKIRI, K.J. "Heat transfer between a gas-solid fluidized bed and a small immersed surface", Chemical Engineering Science, Vol 34, 1979, p. 1019-1029.

143. HOTTEL, H.C. "Radiative heat transfer in combustion chambers", The Melchet Lecture for 1960, Journal of the Institute of Fuel, June 1961, p. 220-234.

144. STOTT, J.B. AND GARROD, C.W., "Calculations of radiative and convective heat transfer in combustion chambers", Journal of the Institute of Fuel, September 1975, p. 115-123.

145. JOHNSTON, T.R. AND BEER, J.M. "The zone method of analysis of radiant heat transfer : a model for luminous radiation", Journal of the Institute of Fuel, September 1973, p. 301-309.

146. HILDEBRAND, F.B. "Introduction to numerical analysis", McGraw-Hill Book Company, Second Edition, 1974, p. 561-575.

147. LAND, T. AND BARBER, R. "Suction Pyrometers in Theory and Practice", Journal of the Iron and Steel Institute, Vol 184, November 1956, p. 269-273.

148. JACKSON, R. "The Measurement of Gas Temperature by Thermocouples", BCURA Monthly Bulletin, Vol 14, No 2, February 1950, p. 33-39.

149. BARBER, R., JACKSON, R. AND THURLOW, G.G., "A Suction Pyrometer for Measuring Gas Exit Temperatures from the Combustion Chambers of Water Tube Boilers", Journal of the Institute of Fuel, August 1954, p. 408-416.

150. LAND, T. AND BARBER, R., "The Design of Suction Pyrometers", Transactions of the Society of Instrument Technology, Vol 6, No 3, September 1954.

151. GODRIDGE, A.M. AND THURLOW, G.G., "The Use of the Suction Pyrometer in Pulverized-Fuel-Fired Furnaces", Journal of the Institute of Fuel, December 1955, p. 601-609.

152. CHEDAILLE, J. AND BRAUD, Y., "Industrial Flames, Volume 1, Measurements in Flames", I.F.R.F., Edward Arnold, Great Britain, 1972.

153. WHEATER, R.L. AND HOWARD, M.H., "Furnace Heat Absorption in Paddy's Run Pulverized-Coal-Fired Steam Generator Using Turbulent Burners, Louisville, Ky., Part 1", Transactions of the ASME Vol 72, October 1950, p. 893-923.

154. NORTHOVER, E.W. AND HITCHCOCK, J.A., "A Meter for the Determination of Local Heat Transfer Coefficient", Proceedings of the Institution of Mechanical Engineers, Vol 178 Pt 31 (i), 1963-64, p. 6-11.

155. NORTHOVER, E.W. AND HITCHCOCK, J.A., "A Heat Flux Meter for use in Boiler Furnaces", Journal of Scientific Instrum., Vol 44, 1967, p. 371-374.

156. HOOGENDOORN, C.J., BALLINTIJN, C.N., AND DORRESTEIJN, W.R., "Heat Flux Studies in Vertical Tube Furnaces", Journal of the Institute of Fuel, December 1970, p. 511-516.

157. LLEWELYN, R.P., "The Temperature Distribution in a Heat Flux Pad Meter", Journal of the Institute of Fuel, July 1969, p. 279-282.

158. KREITH, F. "Principles of Heat Transfer", International Textbook Co., Second Edition, 1965.

159. DUSINBERRE, G.M., "Heat Transfer Calculations by Finite Differences", International Textbook Co. 1961.

160. ALBRECHT, W., "Die analytische Berechnung der Temperaturverteilung in Flossenrohren", Energie Vol 20, No 12, p. 385-389.

161. MORROW, N.L., BRIEF, R.S., AND BERTRAND, R.R., "Sampling and Analysing Air Pollution Sources", Chemical Engineering, 24 January 1972, p. 85-98.

162. HAWKSLEY, P.G.W., BADZIOCH, S. AND BLACKETT, J.H. "Measurement of Solids in Flue Gases", British Coal Utilisation Research Association, Leatherhead, England; Adlard & Son Ltd., Dorking, 1961.

163. BLOOMFIELD, B.D. "Source Sampling" from Air Sampling Instruments for Evaluation of Atmospheric Contaminants, by the American Conference of Governmental Industrial Hygienists, P.O. Box 1937, Cincinnati, Ohio, Fourth Edition 1972.

164. HOLTON, W.C. AND SCHULZ, E.J. "Some Notes on Dust Sampling Equipment and Technique", Trans ASME, October 1953, p. 1327-1331.

165. DAVIS, I.H. "Sampling Probes for Duct and Stack Sampling" from Air Sampling Instruments for Evaluation of Atmospheric Contaminants, by the American Conference of Governmental Industrial Hygienists, Cincinnati, Ohio, Fourth Edition 1972.

166. DENNIS, R., SAMPLES, W.R., ANDERSON, D.M. AND SILVERMAN, L., "Isokinetic Sampling Probes", Industrial and Engineering Chemistry, Vol 49, No 2, February 1957, p. 294-302.

167. NATIONAL COAL BOARD, "Improved NCB Apparatus for Measuring Flue Gas Dust Concentrations", The Steam and Healing Engineer, February 1970, p. 12-15.

168. HAWKSLEY, P.G.W., BADZIOCH, S. AND BLACKETT, J.H. "Improved Sampling Equipment for Solids in Flue Gases", Jnl Inst Fuel, April 1958, p. 147-160.

169. GRANVILLE, R.A. AND JAFFREY, W.G. "Dust and Grit in Flue Gases, Gravimetric Sampling of Solid Particles, Engineering, 27 February 1959, p. 285-288.

170. STAIRMAND, C.J., "The Sampling of Dust-Laden Gases" Trans Instn Chem Engr, Vol 29, 1951, p. 15-44.

171. VDI-WÄRMEATLAS, VDI-Verlag GmbH, 1963.

172. BRANDT, F. "Eine Allgemeine Darstellung der Stoffwerte von Rauchgasen für beliebige Brennstoffen", Brennstoff-Wärme-Kraft, Vol 16, No 2, February 1964.

173. SCHUMACHER, A. AND WALDMANN, H. "Wärme und Strömungstechnik im Dampferzeugerbau", Vulkan-Verlag, 1973.

174. PERRY, R.H. AND CHILTON, C.H. (Editors), Chemical Engineers' Handbook, Fifth Edition, McGraw-Hill, Kogakusha, 1973.

175. ANDERSON, V.L. AND MACLEAN, R.A. "Design of Experiments : A Realistic Approach", Marcel Dekker Inc., New York, 1974.

176. BROWNLEE, K.A. "Statistical Theory and Methodology in Science and Engineering", John Wiley and Sons Inc., Second Edition, 1965.

177. DAVIES, O.L. "The Design and Analysis of Industrial Experiments", Published for Imperial Chemical Industries by Oliver and Boyd (London and Edinburgh), 1963.

178. MORONEY, M.J. "Facts from Figures", Penguin Books Ltd., Great Britain, Third Edition, 1956.

179. WILLIAMS, E.J. "Regression Analysis", John Wiley and Sons, 1959.

STANDARDS REFERRED TO :

BS 893 : 1940 The Method of Testing Dust Extraction Plant and the Emission of Solids from Chimneys of Electric Power Stations.

BS 1016 : Methods for the Analysis and Testing of Coal and Coke.
Part 3 : 1965 Proximate Analysis of Coal
Part 5 : 1972 Gross Calorific Value of Coal and Coke
Part 14 : 1963 Analysis of Coal Ash and Coke Ash
Part 16 : 1971 Reporting of Results

BS 1377 : 1975 Methods of Test for Solids for Engineering Purposes.

BS 1796 : 1976 Methods for the Use of B.S. Fine Mesh Test-Sieves.

BS 1916 : Limits and Fits for Engineering
Part 1 : 1953 Limits and Tolerances
Part 2 : 1953 Guide to the Selection of Fits.

BS 2885 : 1974 Code for Acceptance Tests on Stationary Steam Generators of the Power Station Type.

BS 3405 : 1971 Simplified Methods for the Measurement of Grit and Dust.

APPENDICES

APPENDIX A : Detailed Design of Components

APPENDIX B : Detailed Design and Calibration of Instrumentation

APPENDIX C : Characteristics of the Coals burnt and the Sand used as the Bed Material

APPENDIX D : General Calculations

APPENDIX E : The Overbed Feed System

APPENDIX F : Statistical Analysis

APPENDIX G : Tabulation of Results

APPENDIX H : Details of Radiant Heat Transfer in the Freeboard Region

APPENDIX I : Summary of the Previously Derived Combustion Model

APPENDIX J : Complete Table of Contents, List of Tables and List of Figures.

APPENDIX A

DETAILED DESIGN OF COMPONENTS

A number of details pertaining to different components of the test facility are included on the following pages. These details are not necessary for the general understanding of the operation of the test facility but provide information which may be of value when comparing results with similar forms of equipment.

In addition, a number of photographs of the test rig are included to facilitate an understanding of the layout and general dimensions of the test facility. These photographs have been included after the drawings and are labelled as Plates A1 to A6. A brief description is produced below for each of the figures and photographs.

Figure A1 : Cross Section of the Combustor Vessel

The combustor vessel is supported on three legs and stands some 1 200 mm off the ground level to facilitate the removal of the windbox and to provide easy access to the inside of the flue. The position of the windbox is indicated in dotted lines together with the position of a 100 mm slumped bed of inert material. Special note should be made of the secondary air windboxes, the positions of the pilot burners, and the arrangement of the downcomer pipe for the provision of a natural circulation cooling loop. For simplicity the horizontal cooling tube has not been included in the diagram.

Figure A2 : The Primary Air Windbox

The primary air windbox extends 200 mm into the combustor vessel to which it is bolted. An asbestos seal on the flange which bolts to the vessel prevents any leakage of fluidizing air from the vessel. The figure further includes

the arrangement of the fluidizing nozzles on the upper surface of the windbox.

Figure A3 : Fluidizing Nozzle and Stub Attachment

The fluidizing nozzle is fabricated from hexagonal bar to enable it to be bolted to a stub which is welded to the upper plate of the windbox. Both nozzle and stub are illustrated in Figure A3.

Figure A4 : Layout of the Air Supply Pipework to the Combustor Vessel

Air from the high pressure fan is divided into primary and secondary air flow streams. The positioning of the orifice plates should be noted. A further air connection is required for the pneumatic spreading air.

Figure A5 : Layout of the Coal Feed System

An inclined screw conveyer transports the coal from an external hopper to a storage bunker within the test rig building. This is illustrated in Figure A5 together with the relative position of the coal feedchutes and related drum and screw feeders to the combustor vessel. Pressure switches on the coal bunker start the inclined conveyor when the level falls below the lower switch and stop the conveyor when the level of the coal activates the upper switch.

Figure A6 : General Arrangement of the Cooling Tube in the 1 000 mm Diameter Test Rig

Penetrating tubes were welded into the test rig to accommodate a cooling tube with a maximum outside diameter of about 80 mm. The cooling tube is located 170 mm off centre to enable the movement of the heat transfer probe in the central ash pipe.

From Figure A6 it is evident that the cooling tube can easily be removed and replaced by another having a different diameter.

Figure A7 : General Arrangement of the 76,2 mm Diameter Cooling Tube

The cooling tube is connected to a 25 mm NB cooling water circuit. As the tube to be tested consists of a 76,2 mm NB tube, the relevant expansion and reduction pieces have had to be fitted as illustrated in Figure A7. Eight 1,6 mm grooves have been milled 2 mm deep into the tube at the locations indicated to enable 1,5 mm diameter stainless steel sheathed chromel alumel thermocouples to be silver soldered into the tube wall.

Plate A1 : The Fluidized Bed Combustion Test Rig

The photograph was taken prior to modifications required to introduce the horizontal cooling tube and before the drive for the above bed feeder had been installed. In any event, the general layout of the test rig is clearly illustrated showing the main start-up gas, the pilot burners, the aoove bed feeder and the screw feeder below, the coal bunker, the secondary air windboxes and the ash removal pipe.

Plate A2 : The Cross Section of the Fluidized Bed Combustion Test Rig

The photograph is a sectional drawing of the previous Plate with labels to illustrate more clearly the positioning of the various components.

Plate A3 : Rear View of the Fluidized Bed Combustion Test Rig

The photograph presents a second view of the combustor vessel

in order to illustrate the two primary air ducts, connections to the two secondary air windboxes, the 200 mm downcomer pipe and the control panel in the background.

Plate A4 : Close-up of the Fluidized Bed Combustion Test Rig

The photograph is a close-up of Plate A1 to illustrate more clearly the gas ignition system, the bed pressure and temperature probes and the two coal feeders.

Plate A5 : The Control Panel

The photograph shows the various components associated with the control and monitoring panel. These include the carbon monoxide and oxygen analysers, the manometer boards, the two multipoint recorders, the remote starting switches for the fan, etc, the damper control potentiometer, various alarms and the switch to activate the flame failure protection system.

Plate A6 : External View of the Fluidized Bed Test Building

The photograph illustrates the test building with the expanded combustor vessel projecting through it. A platform provides access to instrumentation fitted in the exhaust gas ducting. The large steam pipe which vents to atmosphere is clearly evident behind the exhaust ducting which is connected to an existing stack via a square sectioned duct. The high pressure fan, main air control damper and modulating motor, together with the associated primary and secondary air ducting should also be noted.

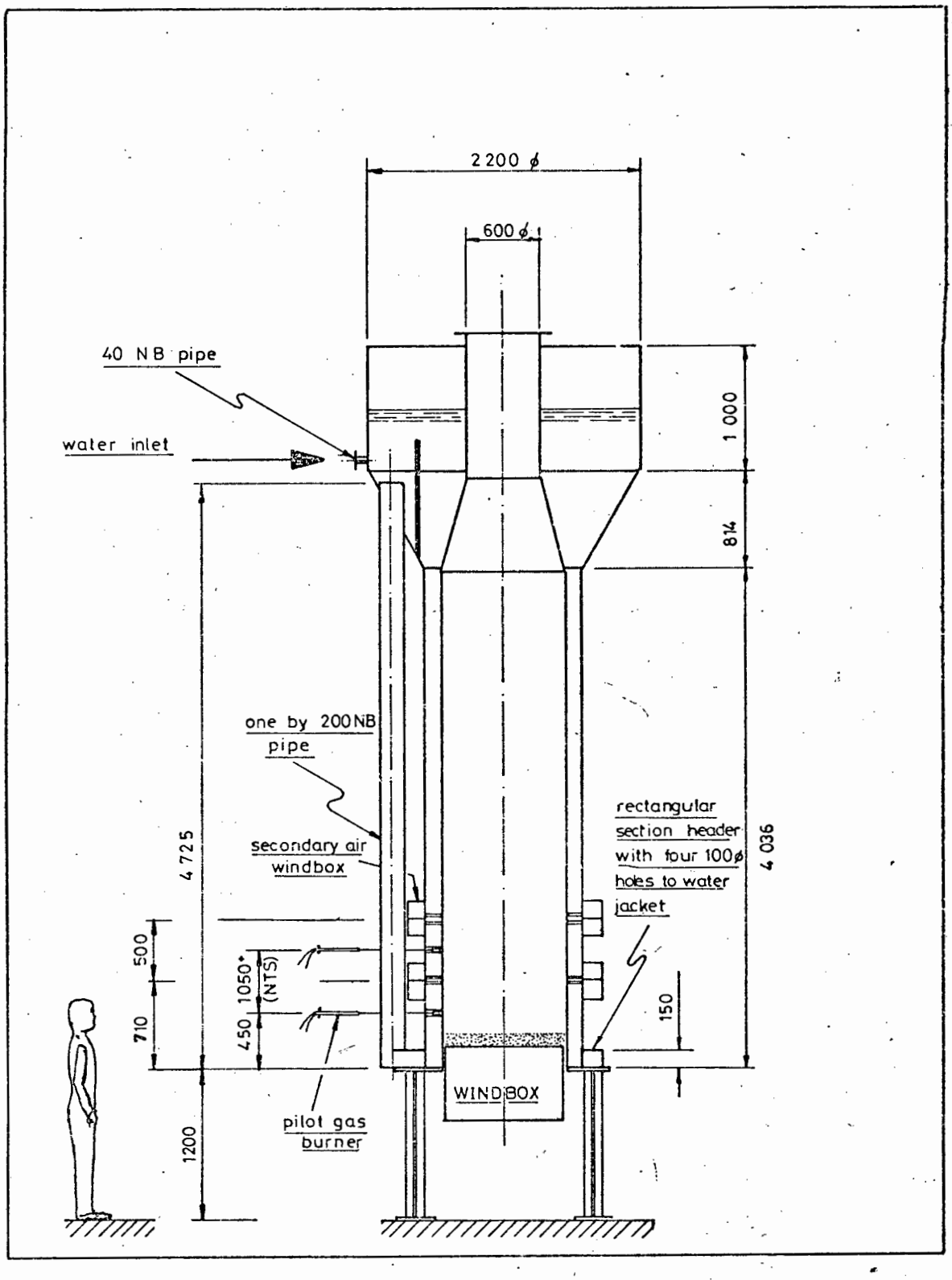

Figure A1 : Cross section of combustor vessel to illustrate the general arrangement of the vessel

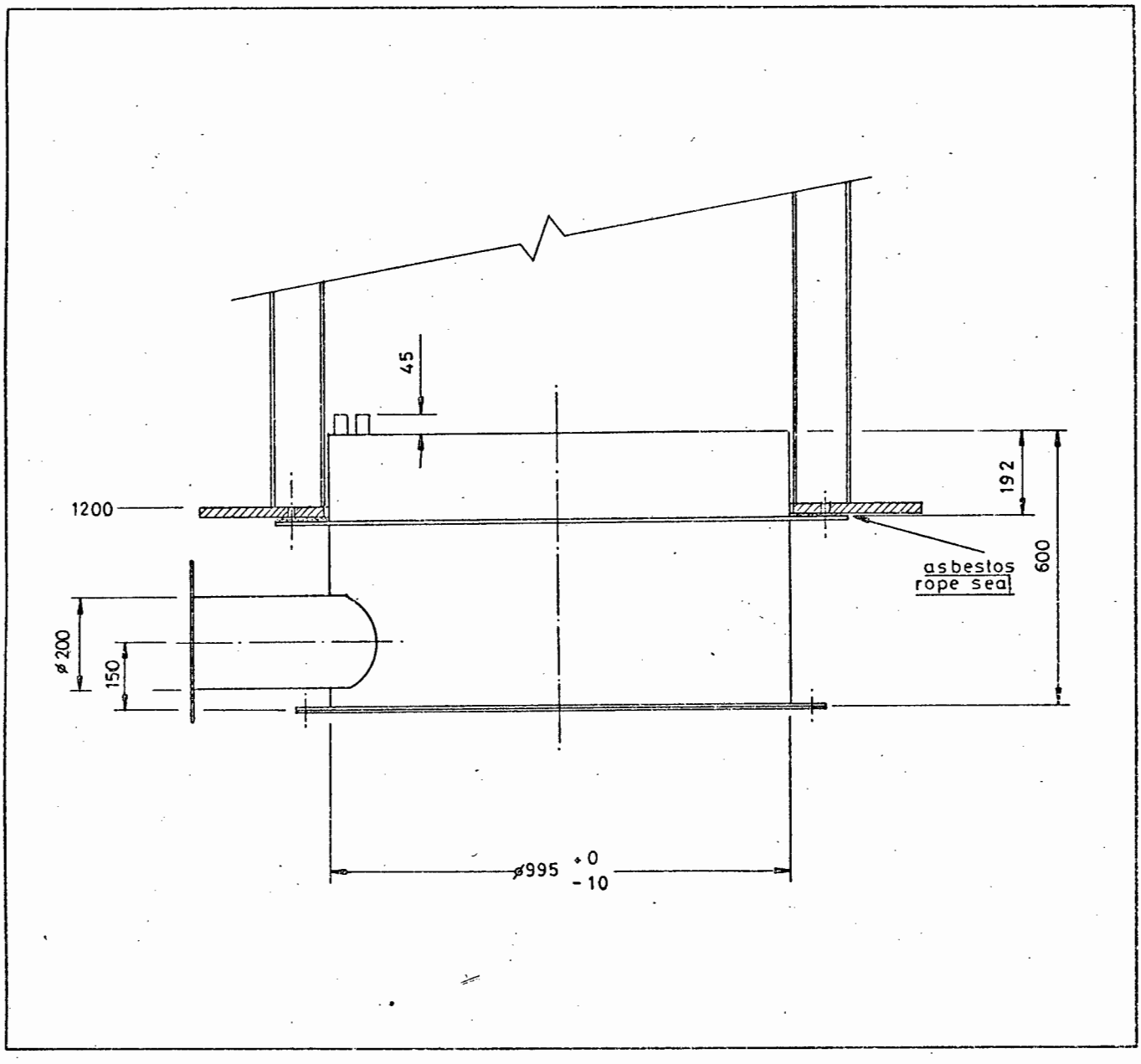

Figure A2 : The primary air windbox

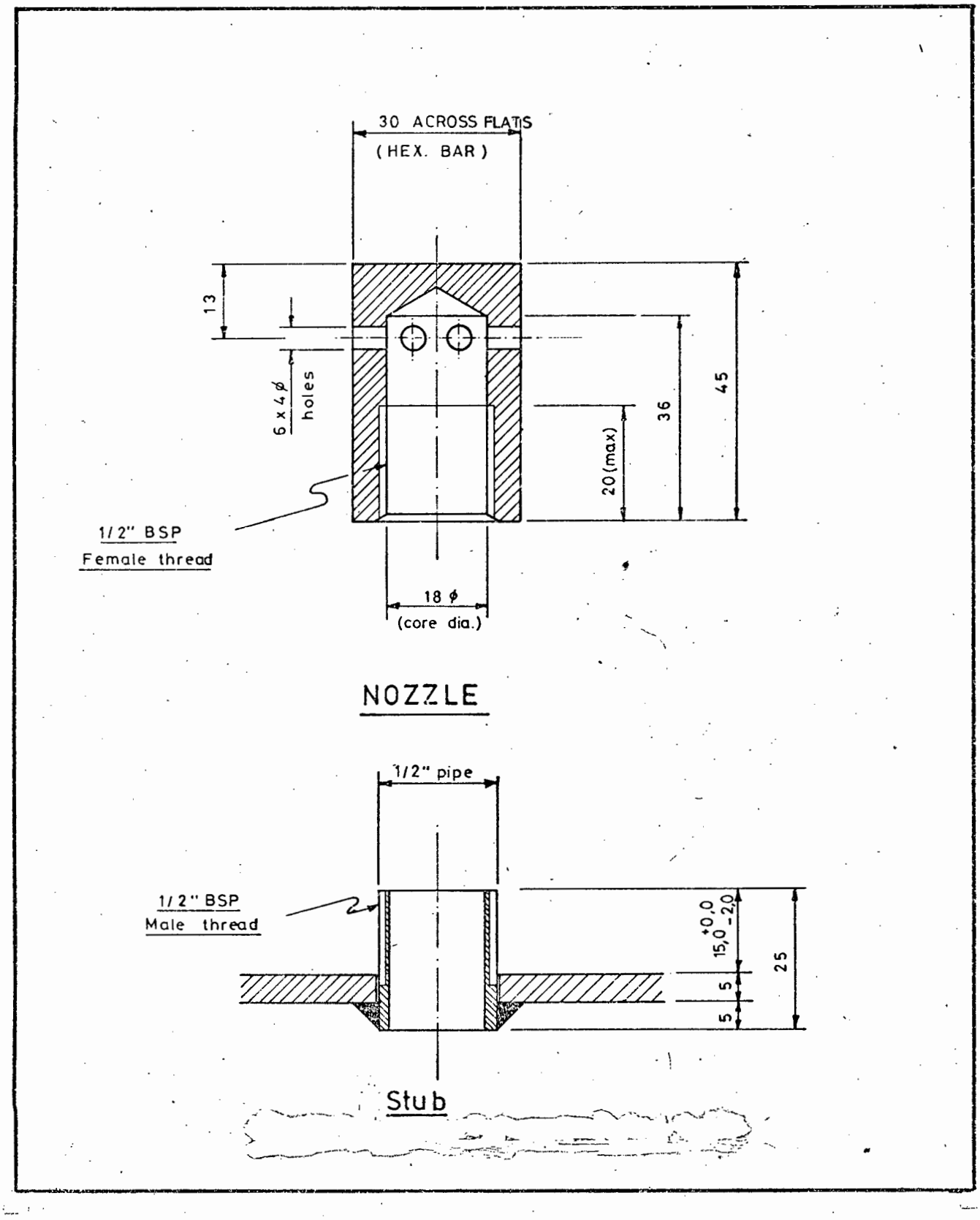

Figure A3 : Detail of Bubble Cap and Stub.

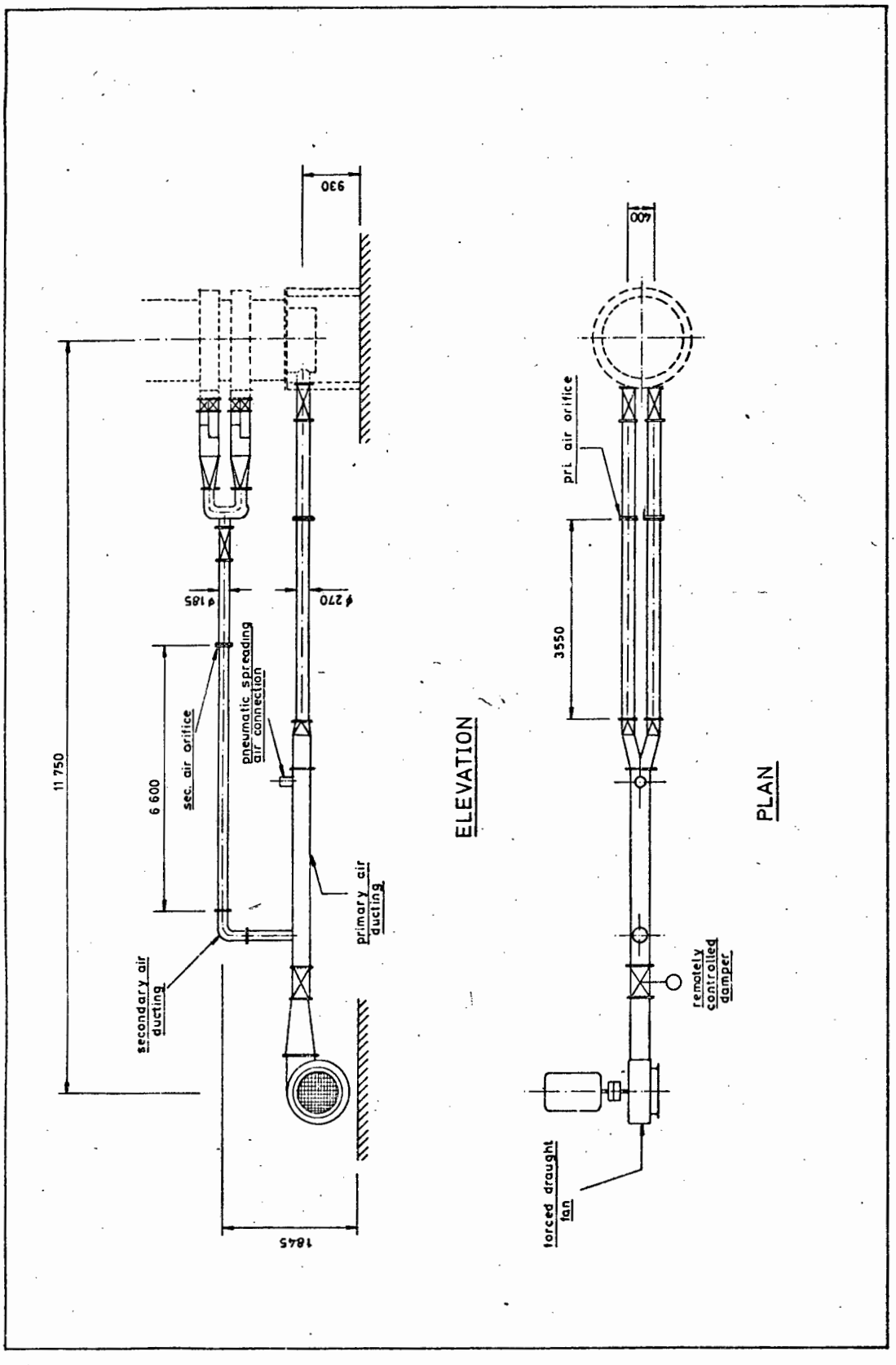

Figure A4 : Layout of air supply to the test rig.

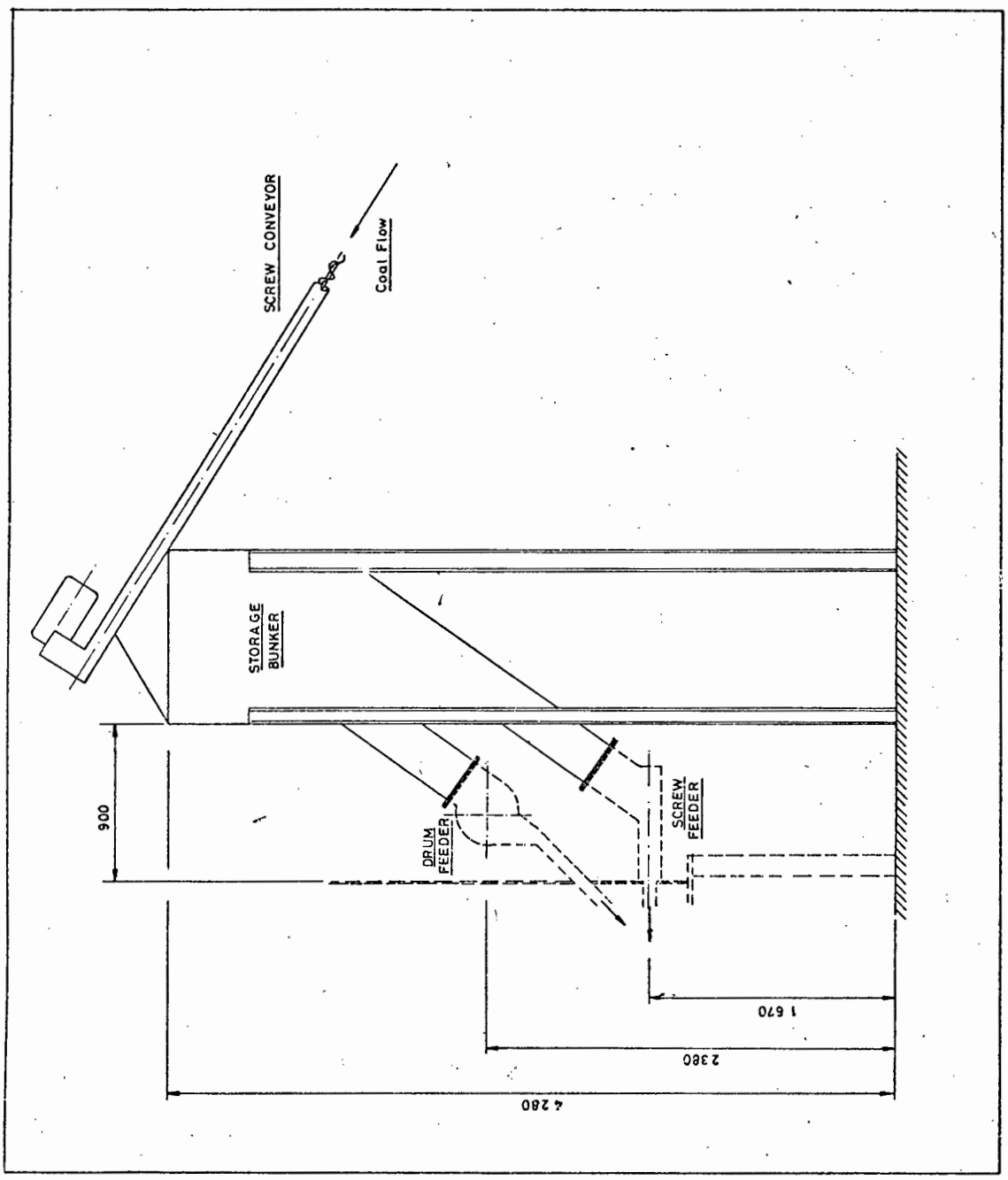

Figure A5 : Layout of the coal feed system

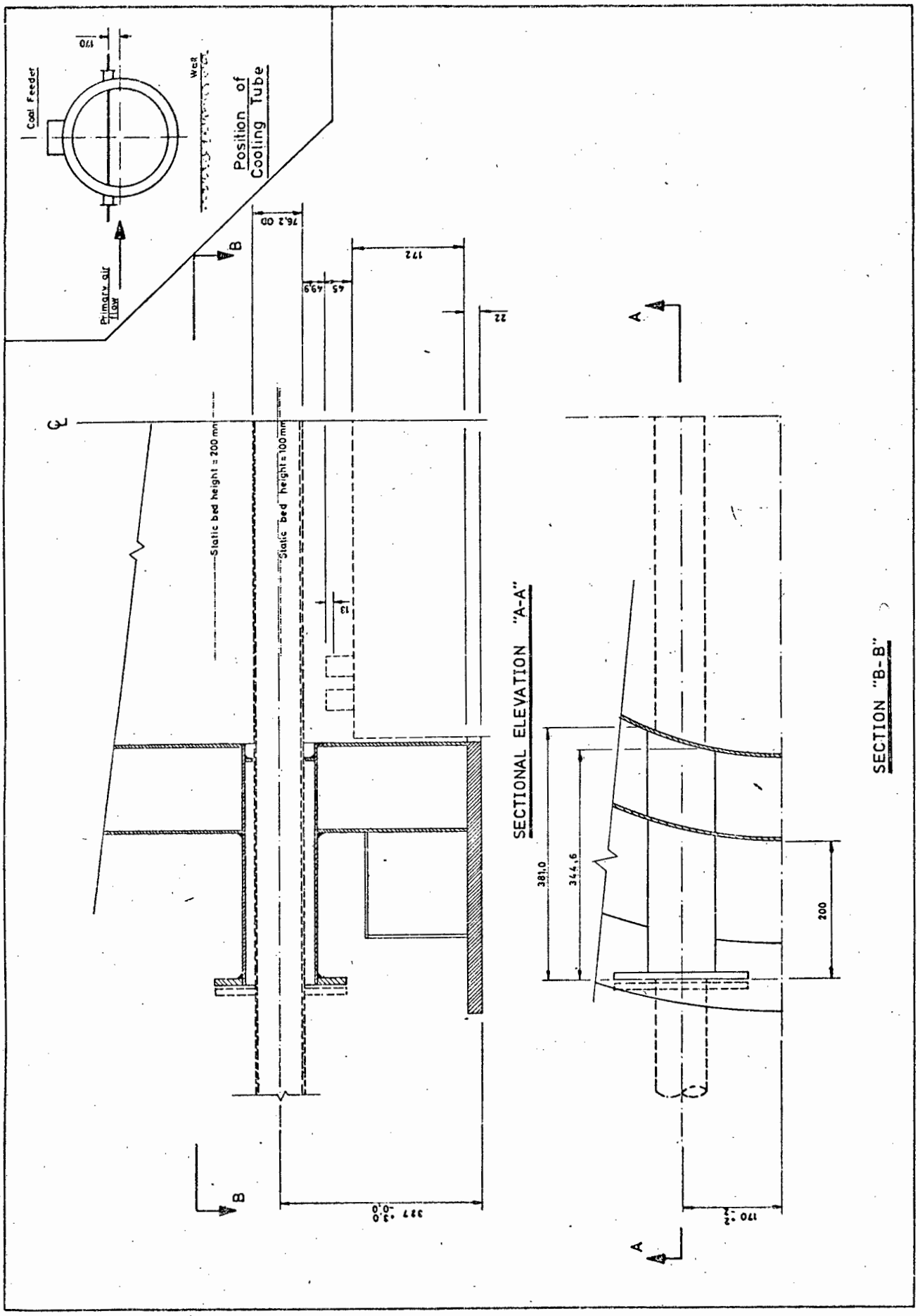

Figure A6 : General arrangement of the cooling tube in the 1000 mm diameter test rig.

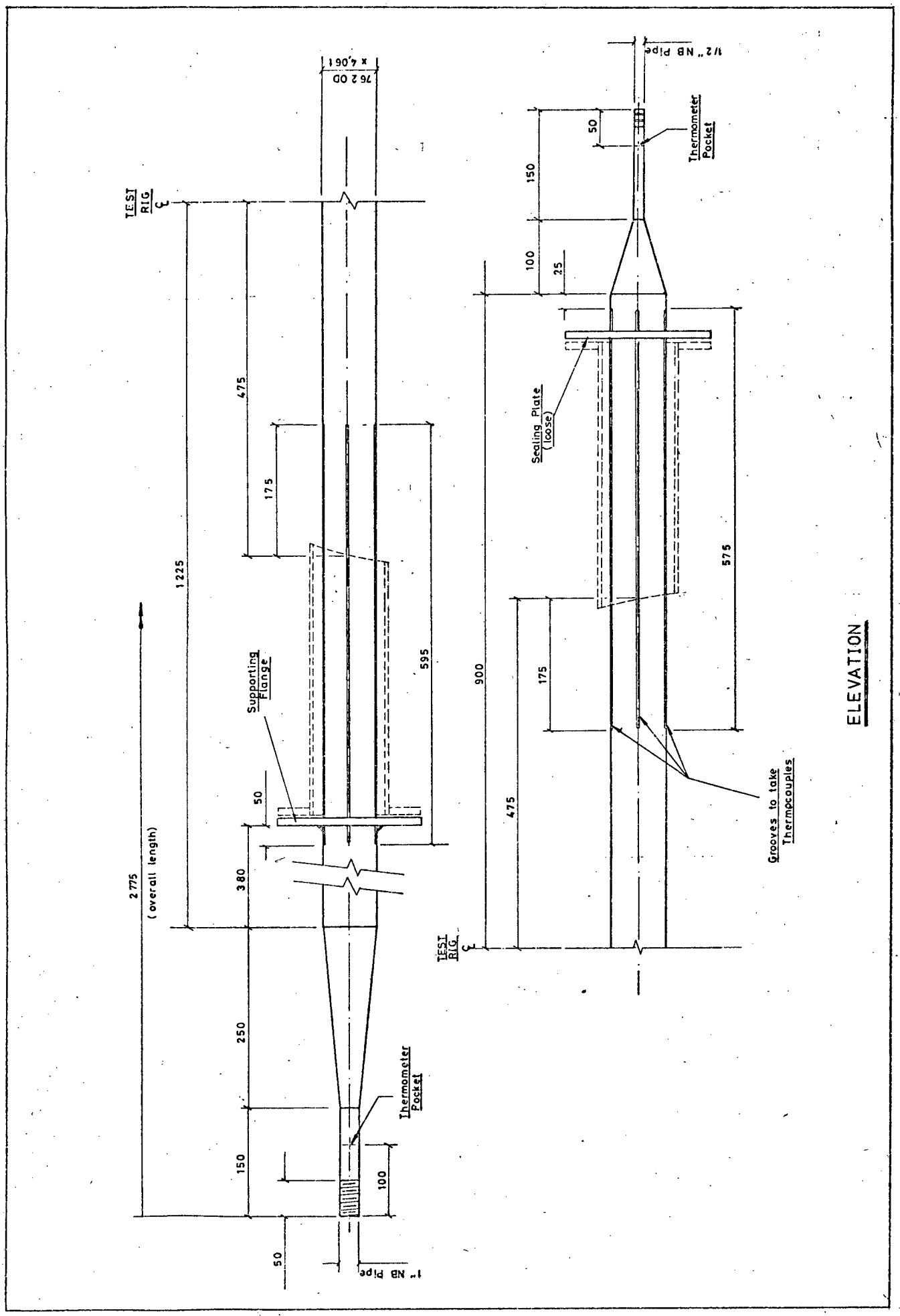

Figure A7 : General arrangement of the 76,2 mm diameter cooling tube.

these operating conditions a more intense combustion takes place at the surface of the bed leading to temperatures in excess of the bed temperature and as a consequence resulting in high rates of heat transfer. The particulates are too dispersed in this zone to remove this excess heat to create the isothermal conditions which exist in the denser fluidized bed.

An important feature of the shallow fluidized bed, is its expansion relative to its original height. This relative expansion is considerably greater in shallow beds than in deep beds. A large number of bed pressure readings were obtained and correlated into an equation relating the bed expansion to the fluidizing velocity. The correlation had the effect of smoothing the dynamic bed height data, particularly in view of the fluctuating pressure readings on which this correlation was based. The expanded bed data, were utilized in deriving a correlation for the heat transfer to an immersed horizontal tube. However, the main function of expanded bed data lies in predicting the amount of surface which can be immersed by the bed under different operating conditions thereby defining the turn-down characteristic of the shallow fluidized bed.

Heat transfer from the bed to both the surrounding wall and an immersed horizontal tube have been studied. The information was obtained at high bed temperatures and at velocities typical of those anticipated for industrial fluidized bed steam generating equipment. In order to derive a correlation for the convective heat transfer coefficient, the radiative and convective components were assumed to be additive in forming the total measured heat transfer coefficient. Further, the gas convective component was assumed to be negligible and as a consequence the resulting correlations relate to the particulate convective heat transfer coefficients. Two correlations were formed, the first referring to the heat transfer coefficient between the bed and the surrounding wall, and the second between the bed and the immersed horizontal tube. Both

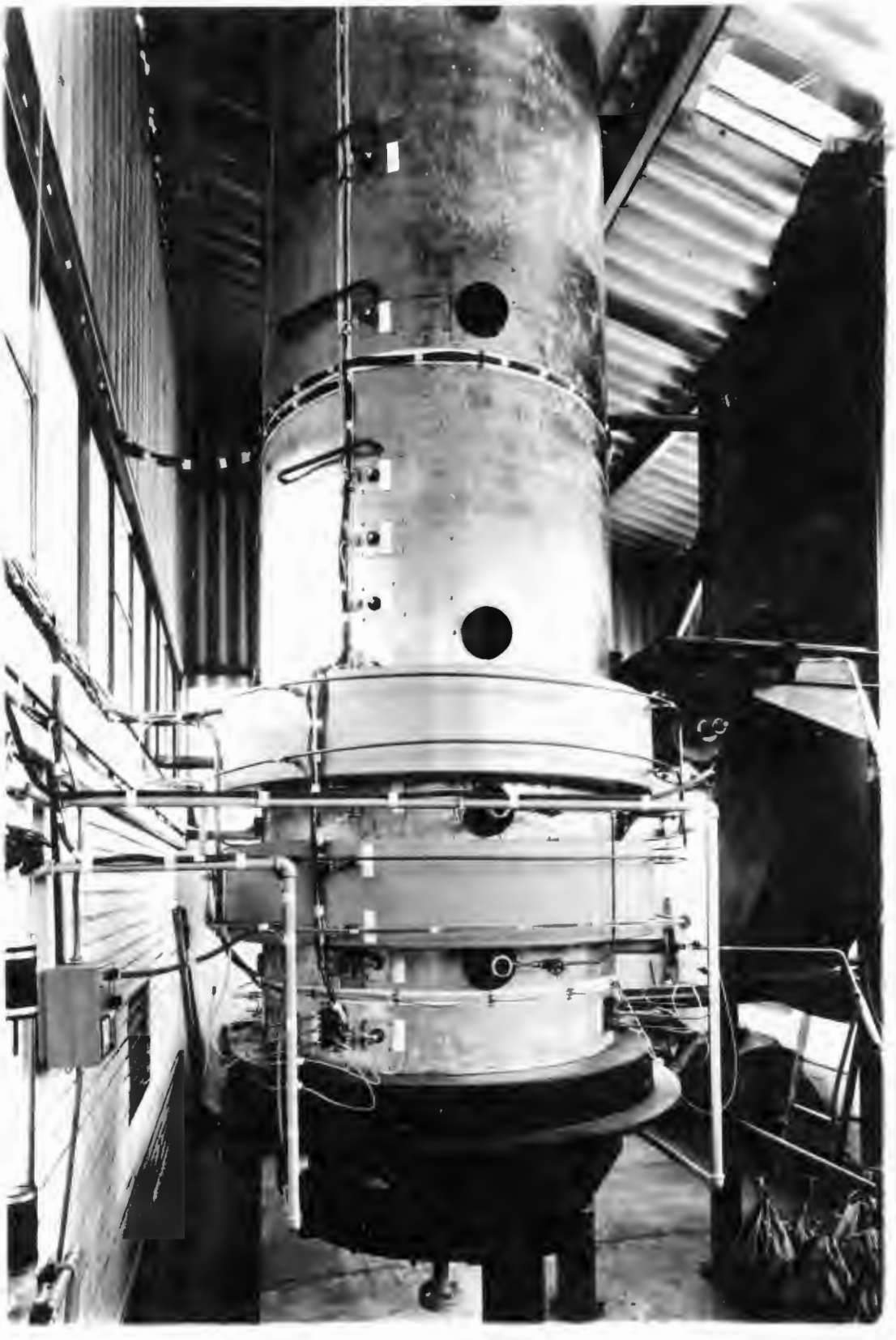

PLATE A1 : The Fluidized Bed Combustion Test Rig

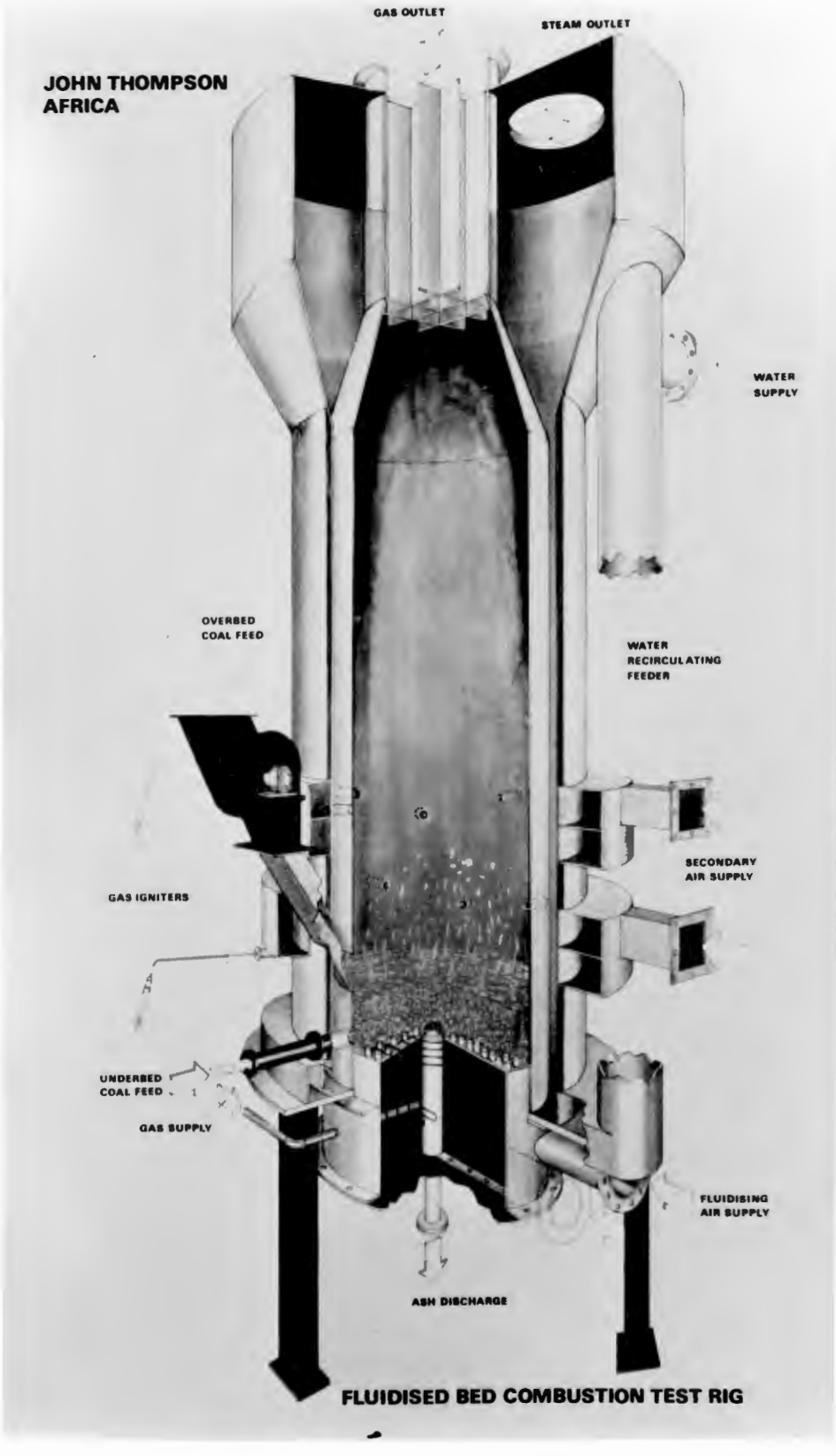

PLATE A2 : Cross-Section of the Fluidized Bed Combustion Test Rig

PLATE A3 : Rear View of the Fluidized Bed Combustion Test Rig

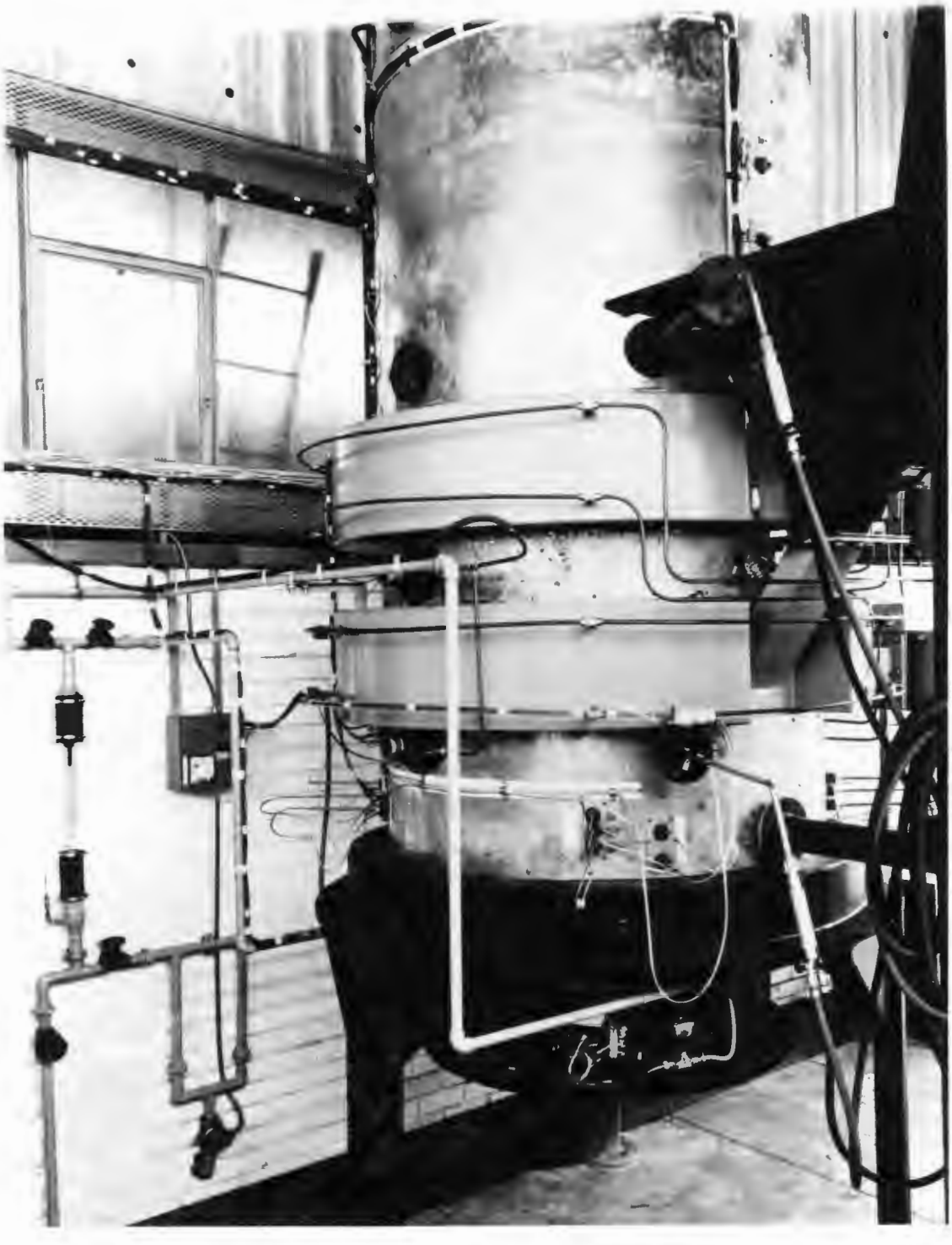

PLATE A4 : Close-up of the Fluidized Bed Combustion Test Rig

PLATE A5 : The Control Panel

PLATE A6 : External View of the Fluidized Bed Test Facility

APPENDIX B

DETAILED DESIGN AND CALIBRATION OF INSTRUMENTATION

Much of the instrumentation was specifically designed for use on the 1 000 mm diameter test facility. Details of the more important instruments are contained in this Appendix. Some drawings have been included at the end of the Appendix to illustrate their manufacture as well as their location on the test facility.

B.1 GAS TEMPERATURE MEASUREMENT

B.1.1 Introduction

It is of importance to be able to measure the temperature of a body of gas accurately, in particular when both combustion and heat transfer processes are taking place. The most obvious method of measurement is to insert a probe into the gas so that it attains the gas temperature. The thermocouple represents the most usual form of the probe and though the simple insertion of a thermocouple into a gas stream may yield reasonable results at low temperatures, i.e. below 200°C, use of such a simple probe for the measurement of high gas temperatures can lead to a substantial difference between the measured and the actual gas temperature (147), (148). "The reason for this is that a thermocouple records its own temperature and, if it is inserted in a mass of hot gas enclosed by walls at a temperature lower than that of the gas, the thermocouple gains heat by convection and radiation from the gas and loses heat by radiation to the walls." (149). The radiation from the gas to the thermocouple is in general much smaller than the loss of heat by radiation from the thermocouple to the surrounding walls. This net heat flow by radiation from the thermocouple is of the same order as the heat flow by convection from the surrounding gas. The

thermocouple reading will therefore be intermediate between that of the gas and the surrounding walls. Therefore, in order to enable the temperature of the thermocouple to approach that of the gas, the radiative heat loss to the walls should be reduced whilst the convective heat transfer should be increased. These requirements can be achieved by making use of a suction pyrometer.

B.1.2 The Design of Suction Pyrometers

A suction pyrometer consists of a thermocouple which is enshrouded by a number of concentric radiation shields. The gas is then drawn over the shields and thermocouple, thereby imparting heat by convection to the system. By increasing the number of radiation shields, the radiative heat loss is reduced. However, on increasing the gas velocity the convective heat transfer increases initially until a velocity is reached at which cooling of the gas sample takes place within the probe as a result of adiabatic expansion. Land and Barber (150) recommend the use of a velocity of 150 m/s. In order to assess the performance of the instrument, the efficiency of the pyrometer is introduced. This has been described by Land and Barber (150) as follows:

> "The accuracy of a suction pyrometer depends on the difference in temperature between the gas and the surroundings of the pyrometer. For this reason it is not possible to state the accuracy of a pyrometer of conventional design as "so many degrees Centigrade". If no gas is sucked past the thermocouple and the radiation shields, the pyrometer will have a certain error; when gas is aspirated past the couple and shields, a certain fraction of this error will be eliminated; we will call this fraction the efficiency of the pyrometer".

The efficiency of the pyrometer can therefore be given by the following equation:

$$\textit{efficiency of pyrometer} = (\vartheta_o - \vartheta)/\vartheta_o \qquad (B1)$$

where ϑ_o is the difference between the true temperature and that observed by a simple thermocouple, and ϑ is the difference between the true temperature and that observed by the pyrometer. Both metallic and refractory shields have been used and though each refractory shield is equivalent to two or three metallic shields because of their lower emissivities and thermal conductivities, the use of refractory shields has a number of disadvantages. In particular, the refractory shields are not very robust and are susceptible to damage as a result of thermal shock, they are difficult to fabricate, and finally, the efficiency of pyrometers with refractory shields has been found to deteriorate seriously with operation (147), (149), (150) as a result of increases in emissivity necessitating frequent calibration to ensure that meaningful results are obtained.

B.1.3 The Selected Design

The most common type of suction pyrometer which is also commercially available is that as described by Land and Barber (150). It was decided to use a similar design which could be manufactured locally. In view of the experience of Godridge and Thurlow (151) when using a suction pyrometer to measure the temperature of "dirty gases" resulting from the combustion of pulverized coal it was decided to modify the design of Land and Barber. The design makes use of three concentric Incolloy 600 steel pipes as the radiation shields. The end of the outer shield is closed by means of a refractory plug, causing the gas to enter the pyrometer at right angles to the axis of the shields. This is similar to the design used by the International Flame Foundation, IJmuiden, (152) who further recommend that the gas extraction aperture be located downstream of the gas flow when performing measurements in a pulverized fuel jet. Details of the

design of the radiation shields are illustrated in Figure B1. In view of the heavy dust burden emanating from the fluidized bed combustion process, such an arrangement would be of advantage to limit the particulate matter extracted by the probe. Godridge and Thurlow (151) have investigated the use of a stainless steel gauze mesh placed over the extraction aperture. Although this did restrict the extraction of particulate matter, the effect of the gauze is to cool the gas, thereby reducing the pyrometer efficiency. However the effect of the gauze can be accounted for by conducting separate tests on the pyrometer with and without the gauze shield. It is therefore recommended that the gauze shield only be used on the pyrometer when operating close to the fluidized bed surface.

The complete probe assembly is shown in Figure B2. The probe consists of a stainless steel water jacket made up from standard tubular components. The radiation shields are attached to the end of the jacket, whilst a ceramic sheathed chromel-alumel thermocouple is fitted down the central axis of the probe such that the tip is located within the radiation shields. Means are provided for extracting the gas over the thermocouple and shields as well as for providing cooling water to the jacket.

B.1.4 Performance and Operating Requirements of the Pyrometer

The performance and operating requirements of the pyrometer having the radiation shields illustrated in Figure B1 can be estimated as follows:

Cooling water pressure at inlet - 1,5 bar (20 to 40 psig)
Maximum gas extraction rate - 139 l/s @ 1 000°C
Maximum gas temperature - 1 150°C
Thermocouple : Ceramic Sheathed Chromel Alumel

Table B1 : Anticipated performance of the pyrometer illustrated in Figure B1 and having gas drawn over it at a rate of 0,039 kg/s

Temperature (°C)	Efficiency (%)	Gas Velocity m/s
600	99	103
800	97	126
1 000	93	150
1 150	87	150

B.1.5 Ceramic Measuring Probes

In view of the high sampling gas flow rate required for the efficient operation of the suction pyrometer, as well as from an economic and operating view point, only two suction pyrometers were fabricated. Therefore a series of modified gas temperature measuring probes have been installed at different levels in the 1 000 mm diameter test rig. Each of the probes consist of a 15 mm OD ceramic radiation shield in which a ceramic-sheathed chromel-alumel thermocouple is located as illustrated in Figure B3. Gas is induced to flow over the thermocouple by connecting the outlet of each ceramic radiation shield to a pipe which after passing through a filter is connected to an instrumentation fan as illustrated in the layout diagram of Figure B4. Each of these ceramic probes is calibrated by means of the higher efficiency multiple shielded suction pyrometers.

B.1.6 Calibration of the Incolloy Shielded Suction Pyrometers

The efficiency as defined by equation (B1) of each of the two Incolloy Shielded suction pyrometers has been determined by the two methods suggested by Land and Barber (150). The efficiencies have been found to be similar to those represented in Table B1 for the relevant operating conditions.

B.1.7 Location of the Gas Temperature Measuring Probes

Gas temperature measurements can be made at five different horizontal planes along the combustor vessel as illustrated in Figure B4. At each plane, two probe access holes of 53 mm ID are provided at right angles to each other. A ceramic measuring probe is located at each of these levels. However, although the suction pyrometers could be installed at any of the five levels, only the two levels illustrated in Figure B4 have been utilized.

B.2 THE HEAT FLUX METERS

The heat transfer performance of furnaces in general assumes an average temperature and therefore a mean heat flux. The furnace section of the 1 000 mm diameter test rig comprises in effect a combined fluidized bed combustion and gasification section, and a freeboard zone in which the gasified components are burnt to completion. This represents a complex combustion system and in order to arrive at an accurate representation of the combustion process a more sophisticated approach is required.

Whilst the measurement of the heat flux in the freeboard will enable an assessment of the combustion process, its measurement through the wall enclosing the fluidized bed will enable the direct evaluation of the bed to wall heat transfer coefficient.

B.2.1 Designs of Heat Flux Meters

Wheater and Howard (153) have calculated the heat flux by measuring external tube wall temperatures by means of 0,65 mm diameter glass fibre insulated thermocouple wire. The thermocouples were protected by means of a metal shield and the heat flux was deduced from this external temperature and the water temperature. Alternatively, two thermocouples may be embedded in the tube wall so that the temperature differential

can be measured directly. However, these seemingly direct methods are difficult to apply, particularly as one has to ensure that the thermocouple does not conduct too much heat away from the point being measured, thereby indicating a false measurement. Northover and Hitchcock have developed a flush mounted disc type heat flux meter (154) as well as a meter based on the same principle for use in the measurement of heat flux to boiler tubes (155) to overcome these problems. The principle is based upon measuring the temperature difference induced across a thin pad which is exposed to the heat flux on the one side whilst being insulated on the other with the heat being allowed to flow towards the periphery of the plate. Anson and Godridge (136) have described the use of a particularly robust form of heat flux pad for measuring the heat flow to cooling water tubes based on a similar principle to that employed by Northover and Hitchcock (154). A portable heat flow meter which permits a differentiation between the convective and radiative heat fluxes has been designed by Hoogendoorn et al (156) which is also based on obtaining a temperature differential across a disc. From the above it is evident that although several designs for heat flux or heat flow measuring devices have been proposed, these can be divided into two general categories. In the first the original direction of the heat flow is undisturbed within the heat flux meter, whilst in the second the heat flow is caused to change direction.

B.2,2 The Design Selected

The basic requirements of a device to measure the heat flux in the 1 000 mm diameter test rig can be listed as follows:

a) it should enable accurate measurement of the heat flow

b) it is to be robust

c) easily manufactured

d) the surface properties should be similar to the heat exchange surface being analysed.

It was decided to apply a design similar to that of Anson and Godridge (136) for the measurement of the heat flux in the 1 000 mm diameter fluidized bed test rig. Details of the heat flux pad are given in Figure B5, whilst the attachment of the pad to the furnace wall is illustrated in Figure B6. The pad receives heat on one side, and is effectively insulated by an air gap of 2 mm at the rear. Two heavy longitudinal welds attach the meter to the wall of the vessel and provide a relatively unimpeded path for the heat flowing from the pad. Provided that the thickness of the pad is small compared to its length, the isotherms or constant temperature lines will be parallel and almost perpendicular to the length of the pad. By inserting a thermocouple in the centre of the pad, the heat flux can be deduced from the reading of a second thermocouple located a distance "l" from the central couple. Anson and Godridge (136) obtain the following formula for the heat flux when using such a thin pad:

$$\Phi = 2 \cdot (T_o - T_1) \cdot k \cdot a / l^2 \qquad (B2)$$

However, a modified formula would be necessary to enable its application to thick pads. Such a formula is given below which enables the use of equation (B2) which has been derived from one dimensional theory for the two dimensional case :

$$\Phi = 2 \cdot C \cdot (T_o - T_1) \cdot k \cdot a / l^2 \qquad (B3)$$

where C is a calibration factor for a particular heat flux pad.

Llewelyn (157) has conducted a two dimensional analysis of the heat flow and temperature distribution in a heat flux pad using complex variable theory. He found that errors arising from the one dimensional treatment for thin pads are negligible unless the outer thermocouple is very near to the end of the pad. He recommends that for thicker pads, the thermocouples be located at a depth of approximately half the thickness of the pad, and that the ratio of the distance between the outer

and central thermocouples and half the pad length L should not exceed 0,6 or :

$$\frac{l}{0,5 \cdot L} < 0,60$$

B.2.3 The Manufacture of the Heat Flux Meters

All the heat flux meters were machined from flat bar by a numerical controlled machine to the dimensions illustrated in Figure 19. It will be noted from the figure that six shallow holes are drilled into the rear of the meter. Three of the holes are of 1,4 mm diameter, whilst the other three are of 1,8 mm diameter. As only the temperature difference is required, it was decided to attach constantan wires to the three 1,4 mm diameter holes for each of the thirty one heat flux pads. The emf generated between the central and an outer constantan wire would thus be a measure of the heat flux rate. In addition to the constantan wires, stainless steel sheathed mineral insulated thermocouples are attached within each of the 1,8 mm diameter holes in four of the pads only.

It was decided initially to investigate the possibility of attaching the constantan wire to the heat flux pads by capacitance discharge welding. However the strength of the resulting connection was very poor even after varying the size of the capacitor, the discharge voltage and the type of closing switch. In view of the resulting weak connection, it was decided to silver solder the constantan wires and thermocouples to the heat flux pads.

Silver soldering of the wires and thermocouples provided a strong and positive connection to the heat flux pad which would be capable of withstanding much abuse during installation. However, it was feared that the silver solder may be lost during the welding of the pad to the test rig. Therefore a strong air blast was applied during the welding process as

well as the application of cooling water after each weld run. Careful adherence to the above procedure resulted in the successful installation of thirty of the thirty one heat flux meters. In the only unsuccessful attachment, an outer constantan wire became dislodged. As only the centre wire and a single outer wire are necessary for the evaluation of heat flux, this meter was not replaced.

B.2.4 Location of the Heat Flux Meters

The location of the heat flux meters is illustrated in Figure B7 which is a development of the furnace walls as viewed from the inside of the furnace. In addition to the thirty one heat flux pads, three stainless steel sheathed 3 mm diameter chromel-alumel thermocouples were attached to the furnace wall. These thermocouples were brazed for about 50 mm along the furnace wall prior to removal through the water jacket. It was hoped to be able to infer heat flux rates from the measured wall metal temperatures, however the thermocouples were found to be relatively insensitive to changes in heat flux and only the heat flux meters have been utilized to measure the heat flow.

B.2.5 Performance Prediction of the Heat Flux Meters

In order to assess the performance of the heat flux pad and further to ensure that the isotherms are not greatly distorted by the geometric configuration of the pad, a detailed heat transfer analysis was undertaken. It was initially decided to solve the heat conduction problem manually by means of a standard numerical relaxation technique (158, p. 96-114), (159, ch.9). However, with 78 points chosen for solution, the method was tedious. An attempt was thus made to solve the problem analytically.

As little heat is transferred along the unwelded edge of the heat flux pad, the evaluation of the heat conduction through the pad can be obtained by considering the two dimensional

steady state conduction of heat in a rectangular section 40 mm long by 4 mm thick containing no sources or sinks. This is represented by Laplace's equation in cartesian co-ordinates.

$$\frac{\partial^2 T}{\partial x^2} + \frac{\partial^2 T}{\partial y^2} = 0 \qquad (B4)$$

The heat flow is symmetrical through the centre-line of the pad and the co-ordinate system is illustrated in Figure B8a. A constant heat flux 'Φ' is assumed at the upper surface, whilst the lower surface is thermally insulated. At the welded edge, ie 20 mm from the centre line, the temperature profile is assumed to be a linear function in 'x'. Thus from Figure B8a, the following boundary conditions for equation (B4) can be established:

$$\begin{aligned} at \quad x &= 0 : & -k\frac{\partial T}{\partial x} &= \Phi \\ x &= a : & \frac{\partial T}{\partial x} &= 0 \\ y &= 0 : & \frac{\partial T}{\partial y} &= 0 \\ y &= b : & T &= f(x) \end{aligned}$$

Albrecht (160) has presented a solution for equation (B4) under similar boundary conditions by making use of the Dirichelet theorem for a discontinuous function. The solution of the equation is therefore not presented in this Appendix. By modifying Albrecht's solution for the particular conditions given by the boundary conditions above, the solution to equation (B4) is given by equation (B5):

$$T(x,y) = T_o + \frac{2\cdot(T_1 - T_2)}{\pi^2} \sum_{n=1}^{\infty} \frac{1 - \cos(n\pi)}{n^2 \cdot \cosh(n\pi b/a)} \cos(n\pi x/a)\cdot\cosh(n\pi y/a)$$

$$+ \frac{2\,\Phi\, b}{k} \sum_{n=1}^{\infty} \frac{\sin(2n-1)\frac{\pi}{2}\cdot\cosh(2n-1)(x-a)\frac{\pi}{2b}\cdot\cos(2n-1)\frac{\pi y}{2b}}{(2n-1)^2\cdot\frac{\pi^2}{4}\cdot\sinh(2n-1)\frac{\pi a}{2b}} \qquad (B5)$$

Equation (B5) has been used in plotting the isotherms of Figure B8b for the following conditions:

(i) heat flow rate at the upper surface is 200 kW/m^2

(ii) thermal conductivity of the material is 50 W/mC

(iii) at the welded edge the temperature varies from 199 to 201°C.

From Figure B8b it is clear that the pad behaves almost in accordance with the one dimensional theory, or as a thin pad. With the monitoring thermocouples 9 mm apart and using the conditions given a temperature differential of 40,5°C is deduced from the thin pad theory using equation (B2). From Figure B8b the temperature difference between the thermocouples is also 40,5°C which implies a correction factor of

$$C = 1,00$$

in equation (B3).

Where constantan wires are inserted in the holes of the heat flux meter, the heat flux can be monitored by measuring the difference in potential between the two iron-constantan junctions. By assuming that the heat flux meter will have a temperature ranging from 200 to 300°C the heat flux meter coefficient relating the heat flux per unit potential difference between the two junctions will be given by

$$\text{heat flux meter coefficient} = 88,98\ kW/m^2/mV$$

B.3 PARTICULATE SAMPLING

A knowledge of the characteristics and composition of the material entrained from a fluidized bed combustor is a major prerequisite for determining the performance of the plant. As it is almost always impossible to collect all of this entrained material, an adequate sampling procedure has to be adopted. It is therefore, the object of this section to provide details of an acceptable dust sampling system as well as the design of the dust sampler used in the 1 000 mm diameter fluidized bed combustion test rig.

Sampling for particulates requires more detailed concern about the sampling rate than does gas sampling. Representative sampling is obtained only if the average velocity of the stack gas stream entering the probe nozzle is the same as that of the gas in the flue at the sampling point, i.e. isokinetic sampling. "If the sampling velocity is too high (super-isokinetic sampling), there will be a smaller concentration of particles collected (because the inertia of the larger particles prevents them from entering the nozzle). Alternatively in subisokinetic sampling, where the sampling velocity is below that of the flowing gas stream, the gas samples would contain a higher-than-actual particulate concentration (because heavier particles will enter the nozzle and light particles will be diverted)" (161). However, Hawksley et al (162,pg.40) indicate that the error from sampling anisokinetically is small for coarse grit particles, i.e. particles much larger than 75 microns, and for fine soot particles or particles smaller than 3 microns. It was therefore evident that isokinetic sampling would be necessary in the analysis of the entrained material from the fluidized-bed combustion test rig.

"A considerable amount of useful sampling technique information has been developed some of which has appeared in the literature, and while efforts are being made by professional and industrial organizations to standardize procedures, progress in this effort is relatively slow" (163). Different investigators tend to utilize different techniques as a matter of preference or to suit the variety of operating conditions which might exist, making the task of standardizing a best procedure most difficult.

Several different types of equipment are commercially available, whilst detailed designs have been published in the literature to enable the potential user to design equipment specific to his needs. The basic principles of the main types of equipment are described below, as details can be obtained from the references.

B.3.1 Apparatus Requirements

The basic apparatus requirements for the sampling of dust laden gases are contained in the standards BS 843 and BS 3405. Holton and Schultz (164) quote similar basic ASME code requirements. The essential features of the equipment are therefore a nozzle for insertion into the gas stream, a filter for removing the particulate matter, means of ensuring isokinetic sampling, a means for measuring the volume flow rate of the gas and an exhausting device.

In terms of BS 843 :

"When sampling a dust laden gas it is essential to ensure that the sample of gas witndrawn at eacn individual sampling point is truly representative of the gas at that point. Having withdrawn such a sample it is then necessary to remove the solid suspended matter and to measure the volume of the gas filtered. The temperature, pressure and humidity of the gas at the point where the volume is measured will need to be determined. To perform the foregoing operations any satisfactory form of sampling device must therefore comprise the following five essential parts :

(i) A tube or nozzle for insertion into the gas stream for withdrawing the gas sample.

(ii) An efficient filter for removing the suspended matter from the gas sample.

(iii) Means for ensuring that the rate of sampling is approximately equal to the gas velocity at the point of sampling.

(iv) Means for measuring the total volume of the gas filtered.

(v) An exhauster for drawing the gas through the sampling nozzle and filter."

From the above broad outline a number of different forms of sampling equipment have been described in the literature. Hawksley et al(162,p.4) divides these into two groups, the first in which the solids-collecting device is mounted outside the flue, and the second in which the solids-collecting device is mounted adjacent to the sampling nozzle. The probe for the 1 000 mm diameter test rig will be of the former group, to facilitate removal of the sample. After a number traverses a single representative point may be established and the sampling device could then be maintained in a fixed position throughout the test.

With respect to the filtering device, this can be achieved by means of a high efficiency cyclone, a wet scrubber type of filter, or use can be made of a dry filtering medium such as filter paper or alundum.

B.3.2 Nozzle and Probe Assemblies

Due to the need for sampling under a wide range of stack conditions, probes with interchangeable nozzles are often used in stack sampling. This permits a wide range of stack velocities to be analysed with a constant pressure drop filter such as a cyclone which may be effective in removing solids of a particular size within a limited velocity range.

"The balance-draught or null type nozzle assembly has been suggested as a means to improve collection accuracy. The nozzles are designed using the null or static balance principle in which the static pressures on the inside and outside surfaces of the nozzle assembly are monitored. When the sample flow rate is adjusted so that the values are equal, it is assumed that isokinetic sampling velocities have been achieved"(165). The null type nozzles illustrated in Reference (165)have been designed for use in ducts where the gas velocity ranges from about 5 to 30 m/s.

A study on the use and effectiveness of null-type or static probes for isokinetic sampling yielded the following results (166):

> "Null-type or static probes do not assure isokinetic sampling unless they have been previously calibrated under typical operating conditions. The location of static pressure holes on the inner and outer surfaces must be based upon aerodynamic considerations. Outside pressure must be measured at a point where surface pressure is sufficiently lower than that of the main air stream to compensate for the unavoidable pressure loss that occurs at the interior of the probe."

Indeed, they found that the deviation from isokinetic flow increases rapidly when duct velocities fall below 5 m/s, whilst furthermore it was found that the likelihood of a non-representative sample with coarse dusts is probable, as deviations at the lower velocities may approach 25% or more.

B.3.3 Filter for Removal of Particulate Material

As mentioned previously, the filter device can consist of a high efficiency cyclone, a wet scrubber type of filter or a dry filtering medium. As the flue gases will be extracted from the rig at temperatures above 600°C, some form of gas cooling would be necessary should a dry filtering medium be used. As the use of a wet scrubber is cumbersome, the application of a cyclone to remove the particulate matter, besides being the most convenient for ease of sampling, would appear to be the best alternative. Further, a cyclone has been designed (167) which theoretically could remove all particles above 1 micron and which has been found to remove 95% of all particles above 5 microns in practice. The cyclone proposed by Hawksley et al (162), (168) effectively collects particles above about 5 microns but cannot remove smoke particles below this size effectively. Should sampling of the smoke particles be necessary, a backing filter can be attached to the cyclone. A further advantage of the cyclone is that it removes particulate matter at a constant pressure drop for a specific volumetric flow rate. The cyclone can thus serve as a gas metering device for use in conjunction with a pitot tube to establish isokinetic sampling conditions.

B.3.4 Sampling Position

Some publications have stressed the need for a number diameters of duct length to be provided from flow disturbances upstream and downstream of the sampling probe (161),(169). However, Stairmand (170) has studied the use of mixing baffles both to obtain uniform gas flow and to ensure that the dust sample extracted should be representative. He found that by using a central baffle obstructing 50% of the free area, good mixing and hence a representative sample could be extracted at a length of three diameters from the baffle. In the discussion to the paper (170), Hurley described the use of an orifice plate having an aperture of 50% of the free area being employed to promote mixing so as to obtain a representative sample two to six diameters from the orifice.

Although the application of baffles and orifices, and the sampling in relatively long straight lengths of ducting is conducive to more accurate results, other inaccuracies in the sampling of particulate matter often result in the use of these stringent requirements being unnecessary. Indeed, compliance with BS 3405 would result in an accuracy of $\pm$ 25% when determining the dust burden. This standard requires that sampling be performed in some cases (from a 90^{o} bend in particular) at a distance of only one flue diameter from the disturbance.

B.3.5 Design Selected

The BCURA isokinetic dust sampler (162),(168) was selected for use on the 1 000 mm diameter test rig. The main reasons for selecting this sampler are listed below:

a) The sample probe is acceptable to the requirements of BS 3405.

b) As no interest in soot or particles less than about 3 microns is envisaged, the sampler can be operated without a filter and therefore the sampling probe and solids separator is a constant

pressure drop device at a specific flow rate, thus simplifying the sampling procedure.

c) The equipment is relatively easy to fabricate.

d) The operation of the equipment has been well documented in the book by Hawksley et al (162).

e) Detailed designs of the equipment are also contained in the above reference (162) resulting in a less rigorous calibration of equipment fabricated to a similar design locally.

The general arrangement of the equipment is contained in Figure B9 whilst Figure B10 contains the general arrangement of the cyclone.

The equipment consists of a number of different sampling nozzles. For the range of velocities expected during operation of the rig, three nozzles have been designed having cross-sectional areas of 1 250 mm^2, 1 000 mm^2 and 600 mm^2 respectively. The nozzle is connected to a 32 mm OD stainless steel probe tube by means of an elbow type connecting piece. Gas is withdrawn via the probe tube to a cyclone which is located outside of the flue gas stream. The cyclone and probe tube located outside of the duct have to be insulated to eliminate corrections required to account for gas cooling when sampling isokinetically. A 3 mm diameter Cr-Al sheathed thermocouple is located within the probe tube to establish the temperature of the extracted gas. A second thermocouple may be placed immediately downstream of the cyclone to ensure that those components outside of the flue gas stream are adequately insulated. The solids removed by the cyclone are deposited in small containers which are simply screwed onto the base of the cyclone.

A deviation from the design proposed by Hawksley et al (162) is the attaching of a pitot tube to the probe to enable gas

velocity variations in the vicinity of the probe to be easily monitored.

B.3.6 Anticipated Operating Curves

It is assumed that the lowest pressure difference which can be measured on an inclined manometer is 0,5 mm Wg. Figure B11 illustrates the free stream velocity corresponding to a particular pressure differential measured by the pilot tube at different temperatures. The constant diameter lines superimposed on the graph indicate the velocities which would be maintained in the particular duct at the respective temperature for the maximum mass flow rate of 4263 kg/h.

Figure B12 illustrates the anticipated pressure to volume characteristics of the cyclone. In order that the cyclone removes particles of size greater than 5 microns efficiently, a minimum pressure drop of 175 mm Wg is specified, whilst the maximum value of 950 mm Wg indicated is as a result of limitations imposed by the suction device or the inconvenience of changing from a water to a mercury manometer. Figure B12 has been drawn to illustrate the operating range of the suction probe whilst using the 1 000 mm^2 nozzle.

B.4 THE HEAT FLUX PROBE

The heat transferred in a shallow fluidized bed is largely dependent on the bed expansion and the prevailing heat transfer coefficient. Further, the high heat transfer in the dense-bed zone would appear to extend to the less dense 'cloud' zone above. In order to have a better understanding of the heat transferred in a fluidized bed combustion furnace, accurate information is required on the effective height of the fluidized bed, on the extent of the heat transferred in the cloud zone and the relative rate of heat transferred in the bed and in the cloud zones.

Information on the in-bed heat-transfer coefficients can be obtained by means of heat flux pads, whilst the expanded bed height can be established by means of static pressure probes. Although the information obtained by the heat flux pads is of sufficient accuracy, their being fixed to the vessel tends to limit their usefulness. Further, the static bed height determined from the static pressure probes does not differentiate between the dense or the cloud zones of the bed.

The movable heat transfer probe overcomes many of these difficulties. Besides being able to give an accurate evaluation of the relative heat transfer coefficient at different levels within the bed, it also enables the heat transfer coefficient immediately above the bed to be measured for the shallower beds. The arrangement of the test rig and access to the bed via the ash port did not permit the extension of the probe to a level greater than 350 mm above the base of the bed thus precluding the measurement of heat transfer coefficients above the deeper beds.

B.4.1 Design of the Heat Flux Probe

The heat flux probe is based on the principle of measuring the difference in temperature between two points in a conductor having a well defined geometry. The probe is introduced via the central ash pipe. Seals have been designed and fitted to the ash pipe to prevent wedging of the probe in the pipe. The general arrangement of the heat transfer probe within the ash pipe and including the relevant seals is illustrated in Figure B13, whilst a diagram illustrating the operation of the probe is contained in Figure 22 of the main body of the thesis.

The heat transfer probe is located at the end of a cooling jacket section and is made up of an 11,5 mm thick stainless steel cylindrical section with cooling water being caused to flow over the core of the cylinder. The cylinder has a diameter of 38 mm with an effective length of 25 mm. The probe was designed to ensure a high velocity of the cooling

water on the inside of the probe thereby ensuring a high internal heat transfer coefficient. A recess on the upper surface allows a stagnant layer of sand to collect on it, thereby restricting the heat transferred. A constriction on the lower side similarly reduces the heat transferred in this region. Therefore heat is transferred almost exclusively in a radial direction through the thick cylinder. The temperature difference between two thermocouples located at well defined positions in the probe yields a direct measure of the heat transferred.

B.5 PERFORMANCE OF THE OXYGEN ANALYSER

A polarographic oxygen analyser was used for the monitoring of the oxygen content of the flue gases. The analyser utilizes a polarographic sensor which is charged with an aqueous potassium chloride solution. This solution is separated from the gases by a Teflon membrane which is permeable to gas. A fixed potential is applied between a cathode and an anode immersed in the solution. Oxygen diffuses through the membrane causing an oxidation reduction reaction resulting in a current flow proportional to the partial pressure of the oxygen present in the sample.

B.5.1 Response of the Oxygen Analyser

The response of the analyser to the sudden introduction of nitrogen when monitoring the oxygen level of dry air and vice versa has been assessed. The results of these analyses are given in Figure B14. The first two curves in this Figure represent the introduction of nitrogen after the sensor had been exposed to air for an extended period, whilst the second set of curves represent the subsequent introduction of dry air to replace the nitrogen. The curves having the poorer response correspond to a sensor in which the electrolyte had been replaced a few hours prior to the test whilst the curves with the better response correspond to that for a sensor which has been in operation for over 24 hours.

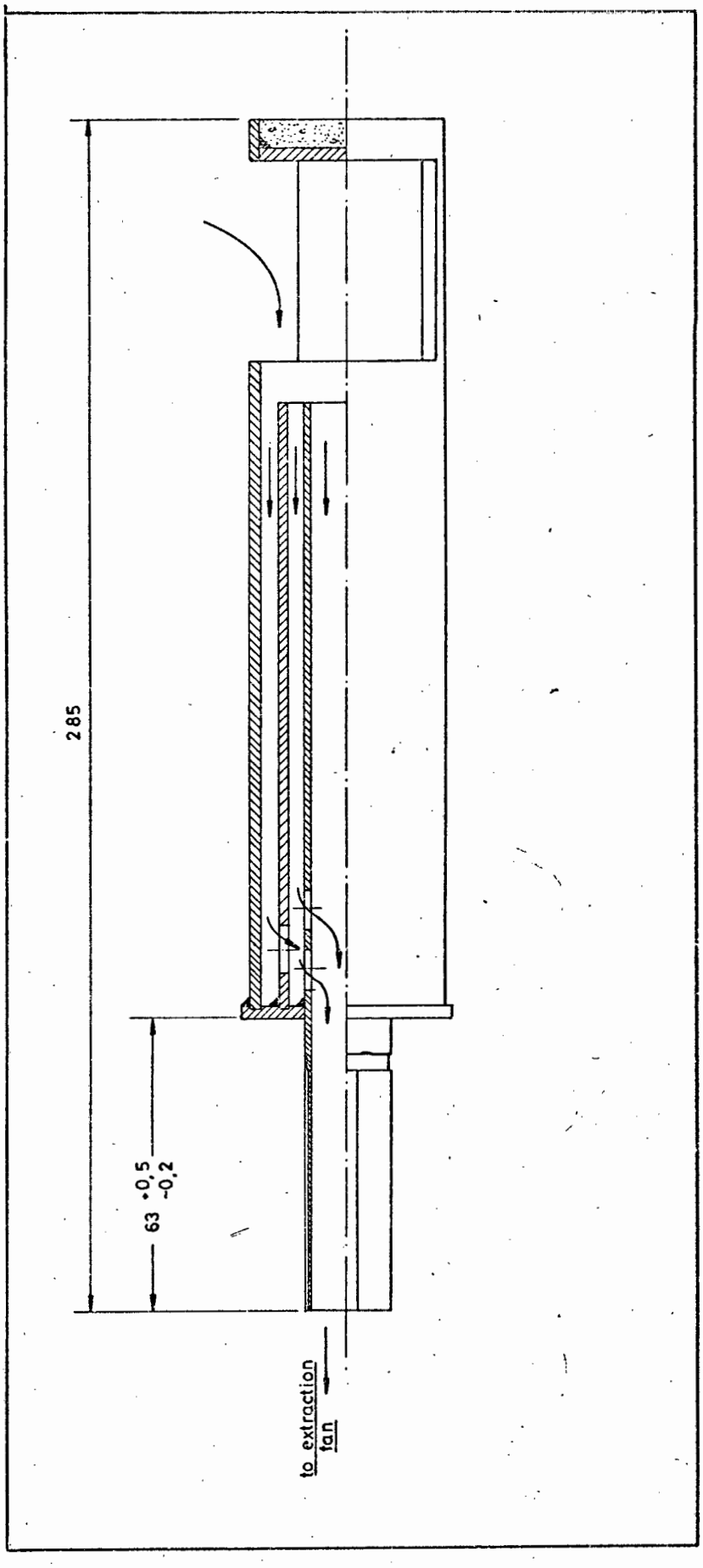

Figure B1 : General arrangement of the Incolloy 600 radiation shields.

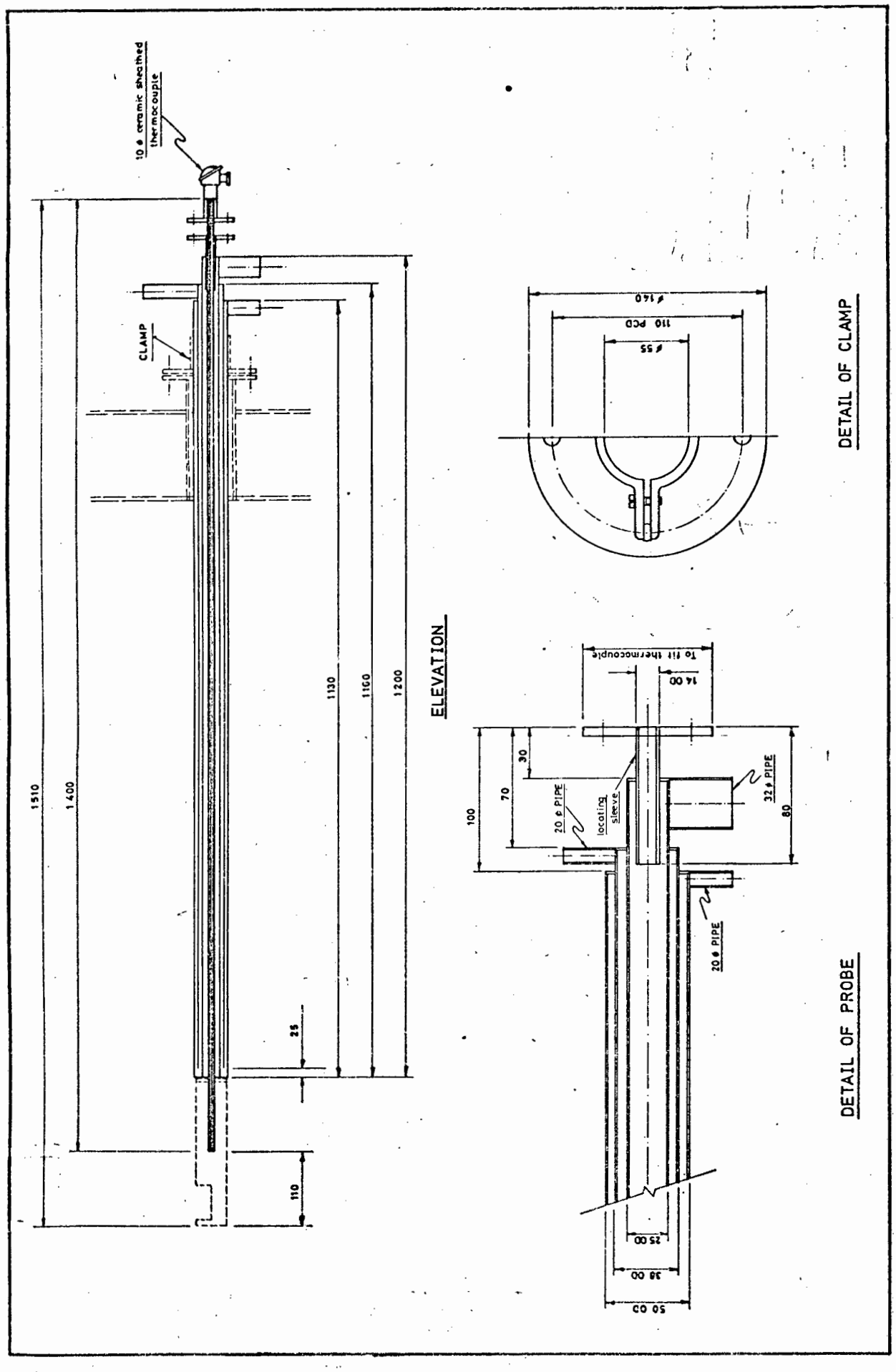

Figure B2 : The water cooled suction pyrometer probe with associated radiation shield.

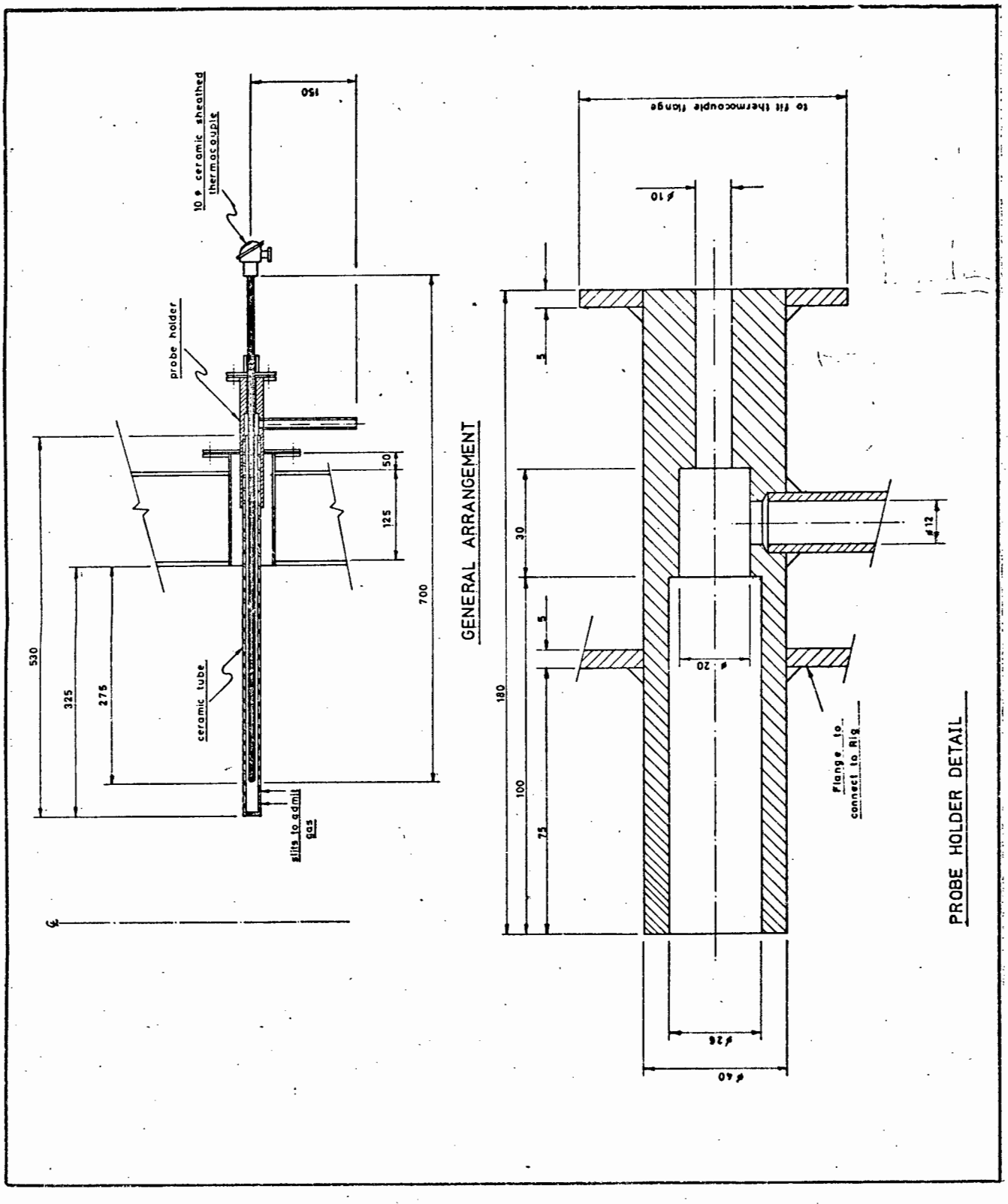

Figure B3 : Details of the ceramic temperature probes

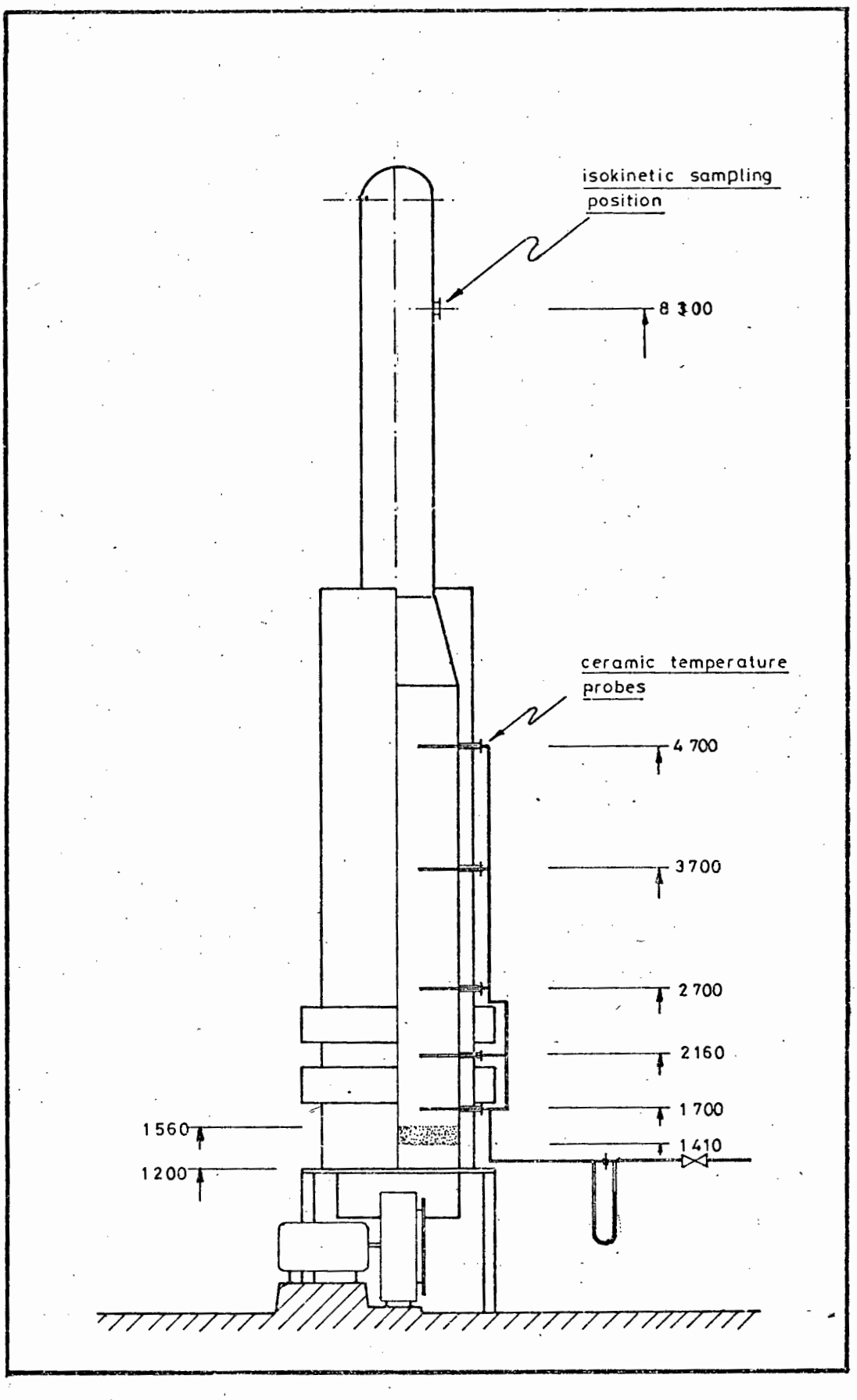

Figure B4 : General arrangement of the temperature probes in the combustor vessel.

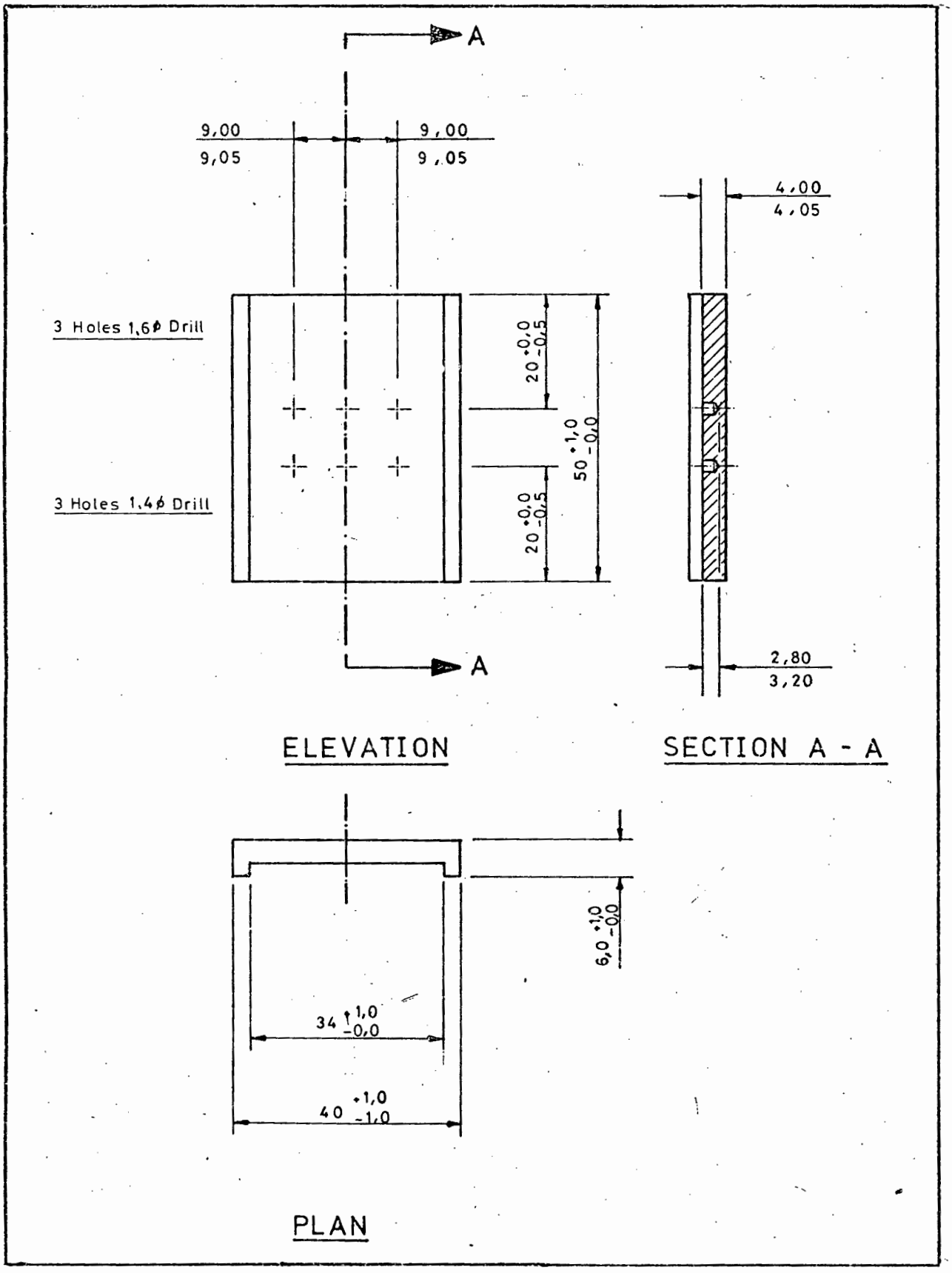

Figure B5 : Details of the heat flux pad.

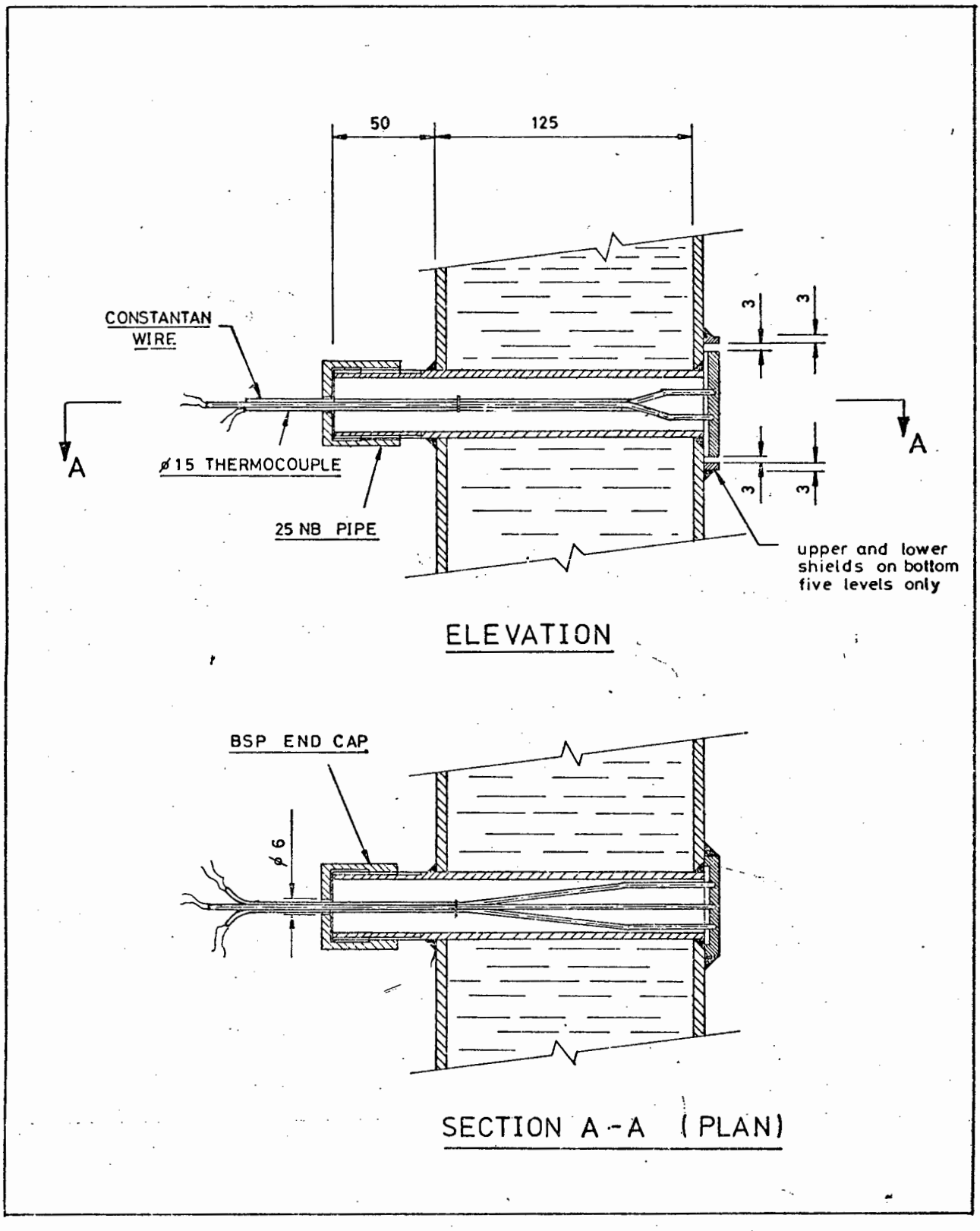

Figure B6 : Attachment of the heat flux pad to the 1 000 mm diameter test rig.

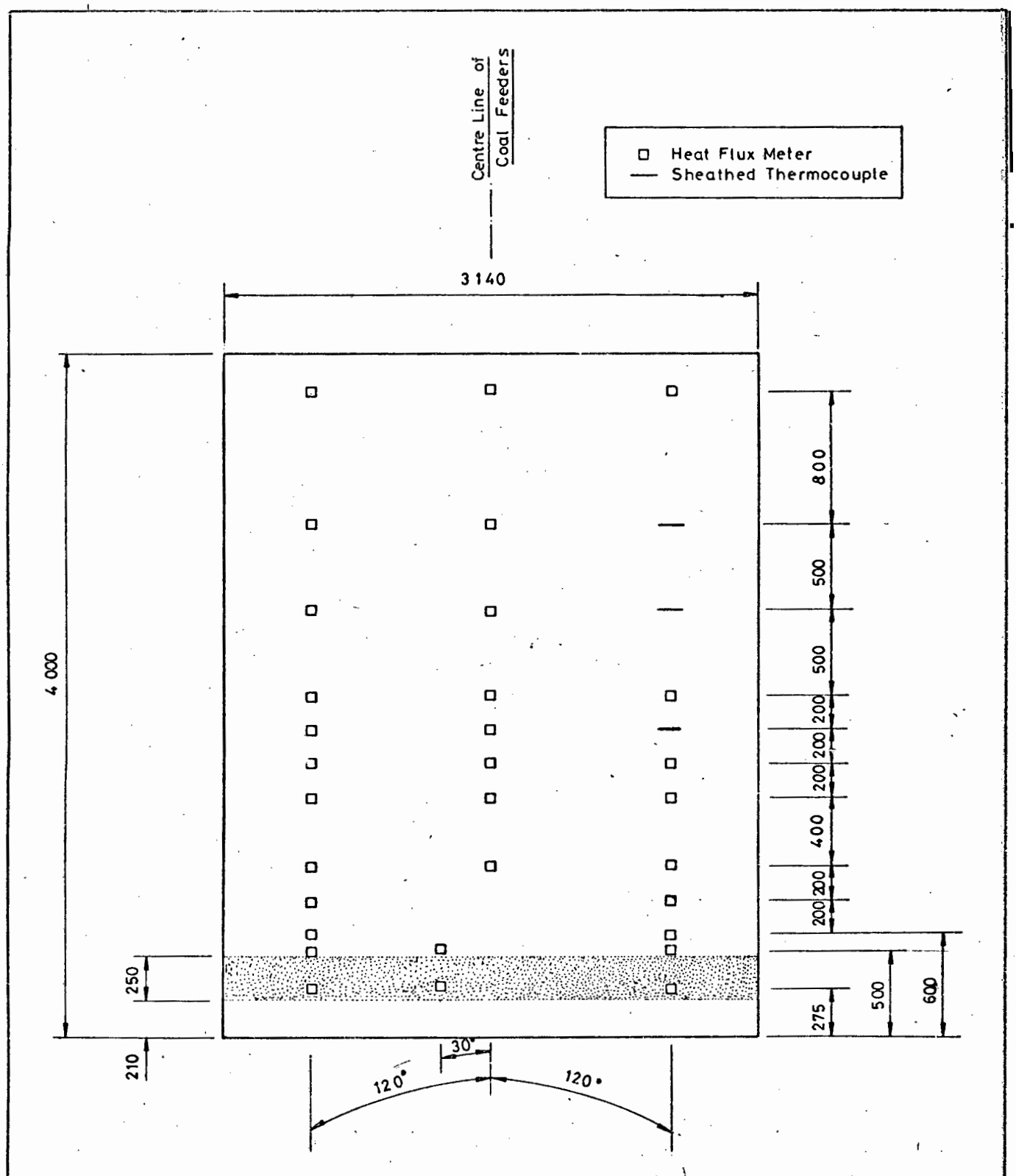

Figure B7 : Diagram to illustrate the location of the heat flux meters on the test rig.

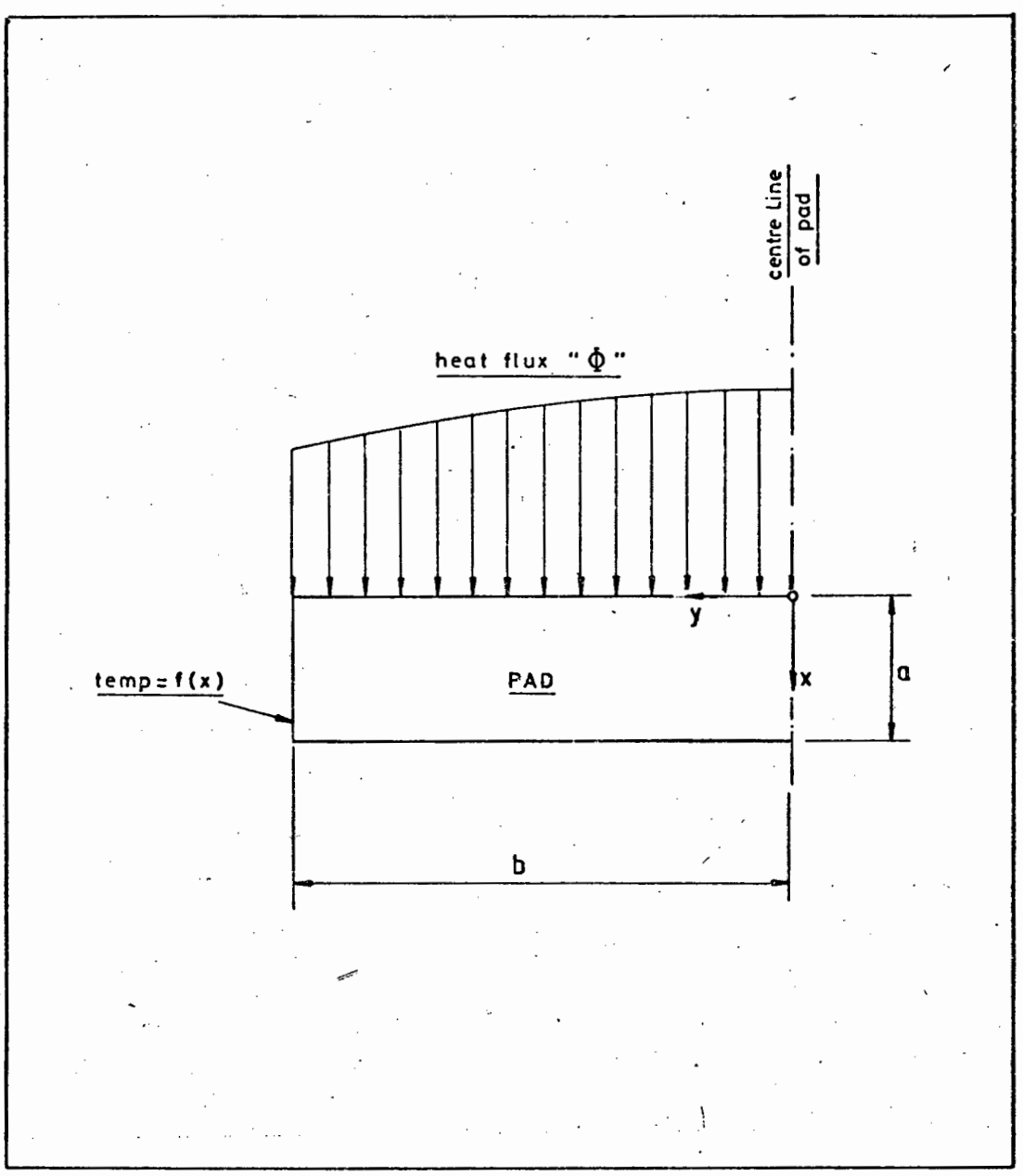

Figure B8a : Cartesian co-ordinate system for the solution of the isothermal lines in the heat flux pad.

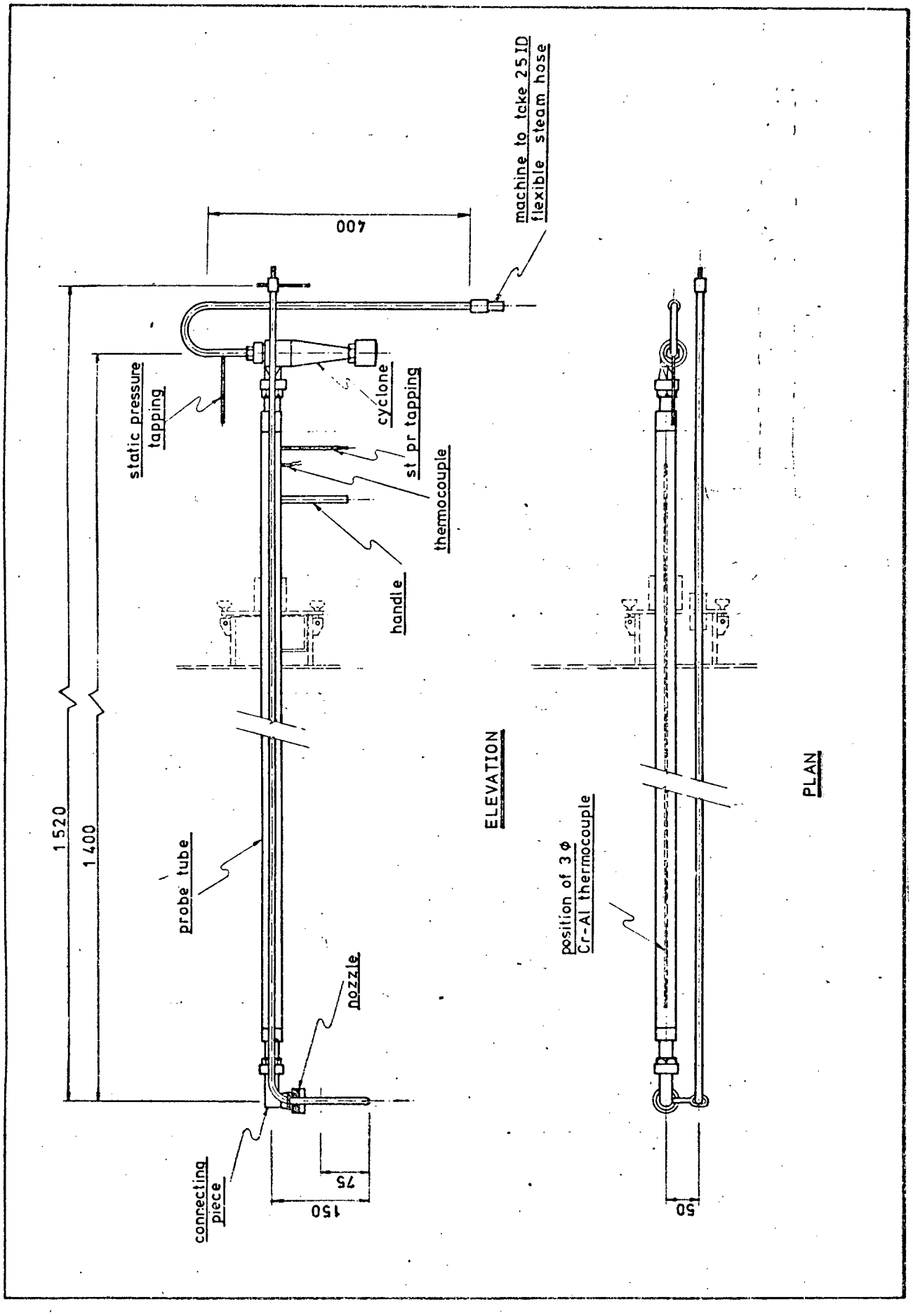

Figure B9 : General arrangement of the isokinetic sampler and pitot tube.

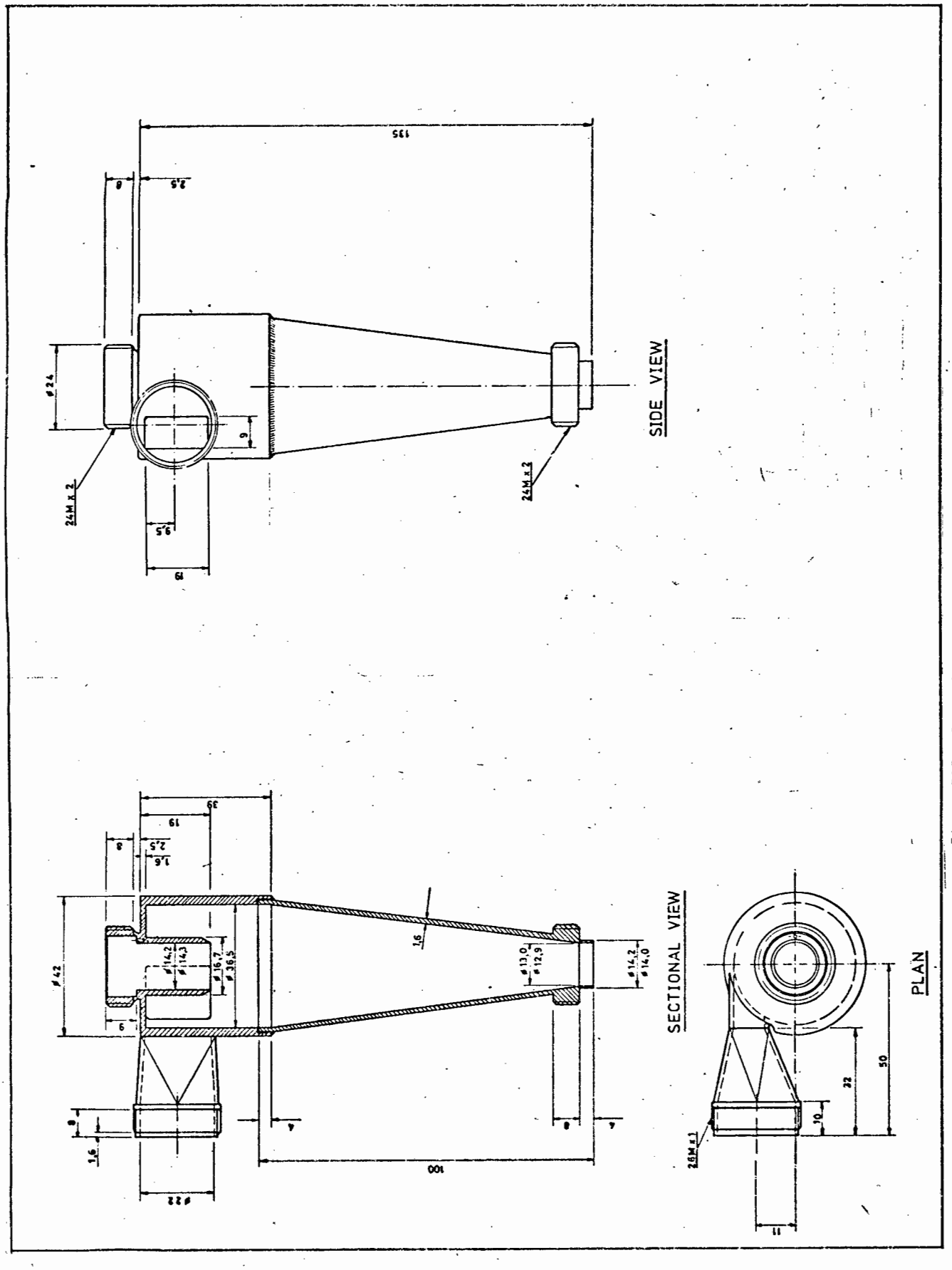

Figure B10 : General arrangement of the cyclone for the isokinétic sampler.

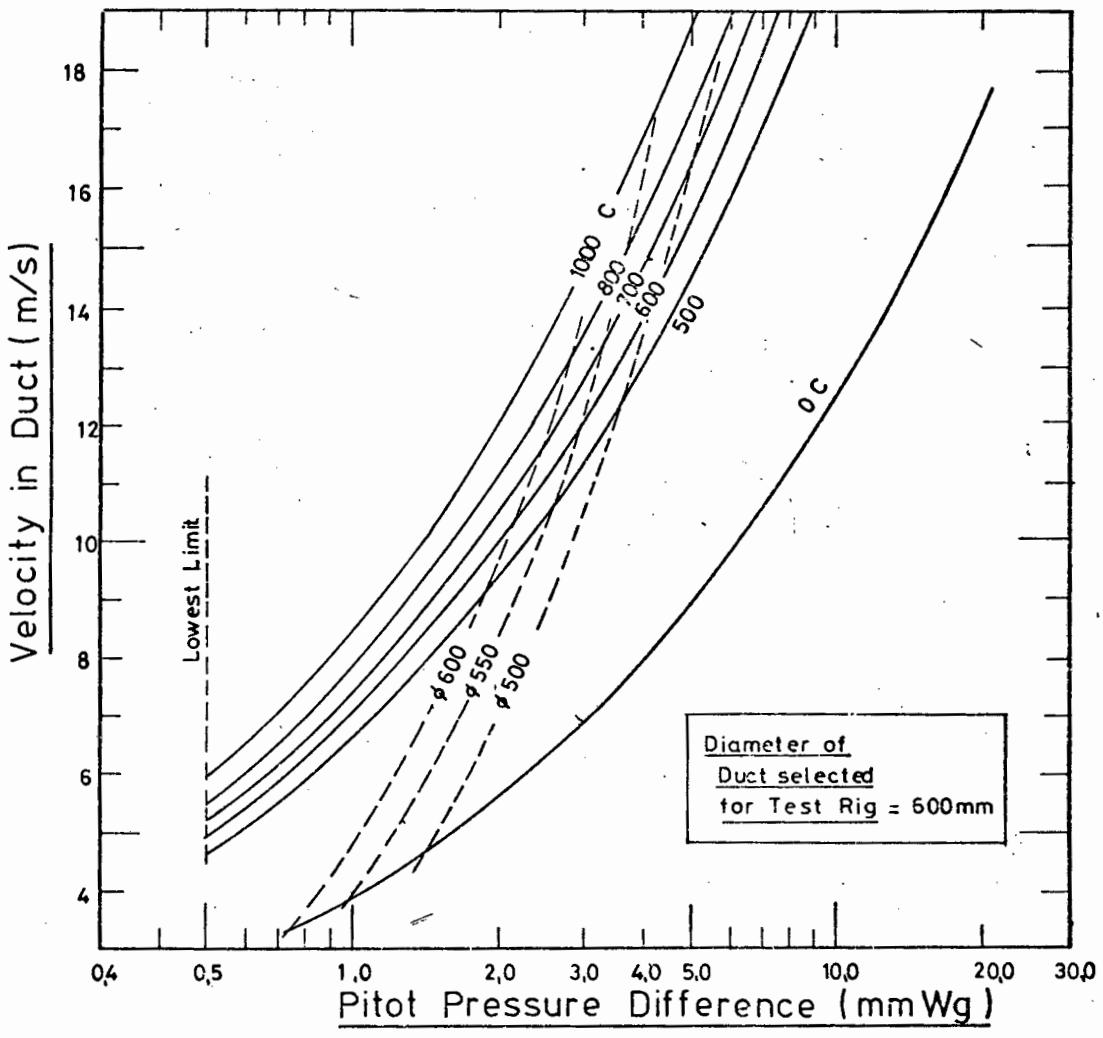

Figure B11 : Free stream gas velocity corresponding to pitot pressure differentials at various gas temperatures.

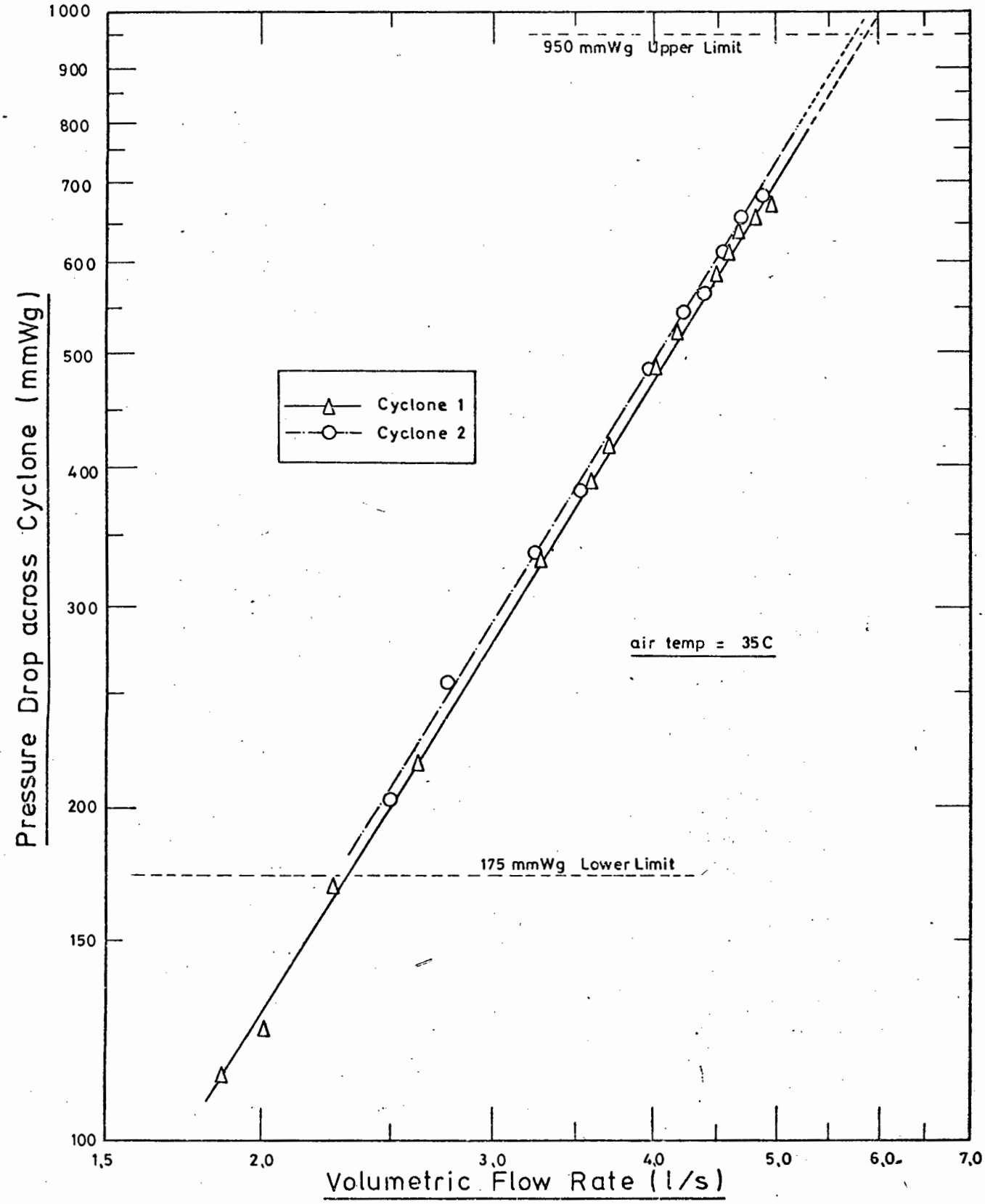

Figure B12 : Pressure volume characteristic of the cyclone for use with the isokinetic sampler.

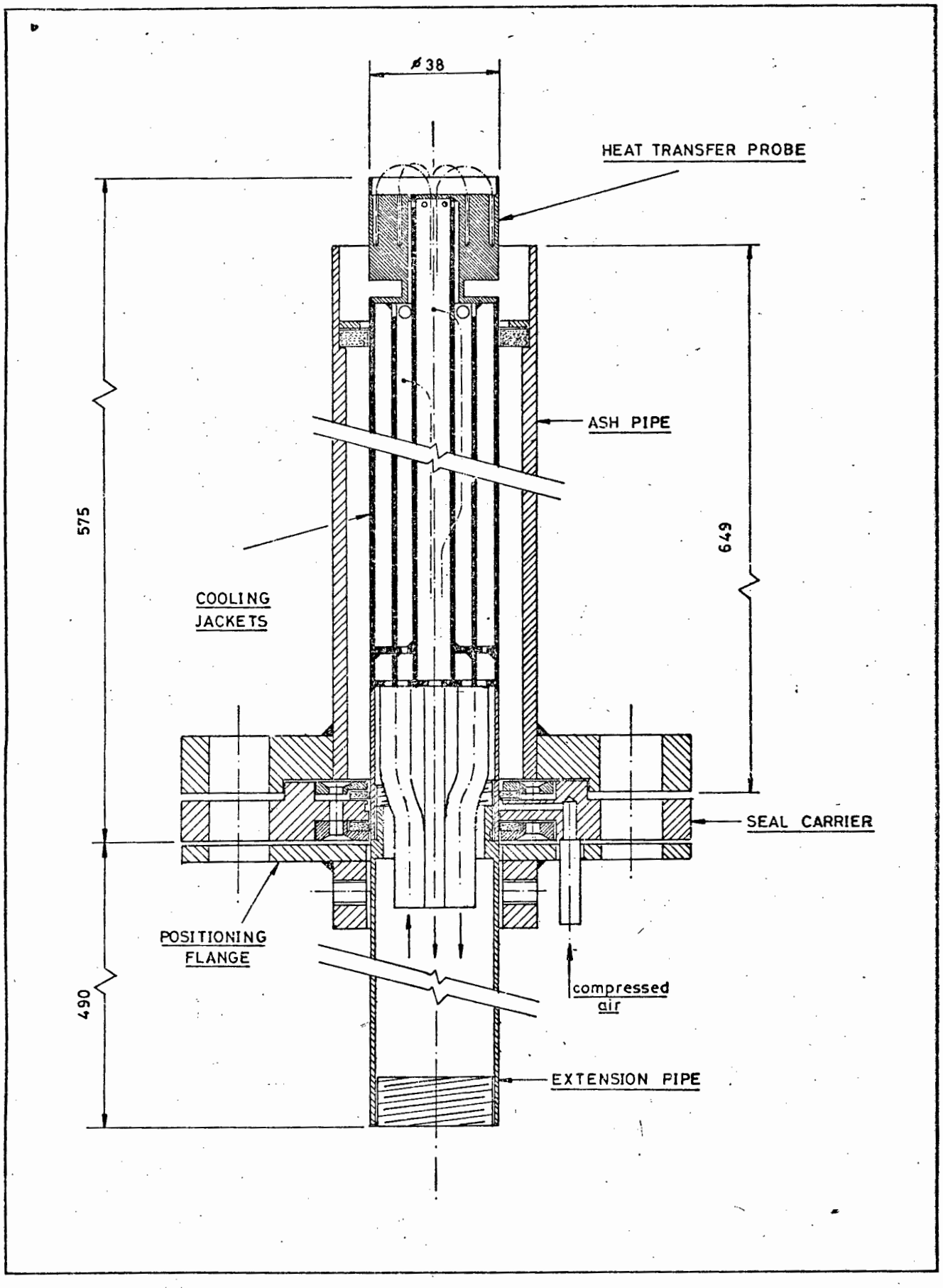

Figure B13 : General arrangement of the adjustable heat transfer probe within the ash pipe.

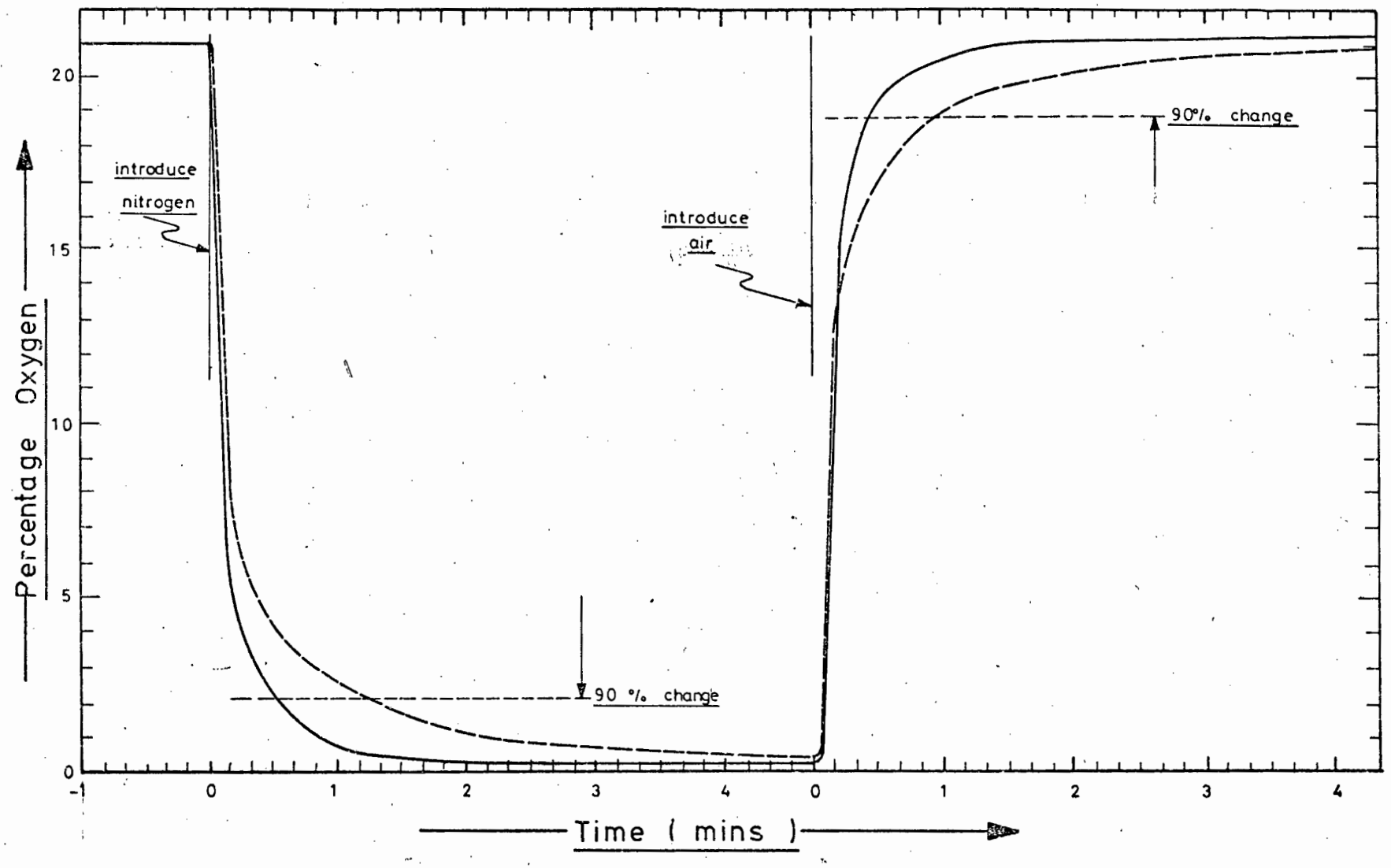

Figure B14 : Response of the oxygen analyser to step changes in oxygen concentration.

APPENDIX C

CHARACTERISTICS OF THE COALS BURNT AND THE SAND USED AS THE BED MATERIAL

Two types of coal have been used for the tests. The coals differ mainly with respect to their size grading whilst being very similar with regard to their calorific value and chemical analyses. The first coal contains a large proportion of fines and is designated as "duff" coal. The second coal is largely devoid of fines and has been referred to as "low fines" coal. The duff coal was burnt during tests 1 to 39 and 51 to 53, whilst the low fines coal was utilized for the remainder of the tests. The surface moisture content for most of the tests for which results have been obtained was low and the coal can be considered to have been fired in an air dried condition. Most of the tests in which wet coal was burnt resulted in poor operation due to erratic feeding and consequently only a few results were obtained with the wetter coal.

C.1 COAL ANALYSES

A number of coal analyses were undertaken during the test period. The variation between analyses was small. The proximate and ultimate analyses of Table C1 are representative of the coals burnt during the test series.

Table C1 : Chemical analyses of the coals on an air dried basis

		Duff Coal	Low fines Coal
Proximate Analysis			
Ash	%	17,98	14,94
Total Moisture	%	2,00	2,50
Volatile Matter	%	26,31	25,35
Fixed Carbon (by diff.)	%	53,71	57,21
	%	100,00	100,00
Ultimate Analysis			
Ash	%	17,98	14,94
Moisture	%	2,00	2,50
Carbon	%	66,93	68,20
Hydrogen	%	3,59	3,87
Nitrogen	%	1,74	1,69
Sulphur	%	0,67	0,74
Oxygen (by diff.)	%	7,09	8,06
	%	100,00	100,00
Heat Content			
Gross Calorific Value	MJ/kg	26,23	27,04
Nett Calorific Value	MJ/kg	25,37	26,20

C.2 SIZE GRADINGS

The coal size gradings have been determined on a cumulative percent by weight undersize and are listed in Table C2. Figure C1 graphically illustrates these gradings as smoothed curves as required by BS 1796 of 1976, whilst these same curves have been plotted on Rosin-Rammler paper as Figure C2

to facilitate their interpretation. Included in both these curves is the size grading of the bed material, i.e. the silica sand. This enables an easy comparison to be made of the different materials.

The silica sand has a very close size grading with a mean particle diameter of 0,847 mm. This sand was used as the bed material for all of the tests to date. Although coal ash remains in the bed material, frequent replacement of the bed material prevented the size grading from changing significantly during a test run or between runs. The size grading of this sand is listed in Table C3.

Table C2 : Coal Size Gradings

Sieve Size (mm)	Duff Coal		Low Fines Coal	
	% ret. on	Cum % by Wt. Undersize	% ret. on	Cum % by Wt. Undersize
6,35	2,2	97,8	13,1	87,0
4,76	5,3	92,5	18,4	68,6
2,00	20,9	71,6	44,6	24,0
1,00	19,1	52,5	15,5	8,5
0,600	13,3	39,2	3,9	4,6
0,420	9,7	29,5	1,3	3,3
0,211	14,4	15,1	1,2	2,1
Pan	15,1	-	2,1	-

Effective Size	0,16 mm	1,00 mm
Uniformity Coefficient	8,12	4,20
Mean Particle Diameter	0,409 mm	1,676 mm

NOTE: 1) The effective size is defined as the corresponding sieve diameter through which 10% of the material will pass.

2) The uniformity coefficient is the ratio of the corresponding diameter through which 60% of the material will pass and the effective size.

Table C3 : Size Grading of the Bed Material

Sieve Size (mm)	% ret. on	Cum % by Wt. Undersize
1,41	0,3	99,7
1,19	2,7	97,0
1,00	16,7	80,3
0,84	25,3	55,0
0,71	47,0	8,0
0,59	7,7	0,3
0,50	0,3	0,0

Effective size : 0,716 mm
Uniformity coeff. : 1,27
Mean Particle dia. : 0,847 mm

C.3 MATERIAL DENSITIES

The bulk densities of the two coals and the silica sand have been determined as:

Bulk densities of :

duff coal = 930 kg/m^3
low fines coal = 850 kg/m^3
silica sand = 1 640 kg/m^3

In addition, the particle density of the silica sand was determined by means of the S.G. bottle method of BS 1377 of 1975 as 2640 kg/m^3.

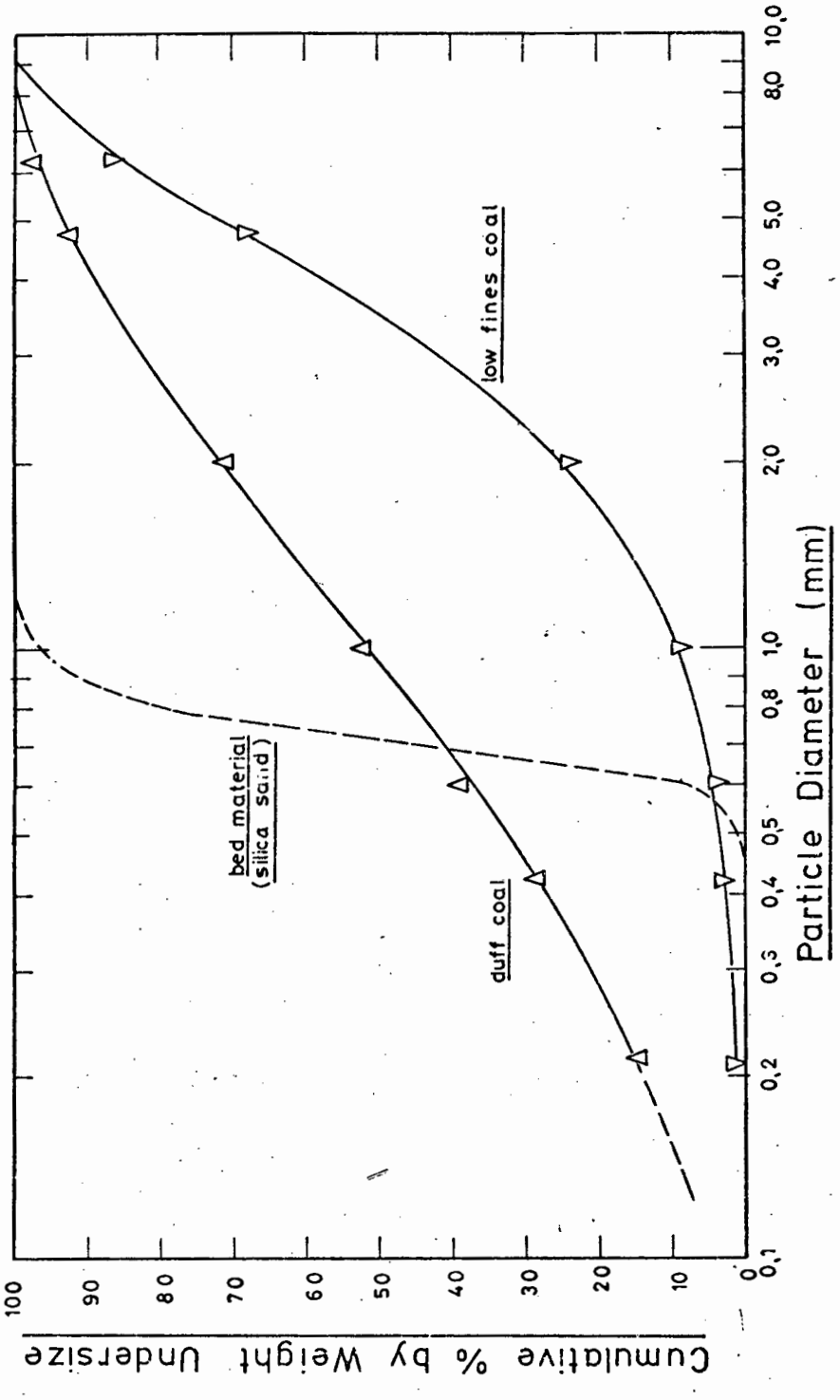

Figure C1 : As received size gradings of the two coals and the bed materials.

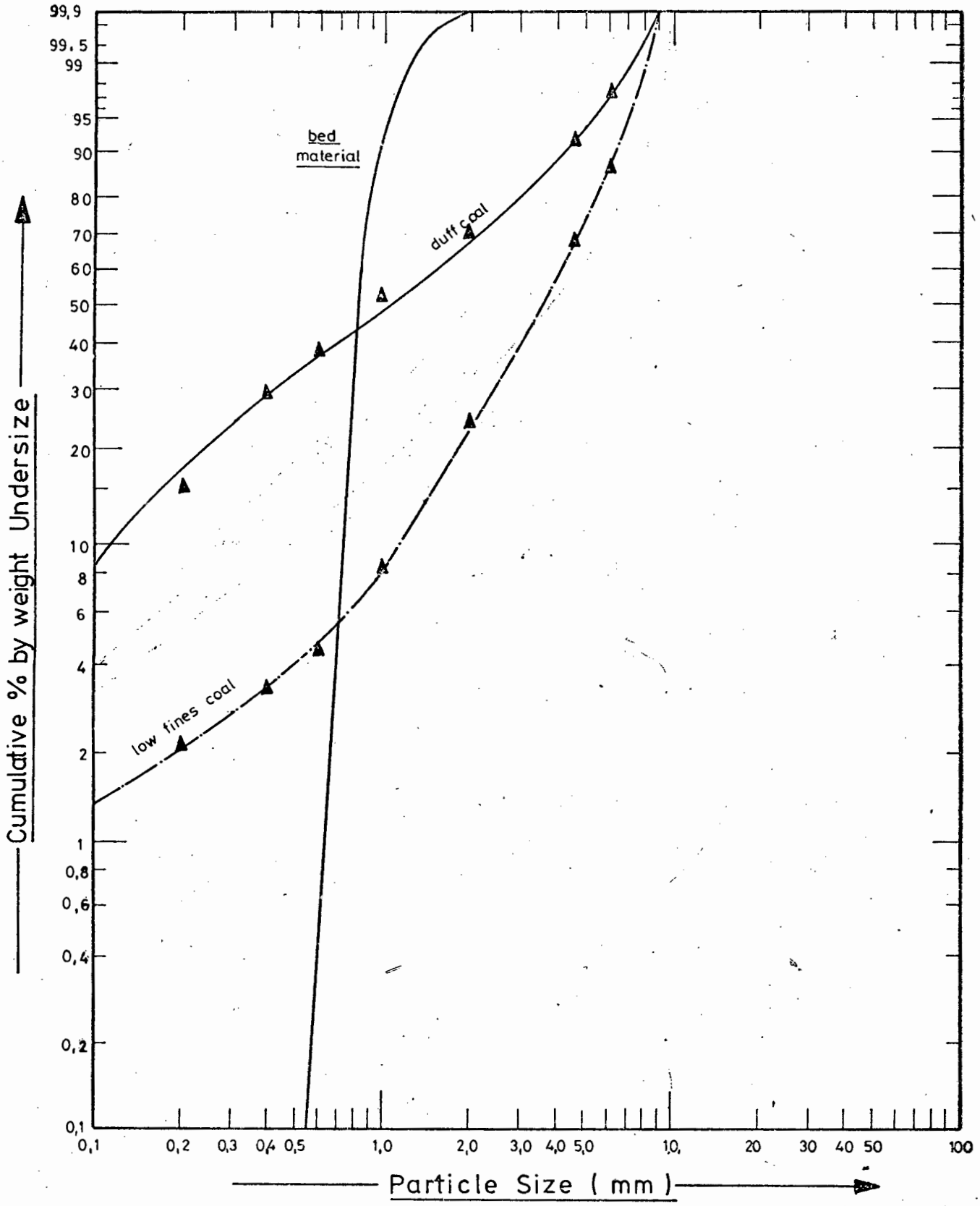

Figure C2 : Size gradings of the two coals and bed material plotted on Rosin-Rammler paper.

APPENDIX D

GENERAL CALCULATIONS

In the assessment of the performance of the 1 000 mm diameter fluidized-bed combustion rig, a number of different calculations have had to be performed. A general outline of these calculational procedures is given in this Appendix.

D.1 COMBUSTION CALCULATIONS ASSUMING COMPLETE COMBUSTION

The familiar chemical reactions resulting in the formation of carbon dioxide, sulphur dioxide and water vapour are assumed to take place during the combustion of coal with the oxygen contained in the air. These reactions are quoted below:

$$C + O_2 \rightarrow CO_2$$

$$S + O_2 \rightarrow SO_2$$

$$H + \tfrac{1}{2}O_2 \rightarrow H_2O$$

By making use of the ultimate analysis of the coal as given in Appendix C, the resulting flue gas components can be determined for the complete combustion of the coal in air for stoichiometric combustion as well as at different excess air levels. It is of value to obtain the flue gas components in order to determine the flue gas properties, as these differ from those of air even though the flue gas is made up mainly of nitrogen. Differences between the properties of air and the resulting exhaust gases are caused mainly by the presence of water vapour and carbon dioxide. Other quantities which are useful in any combustion calculation are the amounts of air required and resulting flue gases per kilogram of coal burnt at different excess air levels. The excess air factor is defined as the ratio of the mass of air supplied to the mass of air required for stoichiometric combustion. The results of two combustion calculations performed for the combustion of the

duff coal with an ultimate analysis given by Appendix C with air are produced in Table D1. The combustion air is assumed to contain 7 grammes of moisture per kg of dry air. The first calculation has been chosen as that of stoichiometric combustion, whilst the second has been performed at an excess air factor of 1,25.

TABLE D1 : Results of Combustion Calculations of Duff Coal with Air of Moisture Content, 7g/kg of Air

Excess Air level (-)	1,00	1,25
Gas Composition (Vol. %)		
Carbon Dioxide	17,73	14,30
Water Vapour	7,08	5,93
Oxygen	0,00	4,02
Sulphur Dioxide	0,07	0,05
Nitrogen	75,12	75,70
Gas per kg of Coal (kg)	9,469	11,63
Air per kg of Coal (kg)	8,680	10,85

D.2 INCOMPLETE COMBUSTION

The combustion of carbon to carbon monoxide instead of carbon dioxide is referred to as incomplete combustion. During some of the tests, and particularly during the use of the underbed feeder substantial quantities of carbon monoxide were measured in the flue gases. Further, when operating the bed sub-stoichiometrically, besides hydrocarbons which are released for combustion in the freeboard, a large quantity of carbon monoxide is generated particularly at the higher bed temperatures.

A fraction of the carbon, $(1-f)$ is assumed to burn to carbon dioxide, whilst the remainder, f, burns to form carbon monoxide. The excess air ratio is defined as the ratio of the actual

amount of air supplied to the minimum amount required for complete combustion, i.e. the stoichiometric combustion air requirement. When carbon monoxide is formed, only half the quantity of oxygen is required to that needed for complete combustion to carbon dioxide. Therefore, by definition of the excess air factor, some oxygen remains in the flue gas even at an excess air ratio of unity should carbon monoxide be formed. The relationship between the excess air factor, oxygen and carbon monoxide concentrations of the dry flue gas are illustrated in Figure D1.

D.3 FLUE GAS PROPERTIES

The relevant thermodynamic properties of air have been extracted from Reference (171)for use in the theoretical model of Chapter 4. Calculations requiring the use of these properties in Chapter 3 however, use the flue gas properties determined by the method suggested by Brandt (172). This approach involves two corrections for the carbon dioxide and water vapour contents of the flue gas to the corresponding value of the property for nitrogen at the respective temperature. As the remaining flue gas components have only a minor effect on the respective properties, the result is very similar to that obtained by considering the effect of each gas component individually and then adding the separate effects by some mixing rule (173).

Figure D2 is a nomograph to illustrate the determination of the mean specific heat at different temperatures, allowing for the water vapour and carbon dioxide concentration of the gas.

D4 OVERALL CALCULATIONS

A number of general calculations have been made. Most of these can easily be deduced from the tabulated results of Appendix G. However, the derivation of the relationship between the heat released in the bed and the bed operating parameters is of interest. This relationship forms the

primary input for deriving the furnace load condition in the theoretical model of Chapter 4.

It has been found that the amount of heat released per unit mass of air burnt remains very much the same for different coal types e.g. bituminous, lignitic and so on, irrespective of the ash content or other parameters. Indeed for bituminous coal, about 3 000 kJ of heat would be released for each kilogramme of air consumed. Further, at a particular bed temperature, the velocity through the bed and hence the air flow rate would be proportional to the heat released. It is therefore of interest to relate the heat released in terms of the bed operating conditions. This concept is developed below:

the gas mass flow rate can be written as

$$M_g = \rho_f \cdot A \cdot u_f \qquad (D1)$$

and $$M_g = m_g \cdot M_f \qquad (D2)$$

the mass of air required per unit mass of fuel burnt can be written as

$$m_a = M_a / M_f = m_{ao} \cdot \lambda \qquad (D3)$$

and the resulting mass of gas produced per unit mass of fuel burnt can similarly be written as

$$m_g = M_g / M_f = (\lambda - 1) \cdot m_{ao} + m_{go} \qquad (D4)$$

Now the heat released per unit mass of air consumed per unit plan area can be written as

$$\frac{\overline{Q}_{lib}}{M_f \cdot m_{ao}} = \frac{GCV}{m_{ao} \cdot A} \qquad (D5)$$

and by manipulation of equations (D1) to (D5) the following equation is derived

$$\overline{Q}_{lib} = \frac{GCV \cdot M_g \cdot m_a}{m_{ao} \cdot A \cdot \lambda \cdot m_g} \qquad (D6)$$

After further manipulation of equation (D6) and substituting the values given in Appendix C for the duff coal, the following relationship is derived relating the heat liberated or released per plan area in terms of the bed operating parameters:

$$\bar{Q}_{lib} = 3020\ \rho_f \cdot u_f / (\lambda + 0{,}0909) \qquad (D7)$$

It should be noted that equation (D7) refers to the gross calorific value. Further it is seen that from equation (D7) the heat liberated is completely defined by the bed operating parameters as the density is almost entirely dependent upon the bed temperature.

Further, it can be shown from equation (D5) that the heat release can be determined from the air flow rate and the excess air factor. This latter factor is easily determined from the flue gas analysis cf Figure D1. Therefore, the heat release can be determined independently of the coal flow rate.

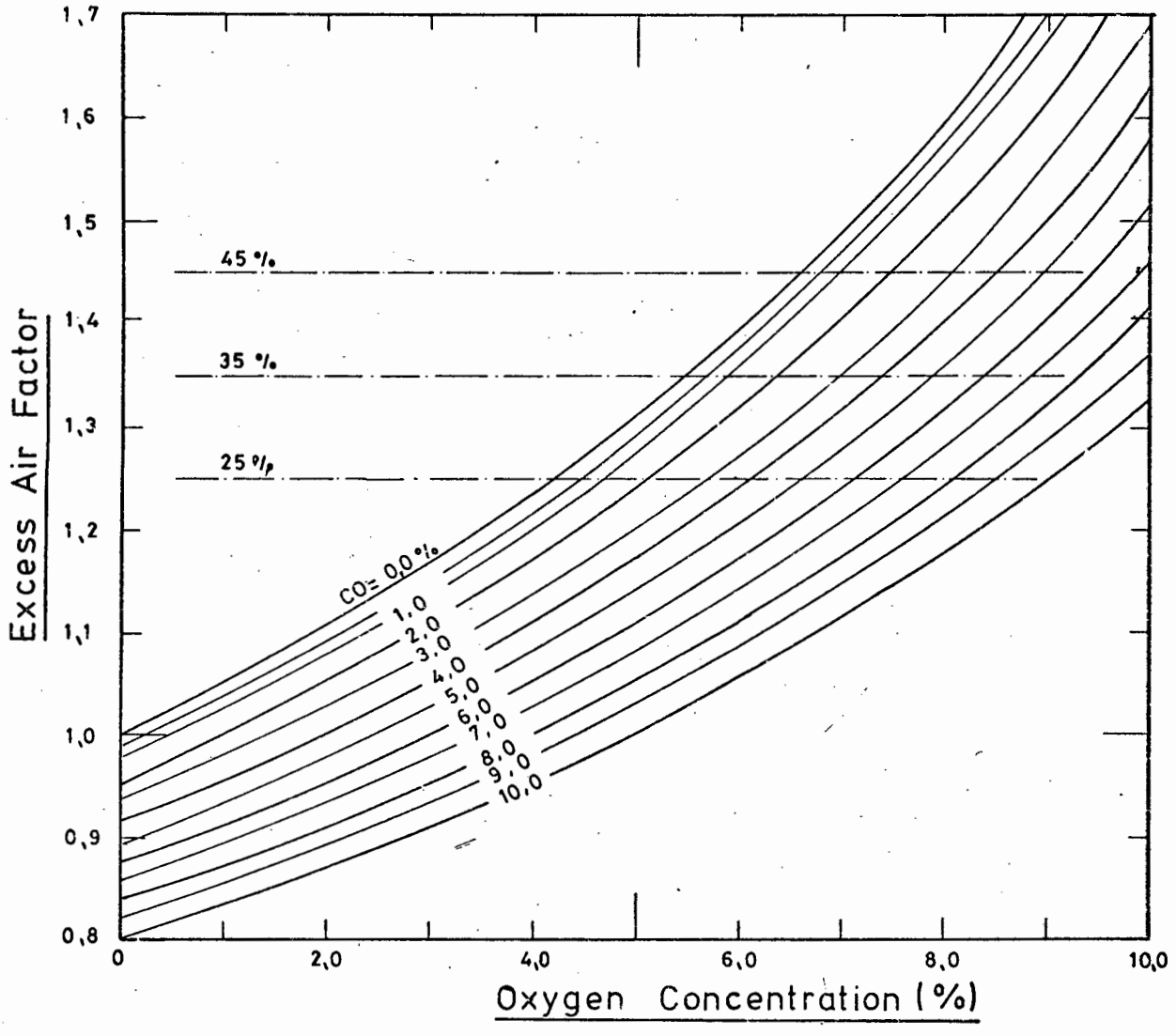

Figure D1 : Relationship between oxygen and carbon monoxide contents of the dry flue gas and the excess air factor.

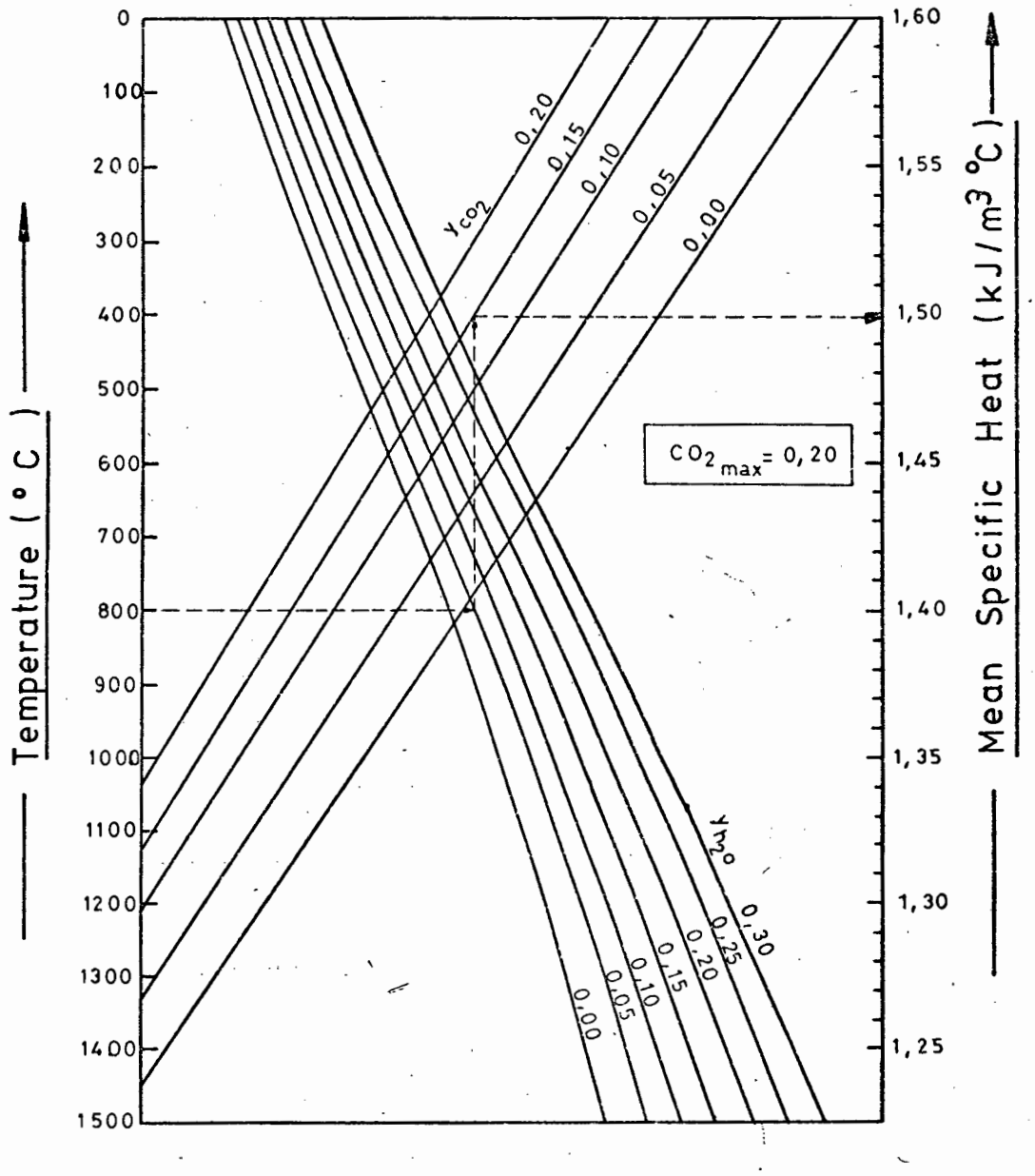

Figure D2 : Mean specific heat of flue gas, referred to normal temperature and pressure as a function of the volumetric fractions of carbon dioxide and water vapour, Brandt (172).

APPENDIX E

THE OVERBED FEED SYSTEM

The overbed feed system comprises a modified rotary drum type feeder and a pneumatic spreader. The design of the spreader was based upon tests performed on a small piece of test equipment having an aperture of rectangular cross section (3,5 mm x 145 mm).

E.1 FLOW CHARACTERISTIC OF THE PNEUMATIC SPREADER

The spreader has been fitted with a 170 mm long aperture which has been designed to enable the installation of removable inserts so as to permit a variation of the dimensions of the discharging aperture thereby changing the flow characteristic. The results of the tests with a 3,5 mm deep aperture are shown in Figure E1 which illustrates the pneumatic spreader discharge pressure as a function of the flow of air discharging from the aperture. The relationship of Figure E1 can be described by equation (E1) below.

$$M = 1{,}91 \cdot 10^{-3} \sqrt{\rho \cdot h^*} \qquad (E1)$$

where M (kg/s) is the air flow rate, ρ (kg/m^3) is the density of air and h* (mmWg) is the pneumatic spreader windbox pressure.

Equation (E1) implies that the discharge coefficient is 0,726.

E.2 PNEUMATIC SPREADING TESTS

E.2.1 Experimental Equipment

A grid was fabricated and installed in the test rig to enable an assessment of the spreading capabilities of the above bed feed system. Details of the grid are illustrated in Figure E2 from which it is seen that the grid is made up of 25 rectangular sections superimposed upon the circular flue of

the test rig. Further, five zones can be established every 200 mm from the pneumatic spreader discharge. The grid can further be raised and lowered with respect to the spreader aperture thereby simulating different bed heights.

E.2.2 Experimental Conditions

Spreading characteristics were evaluated for various pressures of the pneumatic spreader windbox, and for different bed heights. Three different coal flow rates were employed, however, the effect of this parameter on the spreading characteristics could not be detected under the conditions investigated. Ten tests were performed. A summary of the test conditions is illustrated in Table E1.

TABLE E1 : Summary of the main operating parameters for the ten tests undertaken with the pneumatic spreader.

Bed Height (mm) - Windbox Pressure (mm Wg)	100	150	200
100		10	
200	8	3	
300		5	
350	7	2*,6	9

*) where test 2 was conducted using duff coal.

The first two tests were conducted with the duff coal having a grading represented in Appendix C. The low fines coal represented in the same Appendix was used for the remaining tests. However, segregation of the fine from the coarse coal in the coal hopper resulted in a coal grading far coarser than the original coal specification being fed to the test rig by the overbed coal feed system. The "as-fed" coal size

grading is contained in Table E2. This size grading is representative of the coal utilized for Tests 3 to 10. A similar grading analysis was not performed for Tests 1 and 2 during which the duff coal was used.

TABLE E2 : "As-fed" coal size grading of the low fines content coal utilized for Tests 3 to 10.

Sieve Size (mm)	"As-fed" low fines Content Coal	
	% ret. on	Cum. % by Wt. less than
5,80	8,5	91,5
4,00	17,5	74,0
2,80	24,8	49,1
2,00	18,1	31,1
1,40	10,6	20,5
1,00	7,3	13,2
0,850	1,4	11,8
0,600	3,5	8,3
0,425	2,0	6,3
0,300	1,8	4,5
0,212	1,3	3,3
Pan	3,3	-

Effective Size = 0,77 mm
Uniformity Coefficient = 4,16
Mean Particle Diameter = 1,20 mm

E.2.3 Test Results

The coal collected in each of the grid compartments illustrated in Figure E2 was collected and weighed for tests 2 to 10 thus producing a weight distribution. In view of the major proportion of the coal being collected in the central portion

of the collecting grid in the direction of the pneumatic spreading air (i.e. in compartments 23, 18, 13, 8 and 3 of Figure B.2) the results have been formulated in terms of the five zones spaced equidistant from the pneumatic spreader. The accumulation of the coal in the central compartments is illustrated in Figure E3 for Test 6.

In order to establish the effect of particle size on the distribution characteristics of the above bed spreader system, grading analyses were performed on the coal collected in compartments 23 and 3 for tests 5 to 10. These samples would be representative of the material collected in Zones I and V respectively. In addition, a grading analysis was performed on the coal contained in compartment 8 (i.e. representative of Zone IV) for test 10. The grading analyses for Zone I and Zone V were very similar for each of the tests even though the test conditions were markedly different. The grading analyses for Zone I and Zone V for each of the tests can adequately be described by the curves drawn for Test 6 and illustrated in Figure E4. Also included in Figure E4 is the "as fed" coal size grading. A summary of the results of the grading analyses is contained in Table E3.

E.2.4 Discussion of Results

The results of the overbed spreading tests have been graphically represented by Figures E5, E6, E7 and E8. Figure E5 illustrates the effect of grading on the distribution. The "low fines" coal appears to be better distributed over the length of the furnace than the "duff" coal due to the smaller proportion collected in the first 200 mm along the length of the furnace. The effect of bed height is illustrated in Figure E6 whilst the effect of pneumatic air windbox pressure for two different bed heights is represented in Figures E7 and E8.

From the figures it is evident that for a particular fuel size grading, and for a specific height of the coal feed aperture

from the surface of the bed, improvements in the distribution of the fuel can be attained by careful selection of the pneumatic transport air flow rate. In order to enable the results to have more general application with regard to the "as-fed" fuel size grading, the results of the grading analyses of tests 5 to 10 have been examined in more detail.

TABLE E3 : Summary of grading analyses for coal spreading tests

	Windbox Pressure (mm Wg)	Bed Height (mm)	Effective Size (mm)	Uniformity Co-Efficient (-)	Mean Particle Diameter (mm)
Test 5 Zone I	299	150	1,75	2,28	2,52
Zone V			0,56	4,91	1,04
Test 6 Zone I	350	150	1,78	2,22	2,56
Zone V			0,56	4,91	1,05
Test 7 Zone I	349	100	2,10	2,03	2,71
Zone V			0,74	3,96	1,28
Test 8 Zone I	198	100	1,83	2,13	2,60
Zone V			0,55	4,42	1,00
Test 9 Zone I	349	200	1,60	2,30	2,59
Zone V			0,52	4,80	1,00
Test 10 Zone I	99	150	1,40	2,60	2,49
Zone IV			0,25	4,76	0,53
Zone V			0,66	3,53	1,04

In particular, the coal has been divided into five size intervals:

less than 0,5 mm
0,5 to 1,0 mm
1,0 to 2,0 mm
2,0 to 4,0 mm
greater than 4,0 mm

The percentage of coal collected in each of these size intervals for each of the tests for which grading analyses were undertaken is illustrated in the form of a histogram in Figures E9(a) and (b) for Zones I and V respectively. From Figure E9 it is evident, that although the zone nearest the feeder i.e. Zone I, collects mainly the larger particles whilst Zone V collects a larger proportion of fines, the coarse "as-fed" size grading of the coal tends to over-emphasize the collection of particles in the size interval 2,0 to 4,0 mm even in the zone furthest from the feeder. Therefore a further set of histograms viz. Figure E10 (a) and (b) has been derived, based upon the percentage of the particular size fraction in the original coal feed collected in the zone illustrated.

Figures E10 (a) and (b) therefore represent the anticipated size distributions for each particular size fraction and are independent of the original "as-fed" size distribution. In order to obtain the size distribution for a particular size grading, the quantities represented in Figure E10 would have to be adjusted by the weight fractions contained in each size interval.

A major shortcoming of the tests lies in the fact that they have had to be performed in the absence of an upflow of air which would occur during normal operation of the test rig. This deficiency is easily incorporated by accounting for the lift imparted to the particle by an upflow of air in describing the results of the overbed spreader.

E.2.6 Conclusions

The following conclusions may be made:

a) The pneumatic spreader effectively distributes coal in the 1 000 mm diameter test rig.

b) For particular coal gradings and bed heights, a particular spreading air flow rate would result in improved distribution of the coal.

c) The results of the spreading tests have been reduced to a form which is independent of the original coal grading.

E.3 CALIBRATION OF THE COAL FEEDER

The above bed rotary drum feeder was calibrated using the duff coal. The results of the feeder calibration tests are illustrated in Figure E11 and have been fitted by a least squares analysis by equation (E2).

$$M_{fo} = 1,32 \cdot 10^{-3} + 0,0416 \cdot n \qquad (E2)$$

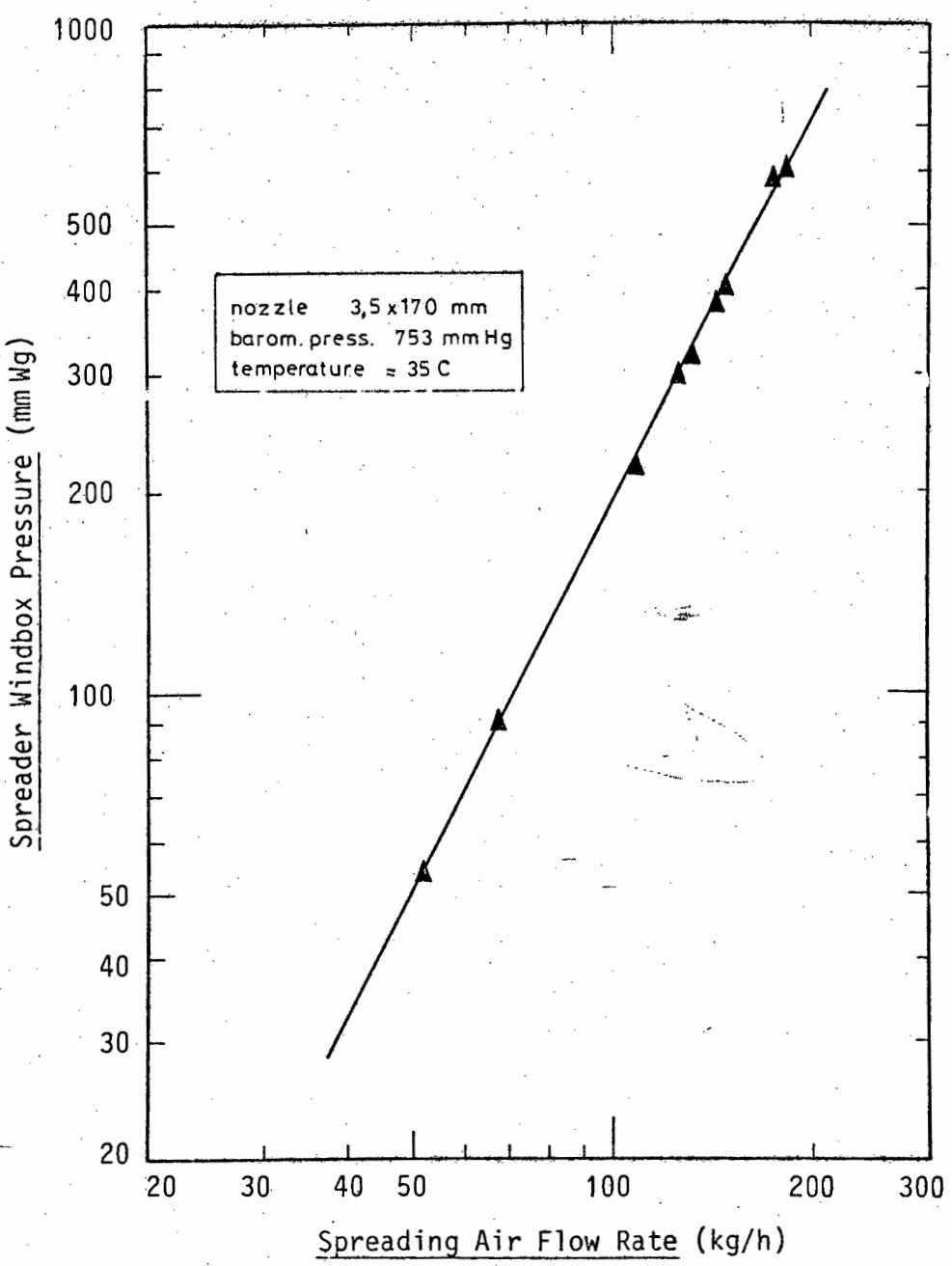

Figure E1 : Pneumatic spreader flow characteristic

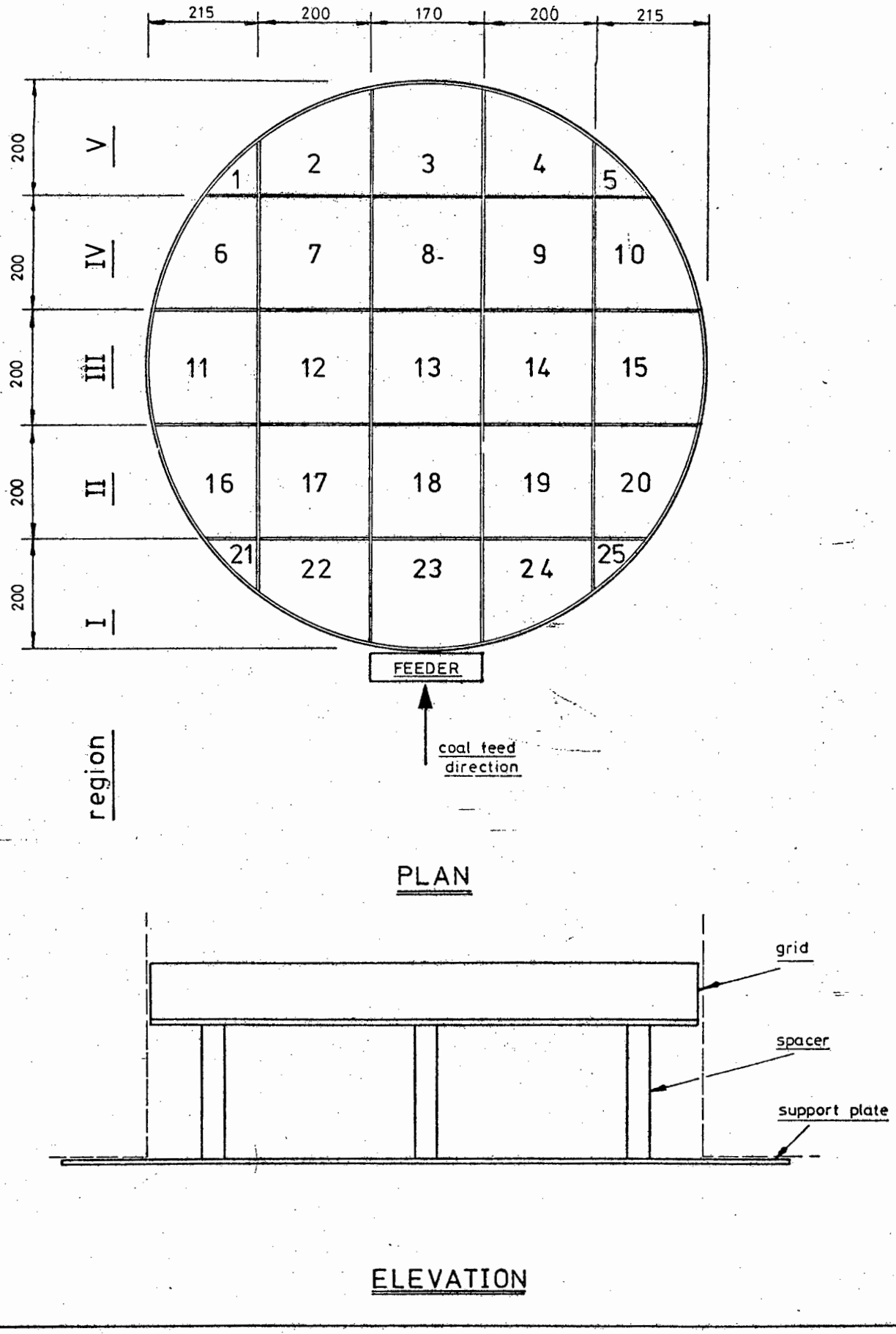

Figure E2 : Pneumatic spreader collection grid.

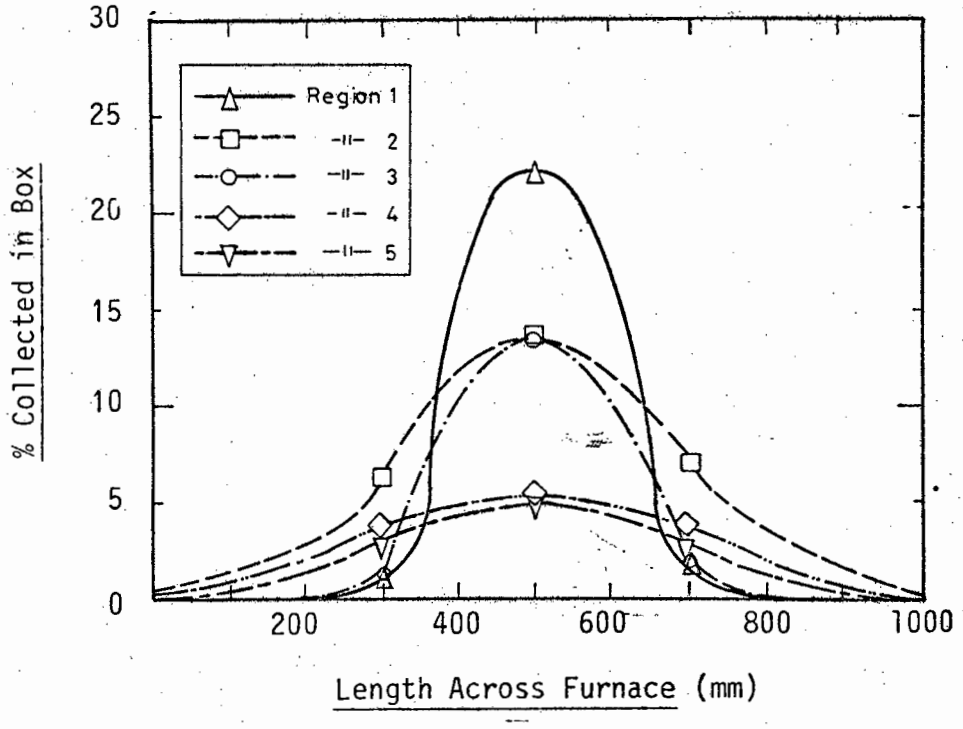

Figure E3 : Weight distribution at right angles to the spreading direction (Test 6).

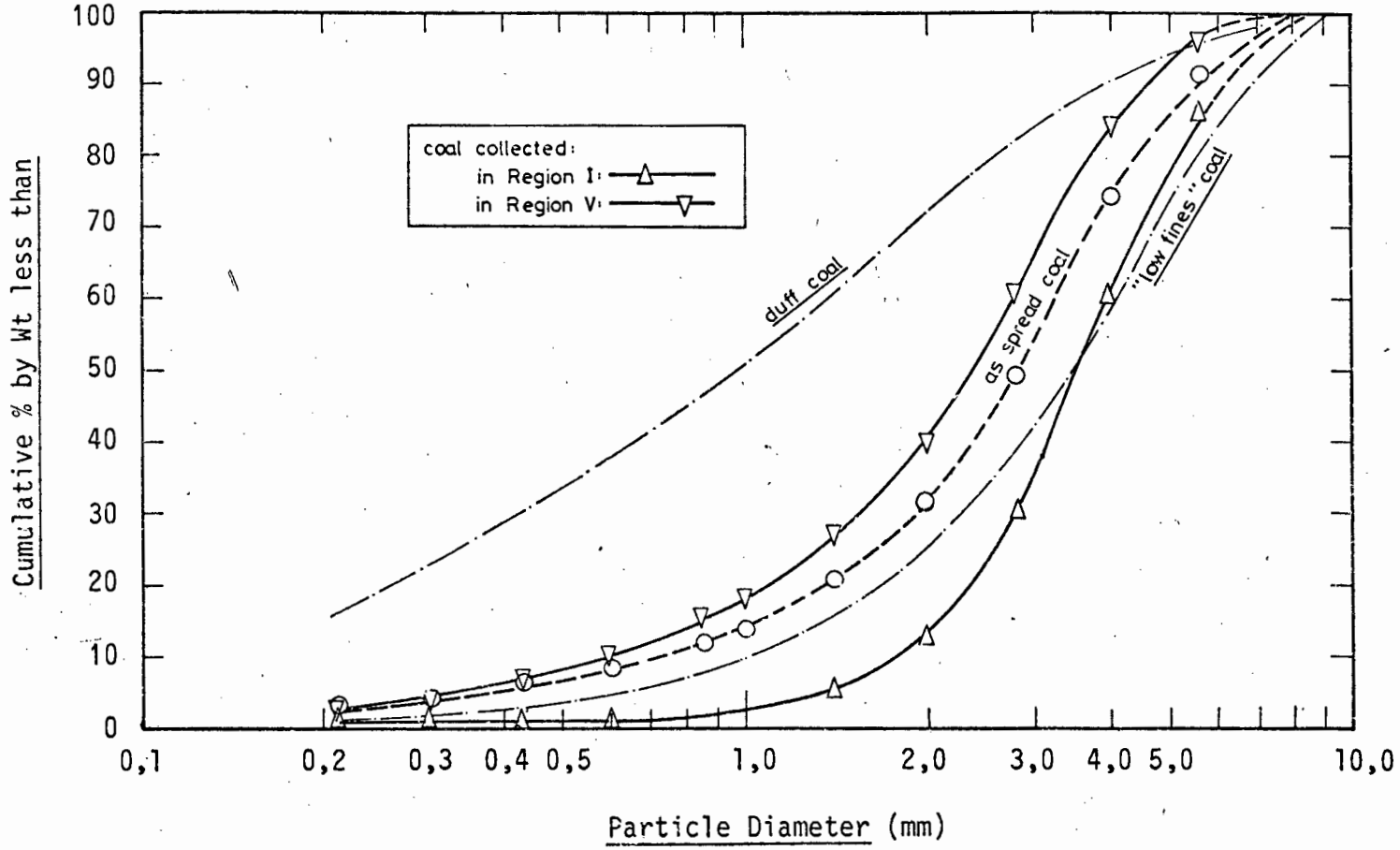

Figure E4 : Grading analyses of particles in Zones I and V for Test 6.

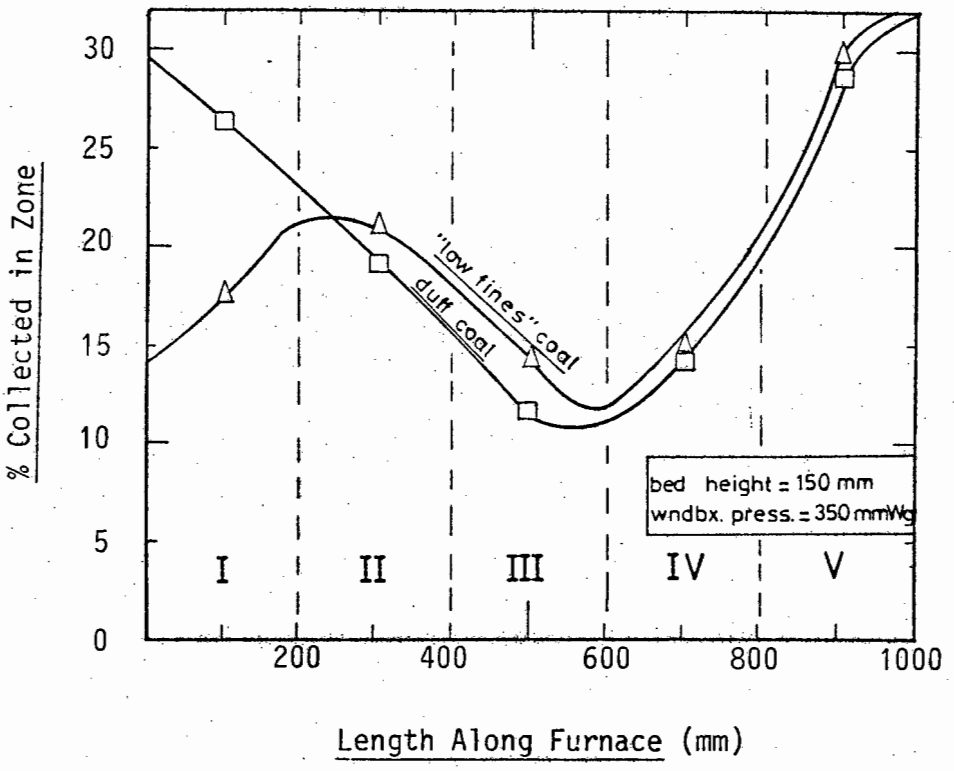

Figure E5 : The effect of two coal gradings on the spreading characteristics.

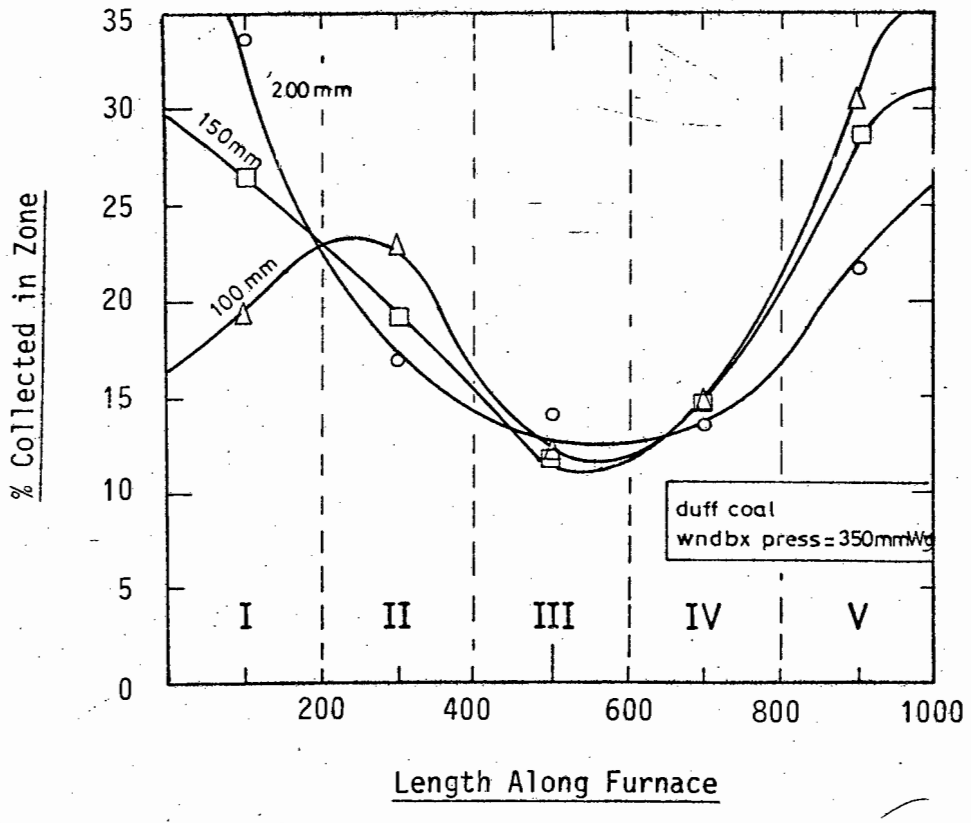

Figure E6 : The effect of bed height at a windbox pressure of 350 mm Wg on the spreading characteristics.

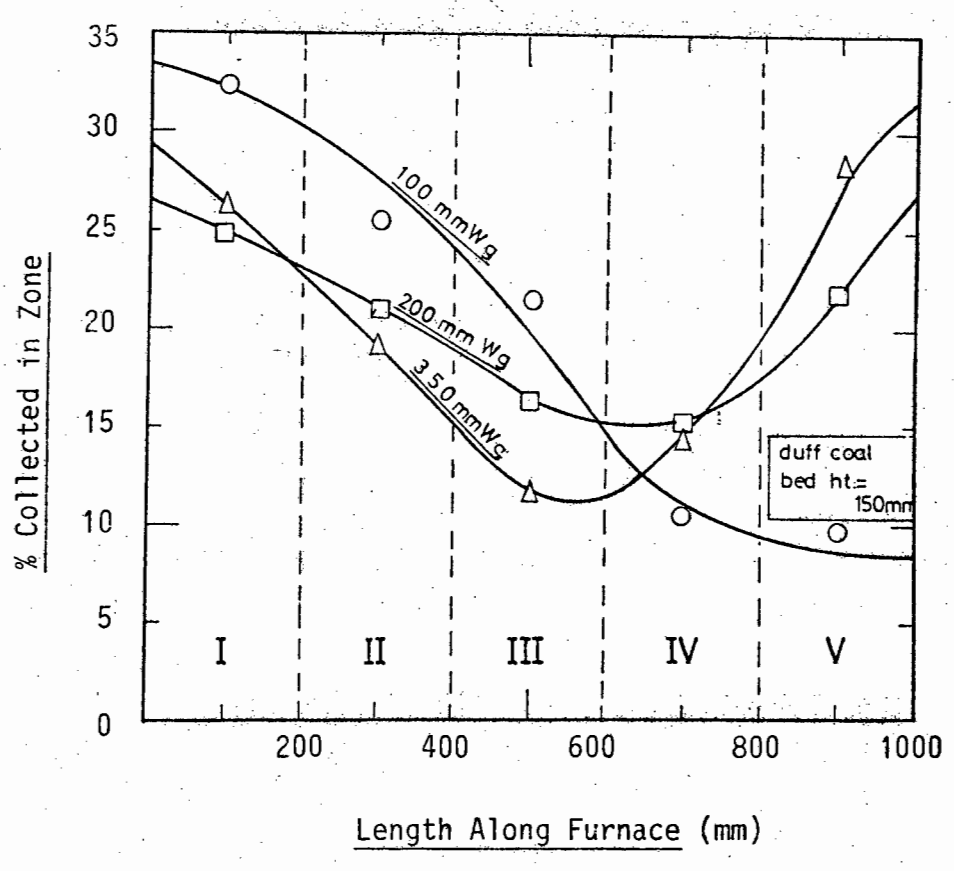

Figure E7 : The effect of windbox pressure at a bed height of 150 mm on the spreading characteristics.

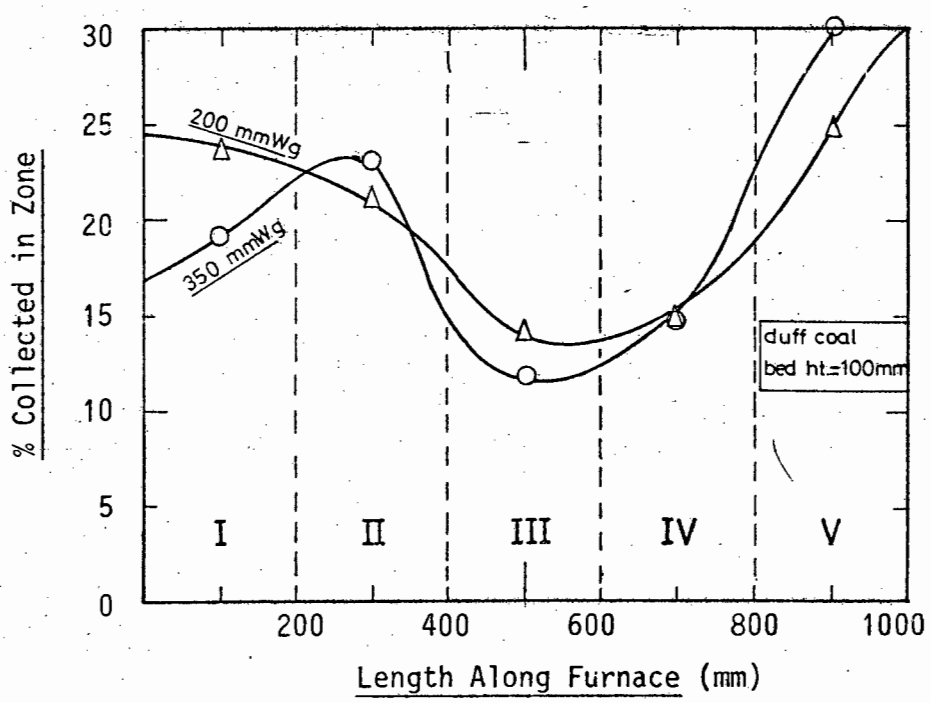

Figure E8 : The effect of windbox pressure at a bed height of 100 mm on the spreading characteristics.

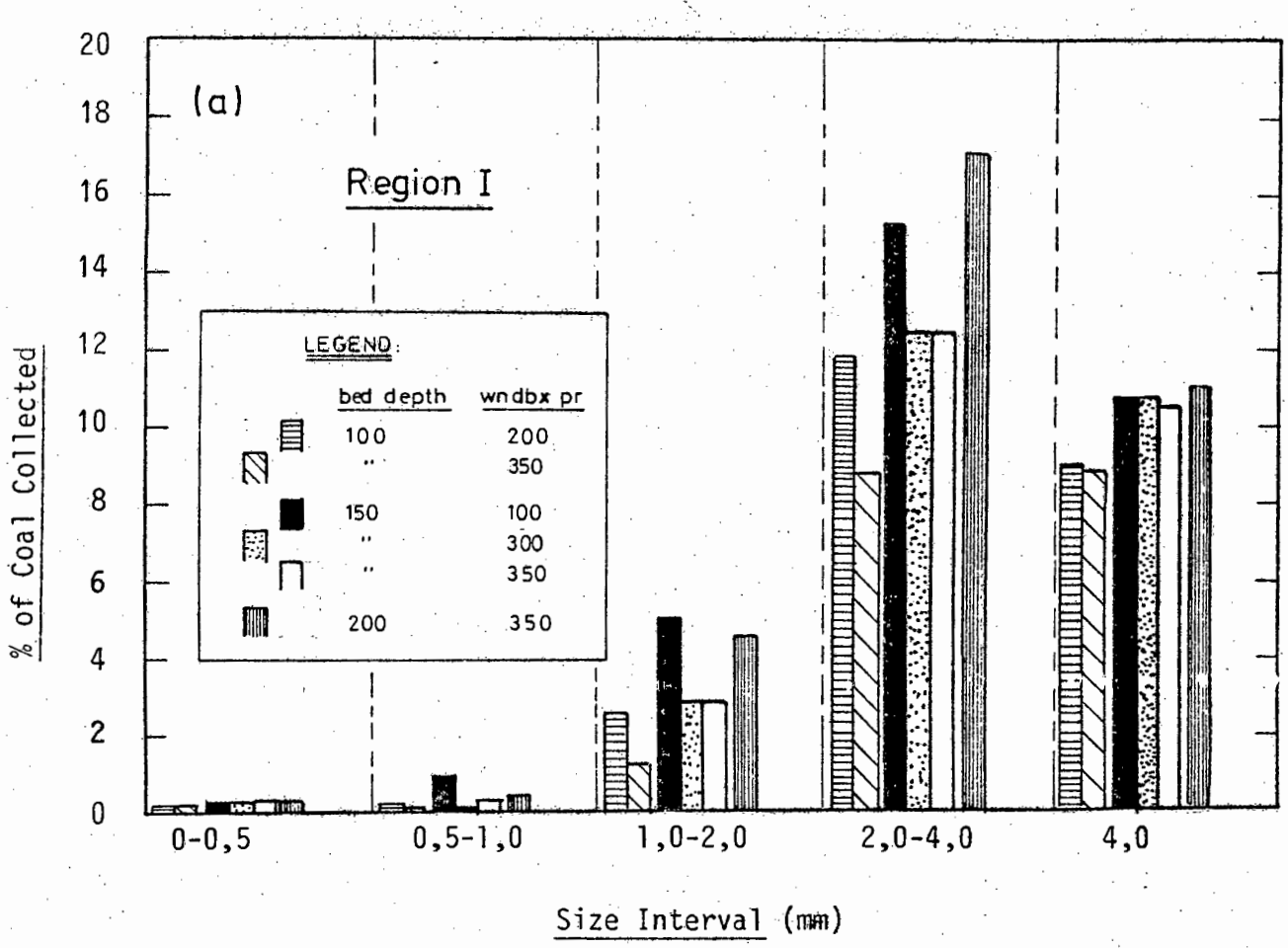

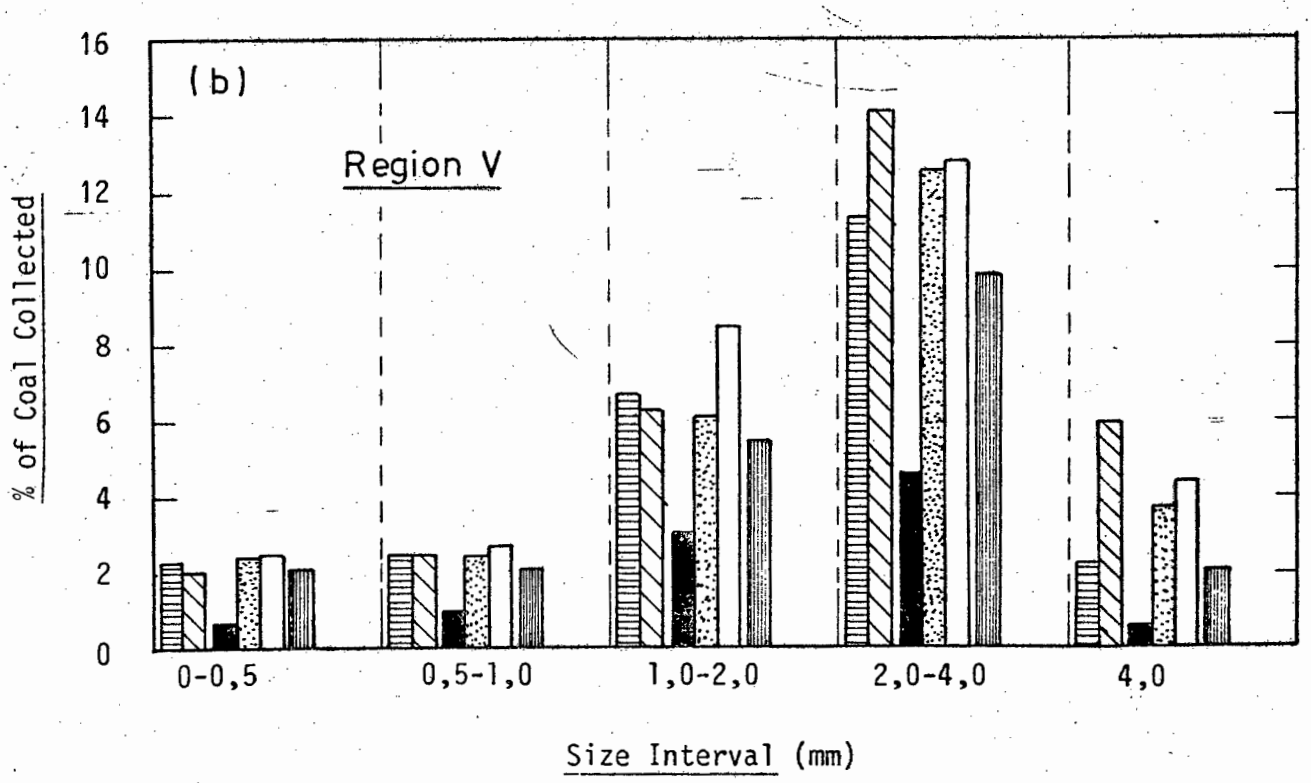

Figure E9 : Percentage of coal collected in specific size intervals.

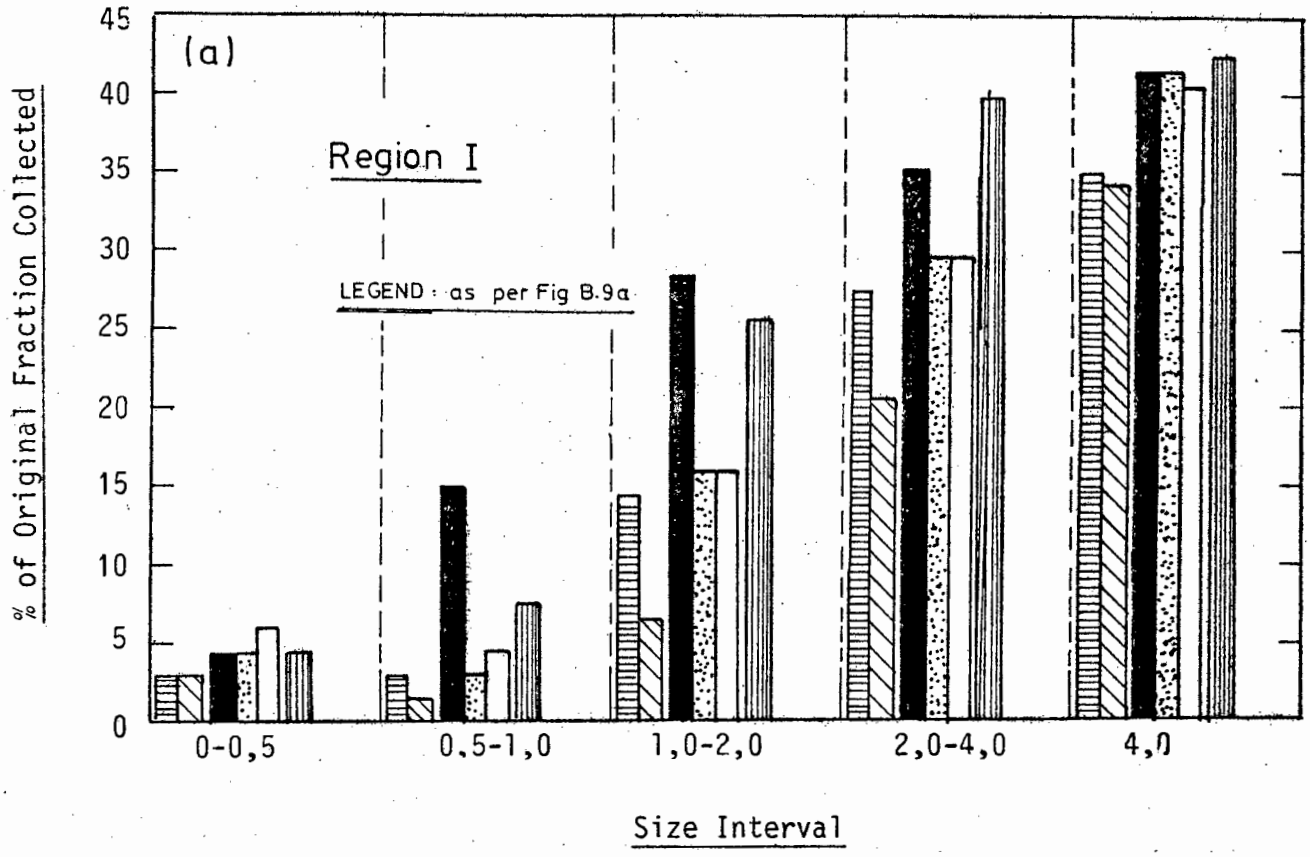

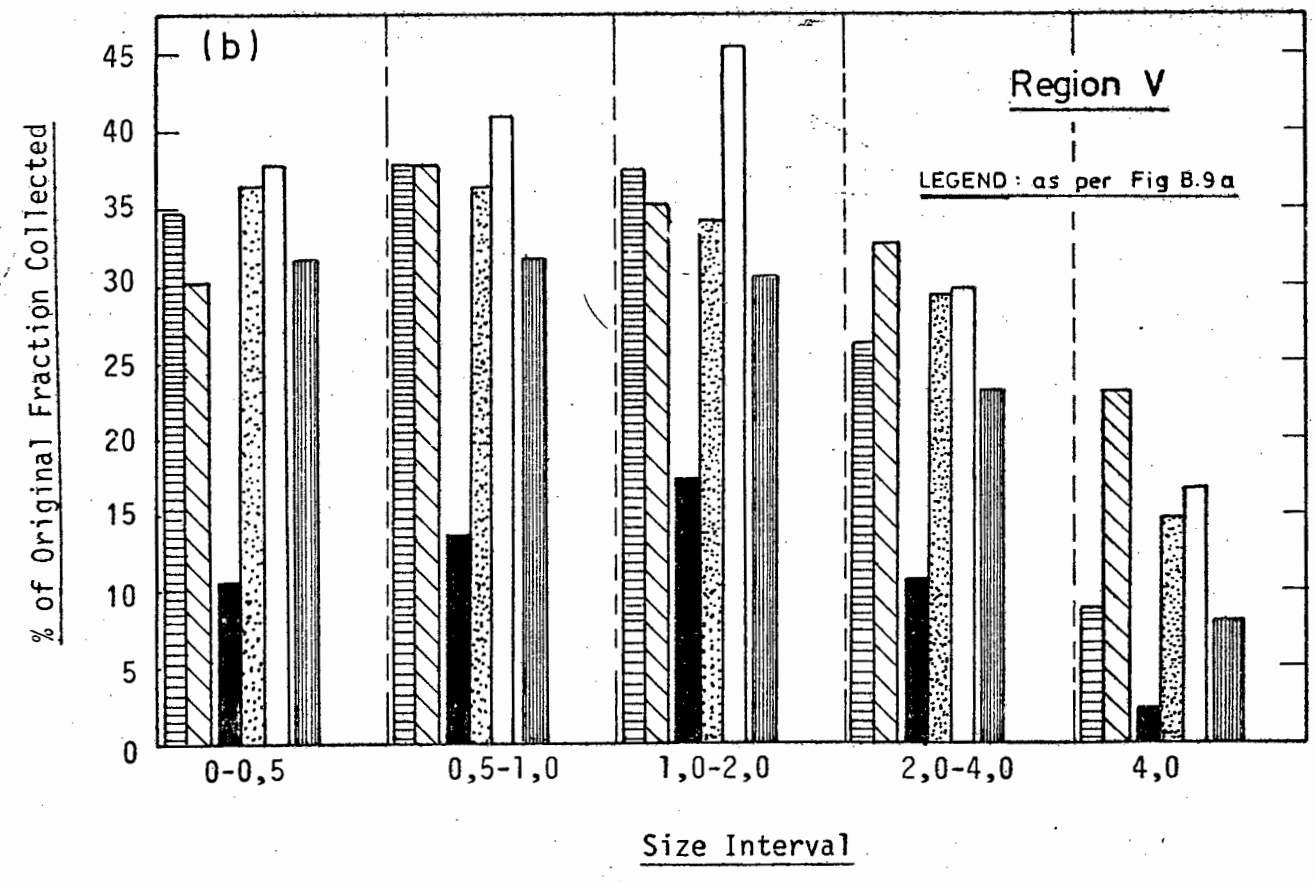

Figure E10 : Percentage of the original fraction of coal contained in the incoming feed of the specific size interval collected in that size interval.

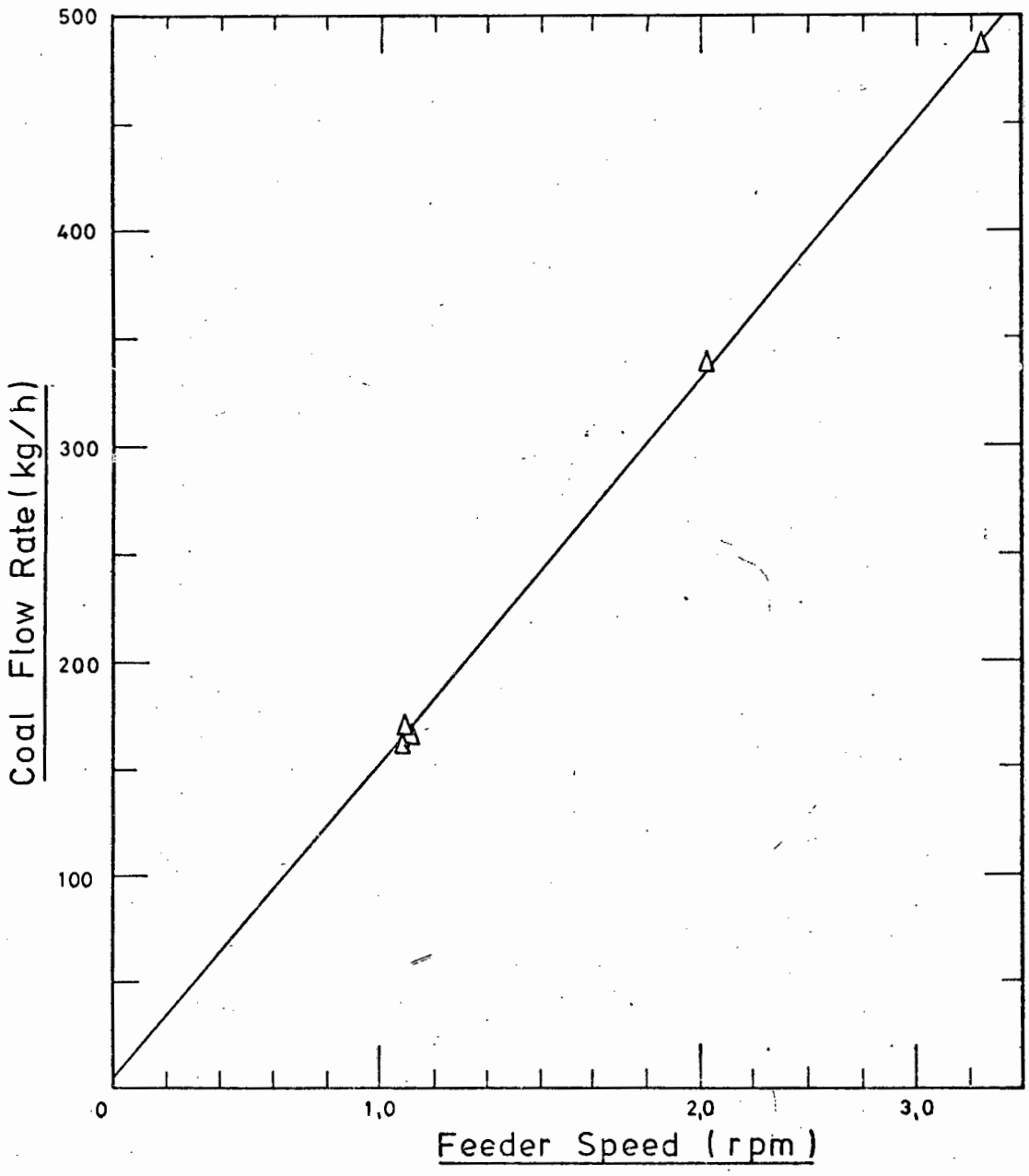

Figure E11 : Coal feeder calibration curve.

APPENDIX F

STATISTICAL ANALYSIS

"Statistical methods are predicated on the single concept of variability. It is through this fundamental concept that a basis is determined for experimental design and analysis of data. In this sense, statistical methods are concerned with deriving maximum information from a given set of data (analysis), and conversely minimizing the amount of data (experimental design) to derive specific information." (174, ch.2). The use of statistics in engineering and in general has been covered in a number of general and specific publications. This thesis has made reference to a number of publications and standard texts on the subject (174), (175), (176), (177), (178) and (179). The more fundamental concepts such as standard deviations, hypothesis testing, correlation coefficients, distribution functions, analysis of variance etc. are not discussed here and the reader is referred to any of the above texts for more details.

A major portion of this thesis is concerned with the determination of the factors influencing the combustion efficiency of the fluidized-bed combustion rig. A general description and definition of the terms and the approach employed in the multiple regression analysis is presented in this Appendix for ease of reference.

F.1 Multiple Regression

Multiple regression methods are used to relate a dependent variable (Y) to a number of independent variables $(X_1, X_2 \ldots X_m)$ Only linear multiple regression will be considered and a model of the following form is postulated:

$$Y = b_o + b_1 \cdot X_1 + b_2 \cdot X_2 + \ldots\ldots\ldots + b_m \cdot X_m \qquad (F1)$$

The coefficients of the model (b_1, b_2, ... b_m) are determined by the method of least squares. This involves minimising the squared differences between the observed value of the dependent variable i.e. Y_0 and that predicted by equation (F1), i.e. Y_p Mathematically the solution is computed by taking the partial derivative with respect to each coefficient of the least squares equation

$$S = \Sigma (Y_0 - Y_p)^2 \qquad (F2)$$

$$S = \Sigma \{Y_0 - (b_0 + b_1 \cdot X_1 + b_2 \cdot X_2 \ldots\ldots + b_m \cdot X_m)\}^2 \qquad (F3)$$

and setting the result of each partial differentiation to zero. This results in the following equations which may be solved simultaneously for b_0, b_1, b_2, ... b_m.

$$\begin{aligned} b_0 &+ b_1 \cdot \Sigma\{X_1\} + \ldots\ldots + b_m \cdot \Sigma\{X_m\} = \Sigma\{Y_0\} \\ b_0 \Sigma\{X_1\} &+ b_1 \cdot \Sigma\{X_1\}^2 + \ldots\ldots + b_m \cdot \Sigma\{X_1 \cdot X_m\} = \Sigma\{X_1 \cdot Y_0\} \\ b_0 \Sigma\{X_m\} &+ b_1 \cdot \Sigma\{X_1 X_m\} + \ldots\ldots + b_m \cdot \Sigma\{X_m\}^2 = \Sigma\{X_m \cdot Y_0\} \end{aligned} \qquad (F4)$$

However it is convenient to transform the above equations into the standard normal equations. The first step in this transformation results in the above equations being transformed to those given by the equations (F5):

$$\begin{aligned} b_1 \cdot (s_{X1})^2 &+ b_2 \cdot s_{X1\ X2} + \ldots\ldots + b_m \cdot s_{X1\ Xm} = s_{X1\ Y0} \\ b_1 \cdot s_{X1\ X2} &+ b_2 \cdot (s_{X2})^2 + \ldots\ldots + b_m \cdot s_{X2\ Xm} = s_{X2\ Y0} \\ b_1 \cdot s_{X1\ Xm} &+ b_2 \cdot s_{X2\ Xm} + \ldots\ldots + b_m \cdot (s_{Xm})^2 = s_{Xm\ Y0} \end{aligned} \qquad (F5)$$

where $(s_{Xi})^2$ is the sample variance of X_i and $s_{Xi\ Xj}$ is the covariance between X_i and X_j A bivariate correlation coefficient for X_i and X_j is defined as

$$r_{ij} = s_{Xi\ Xj} / \sqrt{(s_{Xi})^2 \cdot (s_{Xj})^2} \qquad (F6)$$

and a standard partial correlation coefficient for variable X_j is defined as

$$B_j = \frac{b_j \cdot \sqrt{(s_{Xj})^2}}{\sqrt{(s_{YO})^2}} \qquad (F7)$$

The Standard Normal Equations

By manipulation of the equations (F5) the standard normal equations (F8) are formed.

$$\begin{aligned} B_1 + B_2 \cdot r_{12} + \ldots\ldots + B_m \cdot r_{1m} &= r_{Y1} \\ B_2 \cdot r_{12} + B_2 + \ldots\ldots + B_m \cdot r_{1m} &= r_{Y2} \\ B_m \cdot r_{1m} + B_2 \cdot r_{2m} + \ldots\ldots + B_m &= r_{Ym} \end{aligned} \qquad (F8)$$

The bivariate correlation coefficients r are easily evaluated, and by inverting the resulting matrix of these coefficients, the values for the standard partial correlation coefficients, B, may be determined. One of the advantages of using the standard partial regression coefficients, is that as these coefficients vary between -1 and 1, they may be directly compared. Further, the multiple correlation coefficient is easily determined by equation (F9)

$$R^2 = \Sigma\{B_i \cdot r_{Yi}\} \qquad (F9)$$

F.2 Tests on Coefficients

The Bivariate Correlation Coefficient

In order to determine whether a relationship exists between two variables the bivariate correlation coefficient is tested to determine whether it is significantly different from zero by the statistic

$$t = r \cdot \sqrt{\frac{n-2}{1-r^2}} \qquad (F10)$$

where t is distributed as the Student's t distribution with $(n-2)$ degrees of freedom.

The Standard Partial Correlation Coefficient

In any process a number of independent variables may be arbitrarily defined, and though one may be tempted to use a large number of these variables, the resulting equation will be unwieldy. Further, the contribution of some of the variables in predicting the independent variable may be small, such that these may be eliminated from the regression equation. In order to eliminate those independent variables which do not contribute significantly to the prediction, the values of B must be tested to determine whether they are different from zero. Should the interval estimate of the population standard partial regression coefficient B' include zero, then the hypothesis that B is zero is accepted. The interval estimate of B' is given as

$$B_j + t_{(\alpha/2)} \cdot A \quad < \quad B'_j \quad < \quad B_j + t_{(1-\alpha/2)} \cdot A \qquad (F11)$$

where

$$A = \sqrt{(1-R^2) \cdot g_{ij} / (n-m-1)} \qquad (F12)$$

and

g_{ij} *is a diagonal element on the inverted bivariate correlation coefficient matrix .*

The Multiple Correlation Coefficient

Although a number of variables may be eliminated by the procedure given above, their combined effect may be significant. In order to determine whether the multiple correlation coefficient has been significantly lowered by the elimination of variables the multiple correlation coefficient after elimination of variables R' is compared with the original value R . As this is effectively a test on the equality of two population variances the F-distribution is used. The appropriate statistic is given by

equation (F13).

$$F = \frac{\{R^2 - (R')^2\}\ (n - m - 1)}{(1 - R^2)\ (m - m')} \qquad (F13)$$

where the superscript (') refers to the variables after the variables have been eliminated
and F has $(n-m-1)$ and $(n-m')$ degrees of freedom.

APPENDIX G

TABULATION OF RESULTS

In order to facilitate the comparison of the findings of this thesis with other published information, the results have been presented in greater detail in this Appendix than in the main body of the thesis. Further, the results contain a large body of calculated results which should serve in many instances to highlight the calculation procedure adopted. Table G1 summarizes the test conditions whilst details of each of the particular tests are contained in the subsequent tables.

TABLE G1 : Summary of Test Conditions

Test		8	9	10	12	13	14	15a	15b	15c	16a
Static bed height	mm	135	148	200	218	214	226	219	219	219	200
Mean bed temperature	°C	933	872	868	788	822	850	870	900	865	900
Superficial gas velocity	m/s	1,32	1,20	1,25	1,17	1,13	1,26	1,32	1,72	2,25	1,30
Coal type burnt	-	D	D	D	D	D	D	D	D	D	D
Coal feeder used	-	U	U	U	U	U	U	U	U	U	U
Secondary air	-	O	O	O	O	O	O	O	O	O	O
Immersed cooling tube	-	O	O	O	O	O	O	O	O	O	O

NOTE : 1) for coal type burnt : D = duff coal , L = low fines coal
2) for coal feeder used : U = under bed feed, A = above bed feed
3) secondary air : S = with sec. air , O = without sec.air
4) immersed cooling tube : T = with tube , O = without tube

TABLE G1 (cont.): Summary of Test Conditions

Test		16c	19	20	22	23a	23b	24	28	30a	35a
Static bed height	mm	200	101	101	100	97	97	109	119	100	188
Mean bed temperature	°C	980	900	900	985	945	985	915	930	955	950
Superficial gas velocity	m/s	3,15	2,04	1,68	1,10	1,50	1,55	1,79	1,61	1,82	2,30
Coal type burnt	-	D	D	D	D	D	D	D	D	D	D
Coal feeder used	-	U	U	U	U	U	U	U	U	U	U
Secondary air	-	O	O	O	O	O	O	O	O	O	O
Immersed cooling tube	-	O	O	O	O	O	O	O	O	O	O

Test		35b	37	38a	38b	38c	40a	40b	40c	41a	41b
Static bed height	mm	188	216	231	231	231	189	189	189	198	201
Main bed temperature	°C	950	955	935	908	915	955	960	980	835	931
Superficial gas velocity	m/s	2,24	2,19	2,13	1,42	2,10	1,82	1,58	3,31	1,12	1,23
Coal type burnt	-	D	D	D	D	D	L	L	L	L	L
Coal feeder used	-	U	U	U	U	U	U	U	U	U	U
Secondary air	-	S	O	O	S	O	O	S	O	O	S
Immersed cooling tube	-	O	O	O	O	O	O	O	O	O	O

TABLE G2 : Bed Expansion Data

Test	Bed Temperature ^{o}C	Sup.Gas Velocity u_f m/s	Minimum Fluidization Vel. u_{mf} m/s	Particle Term.Vel. u_t m/s	Static Bed Ht. Hst mm	Dynamic Bed Ht. H_f mm	Mean Bed Voidage $\bar{\alpha}$ -
8	933	1,32	0,244	8,66	135	203	0,601
9	872	1,20	0,249	8,63	148	203	0,563
10	868	1,25	0,250	8,62	200	260	0,538
12	788	1,17	0,258	8,56	218	297	0,560
13	822	1,13	0,254	8,59	214	290	0,557
14	850	1,26	0,251	8,61	226	300	0,548
15a	870	1,32	0,250	8,63	219	306	0,571
15b	900	1,72	0,247	8,64	219	329	0,601
15c	865	2,25	0,250	8,62	219	324	0,594
16a	900	1,30	0,247	8,64	200	299	0,599
16c	980	3,15	0,240	8,69	200	350	0,657
19	900	2,04	0,247	8,64	101	201	0,699
20	900	1,68	0,247	8,64	101	203	0,701
22	985	1,10	0,239	8,69	100	155	0,613
23a	945	1,50	0,243	8,67	97	162	0,641
23b	985	1,55	0,239	8,69	97	162	0,641
24	915	1,79	0,245	8,65	109	138	0,526
28	930	1,61	0,244	8,66	119	166	0,570
30a	955	1,82	0,242	8,67	100	159	0,623
35a	950	2,30	0,242	8,67	188	312	0,638
35b	950	2,24	0,242	8,67	188	317	0,644
37	955	2,19	0,242	8,67	216	349	0,629
38a	935	2,13	0,244	8,66	231	362	0,617
38b	908	1,42	0,246	8,65	231	384	0,639
38c	915	2,10	0,245	8,65	231	377	0,632

TABLE G2 (Cont.) : Bed Expansion Data

Test	Bed Temperature ^{o}C	Sup.Gas Velocity u_f m/s	Minimum Fluidization Vel. u_{mf} m/s	Particle Term.Vel. u_t m/s	Static Bed Ht. Hst mm	Dynamic Bed Ht. H_f mm	Mean Bed Voidage $\bar{\alpha}$ -
40a	955	1,82	0,242	8,67	189	289	0,608
40b	960	1,58	0,242	8,68	189	322	0,648
40c	980	3,31	0,240	8,67	189	357	0,682
41a	835	1,12	0,253	8,60	198	304	0,609
41b	931	1,23	0,244	8,66	201	330	0,635
41c	935	1,26	0,244	8,66	203	358	0,660
41d	1015	1,98	0,237	8,70	205	315	0,610
44b	960	1,76	0,242	8,68	110	179	0,631
44c	905	1,05	0,246	8,65	110	160	0,588
45	985	1,66	0,239	8,69	112	188	0,643
47a	780	1,57	0,258	8,56	114	172	0,602
47b	970	1,82	0,241	8,69	116	195	0,643
47c	935	1,48	0,244	8,66	118	178	0,602
47d	990	1,45	0,239	8,69	120	205	0,649
50a	910	1,80	0,246	8,65	204	319	0,616
50b	935	1,79	0,244	8,66	210	350	0,640
50c	975	2,34	0,240	8,68	216	379	0,658
50d	850	1,35	0,251	8,61	221	284	0,533
50g	795	1,27	0,257	8,57	222	303	0,560
53a	727	1,50	0,264	8,51	132	170	0,534
53c	960	1,40	0,242	8,68	132	209	0,621

TABLE G3 : Results obtained from the Heat Transferred to the 76,2 mm OD immersed Cooling Tube

Test	Bed Conditions			Water Temperatures		Outer Wall Temp.	Water Flow Rate	Heat absor-bed	Heat Flux	Tot. Bed to Wall Ht.trnf. Coeff.
	Bed Temp.	Gas Vel.	Static Bed Height	Inlet	Outlet					
	°C	m/s	mm	°C	°C	°C	kg/h	kW	kW/m^2	W/m^{2}C
44a	950	1,76	110	20,8	38,8	138,4	2713,6	56,85	253	311,2
44b	960	1,76	110	21,2	39,9	130,7	2713,6	59,06	262	316,3
44c	905	1,05	110	22,9	39,0	114,7	2714,4	50,86	226	285,9
45	985	1,66	112	19,2	45,2	147,7	1944,8	58,85	261	312,2
47a	780	1,57	114	31,0	44,2	117,9	2421,3	37,20	165	249,6
47b	970	1,82	116	31,5	52,3	154,6	2407,2	58,28	259	317,5
47c	935	1,48	118	44,0	64,0	151,3	2418,0	56,29	250	319,1
47d	990	1,45	120	23,0	45,8	157,4	2432,4	64,55	287	344,4
50a	910	1,80	204	20,2	42,6	131,8	2017,4	52,60	234	300,2
50b	935	1,79	210	19,6	44,0	146,9	2128,5	60,45	269	340,7
50c	975	2,34	216	21,0	42,5	154,8	2698,3	67,52	300	365,7
50d	850	1,35	221	26,5	41,3	146,0	2686,6	46,28	206	292,0
50e(i)	840	1,34	222	26,1	41,8	145,4	2686,6	49,09	218	313,9
50e(ii)	840	1,34	222	29,7	43,6	145,5	3085,7	49,92	222	319,3
50e(iii)	840	1,34	222	22,8	40,6	143,3	2317,6	48,01	213	306,1
50e(iv)	845	1,34	222	20,8	42,4	141,4	1956,5	49,19	219	310,5
50f	895	1,37	222	20,8	45,0	142,2	1960,1	55,21	245	325,8
50g(i)	795	1,27	222	22,7	42,2	140,8	1949,5	44,25	197	300,5
50g(ii)	790	1,27	222	27,8	40,8	140,4	2734,2	41,37	184	282,9
53a	727	1,50	132	16,2	30,0	141,4	2120,0	34,05	151	258,3
53b	935	1,46	132	17,1	38,6	145,9	2119,3	53,03	236	298,5
53c	960	1,40	132	25,7	52,5	157,0	1954,0	60,95	271	337,2

TABLE G4 : Calculated Results for the Heat Transfer Relationships associated with the 76,2 mm OD horizontal immersed Tube

Test	Heat Flux		Heat Trnf. Coeff.		Nu_{to}	Re_{to}	Ar	P
	Tot. kW/m^2	Conv. kW/m^2	Tot. W/m^2C	Conv. W/m^2C	-	-	-	-
44a	252,5	174,9	311,2	215,5	212,1	826,6	2073	5536
44b	262,3	182,0	316,3	219,5	214,9	817,7	2037	5096
44c	225,9	158,2	285,9	200,2	202,2	525,2	2251	4753
45	261,4	173,4	312,2	207,1	200,1	746,0	1950	5057
47a	165,2	122,8	249,6	185,5	202,2	938,0	2883	5673
47b	258,9	176,1	317,5	216,0	210,3	835,9	2002	5471
47c	250,0	176,3	319,1	225,0	223,4	707,8	2131	5651
47d	286,7	198,5	344,4	238,4	229,7	648,6	1933	5616
50a	233,7	165,7	300,2	213,0	214,5	892,2	2231	5749
50b	268,5	194,7	340,7	247,1	245,3	858,4	2132	6485
50c	299,9	215,8	365,7	263,2	255,7	1065,2	1984	6985
50d	205,6	150,8	292,0	214,2	223,4	726,1	2501	5797
50e(i)	218,1	165,2	313,9	237,8	249,6	728,8	2551	6492
504(ii)	221,7	168,9	319,3	243,2	255,2	728,9	2551	6639
50e(iii)	213,3	160,4	306,1	230,2	241,6	728,8	2551	6284
50e(iv)	218,5	164,6	310,5	234,0	244,8	726,6	2526	6356
50f	245,2	180,9	325,8	240,3	244,1	694,2	2294	6575
50g(i)	196,6	151,9	300,5	232,2	250,6	742,3	2794	6625
50g(ii)	183,8	139,9	282,9	215,4	233,3	748,2	2823	6186
53a	151,3	117,1	258,3	200,0	226,0	972,6	3231	6494
53b	235,6	161,8	298,5	205,0	203,5	702,7	2131	5132
53c	270,7	190,7	337,2	237,5	232,6	649,4	2037	5820

TABLE G5 : Logarithms of the Dependent Variables utilized as Input Data for the Regression Analysis employed in correlating the immersed tube heat transfer data.

Test	Independent Variables					Depen. Variable
	$\ln (Re_{td})$	$\ln(\frac{Hdyn}{Hst})$	$\ln H_{st,r}$	$\ln \theta$	$\ln N$	$\ln P$
44a	6,717	0,460	0,0953	1,500	1,834	8,619
44b	6,706	0,460	0,0953	1,509	1,840	8,536
44c	6,716	0,331	0,0953	1,463	1,186	8,467
45	6,615	0,447	0,1133	1,528	1,781	8,529
47a	6,844	0,434	0,1310	1,351	1,625	8,643
47b	6,729	0,468	0,1484	1,515	1,884	8,607
47c	6,562	0,420	0,1655	1,486	1,621	8,640
47d	6,475	0,415	0,1823	1,533	1,625	8,633
50a	6,794	0,465	0,7129	1,466	1,844	8,657
50b	6,755	0,464	0,7419	1,486	1,848	8,777
50c	6,971	0,519	0,7701	1,520	2,168	8,852
50d	6,588	0,397	0,7930	1,413	1,472	8,665
50e(i)	6,591	0,395	0,7975	1,406	1,455	8,778
50e(ii)	6,591	0,395	0,7975	1,406	1,455	8,801
50e(iii)	6,591	0,395	0,7975	1,406	1,455	8,746
50e(iv)	6,588	0,396	0,7975	1,411	1,462	8,757
50f	6,543	0,402	0,7975	1,454	1,515	8,760
50g(i)	6,610	0,382	0,7975	1,364	1,373	8,799
50g(ii)	6,618	0,382	0,7975	1,358	1,380	8,730
53a	6,880	0,423	0,2776	1,297	1,542	8,779
53b	6,555	0,417	0,2776	1,486	1,613	8,543
53c	6,476	0,407	0,2776	1,509	1,568	8,669

TABLE G 6 : Operating Conditions and Test Results related to the evaluation of the Heat Transfer Coefficient from the Bed to the Peripheral Cooling System

Test	Bed Temp °C	Bed Vel. m/s	Static Bed Height mm	Heat Flux Pad		Heat flux			Ht Trnf Coeff		Nu_p	Ar	D	$\frac{u_f - u_{mf}}{u_{mf}}$	Re_p
				Temp Diff °C	Mn.Pad Temp. °C	Tot. kW/m²	Rad. Comp. kW/m²	Conv. Comp. kW/m²	Tot. W/m²C	Conv. W/m²C	-	-	-	-	-
8	933	1,32	135	47,1	260,7	231,4	74,2	157,2	344,1	233,8	2,583	2138	4,417	4,412	7,050
9	872	1,20	148	41,7	242,1	204,7	58,0	146,7	324,9	232,9	2,665	2396	4,194	3,811	6,964
10	868	1,25	200	40,4	237,3	198,4	57,2	141,2	314,9	224,1	2,570	2415	4,179	4,004	7,295
12	788	1,17	218	37,7	228,5	185,1	43,3	142,8	330,8	255,2	3,076	2834	3,886	3,541	7,671
13	822	1,13	214	38,6	231,6	189,5	48,2	141,3	321,0	239,3	2,883	2644	4,010	3,445	7,043
14	850	1,26	226	37,7	228,5	185,1	53,7	131,4	297,8	211,4	2,450	2501	4,114	4,010	7,542
15a	870	1,32	219	39,9	236,0	195,8	57,6	138,2	308,7	217,8	2,495	2405	4,186	4,288	7,681
15b	900	1,72	219	40,8	239,1	200,2	64,1	136,1	302,9	205,9	2,318	2272	4,296	5,968	9,603
15c	865	2,25	219	37,1	226,7	182,4	56,5	125,9	291,4	201,1	2,311	2429	4,168	7,997	13,186
16a	900	1,30	200	43,1	247,1	211,8	64,0	147,8	324,2	226,4	2,548	2272	4,296	4,267	7,258
16c	980	3,15	200	47,6	262,5	234,0	83,8	150,2	326,2	209,4	2,255	1967	4,589	12,133	15,831
19	900	2,04	101	43,1	247,1	211,8	64,0	147,8	324,4	226,4	2,548	2272	4,296	7,265	11,390
20	900	1,63	101	43,5	248,3	213,6	64,0	149,6	327,7	229,6	2,584	2272	4,296	5,806	9,380

TABLE G6 Cont. : Operating Conditions and Test Results related to the evaluation of the Heat Transfer Coefficient from the bed to the Peripheral Cooling System

Test	Bed Temp ^oC	Bed Vel. m/s	Static Bed Height mm	Heat Flux Pad Temp Diff. ^oC	Heat Flux Pad Mn.Pad Temp. ^oC	Heat Flux Tot. kW/m^2	Heat Flux Rad. Comp. kW/m^2	Heat Flux Conv. Comp. kW/m^2	Ht Trnf Coeff Tot. W/m^2C	Ht Trnf Coeff Conv. W/m^2C	Nu_p -	Ar -	D -	$\frac{u_f-u_{mf}}{u_{mf}}$ -	Re_p -
23a	945	1,50	97	49,8	270,0	244,7	77,3	170,4	326,5	252,4	2,770	2092	4,461	5,177	7,886
23b	985	1,55	97	56,2	291,6	275,8	84,5	191,3	397,8	276,0	2,964	1950	4,608	5,473	7,741
24	915	1,79	109	47,1	260,7	231,4	67,2	164,2	360,4	255,7	2,853	2210	4,351	6,292	9,793
28	930	1,61	119	49,8	270,0	244,7	70,6	174,1	370,7	263,8	2,919	2150	4,406	5,594	8,634
30a	955	1,82	100	48,9	266,9	240,3	77,0	163,3	349,1	237,3	2,590	2055	4,498	6,521	9,445
35a	950	2,30	188	46,2	257,6	226,9	75,9	151,0	327,7	218,1	2,387	2074	4,479	8,488	12,014
35b	950	2,24	188	48,4	265,0	237,6	75,7	161,9	346,8	236,3	2,586	2074	4,479	8,241	11,701
37	955	2,19	216	49,8	270,0	244,7	76,9	167,8	357,2	245,0	2,674	2055	4,498	8,050	11,365
38a	935	2,13	231	46,2	257,6	226,9	72,1	154,8	334,9	228,6	2,523	2130	4,424	7,740	11,347
38b	908	1,42	231	47,3	261,3	232,4	65,5	166,7	359,4	257,8	2,888	2239	4,326	4,770	7,843
38c	915	2,10	231	42,0	243,4	206,4	67,5	138,9	307,3	206,8	2,308	2210	4,351	7,555	11,489
40a	955	1,82	189	45,1	253,9	221,6	77,2	144,4	316,1	205,9	2,247	2055	4,498	6,521	9,445
40b	960	1,58	189	47,1	260,7	231,4	78,4	153,0	330,8	218,7	2,380	2037	4,516	5,541	8,147
40c	980	3,31	189	48,2	264,4	236,7	83,7	153,0	330,7	213,8	2,302	1967	4,589	12,800	16,636
41a	835	1,12	198	39,9	236,0	195,8	50,6	145,1	326,8	242,3	2,835	2576	4,058	3,428	6,850
41b	931	1,23	201	43,1	242,1	204,7	71,4	133,3	297,1	193,5	2,140	2146	4,410	4,040	6,587
41c	935	1,26	203	42,0	243,4	206,4	72,4	134,0	298,5	193,9	2,140	2130	4,424	4,170	6,712
41d	1015	1,98	205	51,4	275,5	252,7	93,6	159,1	341,7	215,2	2,275	1852	4,717	7,355	9,525

TABLE G6 Cont. : Operating Conditions and Test Results related to the evaluation of the Heat Transfer Coefficient from the bed to the Peripheral Cooling System

Test	Bed Temp. °C	Bed Vel. m/s	Static Bed Height mm	Heat Flux Pad Temp. Diff. °C	Heat Flux Pad Mn.Pad Temp. °C	Heat Flux Tot. kW/m^2	Heat Flux Rad. Comp. kW/m^2	Heat Flux Conv. Comp. kW/m^2	Ht Trnf Coeff Tot. W/m^{2}C	Ht Trnf Coeff Conv. W/m^{2}C	Nu_p -	Ar -	θ -	u_f/u_{mf} -	Re_p -
44b	960	1,76	110	56,1	291,6	275,8	77,7	198,1	412,7	296,5	3,227	2037	4,516	6,286	9,075
44c	905	1,05	110	50,7	273,0	249,1	64,6	184,5	394,2	292,1	3,278	2251	4,315	3,261	5,823
45	985	1,66	112	55,3	288,5	271,4	84,6	186,8	389,7	268,3	2,881	1950	4,608	5,933	8,290
47a	780	1,57	114	32,6	211,2	160,2	44,3	118,9	281,7	209,0	2,533	2882	3,857	5,074	10,420
47b	970	1,82	116	48,9	266,9	240,3	80,9	159,3	341,7	226,7	2,454	2001	4,553	6,561	9,264
47c	935	1,48	118	46,7	259,4	229,6	72,0	157,6	339,8	233,2	2,572	2130	4,424	5,073	7,884
47d	990	1,45	120	51,3	274,9	251,8	86,3	165,5	352,1	231,5	2,480	1933	4,626	5,066	7,196
50a	910	1,80	204	43,1	247,1	211,8	66,3	145,5	319,5	219,5	2,457	2230	4,333	6,315	9,909
50b	935	1,79	210	45,3	254,5	222,5	72,1	150,4	327,0	220,9	2,438	2130	4,424	6,341	9,530
50c	975	2,34	216	47,8	263,2	234,9	82,4	152,5	330,0	214,3	2,314	1984	4,571	8,739	11,835
50d	850	1,35	221	39,9	236,0	195,8	53,5	142,3	318,8	231,6	2,685	2501	4,113	4,356	8,063
50g	795	1,27	222	35,3	220,5	173,5	43,7	129,8	302,0	226,0	2,712	2794	3,912	3,947	8,246
53a	727	1,50	132	29,7	201,4	145,9	33,4	112,5	277,6	214,1	2,689	3231	3,663	4,672	10,802
53c	960	1,40	132	52,5	279,2	258,0	78,0	180,0	379,0	264,5	2,879	2037	4,516	4,800	7,224

TABLE G 7 : Logarithms of the Data utilized for the Regression Analysis employed in Correlating the Heat Transfer to a Peripheral Cooling Surface

Test	Dependent Variables						Independent Variable
	$\ln\frac{(Hdyn)}{(Hst)}$	$\ln(H_{st,r})$	ln θ	ln N	ln Re_p	ln Ar	ln Nu_p
8	0,3918	0,3001	1,4855	1,4843	1,9530	7,6677	0,9488
9	0,3672	0,3920	1,4337	1,3379	1,9408	7,7816	0,9801
10	0,3778	0,6931	1,4301	1,3873	1,9872	7,7893	0,9440
12	0,3605	0,7793	1,3574	1,2644	2,0374	7,9496	1,1237
13	0,3512	0,7608	1,3888	1,2369	1,9520	7,8800	1,0588
14	0,3798	0,8154	1,4144	1,3888	2,0205	7,8243	0,8961
15a	0,3918	0,7839	1,4317	1,4558	2,0387	7,7855	0,9143
15b	0,4549	0,7839	1,4577	1,7864	2,2621	7,7285	0,8405
15c	0,5111	0,7839	1,4274	2,0791	2,5792	7,7951	0,8375
16a	1,3879	0,6931	1,4577	1,4509	1,9821	7,7285	0,9354
16c	0,5700	0,6931	1,5237	2,4959	2,7620	7,5841	0,8130
19	0,4916	0,0100	1,4577	1,9831	2,4327	7,7285	0,9354
20	0,4497	0,0100	1,4577	1,7589	2,2386	7,7285	0,9354
23a	0,4231	-0,0305	1,4954	1,6442	2,0651	7,6460	1,0187
23b	0,4310	-0,0305	1,5278	1,6998	2,0465	7,5754	1,0865
24	0,4639	0,0862	1,4704	1,8393	2,2817	7,7007	1,0485
28	0,4398	0,1740	1,4830	1,7217	2,1557	7,6731	1,0712
30a	0,4673	0,0000	1,5036	1,8750	2,2455	7,6281	0,9516
35a	0,5153	0,6313	1,4994	2,1387	2,4861	7,6370	0,8699
35b	0,5103	0,6313	1,4994	2,1091	2,4597	7,6370	0,9501
37	0,5058	0,7701	1,5036	2,0857	2,4305	7,6281	0,9835
38a	0,5003	0,8372	1,4870	2,0464	2,4290	7,6641	0,9253
38b	0,4100	0,8372	1,4646	1,5623	2,0596	7,7136	1,0607
38c	0,4976	0,8372	1,4704	2,0222	2,4414	7,7007	0,8363

TABLE G 7 (Cont.) : Logarithms of the Data utilized for the Regression Analysis Employed in Correlating the Heat Transfer to a Peripheral Cooling Surface

Test	Dependent Variables						Independent Variable
	$\ln\frac{(Hdyn)}{(Hst)}$	$\ln(H_{st,r})$	ln B	ln N	ln Re_p	ln Ar	ln Nu_p
40a	0,4673	0,6366	1,5036	1,8750	2,2455	7,6281	0,8096
40b	0,4354	0,6366	1,5076	1,7122	2,0976	7,6192	0,8672
40c	0,5777	0,6366	1,5237	2,5494	2,8116	7,5841	0,8338
41a	0,3488	0,6831	1,4007	1,2320	1,9242	7,8539	1,0420
41b	0,3737	0,6981	1,4839	1,3962	1,8851	7,6713	0,7608
41c	0,3798	0,7080	1,4870	1,4279	1,9039	7,6641	0,7606
41d	0,4853	0,7178	1,5512	1,9954	2,2539	7,5241	0,8220
44b	0,4602	0,0953	1,5076	1,8383	2,2055	7,6192	1,1714
44c	0,3313	0,0953	1,4621	1,1820	1,7618	7,7192	1,1873
45	0,4468	0,1133	1,5278	1,7805	2,1150	7,5754	1,0582
47a	0,4341	0,1313	1,3499	1,6241	2,3437	7,9663	0,9292
47b	0,4673	0,1484	1,5158	1,8811	2,2261	7,6016	0,8978
47c	0,4201	0,1655	1,4870	1,6239	2,0648	7,6641	0,9448
47d	0,4150	0,1823	1,5317	1,6226	1,9735	7,5668	0,9081
50a	0,4649	0,7129	1,4663	1,8429	2,2934	7,7099	0,8987
50b	0,4636	0,7419	1,4870	1,8470	2,2544	7,6641	0,8910
50c	0,5186	0,7701	1,5197	2,1678	2,4711	7,5928	0,8386
50d	0,3968	0,7930	1,4142	1,4716	2,0873	7,8243	0,9878
50g	0,3820	0,7975	1,3640	1,3730	2,1097	7,9351	0,9977
53a	0,4229	0,2776	1,2983	1,5416	2,3797	8,0805	0,9892
53c	0,4067	0,2776	1,5076	1,5686	1,9774	7,6192	1,0574

TABLE G 8 : Observations and Results obtained from the Heat Transfer Probe introduced to the Fluidized Bed via the Ash Port

Test	Static Bed Height mm	Bed Vel. m/s	Bed Temp. °C	Probe Depth mm	Thermocouple Temperatures Inner °C	Thermocouple Temperatures Outer °C	Outer Probe Temp. °C	Heat Flow W	Heat Trnf. Coefficient Tot. W/m²C	Heat Trnf. Coefficient Conv. W/m²C
47a	114	1,57	780	85	165,5	324	357,2	703,8	557,8	468,7
				135	166,5	295	321,9	570,6	386,4	307,9
				185	165,5	295	322,1	575,0	391,2	312,4
				210	159,3	271	293,8	493,8	340,2	258,8
				235	139,5	239	259,9	441,8	284,6	207,0
				285	115,0	192	208,1	341,8	200,4	128,1
47b	116	1,82	970	135	219,8	429	472,3	926,8	623,8	477,0
				185	235,8	433	474,3	875,6	592,0	444,8
				235	214,5	398	436,5	814,8	511,8	371,2
				285	197,0	348	379,7	670,4	380,6	249,2
				320	182,0	317	344,7	597,2	320,0	194,0
47c	118	1,48	935	85	211,3	410	451,0	880,0	609,2	474,5
				135	212,3	410	450,8	875,6	606,0	471,3
				185	218,3	410	449,6	849,0	586,0	451,5
				235	200,8	367	401,8	738,0	463,8	337,1
				285	169,0	305	332,9	601,6	334,8	218,3
				335	149,0	261	284,5	497,4	256,2	146,3
47d	120	1,45	990	85	221,5	407	445,9	823,6	507,2	360,0
				135	225,8	421	461,9	866,8	550,0	400,0
				185	232,3	443	486,6	933,4	621,2	466,8
				235	232,0	438	481,2	914,8	602,4	449,0
				285	207,0	367	400,5	710,4	403,8	364,3
				335	180,5	324	354,1	637,2	335,8	203,7

TABLE G8 (Cont.) : Observations and Results obtained from the Heat Transfer Probe introduced to the Fluidized Bed via the Ash Port

Test	Static Bed Height mm	Bed Vel. m/s	Bed Temp. °C	Probe Depth mm	Thermocouple Temperatures Inner °C	Thermocouple Temperatures Outer °C	Outer Probe Temp. °C	Heat Flow W	Heat Trnf. Coefficient Tot. W/m²C	Heat Trnf. Coefficient Conv. W/m²C
45	112	1,66	985	85	240,0	471	519,4	1025,8	738,2	578,9
				135	243,5	445	487,2	894,8	602,2	448,9
				185	249,8	450	492,0	889,0	604,2	450,0
				205	248,5	425	497,7	914,8	629,0	473,8
				235	230,3	405	441,6	775,8	474,0	330,2
				265	211,5	362	393,5	668,2	378,6	241,4
50a	204	1,80	910	85	220,3	405	443,7	820,2	589,4	461,6
				185	215,0	384	418,8	748,2	510,4	386,6
				285	229,5	426	467,2	872,6	660,2	528,6
				335	211,0	393	431,1	808,2	565,4	439,7
50b	210	1,79	935	185	229,8	405	441,7	778,0	528,4	395,3
50c	216	2,34	975	185	231,5	417	455,3	821,4	529,6	384,5
50d	221	1,35	850	185	197,0	357	390,5	710,4	518,2	411,3
53a	132	1,50	727	85	172,0	276	297,8	461,8	360,6	287,4
53b	132	1,46	935	35	215,7	403	441,6	829,4	534,2	407,9
				85	213,5	376	410,1	721,6	460,6	332,6
				135	223,2	405	443,1	807,2	549,8	416,4
				185	231,5	417	455,3	821,4	525,0	401,1
				235	219,7	386	420,9	738,4	450,6	329,1
				285	189,0	329	357,7	619,4	359,6	239,5
				325	186,0	292	314,2	470,6	254,0	140,1
53c	132	1,40	960	85	195,5	419	465,8	992,4	672,8	529,6
				135	212,0	416	461,5	952,4	640,2	497,7
				160	241,2	450	493,8	927,2	666,4	518,2
				185	239,0	440	482,1	892,6	625,8	479,7
				210	243,7	447	489,6	902,8	698,4	538,3
				235	237,5	429	468,5	848,2	578,2	434,5
				285	205,5	372	406,3	737,2	446,0	312,8
				325	187,0	327	356,3	621,6	345,0	219,5

TABLE G9 : Observations and Results Relating to the Fluctuations in Temperature of the Outer Thermocouple of the Heat Transfer Probe

Test	Static Bed Height mm	Bed Vel. m/s	Bed Temp. °C	Probe Depth mm	Mean freq. ν s^{-1}	Mean Ampl. A °C	Max. Temp. °C	Min. Temp. °C	(Max-Min.) Temp. °C	$\nu \cdot A$ °C/S
Deeper Bed										
50a	204	1,80	910	185	0,850	2,3	387,0	359,0	28	1,91
50b	210	1,79	935	185	0,625	3,1	411,5	377,5	34	1,94
50c	216	2,34	975	185	0,733	2,2	431,0	401,0	30	1,63
50d	221	1,35	850	185	0,633	2,0	362,0	336,0	26	1,26
Shallower Bed										
53a	132	1,50	727	85	0,608	2,2	304	280	24	1,31
53b	132	1,46	935	85	0,500	3,3	455	413	42	1,64
53c	132	1,40	960	85	0,500	2,9	470	442	28	1,46

TABLE G10 : Observations and Results Relating to the Fluctuations of the Heat Transfer to a Peripheral Cooling Surface from Measurements on the Heat Flux Pad.

Test	Static Bed Height mm	Bed Vel. m/s	Bed Temp. °C	Bed Depth mm	Mean Freq. ν s^{-1}	Mean Ampl. A kW/m^2	Max. Heat Flux kW/m^2	Min. Heat Flux kW/m^2	Max.- Min. Flux kW/m^2	$\nu \cdot A$ $kW/m^2 s$
Deeper Bed										
50a	204	1,80	910	58	0,717	1,91	217,1	198,1	19,0	1,37
50b	210	1,79	935	58	-	-	234,9	211,8	23,1	-
50c	216	2,34	975	58	0,542	1,92	248,3	228,7	19,6	1,04
50d	221	1,35	850	58	0,708	1,59	199,3	180,6	18,7	1,13
Shallower Bed										
53a	132	1,50	727	58	0,658	1,39	154,1	139,4	14,7	0,91
53b	132	1,46	935	58	-	-	248,3	230,5	17,8	-
53c	132	1,40	960	58	0,617	1,35	262,5	244,7	17,8	0,83

TABLE G11 : Test Results Relating to the Overall Performance of the 1 000 mm Diameter Fluidized Bed Combustion Test Facility

Test		15a	15b	16c	19	30b	31a	31b	32
Primary air flow	kg/h	1166	1482	2530	2742	1185,7	1391,6	1374,8	1673,8
Secondary air flow	kg/h	-	-	-	-	-	-	-	-
Total air flow	kg/h	1166	1482	2530	2742	1185,7	1391,6	1374,8	1673,8
Gas flow	kg/h	1254,5	1593,7	2703,7	1842,3	1275,3	1468,2	1478,7	1803,4
Evaporation rate	kg/h	953	1110	1433	821	769,7	592,3	906,7	1135,3
Static bed height	mm	219	219	200	101	105	105	105	201
Superficial gas Vel.	m/s	1,32	1,72	3,15	2,04	1,49	1,47	1,67	1,98
Bed Temperature	°C	870	900	980	900	970	780	960	930
Final gas temperature	°C	590	-	860	740	752	713	789	832
Freeboard pseudo flame temperature	°C	870	900	980	900	970	780	960	930
Oxygen	%	3,0	4,4	-	5,6	-	9,1	-	4,2
Carbon Monoxide	%	1,2	0,64	-	0,45	-	0,5	-	0,7
Carbon Dioxide	%	-	-	-	-	-	9,4	-	14,8
Excess air factor	%	1,25	1,25	1,38	1,64	-	1,72	-	1,22
Carbon in ash	%	59,4	53,7	-	56,7	-	56,1	-	56,7
Equivalent carbon loss	%	33,9	26,9	-	30,4	-	29,6	-	30,4
Heat absorbed by jacket	kW	686,2	799,2	1031,8	591,1	554,2	426,4	652,9	817,0
Heat abosrbed by pipe	kW	-	-	-	-	-	-	-	-
Heat in gases leaving rig	kW	220,2	-	723,0	416,5	293,5	318,4	359,1	464,7
Total heat liberated	kW	906,4	-	1754,8	1007,6	847,7	744,8	1011,9	1281,7
Specific heat liberated	MW/m^2	1,154	-	2,234	1,283	1,079	0,948	1,288	1,632
Heat absorbed above bed	kW	119,6	-	113,7	101,8	96,7	33,6	88,0	61,7
Heat removed by jacket in bed	kW	566,6	-	918,1	489,3	459,5	392,8	564,8	755,3
Heat in gases entering freeboard	kW	339,8	448,4	836,7	518,3	390,2	352,0	447,1	526,4
Total measured heat input (Q_F)	kW	339,8	448,4	836,7	518,3	390,2	352,0	447,1	526,4
Furnace Efficiency	-	0,352	-	0,136	0,196	0,248	0,095	0,197	0,117
$Q_F / \sigma T_F^4 (1 - \theta_o)$	m^2	4,749	5,600	7,855	5,907	3,792	7,043	4,499	5,892

TABLE G11 Cont. : Test Results Relating to the Overall Performance of the 1 000 mm Diameter Fluidized Bed Combustion Test Facility

Test		35a	35b	37	38a	38b	40a	40b	40c
Primary air flow	kg/h	1907,6	1858,9	1799,3	1786,8	1219,2	1886,8	1289,4	2652,0
Secondary air flow	kg/h	-	983,5	-	-	537,6	-	592,9	-
Total air flow	kg/h	1907,6	2842,4	1799,3	1786,8	1756,8	1886,8	1882,3	2652,0
Gas flow	kg/h	2073,6	3058,4	1941,0	1914,7	1868,2	2020,6	1995,7	2794,7
Evaporation rate	kg/h	1263,8	1398,1	1276,2	1280,0	1122,0	1178,2	1157,7	1411,1
Static bed height	mm	188	188	216	231	231	189	189	189
Superficial gas vel.	m/s	2,30	2,24	2,19	2,13	1,42	1,82	1,58	3,31
Bed Temperature	°C	950	950	955	935	908	955	960	980
Final gas temperature	°C	860	-	821	816	810	854	859	936
Freeboard Pseudo flame temperature	°C	950		955	935		955		980
Oxygen	%	2,4	4,8	4,0	5,7	7,4	5,8	8,1	9,5
Carbon Monoxide	%	0,95	0,8	0,8	1,0	0,9	0,5	0,45	0,45
Carbon Dioxide	%	16,3	13,8	13,5	11,5	10,2	13,4	11,4	10,2
Excess air factor	%	1,10	1,26	1,20	1,32	1,49	1,35	1,59	1,78
Carbon in ash	%	58,4	-	61,7	63,0	68,8	52,3	55,5	51,0
Equivalent carbon loss	%	32,6	-	37,4	39,5	51,1	20,5	23,3	19,5
Heat abosrbed by jacket	kW	909,8	1006,4	918,7	921,4	807,7	848,1	833,4	1015,7
Heat absorbed by pipe	kW	-	-	-	-	-	-	-	-
Heat in gases leaving rig	kW	554,5	-	492,8	482,8	467,2	536,1	533,0	821,5
Total heat liberated	kW	1464,3	-	1411,5	1404,2	1274,9	1384,2	1366,4	1837,2
Specific heat liberated	MW/m^2	1,864	-	1,797	1,788		1,762		2,339
Heat abosrbed above bed	kW	65,3		90,8	79,4		71,4		43,4
Heat removed by jacket in bed	kW	844,5		827,9	842,0		776,7		972,3
Heat in gases entering freeboard	kW	619,8	597,8	583,6	562,2	368,4	607,5	413,4	864,9
Total measured heat input (Q_F)	kW	619,8		583,6	562,2		607,5		864,9
Furnace efficiency	-	0,105		0,156	0,141		0,118		0,0502
$Q_F / \sigma T_F^4 (1 - \theta_c)$	m^2	6,460		5,977	6,181		6,221		8,119

TABLE G 11 Cont. : Test Results Relating to the Overall Performance of the 100 mm Diameter Fluidized Bed Combustion Test Facility

Test		41a	41b	41c	44b	44c	45
Primary air flow	kg/h	1020,5	1027,5	1051,0	1427,2	892,5	1310,8
Secondary air flow	kg/h	-	508,4	846,2	-	-	-
Total air flow	kg/h	1020,5	1535,9	1897,2	1427,2	892,5	1310,8
Gas flow	kg/h	1089,8	1662,7	2040,2	1536,5	960,9	1416,3
Evaporation rate	kg/h	688,9	1029,6	1154,2	723,1	606,9	1043,6
Static bed height	mm	198	201	203	110	110	112
Superficial gas vel.	m/s	1,12	1,23	1,26	1,76	1,05	1,66
Bed Temperature	°C	835	931	935	960	905	985
Final gas temperature	°C	701	800	815	704	720	739
Freeboard pseudo flame temperature	°C	835	998	889	960	905	985
Oxygen	%	6,3	3,2	4,7	4,4	4,5	3,5
Carbon monoxide	%	0,3	0,4	0,45	0,4	0,4	0,25
Carbon dioxide	%	12,4	16,4	13,4	14,8	14,7	15,7
Excess air factor	%	1,41	1,16	1,27	1,25	1,25	1,19
Carbon in ash	%	38,7	53,1	61,2	53,5	46,3	40,7
Equivalent carbon loss	%	11,8	21,2	29,5	21,5	16,1	12,8
Heat absorbed by jacket	kW	495,9	741,2	830,9	462,1	386,6	693,3
Heat absorbed by pipe	kW	-	-	-	59,1	50,9	58,9
Heat in gases leaving rig	kW	231,9	410,1	513,7	328,6	210,5	319,1
Total heat liberated	kW	727,8	1151,3	1344,6	849,8	647,9	1071,3
Specific heat liberated	MW/m^2	0,927	1,466	1,712	1,082	0,820	1,360
Heat absorbed above bed	kW	50,1	111,8	54,8	136,1	61,6	121,5
Heat removed by jacket in bed	kW	-	196,8	236,7	-	-	-
Heat in gases entering freeboard	kW	282,0	325,0	331,8	464,7	272,1	440,6
Total measured heat input (Q_F)	kW	282,0	521,8	568,5	464,7	272,1	440,6
Furnace efficiency	-	0,178	0,214	0,0964	0,293	0,226	0,276
$Q_F / \sigma T_F^4 (1 - \theta_o)$	m^2	4,514	4,607	6,250	4,676	3,336	4,066

TABLE G11 Cont. : Test Results Relating to the Overall Performance of the 1 000 mm Diameter Fluidized Bed Combustion Test Facility

Test		47a	47b	47c	47d	50a	50b	50c	50d
Primary air flow	kg/h	1489,5	1464,8	1219,1	1150,3	1529,1	1490,4	1887,4	1206,7
Secondary air flow	kg/h	-	-	-	502,5	-	663,3	734,0	-
Total air flow	kg/h	1489,5	1464,8	1219,1	1652,8	1529,1	2153,7	2621,4	1206,7
Gas flow	kg/h	1566,2	1579,8	1316,4	1786,3	1653,2	2325,5	2835,9	1290,5
Evaporation rate	kg/h	539,6	1148,3	959,6	1268,0	1091,1	1262,6	1498,2	848,3
Static bed height	mm	114	116	118	120	204	210	216	221
Superficial gas vel.	m/s	1,57	1,82	1,48	1,45	1,80	1,79	2,34	1,35
Bed temperature	°C	780	970	935	990	910	935	975	850
Final gas temperature	°C	586	760	670	766	760	826	895	680
Freeboard pseudo flame temperature	°C	780	970	935	1084	910	948	1014,3	850
Oxygen	%	9,8	3,95	3,7	3,2	3,4	3,8	3,6	5,8
Carbon monoxide	%	0,09	0,26	0,21	0,2	0,25	0,6	0,9	0,3
Carbon dioxide	%	10,1	15,3	15,6	16,0	15,8	15,4	15,2	13,6
Excess air factor	%	1,86	1,22	1,20	1,17	1,18	1,20	1,17	1,36
Carbon in ash	%	51,4	42,5	47,6	4,94	50,8	54,2	51,6	-
Equivalent carbon loss	%	19,8	13,8	17,0	18,2	19,3	22,1	19,9	-
Heat absorbed by jacket	kW	351,7	769,4	635,4	849,4	785,3	909,0	1063,4	612,9
Heat absorbed by pipe	kW	37,2	58,3	56,3	64,6	52,6	60,5	67,5	46,3
Heat in gases leaving rig	kW	272,6	367,6	266,2	419,7	384,7	594,2	793,5	265,7
Total heat liberated	kW	661,5	1195,3	957,9	1333,6	1222,6	1563,7	1924,4	924,9
Specific heat liberated	MW/m^2	0,84	1,52	1,22	1,70	1,56	1,99	2,45	1,18
Heat absorbed above bed	kW	103,1	115,5	120,3	148,1	78,5	47,2	46,5	750
Heat removed by jacket in bed	kW	248,6	653,9	515,1	701,3	706,8	861,8	1016,9	537,9
Heat in gases entering freeboard	kW	375,7	483,1	386,5	389,1	463,2	472,5	628,3	340,7
Total measured heat input (Q_F)	kW	375,7	483,1	386,5	567,8	463,2	641,3	840,0	340,7
Furnace efficiency	-	0,274	0,239	0,311	0,261	0,169	0,074	0,055	0,022
$Q_F / \sigma T_F^4 (1 - \theta_0)$	m^2	7,517	4,695	4,249	3,782	5,576	6,737	7,020	5,143

TABLE G12 : Fly Ash Gradings and Carbon Contents

Sieve Size (micron)	Test No 15a			Test No 19			Test No. 30b			Test No. 31a			Test No. 35a		
	% ret on	Cum % by wt. less than	Carbon in Ash %	% ret on	Cum % by wt. less than	Carbon in Ash %	% ret on	Cum. % by wt less than	Carbon in Ash %	% ret on	Cum % by wt less than	Carbon in Ash %	% ret on	Cum % by wt less than	Carbon in Ash %
425															
300															
212															
150	28,0	72,0	68,4	21,0	79,0	64,6	32,4	67,7	70,2	14,7	85,3	71,3	26,5	73,5	71,7
106	12,8	59,2	67,7	18,4	60,6	61,0	16,4	51,3	73,9	12,7	72,6	68,8	14,3	59,2	72,7
75	8,9	50,3)		22,8	37,8)	57,0	10,6	40,7)	67,2	10,7	61,9)		10,7	48,5)	73,3
53	18,7	31,6)	65,0	10,9	26,9)		12,7	28,0)		11,2	50,7)	63,0	11,6	36,9)	
Pan	31,6		45,9	26,9		45,7	28,0		46,6	50,7		38,7	36,9		48,2
Evaluation of Specific Size Intervals															
300→	1,5			-				5,5		-			-		
150→300	26,5			21,0				26,9		14,7			26,5		
75 →150	12,7			41,2				27,0		23,4			25,0		
0 →75	50,3			37,8				40,7		61,9			48,5		

TABLE G12 Cont. : Fly Ash Gradings and Carbon Contents

Sieve Size (micron)	Test No. 37			Test No. 40a			Test No. 40b			Test No. 40c			Test No. 41b		
	% ret on	Cum % by wt less than	Carbon in Ash %	% ret on	Cum % by wt less than	Carbon in Ash %	% ret on	Cum % by wt less than	Carbon in Ash %	% ret on	Cum % by wt less than	Carbon in Ash %	% ret on	Cum % by wt less than	Carbon in Ash %
425															
300															
212															
150	25,9	74,1	67,3	51,6	48,4	64,8	49,9	50,0	68,3	61,7	38,3	60,4	57,4	42,6	60,4
106	16,7	57,4	72,2	8,6	39,8	56,1	8,1	41,9	60,0	9,0	29,3	49,1	7,8	34,8	51,1
75	10,5	46,9)		5,7	34,1)		4,8	37,1)		4,2	25,1)		4,2	30,6)	
53	13,1	33,8)	66,5	4,0	30,1)	53,9	4,6	32,5)	58,5	4,7	20,4)	45,4	3,3	26,3)	54,1
Pan	33,8		47,8	30,1		36,2	32,5		40,0	20,4		33,9	27,3		37,4
Evaluation of Specific size Intervals															
300→	-			31,4			28,0			38,7			26,3		
150→300	25,9			20,2			21,9			23,0			21,1		
75 →150	27,2			14,3			12,9			13,2			12,0		
0 →75	46,9			34,1			37,1			25,1			30,6		

TABLE G12 Cont. : Fly Ash Gradings and Carbon Contents

Sieve Size (micron)	Test No. 41c			Test No. 44c			Test No. 45			Test No. 47a			Test No. 47b		
	% ret on	Cum % by wt less than	Carbon in Ash %	% ret on	Cum % by wt less than	Carbon in Ash %	% ret on	Cum % by wt less than	Carbon in Ash %	% ret on	Cum % by wt less than	Carbon in Ash %	% ret on	Cum % by wt less than	Carbon in Ash %
425				4,1	95,9)	59,4	7,6	92,3)	63,4	6,4	93,7)	63,2	8,8	91,1)	58,9
300				11,6	84,3)		12,9	79,4)		14,4	79,3)		14,6	76,5)	
212				14,0	70,3	53,4	11,7	67,7	57,7	15,0	64,3	58,1	12,3	64,2	49,9
150	66,5	33,4	69,9	12,1	58,2	50,0	10,7	57,0	49,6	12,1	52,2	52,4	9,3	54,9	46,2
106	7,9	25,5	55,1	10,9	47,3	48,2	5,3	51,7)	46,0	9,7	42,5)	51,9	7,3	47,6)	40,1
75	3,8	21,7)	59,2	*	-)		5,5	46,2)		5,3	37,2)		4,1	43,5)	
53	3,6	18,1)		*	-)	31,7	*	-)	23,3	*	-)	37,6	*	-)	26,2
Pan	18,1	-	45,3	47,3	-)		46,2	-)		37,2	-)		43,5	-)	
Evaluation of Specific Size Intervals															
300—	46,0			15,7			20,5			20,8			23,4		
150—300	20,5			26,1			22,4			27,1			21,6		
75—150	11,7						10,8			15,0			11,4		
0 —75	21,7			39,0			46,2			37,2			43,5		

TABLE G12 Cont. : Fly Ash Gradings and Carbon Contents

Sieve Size (micron)	Test No. 47c			Test No. 47d			Test No. 50a			Test No. 50b			Test No. 50c		
	% ret on	Cum % by wt less than	Carbon in Ash %	% ret on	Cum % by wt less than	Carbon in Ash %	% ret on	Cum % by wt less than	Carbon in Ash %	% ret on	Cum % by wt less than	Carbon in Ash %	% ret on	Cum % by wt less than	Carbon in Ash %
425	7,9	92,1)		2,5	97,6)		6,2	93,8)		14,1	86,0)		16,9	83,0)	
300	16,8	75,3)	65,4	11,1	86,5)	69,3	11,9	81,9)	57,2	13,6	72,4)	63,3	10,4	72,6)	60,1
212	15,5	59,8	54,4	12,9	73,6	63,6	12,3	69,6)		11,4	61,0)		10,2	62,4)	
150	9,0	50,8	55,3	8,4	65,2	57,3	12,0	57,6	41,7	9,7	51,3	55,1	8,9	53,5	57,9
106	8,5	42,3)		8,4	56,8)		8,0	49,6)		7,8	43,5)		7,5	46,0)	
75	4,3	38,0)	51,4	4,4	52,4)	52,4	5,4	44,2)	47,5	4,3	39,2)	49,0	4,1	41,9)	51,2
53	*	-)		*	-)		*	-)		4,9	34,3	52,2	6,4	35,5	46,0
Pan	38,0	-)	26,9	52,4	-)	34,9	44,2	-)	35,4	34,3	-	41,5	35,5	-	39,3
Evaluation of Specific Size Intervals															
300--	24,7			13,6			18,1			27,7			27,3		
150-300	24,5			21,3			24,3			21,1			19,1		
75-150	12,8			12,8			13,4			12,1			11,6		
0-75	38,0			52,4			44,2			39,2			41,9		

APPENDIX H

DETAILS OF RADIANT HEAT TRANSFER IN THE FREEBOARD REGION

In the development of the theoretical model for the transfer of heat in the freeboard region above the bed, a model had to be developed for describing the emissivity of the gas and entrained particulates. The formulation of a single clear gas and two-grey gas model for describing the radiation from the gas which was further extended to include the emission from the particulates leading up to a three grey gas model is described in this Appendix. The temperature dependence of the emissivity has been accommodated by the gas emissivity weighting factors rather than in the absorption coefficients. Finally, the direct exchange factors have been tabulated, i.e. assuming a non absorbing medium in the freeboard, whilst the total exchange factors have been tabulated for an absorption coefficient of 0,5 m^{-1} for comparison.

Prior to the evaluation of the relevant radiation parameters, the relative magnitude of the two flue gas components contributing to the gaseous radiation, viz water vapour and carbon dioxide, have to be evaluated. As most of the results have been obtained when burning the coal in a relatively dry condition, an inherent moisture content of 2,5% has been assumed. The resulting flue gas components when burning both the duff coal and the low fines coal were very similar. Indeed, in view of the similar carbon to hydrogen ratio, this similarity in flue gas components when fired with the same moisture content is to be anticipated. The resulting flue gas components as a function of the excess air factor when burning the low fines coal are illustrated in Figure H1. It is evident from the figure that the ratio of the moisture content to carbon dioxide content is of the order of 0,45. With an equivalent amount of surface moisture (i.e. 2,5%), the water vapour to carbon dioxide content of the flue gas would be of the order of 0,75. However, in view of most of

the tests having been performed with air dried coal, a ratio of 0,50 has been assumed. This implies that the ratio of the partial pressures is given by

$$p_w / p_c = 0,50$$

H.1 THE GAS EMISSIVITY

In order to model flue gas as having a water vapour to carbon dioxide partial pressure ratio of 0,5, the coal sample must have a total moisture content of some 3,3%. Therefore the composition of the flue gas for which the gas radiative properties have been determined can be given by :

carbon dioxide	:	13,9%
water vapour		6,95%
oyxgen		4,0%
nitrogen		75,1%
sulphur dioxide		0,05%
excess air factor		1,25

By employing the emissivity data for water vapour and carbon dioxide of Hottel (58) and by making corrections for actual pressure conditions, the additive nature of the components and the spectral overlap Figure H2 can be drawn. The figure represents the total gas emissivity for a flue gas having the water vapour and carbon dioxide contents given above as a function of temperature for a number of values of the product of the partial pressure ($p_c + p_w$) and the mean-beam length. Figure H3 has similarly been drawn to represent the total emissivity as a function of the product of the mean beam length and the partial pressure for various temperature levels.

H.1.1 The One Clear and Two Grey Gas Model

Each of the curves of Figure H3 can be represented as the sum of a number of grey gases (143), (56). A one clear gas and

two grey gas model has been found to adequately represent the emissivity relationships in the range of the product of the pressure and the mean beam length (p.L) from 0,05 m.atm to 1,5 m.atm for each of the gas temperatures. The one clear and two grey gas model can be represented by

$$\varepsilon_{gt} = \sum_{i=1}^{3} a_{gt,i}(1 - exp\{-k_{g,i} \cdot p \cdot L\}) \qquad (H1)$$

where $$\sum_{i=1}^{3} a_{gt,i} = 1 \qquad (H2)$$

and $$k_{g,1} = 0 \qquad (H3)$$

The absorption coefficient of the clear gas is zero i.e. $k_{g,1}=0$, and thus the emissivity weighting factor is included only as a dummy weighting factor. The one clear and two grey gas model has been applied to each of the temperature levels illustrated in Figure H3. The resulting weighting factors and absorption coefficients for the resulting two grey gas components are presented in Table H1.

TABLE H1 : Weighting factors and absorption coefficients for the two grey gases of the gas emissivity model at the different temperature levels

Temperature	Weighting factors		Absorption Coefficients	
	$a_{gt,2}$	$a_{gt,3}$	k_2	k_3
^oC			$m.atm^{-1}$	$m.atm^{-1}$
100	0,352	0,185	1,893	15,61
500	0,343	0,141	1,703	19,74
800	0,326	0,124	1,405	22,49
1000	0,310	0,097	1,476	23,25
1500	0,293	0,058	1,16	28,30

Both the absorption coefficients and weighting factors of Table H1 are seen to be dependent upon the temperature. However, when applying a furnace analysis technique such as the zone method of analysis it is useful to assume that the absorption coefficients are unchanged by temperature, and to accommodate this temperature dependence in the weighting factors. The absorption coefficients for the two grey gases at 800°C have been assumed to represent the absorption coefficients over the entire temperature range. The weighting factors for each of the remaining conditions have therefore been adjusted assuming absorption coefficients for each of the three gases as being given by

$$k_1 = 0,0 \quad m^{-1}.atm^{-1}$$
$$k_2 = 1,405 \quad m^{-1}.atm^{-1}$$
$$k_3 = 22,49 \quad m^{-1}.atm^{-1}$$

The resulting weighting factors for the two grey gases are illustrated in Figure H4 as a function of temperature. A least squares analysis has been applied to relate each of the two absorption coefficients to the gas temperature in terms of a linear relationship as represented by equation (H4).

$$a_{gt,i} = b_{0,i} + b_{1,i} \cdot t \qquad (H4)$$

and the emissivity can be represented by

$$\varepsilon_g = \Sigma \{b_{0,i} + b_{1,i} \cdot t\} \cdot \{1 - exp(-k_i \cdot p \cdot L)\} \qquad (H4)$$

The values of the coefficients presented in equation (H5) are included in Table H2.

TABLE H2 : Table of coefficients for the determination of the gas emissivity represented as a compound grey gas model

i	gas absorption coefficient k_i 1/(m.atm)	$b_{o,i}$	$b_{1,i}$ 1/°C
1	0,000	0,417	$0,168.10^{-3}$
2	1,405	0,416	$-0,102.10^{-3}$
3	22,49	0,167	-0,0664.10-3

H.2 EXCHANGE AREAS FOR THE TEST RIG

The furnace zone has been divided into nine surface zones and seven volume zones. The application of the zone method of analysis has been described in Chapter 4, and for completeness, the resulting direct and total exchange areas are presented in Tables H3 to H8. The division of the furnace into the various zones is illustrated in Figure 46 together with the zone numbering system which further facilitates reference to Tables H3 to H8.

TABLE H3 : Direct exchange areas between two surface zones assuming a clear gas in the furnace

	$s_i s_1$	$s_i s_2$	$s_i s_3$	$s_i s_4$	$s_i s_5$	$s_i s_6$	$s_i s_7$	$s_i s_8$	$s_i s_9$
$s_1 s_j$	0,000	0,401	0,105	0,032	0,011	0,005	0,002	0,001	0,003
$s_2 s_j$	0,401	0,417	0,203	0,055	0,015	0,005	0,002	0,001	0,001
$s_3 s_j$	0,105	0,203	0,417	0,203	0,054	0,015	0,005	0,002	0,002
$s_4 s_j$	0,032	0,055	0,203	0,417	0,203	0,054	0,015	0,005	0,005
$s_5 s_j$	0,011	0,015	0,055	0,203	0,417	0,203	0,054	0,015	0,011
$s_6 s_j$	0,005	0,005	0,015	0,055	0,203	0,417	0,203	0,054	0,032
$s_7 s_j$	0,002	0,002	0,005	0,015	0,055	0,203	0,417	0,203	0,105
$s_8 s_j$	0,001	0,001	0,002	0,005	0,015	0,055	0,203	0,417	0,401
$s_9 s_j$	0,003	0,001	0,002	0,005	0,011	0,032	0,105	0,401	0,000

TABLE H4 : Direct exchange areas between a gas and a surface zone for a clear gas in the furnace

	$s_i g_1$	$s_i g_2$	$s_i g_3$	$s_i g_4$	$s_i g_5$	$s_i g_6$	$s_i g_7$
$s_1 g_j$	0,162	0,039	0,014	0,006	0,003	0,002	0,001
$s_2 g_j$	0,349	0,000	0,001	0,002	0,005	0,018	0,094
$s_3 g_j$	0,094	0,349	0,000	0,001	0,002	0,005	0,018
$s_4 g_j$	0,018	0,094	0,349	0,000	0,001	0,002	0,005
$s_5 g_j$	0,005	0,018	0,094	0,349	0,000	0,001	0,002
$s_6 g_j$	0,002	0,005	0,018	0,094	0,349	0,000	0,001
$s_7 g_j$	0,001	0,002	0,005	0,018	0,094	0,349	0,000
$s_8 g_j$	0,000	0,001	0,002	0,005	0,018	0,094	0,349
$s_9 g_j$	0,001	0,002	0,003	0,006	0,014	0,039	0,162

TABLE H5 : Direct exchange areas between two gas zones assuming a clear gas in the furnace

	$g_i g_1$	$g_i g_2$	$g_i g_3$	$g_i g_4$	$g_i g_5$	$g_i g_6$	$g_i g_7$
$g_1 g_j$	0,114	0,029	0,007	0,002	0,001	0,001	0,000
$g_2 g_j$	0,029	0,114	0,029	0,007	0,002	0,001	0,001
$g_3 g_j$	0,007	0,029	0,114	0,029	0,007	0,002	0,001
$g_4 g_j$	0,002	0,007	0,029	0,114	0,029	0,007	0,002
$g_5 g_j$	0,001	0,002	0,007	0,029	0,114	0,029	0,007
$g_6 g_j$	0,001	0,001	0,002	0,007	0,029	0,114	0,029
$g_7 g_j$	0,000	0,001	0,001	0,002	0,007	0,029	0,114

TABLE H6 : Total exchange areas between two surface zones assuming an absorption coefficient of 0,5/m for the enclosed gas, a bed surface emissivity of 0,5 and an emissivity of 0,7 for the cooling surfaces

	$S_i S_1$	$S_i S_2$	$S_i S_3$	$S_i S_4$	$S_i S_5$	$S_i S_6$	$S_i S_7$	$S_i S_8$	$S_i S_9$
$S_1 S_j$	0,009	0,158	0,048	0,016	0,006	0,003	0,001	0,001	0,001
$S_2 S_j$	0,158	0,290	0,139	0,044	0,014	0,005	0,002	0,001	0,001
$S_3 S_j$	0,048	0,139	0,239	0,123	0,039	0,012	0,004	0,002	0,002
$S_4 S_j$	0,016	0,044	0,123	0,234	0,122	0,038	0,012	0,005	0,004
$S_5 S_j$	0,006	0,014	0,039	0,122	0,234	0,122	0,038	0,013	0,009
$S_6 S_j$	0,003	0,005	0,012	0,038	0,122	0,234	0,122	0,041	0,022
$S_7 S_j$	0,001	0,002	0,004	0,012	0,038	0,122	0,236	0,131	0,067
$S_8 S_j$	0,001	0,001	0,002	0,005	0,013	0,041	0,131	0,265	0,220
$S_9 S_j$	0,001	0,001	0,002	0,004	0,009	0,022	0,067	0,220	0,018

TABLE H7 : Total exchange areas between a gas and a surface zone for a gas having an absorption coefficient of 0,5/m in the furnace, a bed emissivity of 0,5 and an emissivity of 0,7 for the cooling surfaces

	S_iG_1	S_iG_2	S_iG_3	S_iG_4	S_iG_5	S_iG_6	S_iG_7
S_1G_j	0,099	0,025	0,009	0,004	0,002	0,002	0,005
S_2G_j	0,309	0,023	0,008	0,004	0,005	0,015	0,074
S_3G_j	0,096	0,273	0,014	0,005	0,003	0,005	0,018
S_4G_j	0,025	0,085	0,270	0,013	0,005	0,003	0,007
S_5G_j	0,008	0,021	0,084	0,270	0,013	0,005	0,004
S_6G_j	0,003	0,007	0,021	0,084	0,270	0,014	0,007
S_7G_j	0,001	0,003	0,007	0,021	0,084	0,272	0,019
S_8G_j	0,001	0,001	0,003	0,008	0,023	0,090	0,289
S_9G_j	0,001	0,002	0,003	0,006	0,015	0,040	0,136

TABLE H8 : Total exchange areas between two gas zones for a gas having an absorption coefficient of 0,5/m in the furnace, a bed emissivity of 0,5 and an emissivity of 0,7 for the cooling surfaces

	G_iG_1	G_iG_2	G_iG_3	G_iG_4	G_iG_5	G_iG_6	G_iG_7
G_1G_j	0,167	0,044	0,011	0,004	0,002	0,003	0,009
G_2G_j	0,044	0,144	0,038	0,009	0,003	0,002	0,003
G_3G_j	0,011	0,038	0,142	0,038	0,009	0,003	0,002
G_4G_j	0,004	0,009	0,038	0,142	0,038	0,009	0,004
G_5G_j	0,002	0,003	0,009	0,038	0,142	0,038	0,010
G_6G_j	0,003	0,002	0,003	0,009	0,038	0,143	0,041
G_7G_j	0,009	0,003	0,002	0,004	0,010	0,041	0,156

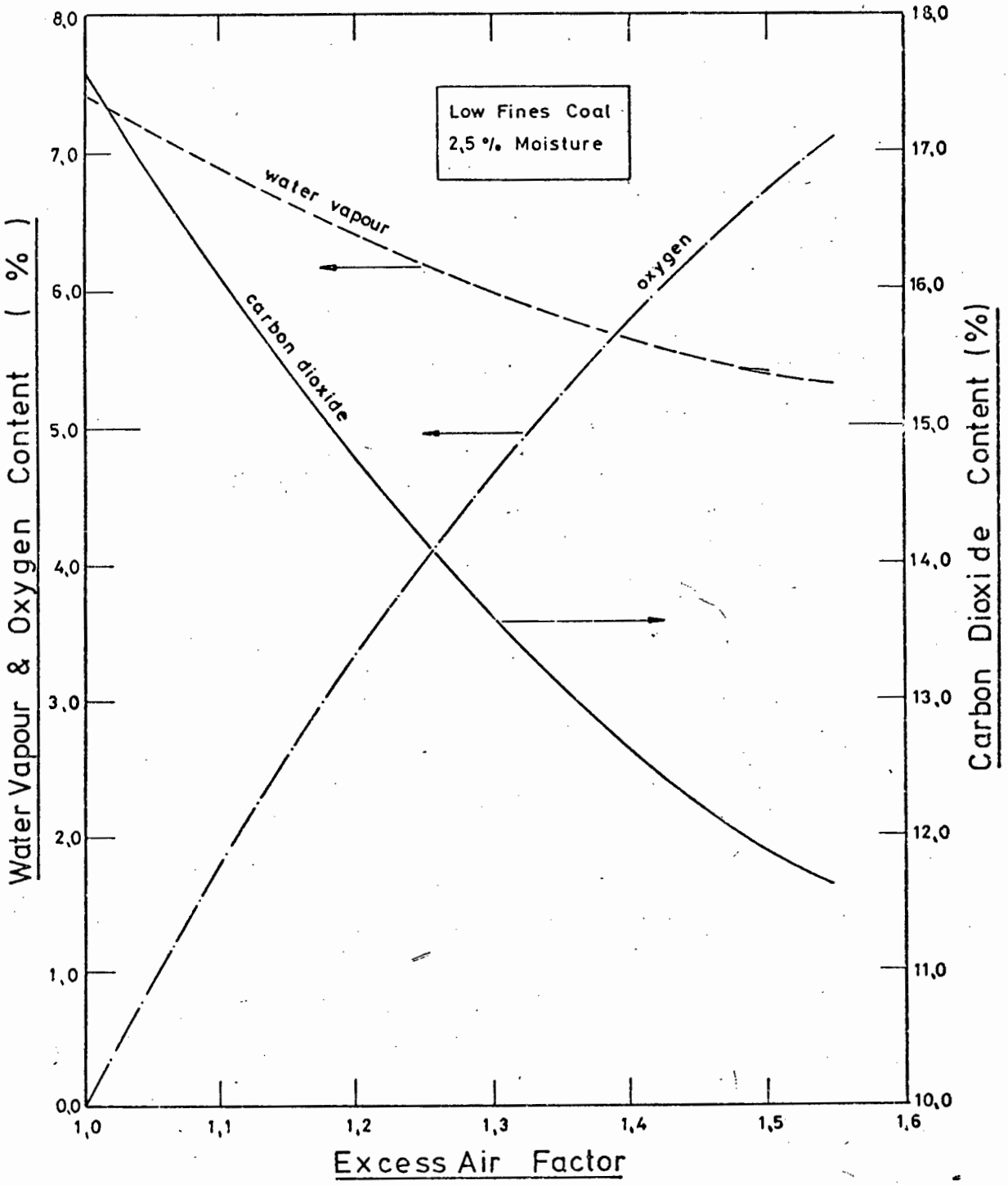

Figure H1 : Flue gas components as a function of the excess air factor.

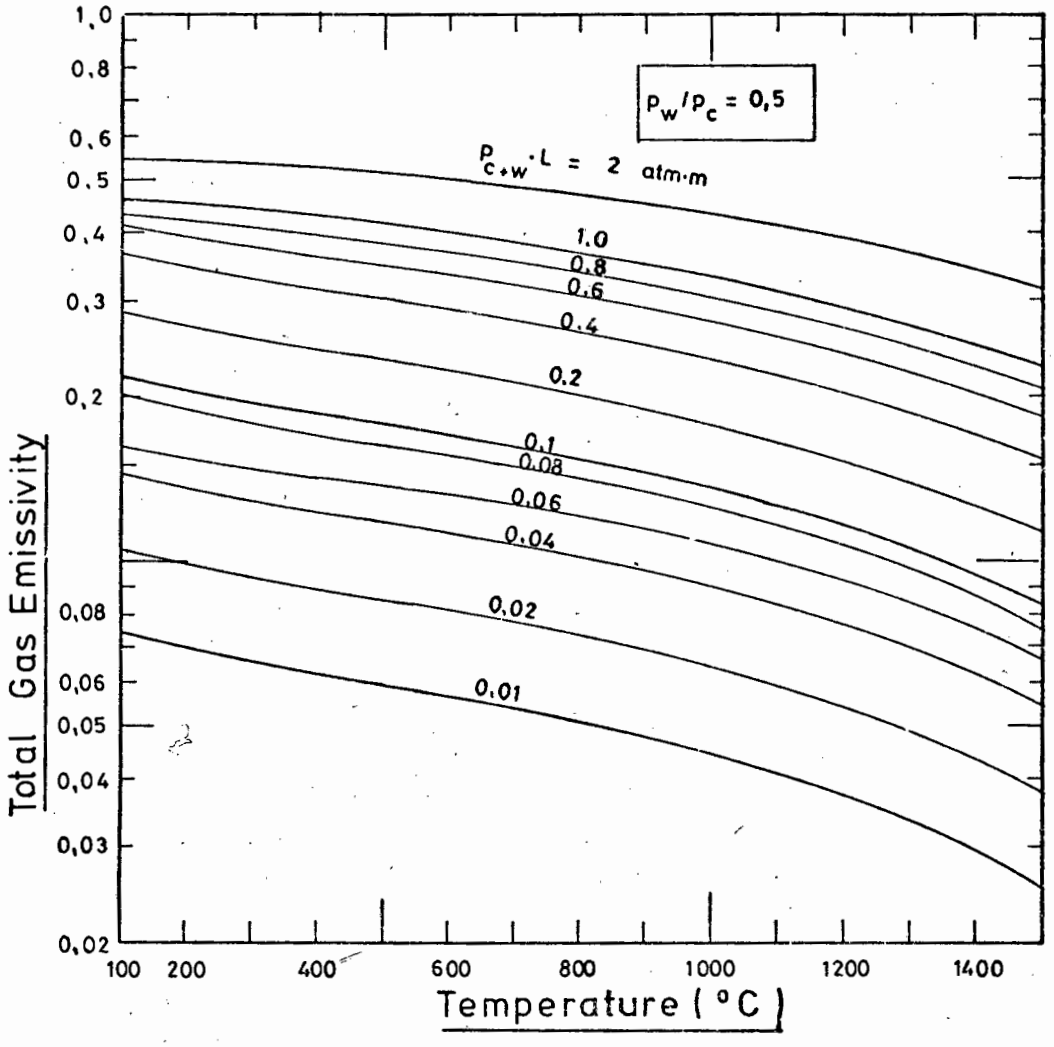

Figure H2 : Emissivity of flue gas, having a water vapour to carbon dioxide partial pressure ratio of 0,5, as a function of temperature for different levels of the product ($p_{c+w} \cdot L$).

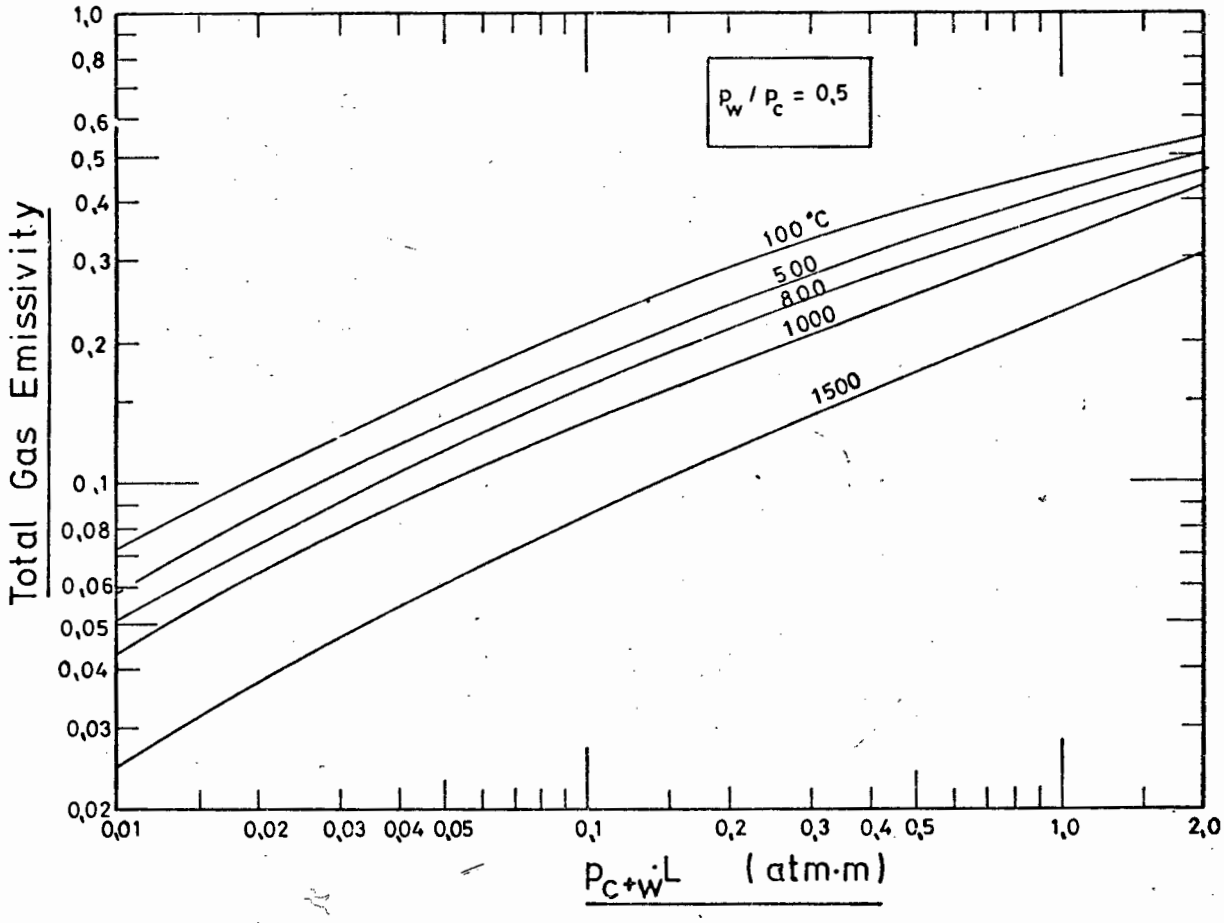

Figure H3 : Emissivity of flue gas, having a water vapour to carbon dioxide partial pressure ratio of 0,5, as a function of the product (p_{c+w}.L) for different levels of temperature.

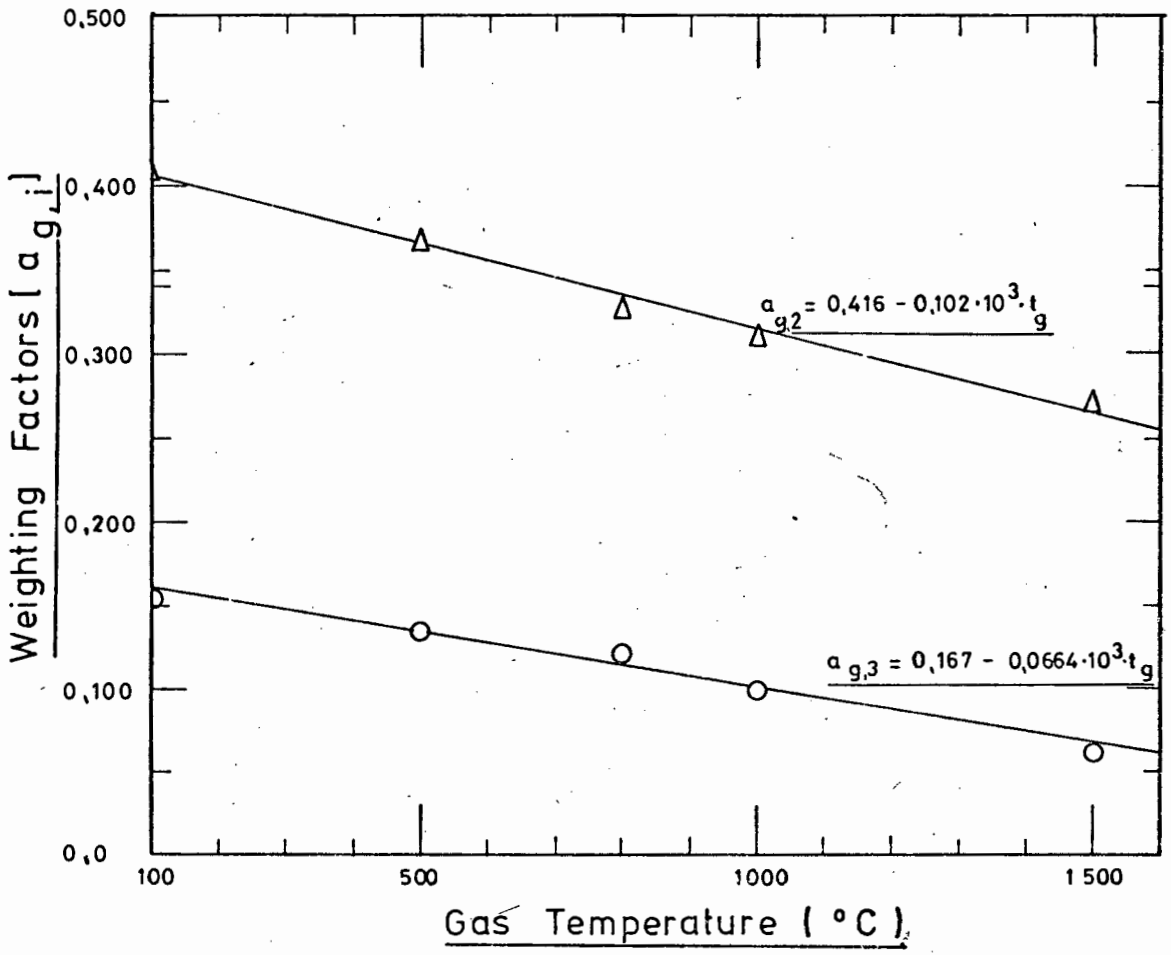

Figure H4 : Weighting factors of the two grey gases, for the gas emissivity model, as a function of temperature.

APPENDIX I

SUMMARY OF AN EARLIER COMBUSTION MODEL (REFERENCE 75)

A combustion and entrainment model was developed for the fluidized bed combustion process during the earlier work (75) associated with the combustion of coal in a 300 mm diameter refractory lined test rig. A large volume of input data was required. Information concerning combustion rate constants, splashing rates to describe the removal of material larger than that which could be removed by elutriation, attrition rate constants, the size and nature of the abraded material and much other data has to be supplied. Clearly the complex nature of the model would not readily lend itself for application in the interpretation of the present results obtained from the 1 000 mm diameter test facility. However, in view of its rigorous approach to the problem, further assumptions could be made to the existing model to provide a simpler and more adaptable method. The model has no direct bearing on the outcome of the conclusions drawn from the present work, therefore only a summary of the earlier theory (75) is presented in this Appendix for completeness.

The model has been developed based on the theories of different authors to explain the fluidized-bed combustion and entrainment processes under steady state conditions. From a knowledge of the original bed size grading and the grading of the fuel fed into the combustor the eventual gradings of the inert and combustible components within the bed as well as of the entrained material can be predicted. A major objective of the model is the prediction of combustion efficiencies and entrainment rates.

I.1 THE OVERALL CONCEPT

The model commences with an estimate of the combustion efficiency and a determination of one of the three parameters, superficial gas velocity, temperature or coal flow rate from

the remaining two which are used as input. The second stage of the calculation is the determination of the combustion efficiency. This is determined by considering the overall consumption of oxygen in the bed and comparing it with the coal feed rate. The efficiency thus determined is compared with the original estimate, and should they differ by more than 0,5% a new estimate for the efficiency is made based on the previous values. A new value for the unknown of the three parameters, velocity, temperature and coal flow is then determined and the calculation repeated until the desired accuracy is obtained. Elutriation rates, particle shrinkage rates and splashing rates have to be supplied as data. Existing correlations have been used for the first two, whilst a splashing rate constant has been determined from the experimental results. It should be emphasized that the splashing rate constant so determined is rig dependent, the most important influencing parameters being the freeboard height and the existence of baffles above the bed.

The third and final stage is concerned with the determination of particle entrainment rates from the bed. Particles are considered to be abraded in the bed and remain in the bed until they are removed either by elutriation, splashing or in the bed overflow. The major difference between this calculation and that for the determination of the combustion efficiency lies in the manner in which the shrinking particle, caused by combustion or abrasion is considered. In the case of combustion, no attrition is assumed to take place and no fines are produced. As a result the particle shrinks by chemical action only. Further, as the burning particles comprise only a small percentage of the entire bed mass, typically 1%, and therefore the overflow quantity or decrease in bed weight is neglected. In the case of attrition, the fines produced are considered and the mass balance of the system results in a more complex equation which is solved by considering particles falling into and out of a small size fraction. The splashing rate constant obtained from the previous stage is applied to the third stage, whilst the resulting ash size distribution is correlated with the

experimentally determined distribution by applying an attrition rate constant.

I.2 THE COMBUSTION MODEL

The model has been based on the two phase theory of fluidization (22), and assumes that the bubble phase is devoid of particles and therefore combustion takes place in the particulate phase. The combustor performance therefore, depends on the rate of transfer of the oxidising reagent from the bubble to the particulate phase and the heterogeneous reaction rate. Avedesian and Davidson (66) have shown that for gas solids contacting these can be measured by two dimensionless groups, the transfer factor X or the number of times a bubble interchanges its volume as it moves through a bed of height H_f, and a dimensionless velocity constant k*. These relationships are represented in equations (I1) and (I2).

$$X = \frac{Q_B \cdot H_f}{u_{BS} \cdot V_B} \qquad (I1a)$$

which can also be written

$$X = K_{bp} H_f / u_{BS} \qquad (I1b)$$

and

$$k^* = k \cdot H_{mf} / u_f \qquad (I2)$$

where k is defined as a first order particulate phase velocity constant by writing the rate of oxygen consumption per unit volume of particulate phase (66). From these relationships, it is evident that for high values of X, the transfer of the reagent to the particulate phase is high and the bed combustion reaction rate would be dependent on the heterogeneous reaction rate. Further, low values of X will result in much of the reagent by-passing the bed in the bubbles resulting in decreases in combustion efficiency as a result of the poor interchange between the bubble and the particulate phases. While the particle shrinks due to the combined action of combustion and attrition, the combustible material is assumed to be removed from the bed in the overflow, by elutriation and splashing.

The combustion model only considers the effect on the combustible matter in the bed. The derivation of the performance equations are summarized below, the complete details may be obtained from References (8, ch 11), (66) and (19).

I.2.1 Assumptions

The basis for the model is the work on the batch combustion of carbon in a fluidized bed by Avedesian and Davidson (66). By comparing the carbon burn-out time, and carbon dioxide and oxygen concentrations in the off gas with theoretical considerations, they deduced that the combustion process of particles in a fluidized bed is controlled by two diffusional resistances, the diffusion of oxygen from the bubble to the particulate phase and secondly the diffusion of the oxygen through the ash to the burning carbon particle. The combustion of the carbon particle is assumed to take place according to the two film theory of combustion, cf Section 1.4. By assuming that mass transfer can be described as a diffusion process and further that the concentration profiles are quickly established, i.e. fast chemical reactions, then equation (I3) representing concentrations about the particle as the particle shrinks results.

$$\frac{d}{dr}\left(r^2 \cdot \frac{dC}{dr}\right) = 0 \qquad (I3)$$

Equation (I3) is solved with the boundary conditions imposed by the reactions of the two film theory given above. By comparing the resulting transfer rate with that which would occur with no chemical reaction other than that which would occur at the particle surface, the molar flow of oxygen to the particle is written as

$$n = 2 \cdot \pi \cdot Sh \cdot G \cdot d \cdot C_p \qquad (I4)$$

The main assumptions of the model can be stated as follows:

1. The two-phase theory of fluidization as proposed by Davidson and Harrison (22) in which a bubble and a particulate phase exist has been assumed.

2. The particulate phase is completely mixed with regard to both the gas and solids within the phase.

3. The bubbles are in plug flow and of uniform diameter throughout the bed.

4. Coal is fed uniformly to all points on the plane at the base of the bed.

5. Coal particles burn in the particulate phase of the bed. The flow of oxygen to the particles is dependent on two diffusional resistances such that the molar flow of oxygen to the surface of the combustible particle is given by equation (I4).

6. Coal particles shrink due to the combined action of combustion and attrition. The rate of shrinkage by combustion is governed by equation (I4) whilst the tiny fragments worn off by attrition are carried away and are not considered as part of the solid population.

7. The volatile component is assumed to be combined with the char and to burn at the same rate as the char.

8. The mass of combustible particles within the bed is much less than the total inert bed mass.

I.2.2 Development of the General Performance Equation

As the gas bubbles pass through the bed, they exchange oxygen with the particulate phase in which the oxygen concentration remains constant and at the same level throughout the fluidized

bed at a value 'C_p'. The oxygen concentration of the bubble changes from 'C_o', the value at inlet to the bed, to 'C_b' which is dependent on the height of the bubble within the bed. The overall gas interchange coefficient between the bubble and the particulate phase K_{bp} is defined by equation (I5).

$$K_{bp} \cdot (C_p - C_b) = u_{BS} \cdot \frac{dC_b}{dh} \qquad (I5)$$

This interchange coefficient can be found by the relationship derived by Davidson and Harrison (22, pg 114) and is given by equation (I6).

$$K_{bp} = 4{,}5 \cdot \left(\frac{u_{mf}}{d_B}\right) + 5{,}85 \cdot \left(\frac{G^{0,5} \cdot g^{0,25}}{d_B^{1,25}}\right) \qquad (I6)$$

By solving equation (I5) to obtain the oxygen concentration in the bubble at a height h above the base of the bed, Gibbs (19) performs an overall oxygen balance over the whole bed to establish the overall oxygen consumption within the bed. This results in equation (I7).

$$\left[\begin{array}{c}\text{overall molar consumption of oxygen in the bed}\end{array}\right] = \left[\begin{array}{c}\text{oxygen entering particulate phase}\end{array}\right]_{h-0} - \left[\begin{array}{c}\text{oxygen leaving particulate phase}\end{array}\right]_{h-H_f} + \left[\begin{array}{c}\text{oxygen entering bubble phase}\end{array}\right]_{h-0} - \left[\begin{array}{c}\text{oxygen leaving bubble phase}\end{array}\right]_{h-H_f}$$

$$= A_t \cdot (C_0 - C_p) \cdot \{ (1 - f) \cdot u_{mf} + f \cdot u_{BS} \cdot (1 - e^{-X}) \} \qquad (I7)$$

Now this oxygen consumption is also equal to the sum of the rates of oxygen consumed by each of the combustible particles within the bed as given by equation (I4). Consider the bed to contain a mass M_c of combustible material with a particle size distribution given by $p_c(d)$, such that $M_c\, p_c(d)\, \Delta d$ represents the mass fraction of combustible material between the particle size of d to $d + \Delta d$ then the molar consumption

of oxygen in the particulate phase can be given by

$$\begin{bmatrix} \text{molar oxygen} \\ \text{consumption} \\ \text{in particul-} \\ \text{ate phase} \end{bmatrix} = \Sigma_{d_{min}}^{d_{max}} \left\{ \frac{M_c}{\rho_c \cdot \pi \cdot d^3 / 6} \right\} \cdot p_c(d) \cdot \Delta d \cdot (2 \cdot \pi \cdot Sh \cdot G \cdot d \cdot C_p)$$

$$= \frac{12 \cdot Sh \cdot G \cdot C_p}{\rho_c} \cdot \int_{d_{min}}^{d_{max}} \frac{M_c \cdot p_c(d)}{d^2} \, dd \qquad (I8)$$

The general bed performance equation is obtained by equating equations (I7) and (I8). This general performance equation is represented by equation (I9) below:

$$A_t \cdot (C_0 - C_p) \cdot \{ (1 - f) u_{mf} + f u_{BS} (1 - e^{-X}) \}$$

$$= \frac{12 \; Sh \; G \; C_p}{\rho_c} \int_{d_{min}}^{d_{max}} \frac{M_c \; p_c(d)}{d^2} \, dd \qquad (I9)$$

Equation (I9) is solved for C_p, i.e. the molar oxygen concentration in the particulate phase. From a knowledge of the coal feed rate to the combustor, a combustion efficiency can be deduced from the molar oxygen consumption which would result in a particulate oxygen concentration C_p. However, in order to solve equation (I9), the size distribution, p_c (d), and mass, M_c, of the burning solids contained in the bed must be known. These quantities are found by making use of an entrainment model with shrinking particles in the bed section, as proposed by Kunii and Levenspiel (8, ch 11) which is briefly developed below.

Consider a fluidized bed system as illustrated in Figure II. Coal of size distribution p_o (d) is fed at a rate F_o to a bed of weight M containing a mass M_c of combustibles of size distribution p_c(d). Coal is lost from the bed in the entrained

gas stream at a rate F_2 with a distribution p_2 (d), and in the bed overflow at a rate F_1 and with a size distribution p_1 (d) which is identical to that of the size distribution of combustibles in the bed. Prior to the development of the general entrainment rate equation, the rate equations for shrinkage and entrainment must be developed.

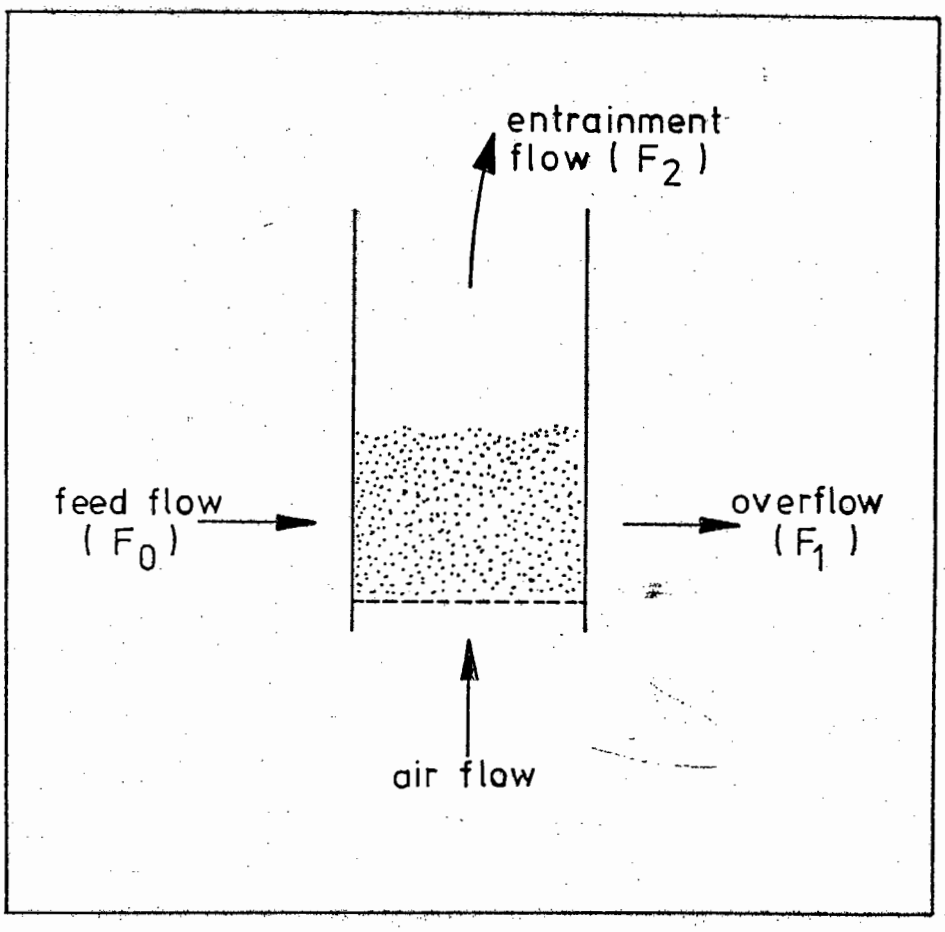

Figure II : Diagrammatic Representation of a Fluidized Bed to Illustrate the Components of the Mass Balance.

a) Rate Expressions for Shrinkage

Coal particles shrink as a result of the combustion process and due to attrition. The attrition of the coal particles is assumed to be a fraction of the combustion rate. The overall shrinkage rate can therefore be expressed as the sum of the

combustion and attrition rate components.

$$\Gamma(d) = \Gamma_c(d) + \Gamma_a(d) \qquad (I10)$$

The rate of shrinkage is assumed to obey a first order rate equation as given by

$$\Gamma(d) = -\frac{dd}{d\tau} \qquad (I11)$$

This rate of shrinkage due to combustion can be assessed by equating the molar flow of oxygen to the particle to the molar consumption of oxygen. From the overall chemical reaction of carbon with oxygen, it is known that one mole of oxygen combines with one mole of carbon to form carbon dioxide. The molar flow of oxygen is obtained from equation (I4) whilst the molar consumption of carbon is considered as the rate of shrinkage of the carbon particle.

$$\begin{bmatrix}\text{molar flow}\\ \text{of oxygen}\end{bmatrix} = \begin{bmatrix}\text{molar consumption}\\ \text{of carbon}\end{bmatrix}$$

$$2\cdot\pi\cdot Sh\cdot G\cdot d\cdot C_p = -\frac{1}{12}\cdot\rho_c\cdot\frac{\pi\cdot d^2}{2}\cdot\frac{dd}{d\tau}$$

$$\frac{dd}{d\tau} = -\frac{48\cdot Sh\cdot G\cdot C_p}{\rho_c\cdot d} \qquad (I12)$$

or

$$\Gamma_c(d) = \frac{48\ Sh\ G\ C_p}{\rho_c\cdot d} \qquad (I13)$$

and

$$\Gamma_a(d) = a\cdot\Gamma_c(d) \qquad (I14)$$

b) Rate Expressions for Entrainment

The entrainment rate is defined as the sum of two components, that due to elutriation, and that due to splashing. The elutriation phenomenon is well understood, and refers to the

selective removal of fines by entrainment from a mixture of particle sizes. This elutriation is therefore defined by the following:

$$\begin{bmatrix}\text{rate of removal of}\\ \text{solids of size } d\\ \text{per unit area of bed}\end{bmatrix} = K^* \cdot \begin{bmatrix}\text{fraction of}\\ \text{bed of}\\ \text{size } d\end{bmatrix}$$

$$-\frac{1}{A}\cdot\frac{d\,m(d)}{dt} = K^* \cdot \frac{m(d)}{M} \qquad (I15)$$

or it can be defined for a particular system as :

$$\begin{bmatrix}\text{rate of removal of}\\ \text{solids of size } d\end{bmatrix} = K \cdot \begin{bmatrix}\text{weight of solids}\\ \text{of size } d \text{ in bed}\end{bmatrix}$$

$$-\frac{d\,m(d)}{dt} = K \cdot m(d) \qquad (I16)$$

where

$$K^* = K \cdot M / A_t \qquad (I17)$$

The elutriation constant K* can be obtained from a number of correlations by different authors, the one proposed by Wen and Hashinger (16) was used. The elutriation constant K is then readily obtained from K* by equation (I17).

The splashing rate has been introduced to account for those particles lost from the fluidized bed system which are too large to be removed by the process of elutriation. The bursting of bubbles at the bed surface results in these particles being imparted with a high momentum and being lost from the fluidized bed. The splashing rate coefficient has been arbitrarily defined by Gibbs (19) by equation (I18).

$$\begin{bmatrix}\text{total combustibles}\\ \text{lost by splashing}\\ \text{in size interval}\\ d \text{ to } (d+\Delta d)\end{bmatrix} = S \cdot M_c \cdot p_c(d) \cdot \Delta d \qquad (I18)$$

where the splashing rate constant 'S' is assumed to be a function of particle diameter. Splashing rate constants have been derived from the experimental work for use in the

theoretical model. Therefore the total entrainment of solids from the bed in the size interval is given by the sum of the elutriated and splashed components as represented in equation (I19).

$$\left[\begin{array}{c}\textit{entrainment of combustibles in the size interval } d \textit{ to } (d+\Delta d)\end{array}\right] = (K + S)\cdot M_c \cdot p_c(d)\cdot \Delta d \qquad (I19)$$

c) Determination of the Mass of and the Particle Size Distribution of the Burning Particles in the Bed

With a knowledge of the rate equations for particle shrinkage and entrainment, a mass balance can be performed over a small size interval to determine the overall flow rates as well as determine the mass and size distribution of the burning particles in the fluidized bed, such that equation (I9) can be solved. Steady state conditions are assumed, with constant particle densities throughout the process. Back-mix flow in the bed enables the assumption of equivalent size analyses for both the bed material and the overflow stream to be made, i.e. $p_1(d) = p_c(d)$. Further the particle shrinkage is given by the general rate expression of equation (III). Referring to Figure I1, Kunii and Levenspiel (8, Ch 11) consider a mass balance on the solids to determine the total particle shrinkage rate, or

$$\left[\begin{array}{c}\textit{total solid shrinkage in the bed}\end{array}\right] = F_0 - (F_1 + F_2)$$

$$= \Sigma \left\{ \begin{array}{l}\textit{shrinkage of all solids in size interval } d \textit{ to } (d+\Delta d)\end{array} \right\}$$

$$= \Sigma \left\{ \rho_s \cdot \left[\frac{M_c \cdot p_c(d)\cdot \Delta d}{\rho_s \cdot \pi \cdot d^2/3}\right]\left[\frac{-\pi d^2 \cdot dd}{dt}\cdot \Delta t\right] \right\}$$

From which on taking the limit as Δd tends to dd, the total solids generation in unit time is found as :

$$\left[\begin{array}{c}\textit{solid shrinkage in the interval}\end{array}\right] = \frac{3\cdot M_c \cdot p_c(d)\cdot \Gamma(d)}{d}\, dd \qquad (I20)$$

For which total shrinkage is found as

$$F_0 - (F_1 + F_2) = \int \frac{3 \cdot M_c \cdot p_c(d) \cdot \Gamma(d)}{d} \, dd \qquad (I21)$$

Further, a mass balance for coal particles in the size interval d to $d + \Delta d$ is written as follows:

$$\begin{bmatrix} \text{total coal consumption in the bed in interval } d \text{ to } (d+\Delta d) \end{bmatrix} = \begin{bmatrix} \text{coal fed to the bed} \end{bmatrix} - \begin{bmatrix} \text{coal leaving in the overflow} \end{bmatrix} + \begin{bmatrix} \text{coal shrinking into interval from larger size} \end{bmatrix} - \begin{bmatrix} \text{coal shrinking out of interval to smaller size} \end{bmatrix} + \begin{bmatrix} \text{coal entrained in off gases} \end{bmatrix} \qquad (I22)$$

By equating equations (I22) and (I2C), and taking limits as Δd tends to zero, Kunii and Levenspiel (8, Ch 11) derive the general differential equation for fluidized beds with shrinking particles and entrainment given by equation (I23) below:

$$F_0 \cdot p_0(d) - F_1 \cdot p_c(d) - M_c \cdot (K+S) \cdot p_c(d) - M_c \cdot \frac{d\,(\Gamma(d) \cdot p_c(d))}{dd} + \frac{3 \cdot M_c}{d} \cdot p_c(d) \cdot \Gamma(d) = 0 \qquad (I23)$$

Kunii and Levenspiel (8) have derived the solution to equation (I23) for the size distribution $p_c(d)$ of the burning coal particles as

$$p_c(d) = \frac{F_0}{M_c} \cdot \frac{d^3}{\Gamma(d)} \cdot I(d, d_{max}) \cdot \int_{d_i=d_{min}}^{d_i=d_{max}} \frac{p_0(d_i)}{d_i^3 \cdot I(d_i, d_{max})} \, dd_i \qquad (I24)$$

where

$$I(d, d_{max}) = exp \left\{ - \int_{d}^{d_{max}} \frac{F_1/M_c + S + K}{\Gamma(d)} \, dd \right\} \qquad (I25)$$

and by assuming the amount of combustibles contained in the overflow to be small, equation (I25) becomes

$$I(d,d_{max}) = exp\ \{ - \int_{d}^{d_{max}} \frac{S + K}{\Gamma(d)}\, dd \} \qquad (I26)$$

To obtain the mass of combustibles in the bed M_c, equation (I24) is integrated over all particle sizes such that

$$M_c = F_0 \int_{d_{min}}^{d_{max}} \frac{d^3}{\Gamma(d)} \cdot I(d,d_{max}) \int_{d_i=d}^{d_i=d_{max}} \frac{p_0(d_i)}{d_i^3 \cdot I(d_i,d_{max})} \cdot dd_i \cdot dd \qquad (I27)$$

Therefore the mass of burning particles is determined from equation (I27) whilst the size distribution of the burning particles can be found from equation (I24). These parameters are then substituted into equation (I9) which is then solved for the resulting particulate oxygen concentration.

I.2.3 Discussion of the Combustion Model

The use of simple shrinkage rate equations has enabled these to be integrated to yield expressions which are easily solved numerically. Development of the equations has been limited to the case where particles shrink steadily and therefore cannot be used where particles break apart or agglomerate into large lumps.

The combustibles loss, and hence the combustion efficiency is determined from the entrained carbon flow. Higher superficial gas velocities result in higher elutriation and hence higher entrainment rates. An important factor affecting the entrainment rate, however, is the mass of coal or carbon particles contained in the bed. High oxygen transfer rates, and the

associated high combustion rates will result in the residence time of the carbon within the bed being small and therefore a smaller mass of carbon will be retained in the fluidized bed. Therefore fast reaction rates will result in high efficiencies. Gibbs (19) has shown that when operating near to stoichiometric conditions, the combustibles loss remains small for bubble diameters up to 100 mm, on increasing the diameter above this value, the combustibles loss increases rapidly. This is due mainly to the decrease in the transfer factor X, cf equation (I1), i.e. the number of times the bubble interchanges its volume as it moves through bed, as the bubble diameter increases. This transfer factor determines the diffusional resistance of the oxygen transfer from the bubble phase to the particulate phase.

In the case of high excess air, as was prevalent during all of the tests performed on the fluidized-bed combustor, the oxygen concentration throughout the bubble and particulate phases would be high since only a small amount of oxygen would be consumed. The combustion would therefore be controlled by local diffusion near the particle, with the transfer from the bubbles having only a small effect.

I.3 THE ENTRAINMENT MODEL

Entrainment has been considered to be made up of a splashing and an elutriation component. The entrainment is considered independently of the combustion process. In this model, inert ash and bed material are assumed to be fed to the bed separately from the carbon flow. The coal flow is assumed to be made up of two components, a pure coal flow which is used in the combustion model, and a pure ash flow which is used in the entrainment model.

The entrainment model is based on the work of Merrick and Highley (17). Although they (17) developed a new expression for entrainment to account for the loss of particles which are

larger than those which would be removed by the elutriation mechanism, this approach was not used in the earlier combustion model (75). Entrainment has been divided into splashing and elutriation as was done in the combustion model. Ash and inert bed material are fed into the bed in which the individual particles are reduced in size until they are eventually entrained in the off gases. Both the fine particles abraded away from the core particles and these reduced core particles are considered in the mass balance.

Attrition in a fluidized bed is therefore the result of the abrasion of the coarse particles to form fine particles with a corresponding reduction in the size of the coarse particles. Merrick and Highley (17) have found that the size distribution of the fines produced is almost constant for a particular bed material, and independent of the bed size distribution or operating conditions. They correlate the production of fines by the following equation

$$F_a = A \cdot (u_f - u_{mf}) \cdot M_b \qquad (I28)$$

However the use of equation (I28) for individual size fractions resulted in the predicted bed size distributions being considerably coarser than found experimentally (17). A correction factor was applied to account for the fact that though the coarser particles are continually in contact with each other, the fines spend some time in the voids created by the larger particles. Therefore a new rate equation was developed including a second abrasion rate constant A* and the proportion of particles in the bed smaller than the size d. The following equation for the production of fines by abrasion of particles of size d results:

$$\frac{dM_d}{dt} = -F_{ad} = -A^* \cdot f_d \cdot (u_f - u_{mf}) \cdot M_d \qquad (I29)$$

such that the sum of all the abrasion rates is the same as that given by equation (I28).

In the development of the mathematical model, the size distributions of the various components are divided up into

a number of size fractions, where i refers to the i th size fraction and where i=1 represents that fraction having the largest mean diameter. A mass balance is then performed on the system for the i th size interval, which results in equation (I30). Figure I2 diagrammatically represents the various components of the mass balance.

$$\left[\begin{matrix}\text{inert feed rate} \\ F_i\end{matrix}\right] + \left[\begin{matrix}\text{gain of particles from next largest size due to size reduction} \\ w_{i-1}\end{matrix}\right] + \left[\begin{matrix}\text{gain of fines by abrasion}\end{matrix}\right] = \left[\begin{matrix}\text{over-flow rate}\end{matrix}\right] + \left[\begin{matrix}\text{loss of weight due to fines production}\end{matrix}\right] + \left[\begin{matrix}\text{entrainment rate}\end{matrix}\right] + \left[\begin{matrix}\text{loss of particles to next smallest size by size reduction} \\ w_i\end{matrix}\right] \qquad (I30)$$

The only parameter which requires special calculation, is the rate of loss of particles to the next smallest size W_i. A mean removal rate constant, Z_m, is defined (17) by equations (I31) and (I32).

$$\frac{dM}{dt} = -Z_m \cdot M \qquad (I31)$$

where

$$Z_i = A_i^* + K_i + S_i + O/M_b \qquad (I32)$$

from which Merrick and Highley (17) deduce an expression for the rate of loss of particles to the next smallest size.

The final flow rates and size gradings are solved by an iterative procedure. The iteration is commenced by estimating the overflow rate and the bed size grading. A mass balance on each size grading is performed resulting in the mass of each size fraction being deduced. Summing each of these individual fractions results in a total bed weight being obtained which is then compared with the desired bed weight. The overflow rate is then adjusted until the bed weight is obtained to the desired accuracy.

I.4 APPLICATION OF THE MODEL

A suite of fifteen subroutines and a main "calling" programme have been developed for use on the UNIVAC computer for solving the theoretical model. Input to the programme consists mainly of the coal and inert feed size gradings on a cumulative percent by weight undersize basis. The particle sizes have a range, typically from about 50 microns to 10,0 mm. In the combustion model, these input size gradings are supplied at arbitrary intervals between each size. For the entrainment model, however, the particle sizes increase as a geometric progression given by equation (I33), where each of the values, namely the minimum diameter, the number of points and the exponent for the progression are supplied as input:

$$d_i = d_{min} \cdot (2)^{(i-1)} \qquad (I33)$$

Intermediate points are obtained by means of Aitken's method of interpolation. The integrations required for the solution of equation (I9) have been performed by means of Gregory's formula for numerical integration. It has been found that the use of a 75 micron step in the integration formula results in satisfactory results, though the computational time is extremely high, about 30 minutes due to the relatively inefficient integration technique. Use of a central difference formula for the integration would improve the computation substantially.

I.5 DISCUSSION OF THE MODEL

I.5.1 The Combustion Model

A major limitation of the combustion model lies in the requirement that the size distribution function of the input coal stream, $p_o(d)$, be a smooth curve. Although the curve of the cumulative percent by weight undersize versus the particle diameter almost invariably yields a smooth curve, the resulting size distribution p_o (d) may be irregular. Indeed, the cumulative size distributions of the coals used in the earlier experimental work result

in very irregular size distribution functions, $p_o(d)$. The smoothed size distribution functions were used as input to the computer model, resulting in combustion efficiencies somewhat higher than anticipated from the experimental work. However by artificially adjusting the attrition rate of the coal, expressed as a fraction of the combustion rate resulted in values for combustion efficiency approaching those achieved during the earlier experimental work (75). By changing the gas velocities, changes in the combustion efficiency of the same order as those found by the regression relationships were found. Variations in the operating temperature have only a minor effect on the resulting combustion efficiency. Adjustment of bubble velocity and diameter effected the required change in the combustion efficiency. These adjustments in fact alter the transfer factor 'X', given by equation (I1).

It is clear therefore that adequate answers are provided by the combustion model. More work is required to establish the precise nature of the attrition and possibly the combustion rate. An improved model for the prediction of bubble diameters and velocities is also required so that the transfer factor 'X' can be derived from first principles rather than having this parameter artificially suppressed or exaggerated, dependent on the bed operating temperature.

I.5.2 The Entrainment Model

The resulting size grading of the entrained material flow predicted by the entrainment model are somewhat coarser than those obtained from the experimental work. However, adjustment of the attrition rates of the ash and bed material alter the entrained size gradings. A further complication is the fact that the size grading of the resulting ash on combustion of the coal particle has been assumed to be similar to that of the original coal feed. This is probably an over simplification, as the ash of most South African coals is generally inherent or homogeneously dispersed in the coal body. Further the coal feed did not appear to contain complete inert lumps of

ash the size of the coal particle. Therefore the ash feed size distribution would on average be smaller than that of the coal feed. It is therefore evident, that much additional information is necessary to be able to fully utilize the entrainment model.

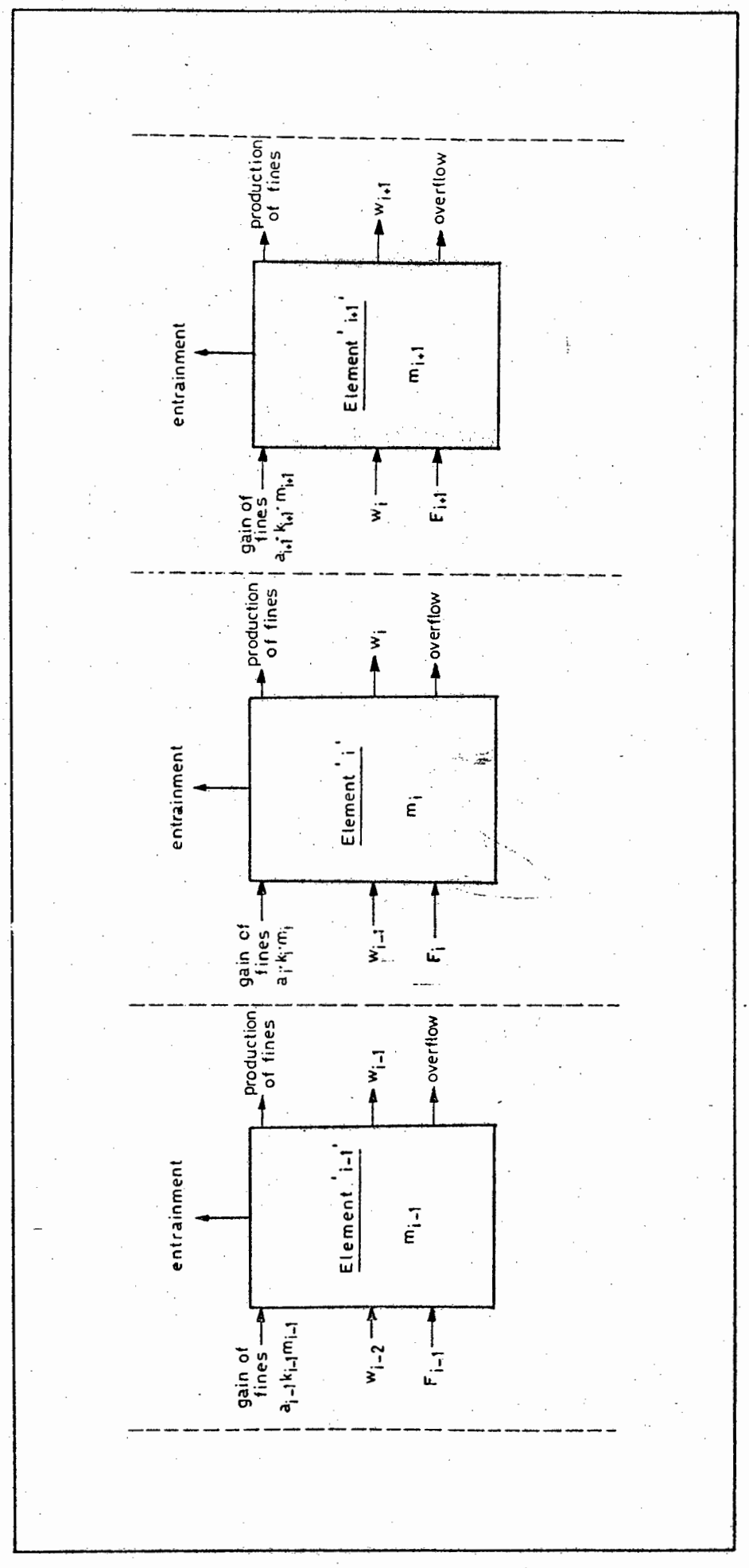

Figure I2 : Diagram to illustrate the mass balance performed on the i th size fraction of the fluidized bed system.

APPENDIX J

COMPLETE TABLE OF CONTENTS, LIST OF FIGURES, LIST OF TABLES

COMPLETE TABLE OF CONTENTS

Page

LIST OF FIGURES

Page

LIST OF TABLES